Modelling excited argon clusters : ggeometries,spectroscopic properties and non-adiabatic relaxation dynamics

Mukul Dhiman

Normandie Université

THÈSE

Pour obtenir le diplôme de doctorat

Spécialité PHYSIQUE

Préparée au sein de l'Université de Caen Normandie

Modelling Excited Argon Clusters: Geometries, Spectroscopic Properties and Non-Adiabatic Relaxation Dynamics

Présentée et soutenue par
MUKUL DHIMAN

Thèse soutenue le 01/06/2022 devant le jury composé de		
M. DAVID BONHOMMEAU	Maître de conférences HDR, UNIVERSITE REIMS CHAMPAGNE ARDENNE	Rapporteur du jury
M. BASILE.F CURCHOD	Professeur associé, BRISTOL - UNIVERSITY OF BRISTOL	Rapporteur du jury
MME JULIE DOUADY	Maître de conférences, Université Caen Normandie	Membre du jury Co-encadrante
M. LIONEL POISSON	Directeur de recherche au CNRS, Université Paris-Saclay	Membre du jury
M. FERNAND SPIEGELMAN	Directeur de recherche au CNRS, UNIVERSITE TOULOUSE 3 PAUL SABATIER	Membre du jury
MME ALEXANDRA VIEL	Directeur de recherche, UNIVERSITE RENNES 1	Président du jury
M. BENOIT GERVAIS	Chercheur-ingénieur au CEA, Université Caen Normandie	Directeur de thèse

Thèse dirigée par BENOIT GERVAIS (Centre de recherche sur les ions, les matériaux et la photonique (Caen))

UNIVERSITÉ CAEN NORMANDIE

ED 591 PSIME

CIMAP

Abstract

In part I of this thesis: We investigate Ar_2^* Potential Energy Curves (PECs) using different *ab initio* techniques in MOLCAS. We find that Multi Reference Configuration Interaction (MRCI) calculations give the best 4*s* PECs. We also studied the geometry of Ar_3^* in its lowest triplet state using Complete Active Space Perturbation Theory 2 (CASPT2), our results were not in-line with the previous study based on the Diatomics-In-Molecules (DIM) approach, as used by Naumkin and Wales. We further investigate the geometry of the lowest excitonic levels of small argon clusters, $Ar_{N=1-13}$, using the Hole-Particle Pseudopotential (HPP) formalism introduced by Dupláa and Spiegelmann. This formalism allows us to model the excited states associated with Rydberg orbitals with higher accuracy than previous DIM studies. In contrast to the DIM method, the HPP formalism predicts the excitation to localise mostly on two atoms rather than three, for the relaxed geometry of the lowest triplet state. The hole localisation on a dimer is associated with the appearance of a large electric dipole, which depends on the isomer geometry. This dipole indicates the strong Pauli repulsion experienced by the Rydberg electron, which pushes it out of the cluster. For clusters at their ground state equilibrium geometry, we observe the formation of a singlet-state band associated with the 4s Ar orbital, well separated from the upper states, which matches quite well with the so-called surface exciton band observed experimentally. We also propose an improvement to the previous DIM study by supplying an *ad hoc* state, which uncouples the 4s $^{1,3}\Sigma_g^+$ state from the higher excited states. On investigation of lowest excitonic levels using Diabatized-DIM (Di-DIM), we observe the symmetry breaking similar to HPP and localisation of excitation on two atoms rather than three, in the geometry of relaxed lowest triplet state.

In part II of this thesis: We propose Excitation Dynamics with Quantum Transition on a whole Di-DIM basis. Here, we give an algorithm for coefficient evolution based on time-averaged Hamiltonian to minimise the perturbations. *On-the-fly* adiabatic PECs is evaluated using Di-DIM method on which a trajectory is evolved non-adiabatically. The Spin-Orbit-Coupling (SOC) is included within the Di-DIM method. The Fewest Switching Surface Hopping (FSSH) is employed for hops between adiabatic surfaces. We use this method to study excitation evolution in a small neutral argon cluster, ($N = 3, 7$), which has not been done previously. We further investigate the fragmentation channels associated with the relaxation following excitation in the lowest singlet excited state of the 4s band. We show the effect of highly degenerate states and their effect on relaxation dynamics. We observe relaxation to a lower triplet state in Ar_3^* and Ar_7^* clusters. We observe the emission of the excited atom to be the dominant dissociation channel with the formation of a ground state cluster. This is followed by the formation of an excimer (Ar_2^*) and atomisation. The observation of excimer with a bigger excited cluster is dependent on the initial cluster size. We do not observe the formation of a stable excited trimer isomer using Di-DIM. We observe that the nature and the number of states used as the input for DIM influences significantly the outcome of the relaxation dynamics.

KEYWORDS: Self-Trapped Excitons(STE's), Hole Patricle Pseudopotential (HPP), Rare-Gas Clusters (RGC), Argon Systems, Molecular Dynamics (MD), Diatomic-in-Molecule (DIM), Electronic Structure Calculation, Excitation dynamics, Mixed Classical Quantum Dynamics (MCQD), Excited Rare-Gas Clusters, Surface hopping, Time Averaged Hamiltonian, Non-adiabatic relaxation dynamics

Contents

Acknowledgements

Studying in Caen France over the last years has been a wonderful experience. I have always enjoyed open-minded and stimulating environment, which has been provided to me by the wonderful people surrounding me in CIMAP and GANIL laboratory. I have to thank many people for making this period a success not only academically, but in terms of general life experience.

First of all, I would like to thank Benoit Gervais who gave me this opportunity to carry on my research endeavours. His deep knowledge has been utmost stimulating and making me challenge my intellectual limits. He has always been patient and supportive.

Next, I am gratified to have a colleague like Eric Giglio. He is as much integral part of my thesis as is Benoit and Julie. He helped me enormously with his discussions, that stirred my thought process to bring about new ideas. The coffee breaks leading to hours of discussion. He inspired me and helped me to boost my confidence in difficult times, helped me think out of the box and to question things beyond traditional boundaries. I can not imagine my PhD without his invaluable support.

I would also like to thank all the members of our SIMUL team. In particular, I would like to extend my warm regards to Julie Douady, who is also my co-supervisor, for her assistance in simulations and discussions on MOLCAS with Emmanuelle Jacquet. I would like to thank both of them for their invaluable support during this thesis, academic and personal, especially in first few months of my arrival in Caen.

Warm thanks goes to my dear friends Judith Jeyafreeda, Jacobs Ramon, Taras, Diago, Nishu, Alma, Gaurav Dhiman and Alexandra for sharing the precious moments with me, where I needed to forget science. I would also like to extend my gratitude to all my friends in Caen, back home in India and around world for their support. I thank Min Liu, Tristan, Massimo Lager and Eric Giglio for sharing coffee and the feeling of sunny places. And I thank OPTIC group of UNICAEN for their big efforts to support us PhD students here.

I want to thank Marie Legay-Meleux for her assistance with all her administrative help. I would also like to thank Sarah and Lucy for resolving all the administrative issues in the Lab.

I am grateful for ED-PSIME doctoral school of University of Caen, Normandy University and french administration for for supporting my research work over the last three years. I would like to thank CIMAP lab for funding my several travels related to conferences, workshop and meetings.

And finally and most importantly, I would like to thank my parents, without their enormous support I could not have been here. I would like to thank them for being there for me, always.

Publications

- Mukul Dhiman, Julie Douady & Benoit Gervais (2022) Geometry, absorption and luminescence of small Ar clusters, Mol. Phy., DOI: 10.1080/00268976.2022.2049905. [1] For Part 1.

Introduction

In the development of the theory of dielectrics, the wide use of the exciton concept, introduced in 1931 by Frenkel[2], has proved especially fruitful. This concept has proved highly effective in studying energy migration processes in solids, certain polymers, and some biological objects. In natural sciences, the study of photo converters has been a cornerstone of several scientific endeavours and discoveries. Starting from understanding the underlying mechanism in biological media to convert photon energy to our ability to produce electricity in photovoltaic cells, has motivated generations of scientists to work on the possibility to understand and improve the efficiency of these processes. The work presented in this thesis is also motivated by the endeavours to have a better understanding of the atomic-level interactions to further enhance the efficiency of such photo-converter cells. The dynamics of exciton play a pivotal role in understanding and improving the efficiency of the photo conversion mechanism. They are used to determine the optical properties of different materials, such as absorption but also emission via fluorescence or phosphorescence [3]. They are used to understand transport of energy with zero net charge [4, 5, 6] and chemical reactions [7]. In biological media, the work done on photosynthesis [8, 9] shows the role played by the exciton.

The study of exciton and charge transfer is essential for electronic excitation in condensed matter and nanoscale systems. The formation of long-lived electron-hole pair is stabilised by its interactions with surrounding lattice atoms, forming the simplest exciton. The existence of excitons is not limited to bulk, but a great deal of research has been done for exciton in Rare-Gas (RG) clusters. The RG cluster being a small system, i.e., constituting from several 100 atoms to 10^6 atoms and more, can be treated on the same ground as nanoparticles and they act as a bridge between isolated systems made of few atoms to condensed matter physics. The idea behind being, that the rare gas has a wide band gap and closed shell, which allows us to study the properties of electron-hole quasi-particle, unlike metals in which excitons are not formed. The possible study is of fundamental interest to get properties like structure, spectroscopy, magnetism, dynamics, thermodynamics and mechanics.

Recent, advances in experimental techniques to resolve electronic motion have rejuvenated the interest in cluster dynamics. The initial investigation of exciton relaxation in an Argon rare-gas cluster by the means of a pump-probe experiment in the *ps* regime was carried out by L. Poission *et al* [10]. The linear decay and formation of self-trapped surface excitons were observed which is not very well understood. The modelling of such systems is a tremendous challenge and no one-size-fits-all solutions can be expected. The literature is scarce that studies the dynamics of excitons on rare-gas clusters. The work of Johnson[11] and Cui[12, 13] was limited to single electronic states. They provided the study of sputtering, however, they do not give the relaxation dynamics that lead to the formation of the exciton.

In this thesis, the objective is to study the dynamics of exciton in Argon rare-gas clusters to understand and provide theoretical support for experimental observations. We start in chapter 1 by providing an overview of excitons in argon solids and clusters, their properties and some of the theoretical models to study them. Where we will first revisit the relation between material properties and exciton characteris-

tics using the distinction between organic and inorganic materials with the connection to rare-gas systems. In chapter 2 we give the *ab initio* techniques to get the potential energy curves (PECs) for excited and ionised argon dimer. These methods are size intensive, therefore, to study bigger systems, in chapter 3, we give semi-empirical methods like diatomic-in-molecules (DIM) and hole-particle pseudopotential (HPP) to study the geometry of the lowest-energy excited state for Ar_N^* clusters (N=3-15). The discussion on PECs using *ab initio* and semi-empirical methods along with the lowest energy isomer geometries of the excited argon clusters in chapter 4 make the first part of this thesis. In the second part, we start by giving a brief introduction of methods developed over several decades to study non-adiabatic dynamics in chapter 5. In the following chapter we give our algorithm to do the same to study excitation evolution in chapter 6. This work is based on previous studies of ionic rare-gas clusters. We present our results of dynamics on small argon cluster in chapter 7 and finally conclude this thesis in chapter 8 with its possible application of our dynamics model and future prospects.

Unless otherwise indicated, throughout this thesis atomic system of units is used, i.e., $m = 1$, $e = 1$, $\hbar = 1$ and $4\pi\varepsilon_0 = 1$. The unit of length is the Bohr radius $a_0 = 0.529167$ Å, the unit of energy or hatree is twice the ionisation potential of the hydrogen atom which is, 1 Hatree = 2 Rydberg = 27.2113957 eV or in wave number, 219474.625 cm^{-1}.

Chapter 1

Introduction to Exciton in Rare Gas Clusters

It is known that the Rare-Gas (RG) atoms are weakly bound to each other in their ground states by van der Waals (London dispersion) forces in the long-range and Pauli repulsion in the short-range. On ionisation, stronger electrostatic forces come into play making ionic clusters compact and stable. However, a meta-stable state is formed when an electron is promoted to an excited state by photo-excitation or ion collision. This meta-stable state is made of a correlated electron-hole pair (a quasi-particle) termed an exciton.

Rare gas aggregates with their dominant dispersion forces can either exist as a cluster of atoms or they can be in form of solid crystals making them a part of condensed matter physics. Excitons formed in the *simplest* solids of nature, namely Face-Centered-Cube (FCC) rare-gas solids (RGS), are often regarded as some exotic entities, without any significance for practical life. The RG systems are elegant and simple due to their uniformity and barely interacting closed-shell atoms. With their uncanny resemblance in spectroscopic properties of clusters and solids [14, 15, 16]. Therefore, they are considered to be an ideal candidate to form a bridge between small and medium systems like clusters (atomic and molecular physics) and bulk (condensed matter physics). Rare-gas crystals exist only at cryogenic temperatures, and most of the optical spectroscopy of excitonic processes must be done in the vacuum ultraviolet. All the pioneering work done on the rare gas excited system, from their creation to their "fate" in the solids has been summarised in the book by Knox [17].

With the motivation to do dynamics as given in the introduction, in this chapter, we will give a brief introduction about exciton, their electronic structure, spectroscopic properties, evolution through the solids and clusters and theoretical models developed to study exciton.

1.1 What is an exciton?

When an electron is photo-excited from the valence band as shown in the figure 1.1, a hole is created which is not screened by the valence electron like in metals and therefore, an exciton exists only in insulator-type materials or in organic and inorganic type semiconductors. If the energy of an incident photon is less than the ionisation energy of the electron, it will be captured in a low-lying conduction band. The conduction band is a mean-field concept which corresponds to Lowest Unoccupied Molecular Orbitals (LUMO) to have an extra electron. With correlations taken into account, we observe the formation of an exciton band lower than the conduction band, therefore, reducing the band gap and enabling a long-lived exciton. This

electron-hole pair is electrically neutral. However, due to the presence of electrostatic forces between the electron and the hole, the electron does not diffuse throughout the crystal but remains bound to the hole. This spatially correlated electron-hole pair, when considered together, is called an exciton. The exciton can also be formed by other processes like the injection of free electrons or holes in the materials, collision processes, etc.

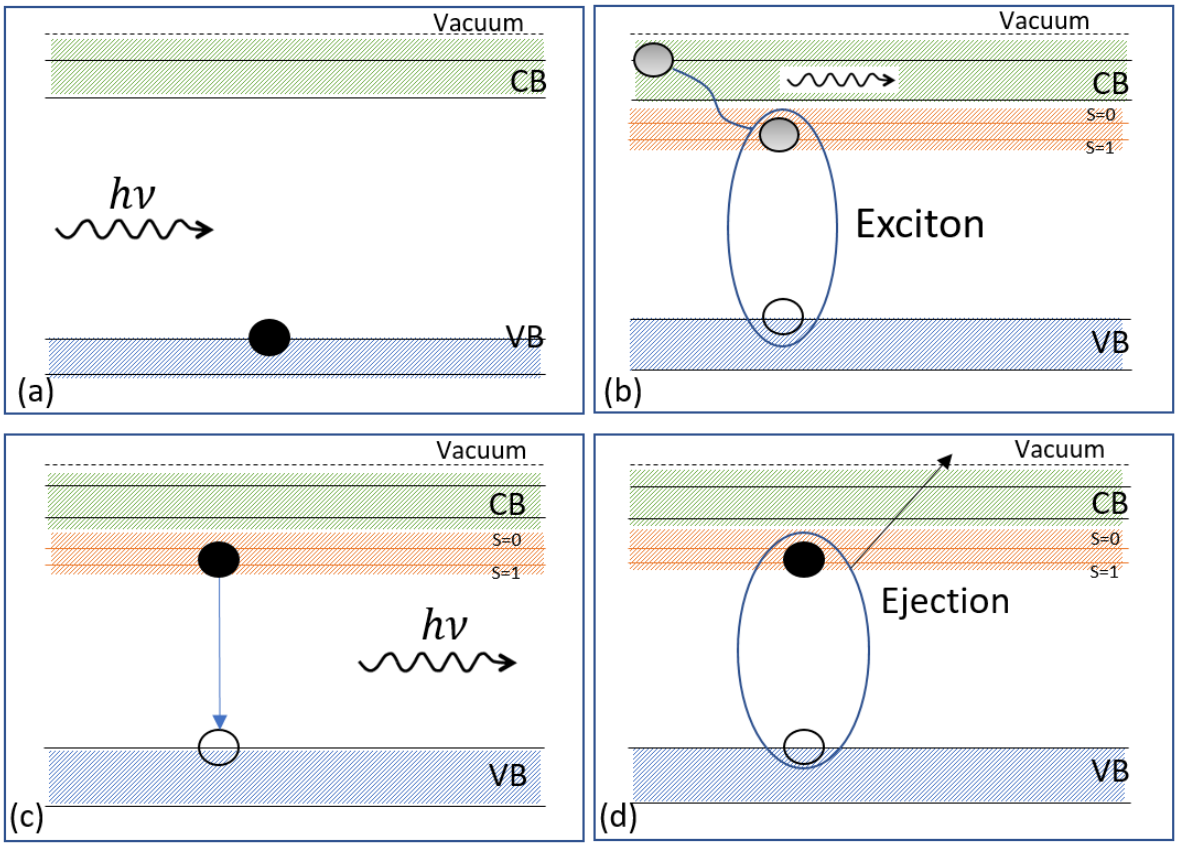

Figure 1.1: (a) The excitation of an electron from the valence band (VB) to the conduction band (CB). (b) shows the decay of excitation from high conduction band to lower exciton band leading to formation of the electron-hole pair. (c) shows the electron-hole recombination with emission of a photon. (d) shows the possible emission of the electron-hole pair with the associated atom to the continuum shown by the dotted line also called desorption.

We observe a long-lived triplet excited state due to the forbidden transition from the low-lying triplet to the ground state. This triplet state decays by radiative recombination of the electron-hole pair. In the exciton band, the triplet is lower than the singlet. Being neutral long-lived species, they can transfer energy without charge [5] and the decay by recombination of emission of photon 1.1(c). However, with enough energy, this excited electron-hole pair may have energy greater than the binding energy that eventually leads to the emission of an excited neutral species referred to as desorption in solids and sputtering in clusters 1.1(d).

In a brief introduction, the existence of such an electron-hole pair was first introduced by Frenkel [2] and was further generalised by Wannier [18] and Peierls (1932) and implemented to study excitation in aggregates of molecules. The details on static and dynamic properties of exciton depend on the material in which they are formed. In the literature we have two types of excitons: Wannier Mott and Frankel excitons, as shown in Figure 1.2.

The Wannier-Mott exciton, also sometimes referred to as free exciton is associated with the excited electron orbital delocalised over several atoms, i.e., the radius of these excitons is much larger than the inter-atomic distance making a unit cell. This type of exciton is formed in inorganic materials with a small

band gap and a large dielectric constant ($\varepsilon_r > 10$), such that the coulomb effect between electrons and holes is small due to dielectric screening. Due to these effects, the binding energy is small, typically of order 0.01 eV.

The Frenkel exciton is usually tightly bound to the atom with a radius smaller than the inter-atomic distance. They usually have large band gap and are found in organic semiconductors with small dielectric constant. With minimal screening effects, the binding energy of these excitons is increased and lies between $0.1 - 1$ eV. As the organic materials are formed by molecular binding blocks, they can host Frenkel exciton for their localisation character [19].

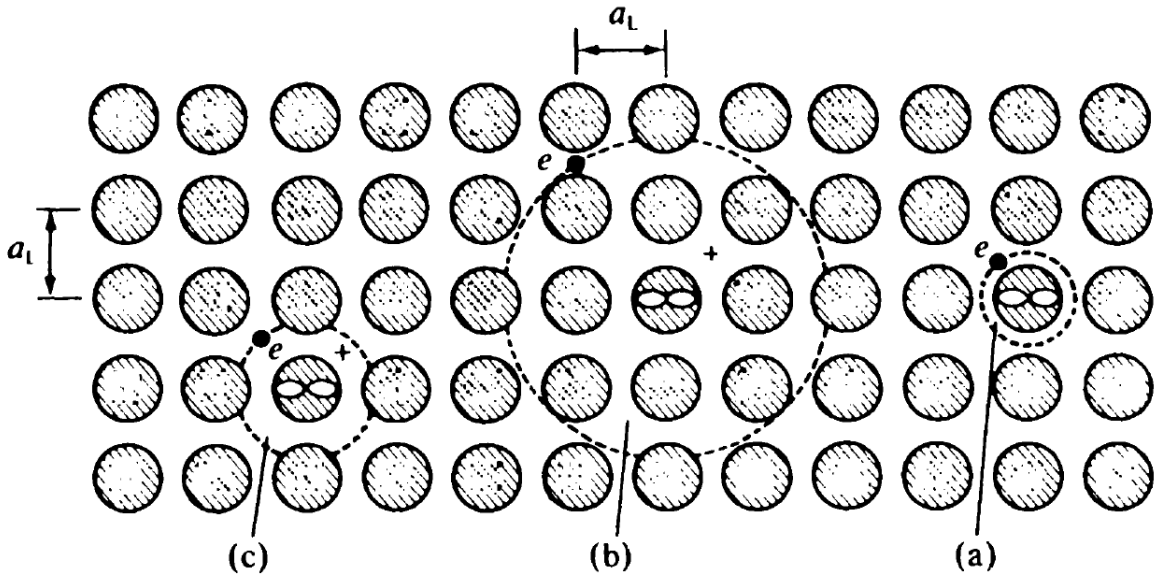

Figure 1.2: (a) Small radius Frenkel exciton where the radius a is small compared to the lattice constant a_L. (b) The large-radius Wannier-Mott exciton where the radius a is much larger than lattice constant (c) Intermediate or charge-transfer exciton where a is similar to lattice constant and close to nearest neighbour. (Taken from book [20]) which refers to Kalinowski *et al.* 1977 [21].

The existence of exciton in the rare-gas system can be broadly distinguished as Free Exciton (FE) or trapped excitons. The trapping state is associated with the formation of a Self-Trapped-Excitons (STEs) which is identified as an electron-hole pair trapped at a local lattice site or in a potential well. The Self-Trapped-Excitons can either stay in the centre of the cluster concerning the hole called Atomic type Self-Trapped-Excitons (a-STEs) or migrate/relax to the surface due to interaction with lattice in rare gas clusters forming Molecular type Self-Trapped-Excitons (m-STEs). STE provides a way of channelling electronic excitation into energetic atomic processes in pure crystals, such as lattice defects and atomic desorption from the surfaces. In their absence, electronic excitation would remain completely delocalised in a perfect crystal.

This work is based on the two excellent books on STEs by Song [15] and Pope and Swenberg [20], giving in great detail the developments in the study of the exciton in all material types. Besides that, two review papers by I.Y. Fugol' [22, 16] discuss the evolution of FE and STEs in condensed rare gas crystals using numerous spectroscopic data while discussing the exciton-phonon interaction and polariton effects, the mechanisms of self-trapped barrier overcoming, the defect formation under excitation and the kinetics of exciton and energy transfer. I.Y. Fugol' also discussed the coexistence of FE and STEs, which was theoretically predicted by Rashba [23].

The framework of the theoretical study of excited states in a cluster or a solid is built on the individual

study of excited monomers and dimers. Thus, for a given arrangement of such monomers and dimers, it is possible to have the interpretation of properties of larger aggregates. Hence, the *ab initio* nature of excited monomers and dimers is significant. The excited dimers, also known as excimers, have different properties from excited monomers and ground-state atoms. Excimers in inorganic systems were determined long before their identification in organic systems. Thus, the Hg* + Hg $\rightarrow$ Hg_2^* reaction was recognised by Rayleigh [24] in 1927. Here, an excited Hg* atom reacts with a ground-state Hg atom to produce an excited dimer or excimer; the ground-state atoms do not form a stable physical dimer. The same situation exists with the noble gases, e.g., He_2^* is a stable Helium excimer and Xe_2^* is a stable Xenon excimer whose fluorescence properties are used in laser applications.

The possibility to study the excitation transfer in solids and clusters for such a simple system and their possible applications in Lasers and Solids led to a landslide of experimental and theoretical work on exciton. With the rapid advancements in solid-state physics and the ease of forming RG crystals, considerable experimental work has been done on solids compared to that on clusters. In this chapter, we will review the state-of-the-art experimental and theoretical work relevant to the understanding of exciton properties in rare gas clusters, focusing on Ar clusters. As the properties of rare gas clusters and solids are similar, for convenience, we will refer to everything as Rare Gas Clusters (RGC) unless mentioned otherwise. For comparison, we will discuss other RGCs when required.

1.2 Electronic Structure

The knowledge of the electronic structure of a system made of nuclei and electrons provides the ability to predict the physical and chemical properties of the system. It is a cornerstone of physical chemistry and is used to understand chemical reactions, bond formation and dissociation, geometry prediction and much more. Therefore, we will present here the current understanding of the electronic structure of Ar clusters and solids.

The first estimates of the electronic structure were given by Mulliken [25] for Xe_2^* in which he proposed to consider the excited states to be represented by diffuse Rydberg state on the ground-state ionic core. This is a good approximation because the ionic core is seldom perturbed by the Rydberg electrons, at least for inter-nuclear separation in the vicinity of the equilibrium distance of the ionic core. He proposed an excellent interpretation of the excited state in which an electron is excited from the ground state Highest Occupied Molecular Orbitals (HOMO), σ_u, π_g, π_u and σ_g $5p$-orbitals into the Rydberg orbital. Creating a hole in the anti-bonding MO, σ_u and π_g makes the system stable whereas creating a hole in the bonding MO, π_u and σ_g, makes it unstable. Therefore, the PECs associated with holes in the σ_u and π_g MOs would be binding and those of π_u and σ_g would be non-binding, giving deeper potential energy well for excited states for the hole in σ_u MO because of its anti-bonding nature. Therefore, the lowest energy Rydberg states for Rg_2 are the $^3\Sigma_u^+$ and $^1\Sigma_u^+$ associated to $[Rg_2^+, X^2\Sigma_u^+]ns\sigma_g$ with relative energy ordering being triplet below singlet.

The $^{2S+1}\Sigma_p^{p'}$ electronic state labels (term symbols) apply to the Λ, S coupling scheme [26] and include quantum numbers for the total electron spin (S), the component of electronic orbital angular momentum along the inter-nuclear axis (Λ; $\Lambda = 0 \rightarrow \Sigma$, $\Lambda = 1 \rightarrow \Pi$, etc.), and the wave function's inversion parity ($p = g$ if even and u if odd) and reflection parity ($p' = +$ or –) in a plane containing the inter-nuclear axis. States having $\Lambda = 0$ are either Σ_p^+ or Σ_p^-. Each state with $\Lambda_p > 0$ comprises two symmetry states (Λ_p^+ and Λ_p^-, sometimes referred to as lambda doublets), with the superscript + or – having the same meaning as that

for the $\Lambda = 0$ states. Also associated with each Λ, S state are sub-states labelled by values of the quantum number Ω, which specifies the value of the total electronic angular momentum along the inter-nuclear axis. For Λ, S coupling [27], Ω is the sum of Λ and the component of the total electron spin along the inter-nuclear axis.

One of the first comprehensive PECs for a rare gas in its excited state was calculated using configuration interaction (CI) by Cohen and Schneider [27, 28] for Ne_2^*. They provided a scheme to include spin-orbit-coupling (SOC) and discuss briefly non-adiabatic couplings (NAC). The first lowest energy PECs for excited Ar dimer were obtained using *ab initio* CI-based using Slater-type orbitals (STOs) by Saxon and Liu [29]. Improvements were obtained later with the use of Gaussian-type orbitals (GTOs) by Spiegelmann *et al.* [30, 31] using the SOC scheme as given by Cohen and Schneider [27]. Spiegelmann *et al.* also reported many PECs of 4s and 4p Rydberg states. Yates *et al.* [32] used an STO basis set with a refined effective core potential and calculated the PECs of the 4s and 4p Rydberg states by the polarisation CI method. Further work offered by Mizukami and Nakatsuji [33] using a large GTO basis set by symmetry adapted cluster (SAC) expansion and SAC-CI methods, however, compared to previous and future work, they did not recover the correct PECs. Recently, a semi-empirical hole-particle pseudopotential (HPP) method given by Duplaa and Spiegelmann [34] gives a good estimate of the PECs of Ar excimer and provides a possibility for being scaled up for systems bigger than a dimer.

The electronic structure of condensed rare gas (except the He) valence band derives from the highest occupied atomic p atomic orbitals, with weak bonding. The valence band is relatively narrow and the hole mass is large leading to low hole mobility. The conduction bands are wide and nearly free-electron-like. The energy gaps are very large. For example, the energy gap in Ar is 15.75 eV, much higher than LiF. Thereby, RG systems claim the title of having the widest solid-state band gaps in nature. The effect of correlation is also important to obtain reliable energy gaps and bandwidths. Fowler showed that a substantial correction to the band gap in the order of a few eV is made through polarization correlation in large gap materials [35]. This wide band gap places the conduction band above the vacuum level and the electron affinity of Ar is thus negative, i.e., an additional electron does not bond to Ar clusters or solids.

Furthermore, drift mobility helps to understand the effects of phonon interaction with the electronically excited states. The drift mobility of carriers in liquid and solid rare gases are summarised in Table 1.1. We see the hole mobility is low in all the cases, which is expected, as the hole mobility depends on the hole-hopping which is difficult in rare gas clusters or solids aside from exceptionally low hole mobility 10^{-4} cm^2/Vs for He^4 and other rare gas is around 2×10^{-2} cm^2/Vs. With significantly low mobility, the mechanism for excitation transport comes from the thermally activated hopping. Therefore in solids, holes have a higher tendency to self-trap. However, they have an exceptionally high electron mobility of order few thousand cm^2/Vs due to a long mean free path and empty conduction band. The electron mobility of a typical metal ranges between 30-50 cm^2/Vs and for crystalline silicon is around 1000 cm^2/Vs.

Table 1.1: Drift Mobility [cm^2/Vs s] of carriers with charge $\pm$ e in solids and condensed gases. Mobilities which exhibit thermally activated behaviour are indicated by *. (μ_S^- and μ_L^- are drift electron mobility and μ_S^+ and μ_L^+ are drift hole mobility for solid (S) and liquid (L) condensed gases) at the triplet point. Table is adapted from [15]

Atom	Temperature(K)	μ_S^-	μ_L^-	μ_S^+	μ_L^+
^{4}He	4.2	$*10^{-4}$	$*2 \times 10^{-2}$	$*10^{-4}$	5×10^{-2}
Ne	25	600	$*1.6 \times 10^{-3}$	$*1.05 \times 10^{-2}$	1.6×10^{-3}
Ar	84	1000	475	$*2.3 \times 10^{-2}$	
Kr	116	3600	1800	$*4 \times 10^{-2}$	
Xe	161	4000	1900	1.7×10^{-2}	

Regarding exciton formation and trapping, one of the interpretations of exciton given in the book on STEs by Song [15] suggests that when a conduction electron repels surrounding rare gas atoms, it creates lattice expansion or bubble around the charged centre. The creation of this bubble around conduction electron or exciton is associated with negative electron affinity in the condensed phase of the light rare gases. The negative electron affinity for an internal surface would be a part of distortion energy to create the bubble [15]. The short-range potential of a closed-shell atom is strongly repulsive to an excited electron, consequence of the orthogonality requirement of the excited orbitals for occupied orbitals and dominates other terms such as the long-range attractive polarisation energy. In heavier rare-gas atoms, the potential gradually becomes less repulsive as the short-range screened Coulomb potential and exchange interaction become significant.

The work by Druger and Knox [36] on solid Ar showed that by minimising the total energy concerning various trapping sites, the two-centre self-trapped holes are observed to be stable. This was done using potential energies obtained for ionic dimers in free space. They also found that the stability derives almost entirely from the molecular bond between the two Ar atoms and that the bond length of the excited Ar_2 pair is nearly unchanged in the crystal concerning a free Ar excimer. This work also included the examination of the self-trapped hole in Kr and Xe. Using a representation of the hole simpler than that of Druger and Knox, Song [37] and Umehara [38] have studied the hole self-trapping and reached similar conclusions.

1.3 Spectroscopy

The vacuum ultraviolet (VUV) continua produced by $A^1\Sigma_u^+ \rightarrow X^1\Sigma_g^+$ transitions in the rare gas dimer have served as background source for VUV absorption spectra [39, 40] for more than half a century. It is also used for excitation of photo-chemical processes or fluorescent devices like plasma display pixels. These continua generally exhibit two intensity maxima, often referred to as the first (shorter wavelength λ) and second continua.

1.3.1 Excimers

The high-resolution synchrotron and laser spectroscopic techniques developed in the last decades has provided the possibility to examine the Rydberg states of heavier rare-gas dimers, which was difficult as the lowest excited states predissociated to various degrees. Primary photo-excitations from $^1\Sigma_g^+$ or $^3\Sigma_u^+$ states have revealed a great deal of electronic structure information. The review article by Ginter and Eden [41] goes through all the rare-gas systems. We will discuss only the Ar dimer here, on the basis of the review by Ginter and Eden [41].

Much of the spectral data available for characterising the Rydberg states for Ar dimer comes from laser excitation spectroscopy based on $^3\Sigma_u^+$ state with additional information provided from single or multi-photon absorption from the $^1\Sigma_g^+$ state. Rydberg series converging on the ionic core of the Ar dimer molecule was first observed in electron beam excitation spectrum [42, 43] as discussed by Herzberg [44] . The laser excitation high resolution spectrum of Ar_2 [45] in the 335-470 nm region is shown in figure 1.3.

The experimental work done in previous decades [45, 46, 47] on the nature of Rydberg states was to study the role played by the ionic core, the energy ordering and proper assignment of states and resolution of spectroscopic data with resolution of rotational levels. This is supported by the theoretical model developed by Duplaa and Spiegelmann [48], which will be discussed later.

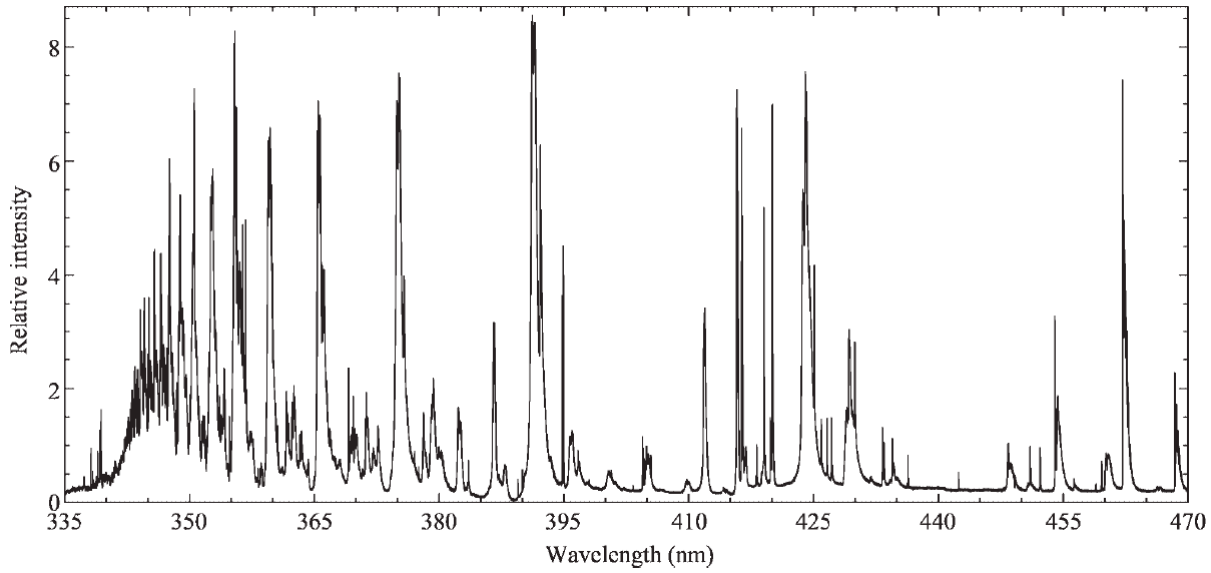

Figure 1.3: The laser excitation spectrum of Ar_2 in the lowest triplet excited state in the 335-470 nm region. Obtained by [45], adopted from [41].

1.3.2 Excitons in Bulk

The similarity in spectroscopic results from cluster and solid RG have been shown by the formation of m-STE in luminescence spectroscopy [14]. Formation of bulk and surface excitons in an absorption spectrum are shown in figure 1.4.

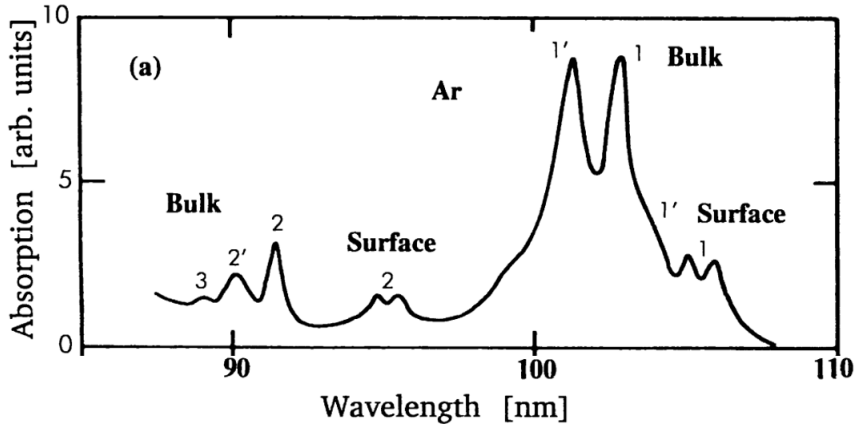

Figure 1.4: The Absorption spectrum of 30 $\AA$ Ar layer showing $n = 1,2,3$ and $n' = 1,2$ bulk exciton peaks and $n = 1,2$ and $n' = 1$ surface exciton peaks. This figure shows the different types of exciton identified in the excitation spectrum of a cluster or bulk Ar system. Adapted from book of Song [15].

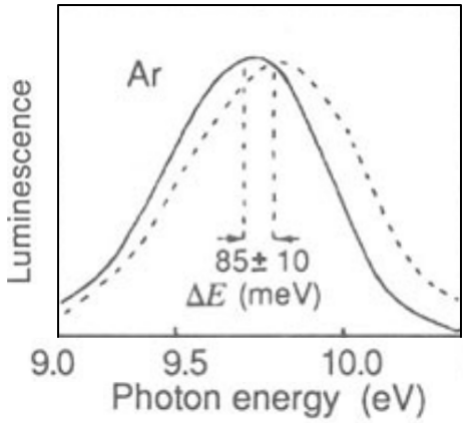

Figure 1.5: Resolved singlet-triplet splitting in STE luminescence of solid Ar at 6 K, under excitation by photons of energy 12.15 eV. The spectra shown by full curves is long-lived phosphorescence from $^3\Sigma_u^+$. Spectra shown by broken curves is fast fluorescence from $^1\Sigma_u^+$. Adapted from book of Song [15] obtained by Roick [14].

The presence of STEs is accounted for by observation of the Stokes-Shifted luminescence band. Singlet with lifetime **in the** nanosecond and triplet with a longer lifetime **in the** microsecond range, are both associated with the STEs luminescence band. The figure 1.5 shows the m-STE luminescence band for singlet and triplet for a temperature of 6K, where the solid line is attributed to the radiative recombination in microsecond range from the $^3\Sigma_u^+$ STE state and the dashed line in the nanosecond range to radiative recombination of $^1\Sigma_u^+$ STE state. It is also observed that, the band formation is independent of the change in temperature [14]. Luminescence results in general from long-lived electronic excitations which are in thermal equilibrium with the lattice.

Given enough sensitivity, it **is** also possible to observe luminescence from centres without thermalisation also known as "hot luminescence", i.e., from STEs which are not in thermal equilibrium with lattice. Heavy (low hole mobility) rare gas like Xenon shows weak hot luminescence while light gas like Neon shows strong hot luminescence. In light rare gas solids this peculiarity comes from the fact that the vibrational quantum of the excimer is much larger compared to the phonon energy of the host lattice (For $n \to n-1$ transition, the spacing in the excimer spectrum $|E_n - E_{n-1}| >> \hbar\omega_D$ ω_D is Debye frequency of solid).

In other words, the relaxation can not reach the lowest vibrational state within the radiative lifetime of light rare gas like Ne, shown by Yakhot *et al* [49]. However, Ar is an intermediate case. For Ar, we have to discriminate between the thermalisation of STEs at the surface or bulk as observed by E. Roik 1984 *et al.* [14]. Following their work, we can say that the qualitative difference in the effects of exciton-phonon interaction between bulk and surface is related to the dimensionality of the system [50].

A fluorescence spectra is shown in figure 1.6, for system sizes from for few atoms (a-d) [51, 52] to bulk (e) [53] which is a thin film of 4 μm. This spectrum shows similarities in the spectral properties of the bulk and clusters. It is to be noted that the fluorescence spectrum shows the formation of surface and bulk excitons between 100 to 105 nm ($\approx$ 11.5-12.4 eV). The relative intensity of the surface exciton diminishes while transitioning from small clusters to condensed matter.

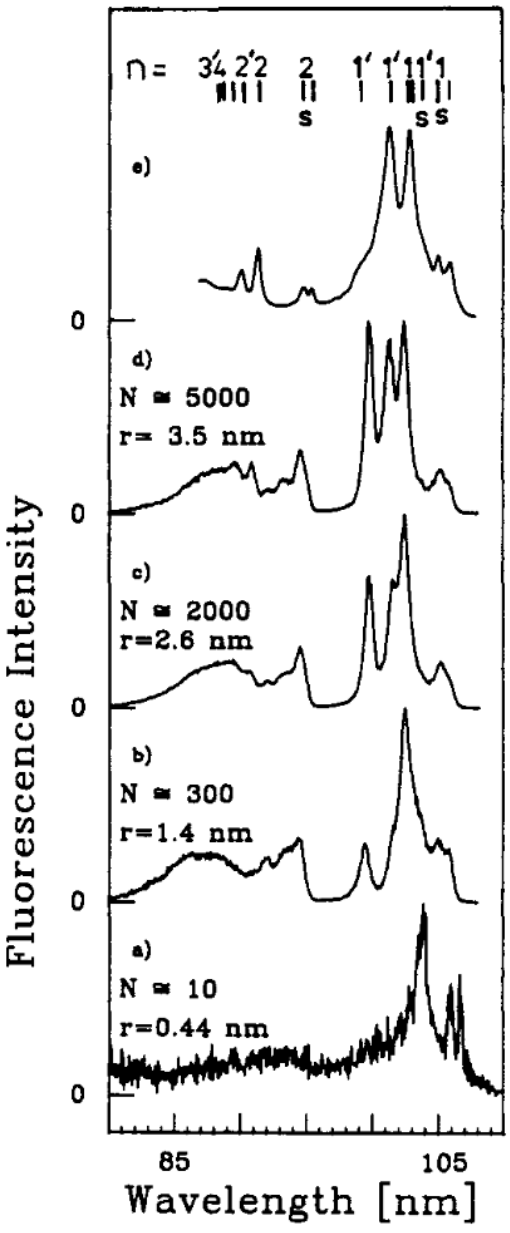

Figure 1.6: Fluorescence (excitation) spectra of Ar clusters in comparison with an absorption spectrum (e) of a thin film (d = 4 μm) [51, 52, 53]

The evolution of excitons energy level and size dependence in clusters was reported by Möller *et al.* [50], for the two types of excitons, Wannier exciton ($n = 2, 3$) which are characterised by extended orbitals with large radius and Frenkel type exciton ($n = 1$ or $1'$) which extend to nearest-neighbour only. The team

of Möller *et al.* [51, 54, 50, 55, 56] in Hamburg (HASYLAB) studied the Ar cluster properties for a decade and gave some insightful spectroscopic results. Möller *et al.* showed correspondence between the excitation spectra of the Ar cluster and that of solids. The characteristic absorption was observed in the range of 11.5 - 12.9 eV. In their group, they used the Frenkel-exciton model to study these systems while considering the resonant excitation transfer [56]. While studying the optical properties [51] for a number N of atoms from 10 to 10^6, they reported surface and bulk excitation. For larger clusters, they observed the continuum to be getting weaker in favour of Wannier exciton as observed in solids.

Study of transient absorption and luminescence in rare gas crystals by Dossel *et. at* [57] in 1983 showed long-lived $^3\Sigma_u^+$ state. They found close similarities between the lowest excited states of STEs in the crystals and free excimer in the energy region up to 1.5 eV above the lowest excited state. Higher energy levels and the continuum states of the self-trapped exciton are strongly influenced by the solid-state effects.

1.3.3 Desorption and Emission

The phenomenon in which species (neutral molecules, ions, excited neutrals, ionic dimers, etc.) are ejected when solids are irradiated by some energetic particles (electron, ion, photon, etc.) is known as Desorption Induced by Electronic Transitions (DIET) [58, 59]. Based on the desorbed species, it is possible to get useful information about such dynamical aspects, in which exciton is assumed to play an essential role. The kinetic energy of the ejected species ranges from below 0.1 eV to 0.8 eV, which is much higher than thermal energies.

Electron Stimulated Desorption (ESD) of rare gas solids has been investigated by several experimental groups [60, 61, 62, 63, 64]. Børgesen *et al.* 1982 [60] presented one of the first results on electron-induced erosion of rare gas solids and suggested an exciton decay model for ESD of rare gases. Coletti *et al.* 1984 [63] studied the luminescence properties of solid Ar by electron excitation (few eVs to 100 eV). They observed a sharp threshold of desorption and luminescence, which is the same for both processes. This threshold is at the same energy as that of the impinging electrons. The desorption rate was found to be proportional to exciton density at the surface while the surface nature of different luminescence bands was established. The mechanism of desorption is assigned to the formation of a cavity in the solid Ar. Arakawa *et al.* 1989 [64] also showed the desorption of neutral excited species from solid Ar.

The desorption due to ion collision has been extensively studied, and the emission of species has been reported. The emission from solids results from high energy exciton deposited on lattice sites which when decays, carries a lot of energy. We may expect similar behaviour from the big excited cluster.

The excited Ar dimer desorption was observed by C.T. Reimann *et al.* [65, 66]. The experiment was done by irradiation of thin solid Ar film with MeV He ions. They observed a broad luminescence band between 9.80 and 11.17 eV (1110 - 1265 Å), which is associated with the decay of vibrational states of an Ar dimer in its lowest excited electronic state $Ar_2^*(^3\Sigma_u^+; 1_u, 0_u^-)$ and trapped in bulk as shown in figure 1.7. This result is typical of an m-STE. They hypothesised, the Kinetic Energy (K.E.) of this ejected dimer to be around 0.1 eV after dissociative recombination of an electron with a near-surface self-trapped hole. Recently, time-resolved spectroscopy gave further insight to cluster dynamics where they reported the transition from the nascent excited state to a relaxed exciton in Ar clusters is reported by Lietard *et al.* [10].

The work by Grosjean *et al.* [67] addresses the luminescence efficiency of the 9.8 eV M-band, which is formed by the decay of Ar_2^* in the solid Ar on irradiation with 1.5 MeV $\alpha-$particles. They found that 54% of luminescence was due to dimer emission irrespective of the ion energy, which implies the M-band population is the major relaxation pathway for electronically deposited energy in solid Ar. Hence, we can

say that the $^3\Sigma_u^+$ state plays a central role in this emission process.

The estimates of the kinetic energy of the desorbed species from the conversion of inter-nuclear (potential) energy in the gas phase have been reported as well. Such emissions from gas-phase systems are connected to the rich overlap between attractive and repulsive potential surfaces initially provided by Mulliken[25]. This is further elaborated in the study of solid and gaseous Ar by several authors [66, 68, 69].

Johnson *et al.* [11] have made several simulations of sputtering in rare-gas solids using molecular dynamics methods. They used Castex *et al.* [30] PECs for Ar_2^*. They evaluated the cavity formation around the a-STE in the bulk and at the surface. The absorption energy shift, which measures the extent of the repulsive interaction between the excited electron and the neutral Ar atom, has also been evaluated.

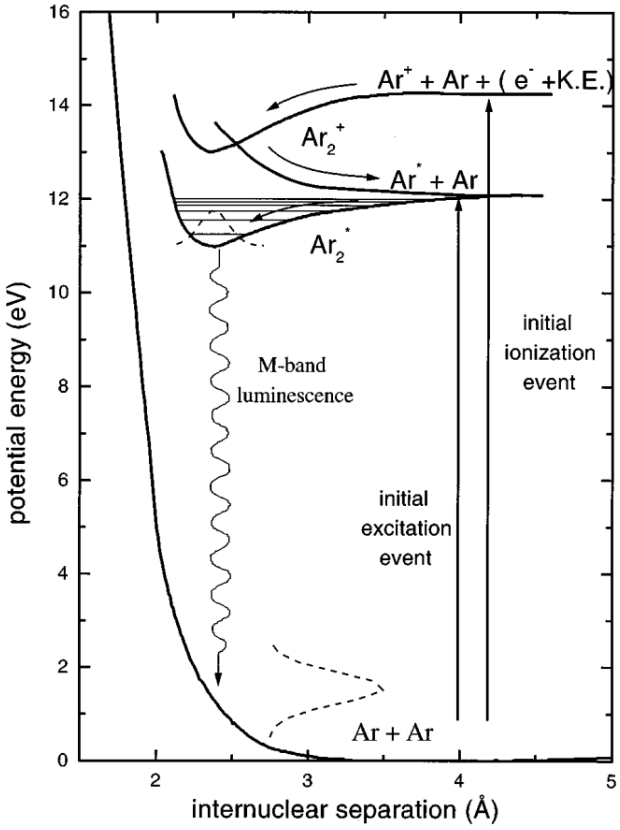

Figure 1.7: Ar-Ar potential-energy curves in the solid state. The arrows indicate decay sequences. The decay of the Ar_2^* gives rise to the M band [67].

They reported the formation of a cavity as a result of the expanding first shell atoms with a magnitude of about 0.2 $\AA$. This is considerably smaller than the corresponding value of about 1 $\AA$ which is expected to be due to the much smaller value of the negative electron affinity in solid Ar. They examined several conditions like, the ejection of excited atoms on the (100) and (111) faces. The number of surrounding neighbours of the excited atom has been varied to take into account the fact that the surface may not be perfect during sputtering. They summarised; (i) The kinetic energy of the ejected atom depends on the number of neighbours, i.e., the larger this number, the higher the ejection energy. This implies that the energies are slightly higher for the (111) face than for the (100) face. This is understandable when it is recalled that the repulsive potential between the excited atom and the ground state atom is the driving force of desorption. (ii) The kinetic energy of the ejecta is found to be of the order of 0.1 eV for all versions of potentials used. This is smaller than the observed value of 0.4 eV [70]. This point is also noted in the simulation of the dimer ejection from the Ar surface, as discussed below.

Cui *et al.* [12, 13] have applied the same technique to study the ejection of dimer from the surface of solid Ar. The work is similar to that for the excited atom ejection described above with the following details which have to do with an excited molecule in this case. The particular pair of atoms which constitute the excimer (m-STE) is represented by a Morse potential fitted to $^{1,3}\Sigma_u^+$: potential energies from [30]. The interaction between the atoms forming the excimer and the neighbouring ground state atoms is simulated by an average potential between (Ar^* + Ar) and (Ar + Ar), hence neglecting any directionality of the bonding. The results obtained by Cui *et al.* are summarised in the following: (1) The eight neighbours nearest to the centre of the excimer expand by $0.5 - 0.6$ $\AA$. The cavity energy shift in the bulk is about $0.5 - 0.6$ eV,

which is in good agreement with the luminescence shift of 0.6 eV. (2) The calculated centre-of-mass kinetic energy of ejected excimer is less than 0.1 eV. This is much smaller than the experimental value of 0.8 eV [66]. (3) There is a better chance of ejection from the (111) face than from the (100) face. Also, the smaller the number of neighbouring atoms, the smaller the ejection energy. These findings are analogous to those in the excited atom ejection. (4) Excimers formed between two adjacent layers of atoms at the surface do not undergo ejection in the case of the (100) face. (5) Vibrationally excited excimer has a significantly better chance of ejection.

However, since the PECs driving the dynamics in these works is of a single excited state which is a significant simplification. As we will see later in this thesis, the density of excited states and degeneracy in the Ar is high, which plays an important role, but is not taken into account in these calculations.

1.4 Dynamics of STEs and Excitation transfer

As discussed previously, in solids, the dynamics of trapped excited states on lattice sites involve the relaxation of atomic structure by desorption or by migration of excitation to the surface. The exciton dynamics of self-trapping was shown by several experiments for Ar clusters [10] and solids [14]. The mechanism was predicted by Rashba [23] and is explained pretty neatly for solids in review by Roick as, "In the 'stiff' (corresponding to the three-dimensional system or solids) case, the free-exciton state is locally stable. Depending on the strength of the exciton-phonon coupling, there may be an additional energy minimum higher or lower in energy than the free-exciton state. In either case, the two minima are separated by a potential barrier. In the 'limp' (one-dimensional systems or atomic species) case, no potential barrier exists. There is a continuous change from the free to the self-trapped state with increasing coupling strength. In the 'marginal' (two-dimensional system or clusters) case, the free state can be locally stable or not. Whether the free exciton is locally stable or unstable is determined by the coupling strength", given by Roick [14]. The figure 1.8 gives the configuration coordinate for different cases.

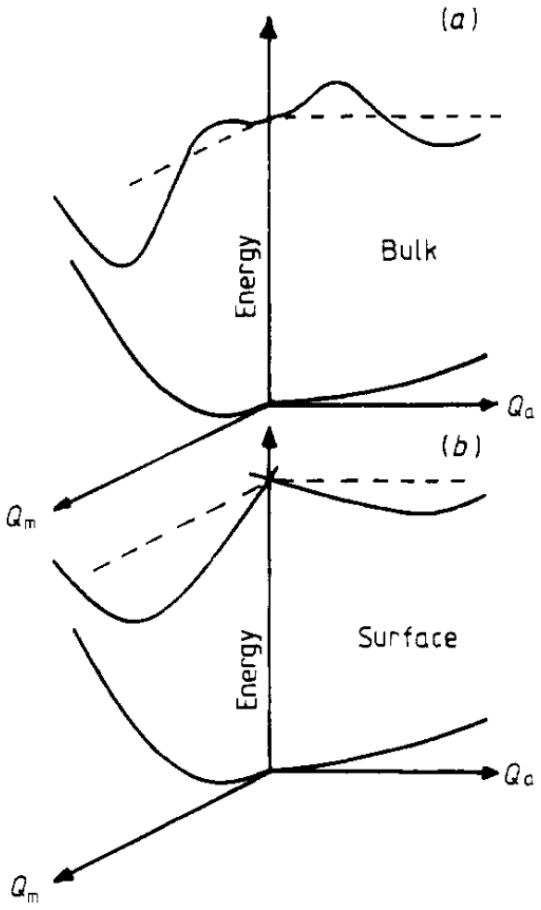

Figure 1.8: Configuration coordinate diagram taken from [14]. (a) On the central axis we have the free exciton formed in bulk, this exciton experiences a smaller barrier towards m-STE (Q_m) than towards a-STE (Q_a). (b) With a free exciton on the central axis, there is no barrier predicted therefore leading to formation of either a-STE or m-STE on the surface.

Figure 1.8 gives a schematic representation of the reaction coordinate leading to the formation of an a-STE and m-STE in different system types. It is not perfect but gives a good approximation to consider a 2D boundary for a 3D system, i.e., this assumption simplifies the study by considering the motion of an exciton

on the surface than in bulk. Figure 1.8a gives the information of both the self-trapping species which are separated from a free-exciton state by a barrier. The first estimate of the barrier height was given according to continuum theory by Fugol[22]. The height of the barrier estimated by Fugol for m-STE ($\approx$ 2 meV) and a-STE ($\approx$ 10 meV) is quite different. This points to the possibility of an overwhelming majority of the excitons in bulk trapped in the molecular configuration. This is consistent with the observation by [14], where they report the presence of a-STE to be negligible. The work done in this thesis can provide a better theoretical estimate of this barrier. Figure 1.8b gives the situation of a 2D system considered to be at the surface. In such a system, both the barriers are absent and both self-trapping configurations are populated. This is consistent with the observations of the co-existence of the a-STE and m-STE [14].

There are other methods in which the hole is localised on a single atom to do the same, however, these methods are limited as they are unable to take into account the hole hopping which is essential for excitation transport [15]. There are methods now available as we shall discuss in the next section, which allow hole delocalisation.

Though the electronic structure for solids and clusters are similar, a difference lies in the density of states and possible rearrangement of the atoms. The emission of species from a rare-gas cluster is not very well observed or reported, nor there is well-established theoretical work to simulate the formation of excitons in such clusters.

1.5 Theoretical Framework

To study exciton dynamics, we need to use quantum mechanics as we intend to study the motion of electrons. In quantum mechanics, with the knowledge of wave function for a given system $\Psi(\mathbf{r},\mathbf{R})$, we can know any property of a system. An atomic and molecular system is defined by the motion of electrons and nuclei and their interaction among themselves. The solution of the full wave function is not accessible for the study of clusters.

In the following section, we will introduce theoretical basics which are essential to perform dynamics on excited-state RG systems. We will introduce essential approximations, *ab initio* and model methods for calculation of electronic structure, geometry optimisation techniques and how to do dynamics.

One of the initial approximation in all of the condensed matter and quantum chemistry is Born-Oppenheimer Approximation (BOA). This was proposed by Born and Oppenheimer[71] in 1927. It takes the advantage of great difference in masses of electron and nuclei, $m_p/m_e \approx 10^3$, to decouple the motion of nuclei and electrons. So, instead of solving the Schrödinger equation for all the particles simultaneously, it is proposed to regard the nuclei as fixed in position and solve the Schrödinger equation for the electrons in static electric potential due to the presence of nuclei at that particular arrangement. This can been seen when we look at the Hamiltonian operator

$$\hat{H}(\mathbf{r},\mathbf{R}) = \hat{T}_N(\mathbf{R}) + \frac{e^2}{4\pi\varepsilon_0}\frac{Z_A Z_B}{R} + \hat{H}_e(\mathbf{r},\mathbf{R}) \tag{1.1}$$

where $\hat{T}_N(\mathbf{R})$ is the kinetic energy of the nuclei, second term is the Coulomb repulsion between the nuclei and $\hat{H}_e(\mathbf{r},\mathbf{R})$ is the Hamiltonian for electrons containing their kinetic energy, mutual repulsion and attraction by the nuclei. According to BOA, we treat the nuclear motion classical kinetic energy term and solve the Schrödinger equation to get $\Phi_e(\mathbf{r},\mathbf{R})$, the electronic wave function and associated eigen energy $E_e(\mathbf{R})$

$$\hat{H}_e(\mathbf{r},\mathbf{R})\Phi_e(\mathbf{r},\mathbf{R}) = E_e(\mathbf{R})\Phi_e(\mathbf{r},\mathbf{R}) \tag{1.2}$$

Note, both Φ_e and E_e depend parametrically on $\mathbf{R}$. We can get, $\Psi(\mathbf{r},\mathbf{R}) = \Phi_n(\mathbf{R})\Phi_e(\mathbf{r},\mathbf{R})$ for each $E_e(\mathbf{R})$.

This approximation is still treats the system quantum mechanically. However, to solve this for more than few atoms, we are limited due to large configuration space. This problem scales as C_m^N where N is the number of atoms and m is the possible configurations. As a side-note, this approximation is good provided the motion of nuclei is slow relative to electrons; in other words the kinetic coupling among the different $E_e(\mathbf{R})$ is negligible.

1.5.1 Exciton States

As exciton is a pair of an electron and hole, it is a two-particle system. Nevertheless, the interaction of the exciton with the rest of the system is approximated as a single quasi-particle.

While building up the wave function to represent the exciton, it is necessary to take into account the electron-hole correlations. If we consider the hole to be created in valence band spin-orbital $|a\rangle$ and the electron in the conduction band spin-orbital $|x\rangle$, then the Slater determinant representing such a state is given by $\Phi(a;x)$. Based on the spin configuration, we have either spin-singlet or triplet states. A good basis should exhibit the translational symmetry of the exciton in the cluster and spatial correlation between the exciton and the rest of the electrons in the system. The single Slater determinant does not have a well-defined spin unless it is a closed-shell system, i.e unless the spatial orbitals are doubly occupied this single Slater determinant is not an eigenfunction of the spin operator. Hence, as the exciton states are open-shell systems, they are not sufficient to demonstrate both dependencies. Besides that, the single Slater determinant does not allow the possibility for the hole to be shared among different atoms, which is important for exciton migration.

This theory for excitons can be used for any material, with precision dictated by the approximations needed to make the solution of Schrödinger's equation tractable. But intuitive reasoning, quantitative estimates from material parameters, and descriptive generalisations are challenging on such a basis-set. This is where models such as the Wannier and Frenkel excitons are useful.

1.5.2 Electronic Structure

In cluster dynamics, the computation of electronic structure is a cornerstone, as it is referred to as the energy landscape inside an atom where exciton dynamics would take place. We can compute the energies of an individual electron by considering an effective potential formed by other electrons which makes it Self-Consistent-Field (SCF) calculations or by carefully considering the electron's motion concerning each other, in a variational approach making it Configuration Interaction (CI) calculations. For an RG system, the electronic structure calculation beyond SCF approximation is required as the binding forces in RG systems are dispersion forces which are important for long-range interactions and are not accounted for in SCF-based calculations. The *ab initio* methods beyond SCF are computationally expensive as we reach the limit with the wave function approach for clusters due to the large basis set and several associated configurations. This is particularly important in rare-gas systems due to the highly diffused nature of the Rydberg orbital which is essential for good estimates of energies. However, there are several techniques developed to solve it for small systems. As an example, the best *ab initio* dimer PECs for excited Ar were obtained using the CIPSI method [31, 72]. These results have been the basis for several other studies [73, 74].

To obtain the electronic structure of Ar clusters in this thesis, we have explored *ab initio* and non-*ab initio* methods. With the motivation to perform dynamics, initial reference PECs were obtained using post-SCF

and CI-based methods which were intended to be used in Diatomics-In-Molecules (DIM) method, with the quantum chemistry code MOLCAS [75]. They are then compared to previous *ab initio* calculations. However, as we will see later the *ab initio* calculation results can not be used in DIM directly.

DIM is a reasonable method which allows for hole-migration and has been shown to give results comparable to *ab initio* calculations for ionic clusters [76]. The study of excited isomers and spectroscopy has been done by Naumkin [74] using DIM giving reasonable results when compared to experiments for absorption and emission energies. The excimer PECs used in this model were obtained by Spiegelmann [31]. However, the quality of these results is difficult to assess as there are not enough results in the literature to compare with.

The CI-based Hole-Particle Pseudopotential (HPP) method given by Duplaa and Spiegelmann [34] to study excited RG cluster was used to study spectroscopy. This method has been used to study several small RG clusters and the results agreed with experiment [48, 77, 78, 79]. Following the success of the HPP method [34] to predict adequate experimental results, we have employed it to study the lowest energy structures of excited Ar systems. The results using DIM were inadequate and it needs further exploration. As HPP is a CI with singles (CIS) excitation-based method which is expected to be close to *ab initio* type calculation. Using this method, photo-excitation spectra have been observed for small clusters [77] and lead to the features observed in experiments.

1.5.3 Dynamics

Until now, the electronic structure is calculated for fixed nuclear positions. However to do dynamics of a system it is important to free the nuclear motion and solve full Time Dependent Schrödinger's Equation (TDSE) for $\Psi(\mathbf{r},\mathbf{R})$. The quantum mechanical treatment of the nuclear motion is already a very cumbersome task even in the BOA. Now, if we consider the nuclear motion to be classical while keeping the quantum mechanical treatment of electrons, we come to Mixed Quantum Classical Dynamics (MQCD).

The time dependence of $E_e(\mathbf{R})$ now comes from the nuclear coordinate $\mathbf{R}$ dependence on time $\mathbf{R}$(t). Then, it is possible to obtain forces by differentiating with respect to nuclear coordinates;

$$\mathbf{F} = -\nabla E_e(\mathbf{R}) \tag{1.3}$$

Therefore, the basics of MQCD is to calculate the electronic structure for the given nuclear coordinate, find the forces acting on each nuclei using the above equation (1.3), and get new nuclear coordinates using some propagation algorithm, updating the coordinate and repeating the steps by calculating the electronic structure again. The problem with this method is that, we are always looking at the same electronic state and the possibility to observe relaxation to lower electronic states is not taken into account. To do that, we need to take into account Non-Adiabatic Coupling (NAC) between the electronic states. However, to include NAC is not straightforward. The important thing to consider is switching of state when NAC is active. This is not very well defined and there are several methods like Ehrenfest technique or evaluation of derivative overlap or using approximate methods like Hellman-Feynman theorem. However, the most computationally cheap and somewhat acceptable is a probabilistic method called surface-hopping given by J.C. Tully [80] which is used to enable non-adiabatic dynamics.

The dynamics is performed using the DIM method as it is computationally cheap and takes into account hole-migration or charge transfer. The propagation of trajectories (nuclear motion) on the potential surface is achieved using Beeman algorithm which is build on Verlet integration method by including velocity

update with coordinate update. A constant Spin-Orbit Couplings (SOC) is used throughout inter-atomic which will be shown later.

Part I

Electronic Structure and Geometry

Chapter 2

Electronic Structure of Excited Rare-Gas Clusters

Electronic structure calculation is the backbone of all atomic and molecular physics, quantum chemistry and condensed matter physics as discussed previously. However, to obtain electronic structure for any system with more than few electrons is by no means easy and the problem becomes more challenging as the number of electrons increases. In the framework of the BO approximation, the important step is to solve the electronic part of the Schrödinger Equation. To solve this, over the past century, there has been immense development for explicit and approximate methods for all type of systems.

In this chapter we will briefly discuss the *ab initio* methods that allow us to calculate potential energy curves (PECs) by solving the electronic Schrödinger's equation. Then we will show how to use some of the *ab initio* methods in MOLCAS quantum chemistry software [75] to get PECs for the excited and the ionised Argon dimer. Although bigger excited systems hardly tractable by using *ab initio* method, we will present the possibility to study the excited Ar_3^* trimer using such calculations. Finally, we conclude by presenting our results for the dimer and trimer.

2.1 The Electronic Structure Theory

In a system made up of M nuclei and N electrons, the electronic Schrödinger's equation 1.2 is:

$$\hat{H}_e \Psi_e(r,\{\mathbf{R}\}) = E_e(\{\mathbf{R}\})\Psi_e(r,\{\mathbf{R}\}) \tag{2.1}$$

where the electronic non-relativistic Hamiltonian $\hat{H}_e$ is written as follows:

$$\hat{H}_e = -\sum_{i=1}^{N}\frac{\nabla_i}{2} - \sum_{i=1}^{N}\sum_{A=1}^{M}\frac{Z_A}{r_{iA}} + \sum_{i=1}^{N}\sum_{j>i}^{N}\frac{1}{r_{ij}} \tag{2.2}$$

where i and A denote the i^{th} electron and the A^{th} nucleus respectively. Z_A is the atomic number of atom A, $r_{iA} = |\mathbf{r}_i - \mathbf{R}_A|$ is the distance between i^{th} electron and the A^{th} nucleus and $r_{ij} = |\mathbf{r}_i - \mathbf{r}_j|$ is the distance between each electron pair i and j.

2.1.1 Hartree-Fock Approximation

If we neglect the electronic Coulombic interaction, the corresponding electronic Hamiltonian reduces to the sum of N $\hat{h}_i$ one-electron operators:

$$\hat{H}_e^{\text{Hartree}} = -\sum_{i=1}^{N} \frac{1}{2}\nabla_i - \sum_{i=1}^{N}\sum_{A=1}^{M} \frac{Z_A}{r_{iA}} = \sum_{i=1}^{N} \hat{h}_i \tag{2.3}$$

The associated wave function is thus a simple product of mono-electronic functions given as Hartree-product:

$$\Psi_e^{\text{Hartree}}(r,\{\mathbf{R}\}) = \prod_{i=1}^{N} \chi_i(\mathbf{x}_i,\{\mathbf{R}\})$$

with

$$\hat{h}_i\chi_i(\mathbf{x}_i) = \varepsilon_i\chi_i(\mathbf{x}_i)$$

In the Hartree approximation, the electronic energy is $E_e(\{\mathbf{R}\}) = \sum_{i=1}^{N} \varepsilon_i$ and the mono-electronic function $\chi_i(\mathbf{x}_i)$ corresponds to a *spin-orbital* which can be decomposed as $\chi_i(\mathbf{x}_i) = \chi_i(\mathbf{r}_i,\sigma_i)$ where σ_i is the spin projection for an electron.

The Hartree wave function does not fulfil the anti-symmetry principle together with the principle of the indistinguishably of the electrons. To overcome this problem, the Hartree-Fock (HF) theory proposes that the many-electron wave function of the system can be described by a single Slater determinant made of the N one-electron molecular orbitals (MO) or spin orbitals as:

$$\Psi = \frac{1}{\sqrt{N!}}\begin{vmatrix} \chi_1(\mathbf{x}_1) & \cdots & \chi_N(\mathbf{x}_1) \\ \vdots & \ddots & \vdots \\ \chi_N(\mathbf{x}_1) & \cdots & \chi_N(\mathbf{x}_N) \end{vmatrix} = |\chi_1\chi_2\cdots\chi_N\rangle \tag{2.4}$$

In the HF theory, the coulombic electron-electron repulsion is taken into account in an averaged way (mean field approximation) [81] and the corresponding energy can be written in terms of integrals of the one- and two-electron operators :

$$E_e^{HF} = \sum_{i=1}^{N} \langle i|h|i\rangle + \frac{1}{2}\sum_{i,j}^{N}([ii|jj] - [ij|ji]) \tag{2.5}$$

where the one electron integral is

$$\langle i|h|i\rangle = \int dx_1 \chi_i^*(\mathbf{x}_1) h_{(1)} \chi_i(\mathbf{x}_1) \tag{2.6}$$

and the two-electron integral is

$$[ij|kl] = \int d\mathbf{x}_1 d\mathbf{x}_2 \chi_i^*(\mathbf{x}_1)\chi_j(\mathbf{x}_1)\frac{1}{r_{12}}\chi_k^*(\mathbf{x}_2)\chi_l(\mathbf{x}_2) \tag{2.7}$$

with $\mathbf{x}_i = (\mathbf{r}_i,\sigma_i)$, $|i\rangle = |\varepsilon_i\rangle$.

If we apply the variational theorem, we can obtain the best approximate wave function by varying the orbital parameters until we minimise the energy. The variational theorem leads to the resolution of the HF equations which form a set of coupled integral differential equations. Since the Fock operator depends on it's own solution, the process must be done iteratively. This is why the solution of the Hartree-Fock

equations are called the self-consistent-field procedure (SCF). The Fock operator is defined as:

$$F(\mathbf{x}_1) = h(\mathbf{x}_1) + \sum_{j}^{N} [J_j(\mathbf{x}_1) - K_j(\mathbf{x}_1)] \tag{2.8}$$

where the coulomb and the exchange operators are

$$J_j(\mathbf{x}_1) = \int d\mathbf{x}_2 \chi_j^*(\mathbf{x}_2) \frac{1}{r_{12}} \chi_j(\mathbf{x}_2) \tag{2.9}$$

$$K_j(\mathbf{x}_1)\chi_i(\mathbf{x}_1) = \int d\mathbf{x}_2 \chi_j^*(\mathbf{x}_2) \frac{1}{r_{12}} \chi_i(\mathbf{x}_2)\chi_j(\mathbf{x}_1) \tag{2.10}$$

The spatial part of each spin-orbital can be expressed as a linear combination of N_b atomic orbitals (LCAO):

$$\chi_i(\mathbf{r}_1) = \sum_{a=1}^{N_b} c_a^i \phi_a(\mathbf{r}_1) \tag{2.11}$$

Solving HF equation in a space spanned by the set of N_b basis function for the orbitals $\chi_i(\mathbf{r})$, the system of integro-differential equations reduces to a set of non-linear algebraic equations known as the Hartree-Fock-Roothan equations:

$$F(x_1)\chi_i(x_1) = \varepsilon_i \chi_i(x_1) \tag{2.12}$$

We can perform different types of HF calculations: restricted (RHF), unrestricted (UHF) or restricted open-shell (ROHF) depending on how much variational freedom is given to the spatial part of the one-electron wavefunctions with different spins. The HF theory does not take into account the correlation between the electrons but it provides a good starting point for more elaborate theoretical methods which are better approximations to the electronic Schrödinger equation.

2.1.2 The Density Functional Theory

Density-Functional-Theory (DFT) computational techniques have also been employed to model quantum chemistry problems to investigate ground-state electronic structure of many-body systems for some atoms, molecules or condensed phases. This method is based on the electron density rather than the electronic wave function and takes into account correlation energy. The central idea of the DFT is to promote $\rho(\mathbf{r})$ as the key variable in determination of the electronic energy for a given system as:

$$E_e^{DFT} = E[\rho] = T[\rho] + V_H[\rho] + V_{ext}[\rho] + E_{ex}[\rho] \tag{2.13}$$

where $T[\rho]$ is the kinetic energy of a system of non-interacting electrons, $V_H[\rho]$ represents the Hartree energy (the interaction energy) of a classical charge distribution of density $\rho(\mathbf{r})$ and $V_{ext}[\rho]$ is the external potential created by the nuclei. $E_{ex}[\rho]$ is called the exchange and correlation functional and contains the difference between the kinetic energy of the real system and that of the non-interacting system adding the difference between coulomb and Hartree energies. DFT is in principle an exact theory for the ground state if one knows the "exact" exchange and correlation functional. However, in practice this functional is an approximation. Local Density Approximation (LDA), Generalised Gradient Approximation (GGA), meta-GGA and hybrid functional are some of the most widely used approximations. Though DFT is used for ground state study, in its time-dependent form it is used to study excited states. For weakly interacting systems, like rare-gas clusters, however DFT is not sufficiently accurate, and it is not used in this thesis.

2.1.3 The Multi-Configuration Self Consistent Field Theory

The Multi-Configuration Self Consistent Field (MCSCF) Theory is a more elaborate SCF method. In this method we select the determinants that are necessary to describe correctly the multi-reference nature of a system. The prototypical example is the bond dissociation of a radical pair. In the current system of excited Argon pair, by having the multi-reference wavefunction, excitation is allowed to be localised on any atom, which would not be possible in single reference method.

A multi-reference wavefunction is formed by a finite linear combination of Slater Determinants making this a multi-configurational problem given by:

$$|\Psi_{\text{MCSCF}}\rangle = \sum_I c_I |\phi_I\rangle \tag{2.14}$$

Each determinant is built from some guess spin-orbitals which are optimised to lower the total energy as much as possible. Thus using the variational principle, we not only optimise the coefficients of the determinants but also the spin-orbitals used to construct the determinants. In a sense, the MCSCF method is a combination of the Configuration Interaction (CI) method (discussed in next section) and SCF method.

The MCSCF method is mainly used to generate a qualitatively correct wavefunction, i.e. to recover the "static" part of the correlation energy. There are several ways to generate the configurations: the Complete Active Space Self-Consistent Field (CASSCF) and the Restricted Active Space Self-Consistent Field (RASSCF) methods.

- **The Complete Active Space (CASSCF) method**
  From the molecular orbitals (MO) computed, a HF calculation, we partition the space of these orbitals into an active and an inactive space. The inactive space of spin-orbitals is chosen from the low energy orbitals, i.e. the doubly occupied orbitals in all determinants (inner shells or core orbitals). The remaining spin-orbitals belong to the active space. Within the active space, we consider all possible occupancies and excitations of the active MO to obtain the set of determinants in the expansion of the MCSCF wavefunction (hence, "complete"). A common notation used for CASSCF is the following: $[n,m]$-CASSCF, where n is the number of electrons distributed in all possible ways in the m MOs.

- **The Restricted Active Space Self-Consistent Field (RASSCF) method**

  For large CI expansion, the CASSCF calculation becomes impracticable. To overcome limitation, we can use the Restricted Active Space Self-Consistent Field (RASSCF) method. In the RASSCF method, the active orbitals are now divided into 3 spaces, RAS1, RAS2 and RAS3 as shown in Figure 2.1. In RAS1 we have holes. In RAS2 we include occupied and virtual MOs to make a full CI, and in RAS3 we include some virtual MOs that are empty in the HF determinant. The RASSCF method allows us to generate configurations by a combination of a full CI in a small number of MOs in RAS2 and for example a CISD in somewhat large orbital space in RAS1 or RAS3.

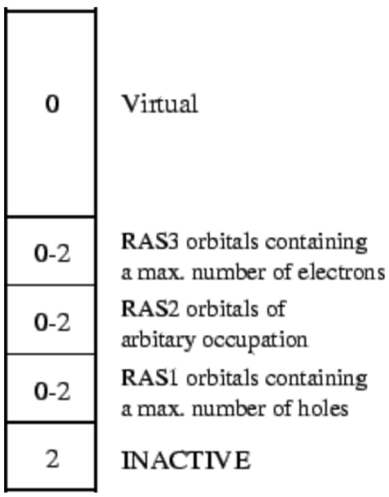

Figure 2.1: RAS space in which valence and free electrons and holes are placed in MOLCAS

MOLCAS provides a wide variety of options to perform MCSCF based calculations and therefore these are usually used to provide a reference wavefunction for other multi-reference methods. Careful selection of active and frozen spaces is essential for these calculations. Taking highly diffuse basis set, it is possible to study Rydberg states, as discussed in section 2.2.

2.1.4 The Coupled Cluster Theory

The Coupled Cluster (CC) theory is a post-HF method which is one of the most accurate and reliable technique to include electron correlations. Instead of linear expansion, the wavefunction is expanded on exponential ansatz over a Slater determinant $|\Phi_0\rangle$ usually constructed from Hartree-Fock:

$$|\Phi_{CC}\rangle = e^{\hat{T}}|\Phi_0\rangle \tag{2.15}$$

where $\hat{T} = \hat{T}_1 + \hat{T}_2 + \hat{T}_3 + \ldots$ is called the cluster operator, which acts on $|\Phi_0\rangle$ to produce a linear combination of excited Slater determinants. Taking into consideration the structure of $\hat{T}$, the exponential operator $e^{\hat{T}}$ may be expanded into a Taylor series:

$$e^{\hat{T}} = 1 + \hat{T}_1 + \hat{T}_2 + \frac{\hat{T}_1^2}{2!} + \frac{1}{2}\hat{T}_1\hat{T}_2 + \frac{1}{2}\hat{T}_2\hat{T}_1 + \hat{T}_3 + \frac{\hat{T}_2^2}{2!} + \ldots \tag{2.16}$$

where,

$$\begin{aligned} \hat{T}_1|\Phi_0\rangle &= \sum_{i}^{\text{occ}}\sum_{a}^{\text{vir}} t_i^a|\Phi_i^a\rangle \\ \hat{T}_2|\Phi_0\rangle &= \sum_{i<j}^{\text{occ}}\sum_{a<b}^{\text{vir}} t_{ij}^{ab}|\Phi_{ij}^{ab}\rangle, \end{aligned} \tag{2.17}$$

where $\hat{T}_1$ corresponds to the single excitation, $\hat{T}_2$ to the double excitation and so on. The classification of the CC methods is based on the highest number of excitations allowed in the definition of $\hat{T}$, it begins with the letters "CC" followed by "S" for the single excitation, "D" for the double excitation, "T" for the triple excitation ... etc . For the ground-state, the most popular CC calculations is the CCSD(T) where the single and double excitations are included and the triples are calculated with perturbation theory.

Unfortunately the CC approach is well adapted only for the calculation of the ground state PES of a system. However, with some modifications it is possible to obtain PECs for single open shell systems. In particular for an Ar_2^+, we can determine the lowest energy PECs in a given spatial symmetry as shown in section 2.3.

2.1.5 The Configuration Interaction Theory

The goal of the Configuration Interaction (CI) theory is to improve the HF or MCSCF solution by increasing the space of all possible many-electron wavefunctions from a single Slater determinant to a set of, in principle, complete Slater determinants. The CI wavefunction is a linear combination of all possible Slater determinants formed from a finite set of spin orbitals $\{\chi_i\}$. The N-electron basis functions can be written as substitutions or excitations from the single HF determinant $|\Psi_0\rangle$:

$$|\Psi_{CI}\rangle = c_0|\Psi_0\rangle + \sum_{a,r} c_a^r|\Psi_a^r\rangle + \sum_{a<b,r<s} c_{ab}^{rs}|\Psi_{ab}^{rs}\rangle + \sum_{a<b<c,r<s<t} c_{abc}^{rst}|\Psi_{abc}^{rst}\rangle + \ldots \tag{2.18}$$

where $|\Psi_a^r\rangle$ is the Slater determinant formed by replacing the spin-orbital a in the HF determinant $|\Psi_0\rangle$ with the spin orbital $r\ldots$ and so on. The basic idea of Configuration Interaction (CI) is to diagonalise the N-electron Hamiltonian 2.2 in a basis of N-electron functions, or Slater determinants and to use the variational principle to minimise the energy. The CI energy is thus by definition :

$$E_e^{CI} = \frac{\langle \Psi_{CI}|\hat{H}_e|\Psi_{CI}\rangle}{\langle \Psi_{CI}|\Psi_{CI}\rangle} \tag{2.19}$$

It is possible to reduce the size of the N-electron basis set $|\{\Psi_i\}\rangle$ when we are interested in the wavefunctions of a given spin (singlet, triplet, ...) and/or spatial symmetry (Σ, Π, ...) since the Hamiltonian matrix is block-diagonal according to space and spin symmetries. If one performs the matrix mechanics calculation using all possible N-electron basis functions $|\{\Psi_i\}\rangle$ the procedure is called full CI (FCI) and corresponds to the best calculation that can be done for a given basis set of spin orbitals $\{\chi_i\}$. If the number of spin-orbitals produced by HF is $2M$, the number of determinants constructed is then C_{2M}^N, where N is the number of electrons.

Unfortunately, FCI is computationally intractable for any but smallest systems, due to the huge number of N-electron basis functions required. In practice, the CI space could be reduced which corresponds to truncated CI methods. The widely-employed CI singles and doubles wavefunctions (CISD) includes only those N-electron basis functions which represent single and double excitation(s) relative to the HF reference. The CISD calculations accounts typically for about 95% of the correlation energy in small molecules at their equilibrium geometries. But these truncated CI methods are not size consistent (contrary to the truncated CC methods) and are not well adapted to reproduce accurately the dissociation of the system.

The Multi-Reference Configuration Interaction (MRCI)

Excitation energies of truncated CI methods such as the ones described above are generally too high, since the excited states are not as well correlated as the ground state. For equally correlated ground and excited states, one can use the Multi-Reference Configuration Interaction (MRCI) method. In the MRCI method, we can use more than one reference determinant (i.e. in equation 2.18, we use several $|\Psi_0\rangle$) to generate singly, doubly, and higher excited states (this is not the case with CC and MPn methods as they are single reference method).

The MRCI approach thus gives a better correlation of the ground and excited states, as it allows us to perform calculations of several states simultaneously in a well balanced way. It is important for our system under consideration as it has more than one dominant determinant and this allows us to obtain good estimate for excited-state PEC.

2.1.6 The Complete Active Space Perturbation Theory 2 (CASPT2)

Another method based on Perturbation Theory, which includes dynamic correlation effects in conjunction with MCSCF given by B.O. Roos [82] and further developed by several authors [83, 84, 85, 86] is called CASPT2 (Complete Active Space Perturbation Theory 2) where '2' is the order of perturbation. In this method, the N-electron space is formed by taking the MCSCF wavefunction as reference and by applying perturbation theory we obtain the second order perturbation correction to the energy. Being a perturbative method, it is relatively fast compared to other methods but this method is highly sensitive to the reference orbitals and at higher resolution of energy with some computational error induced due the system size, the quality of results worsen very quickly.

2.1.7 Summary

The selection of a method to get the electronic structure depends on the system to be studied. As shown in this section, a post-HF type method is essential to study our excited system. MCSCF methods lack dynamical correlations, CI methods are not size consistent, CC methods are size extensive but not adapted for the excited state, DFT based methods rely heavily on supplied functional(s) and Perturbation Theory (PTn) based methods need good reference wavefunctions. In the next section we will discuss how to use the methods introduced in this section to study excited Argon clusters.

2.2 Argon Excimer (Ar_2^*) Potential Energy Curves

The simulation to study excited Ar cluster is always a challenge as this is an open-shell problem and the number of possible excited states is infinite. Besides that, performing such calculations on rare gas clusters is more challenging even for single excitation as the hole contribution comes for correlated np-orbitals. There are several ways to model this problem given briefly in chapter 1. Picking up from discussion in section 1.5.2, we will discuss here how can we obtain electronic structure of excited Argon excimer (Ar_2^*).

As discussed in previous section 2.1, the single-determinant methods are good to estimate ground state PECs. However, they are not suitable for excited state calculations as, using single reference it is not possible to have excitation being localised on one of the atom in their dissociation limit. Therefore, to study excited states, it is imperative to use some multi-reference methods.

The desirable methods to study excited Argon systems are CASPT2 or MRCI calculations, which are based on reference space created using RASSCF method. The RASSCF calculation does not include dynamical correlations, however the results it produces are accurate in energy ordering for argon excimer.

There are eight PECs in triplet and singlet spin-states of Ar_2^* that are essential for modelling of excited Argon clusters. These are the $^{1,3}\Sigma_{u,g}^+$ and $^{1,3}\Pi_{u,g}$ which come from the $3p^5 4s$ configurations of the Ar atom. The configuration space is reduced by symmetry considerations, core freezing and selection of active orbitals depending on the type of calculations, which is discussed in this section.

2.2.1 Argon Excimer Molecular Orbital

The molecular orbitals for excited Argon are formed by linear combination of atomic orbitals. As Argon is a rare-gas atom and the ground state can be obtained in a good approximation as a single determinant, it has fully occupied atomic orbitals in its ground state. The main configuration is thus given by: $1s^2 2s^2 2p^6 3s^2 3p^6$

In the calculation presented in this thesis, the atomic orbitals are defined by combination of Gaussian wave functions. The molecular orbitals of the dimer are formed by linear combination of such atomic orbitals as:

$$\chi_{(\sigma,\pi)_{(g,u)}}(\mathbf{r}) = c_A \phi_{ns,np}(\mathbf{r}_A) + c_B \phi_{ns,np}(\mathbf{r}_B) \tag{2.20}$$

where A, B are the two atoms with their nuclei position $\mathbf{R}_A$ and $\mathbf{R}_B$ and $\mathbf{r}_x = \mathbf{r} - \mathbf{R}_x$ for any nuclei. The excimer is linear and thus has the $D_{\infty h}$ symmetry. For the sake of simplicity, the calculations are performed in D_{2h} symmetry, i.e., $c_A = \pm c_B$.

The non-normalised molecular orbitals associated to $3p$ orbitals subspace are given as:

$$\sigma_{g3p_z} = \frac{1}{\sqrt{2}}\left[\phi_{3p_z}(r_A) + \phi_{3p_z}(r_B)\right] \qquad \sigma^*_{u3p_z} = \frac{1}{\sqrt{2}}[\phi_{3p_z}(r_A) - \phi_{3p_z}(r_B)] \tag{2.21}$$

$$\pi^*_{g3p_x} = \frac{1}{\sqrt{2}}[\phi_{3p_x}(r_A) - \phi_{3p_x}(r_B)] \qquad \pi_{u3p_x} = \frac{1}{\sqrt{2}}[\phi_{3p_x}(r_A) + \phi_{3p_x}(r_B)] \tag{2.22}$$

$$\pi^*_{g3p_y} = \frac{1}{\sqrt{2}}[\phi_{3p_y}(r_A) - \phi_{3p_y}(r_B)] \qquad \pi_{u3p_y} = \frac{1}{\sqrt{2}}[\phi_{3p_y}(r_A) + \phi_{3p_y}(r_B)] \tag{2.23}$$

where σ_{g3p_z} is a symmetric (gerade) bonding σ orbital and $\sigma^*_{u3p_z}$ is anti-symmetric (ungerade) anti-bonding σ^* orbital associated to $3p_z$ spatial orbital, etc. The formation of molecular orbitals for the Argon dimer is illustrated in the Figure 2.2. The following diagram shows the formation of MOs from atomic orbitals of two argon atoms (A and B) given in their ground state. The excitation configurations are made by excitation of an electron from 3σ or 3π molecular orbital to 4σ molecular orbital. The dimer ground state configurations can be represented with valence orbital as:

$$|\chi_0\rangle = \left(\sigma_{gz}\bar{\sigma}_{gz}\pi_{xu}\bar{\pi}_{xu}\pi_{yu}\bar{\pi}_{yu}\pi^*_{xu}\bar{\pi}^*_{xu}\pi^*_{yu}\bar{\pi}^*_{yu}\sigma^*_{uz}\bar{\sigma}^*_{uz}\right) = \sigma^2_{g3p_z}\pi^4_{u3p_x}\pi^4_{u3p_y}\sigma^2_{u3p_z} \tag{2.24}$$

where σ_{gz} corresponds to the σ_{g3p_z} orbital and $\bar{\sigma}$ is for the opposite spin. The excited configuration associated to creation of a hole in spin orbital $\bar{\sigma}^*_{u3p_z}$ and having an excitation in spin orbital $\sigma^\dagger_{g4s}$ is written as:

$$|\bar{\sigma}^*_{u3p_z}\sigma^\dagger_{g4s}\rangle = |\sigma^2_{g3p_z}\pi^4_{u3p_x}\pi^4_{u3p_y}\sigma_{u3p_z}\sigma_{u4s}\rangle \tag{2.25}$$

The molecular term symbols which represents the homogeneous diatomic systems are used in this thesis. They are given by,

$$|\Sigma^+_u\rangle := |\sigma^*_{u3p_z}\sigma^\dagger_{g4s}\rangle \quad \& \quad |\Sigma^+_g\rangle := |\sigma^*_{g3p_z}\sigma^\dagger_{g4s}\rangle$$

$$|\Pi_u\rangle := |\pi^*_{u3p_x}\sigma^\dagger_{g4s}\rangle \quad \& \quad |\Pi_g\rangle := |\pi^*_{g3p_x}\sigma^\dagger_{g4s}\rangle$$

where all the spin configurations (not specified here) for the given state are taken into account. The excitation to molecular orbitals formed from $4p$ atomic orbitals are also taken into account (not in this diagram). Note that, the spin-adapted configurations are no longer singlet determinant.

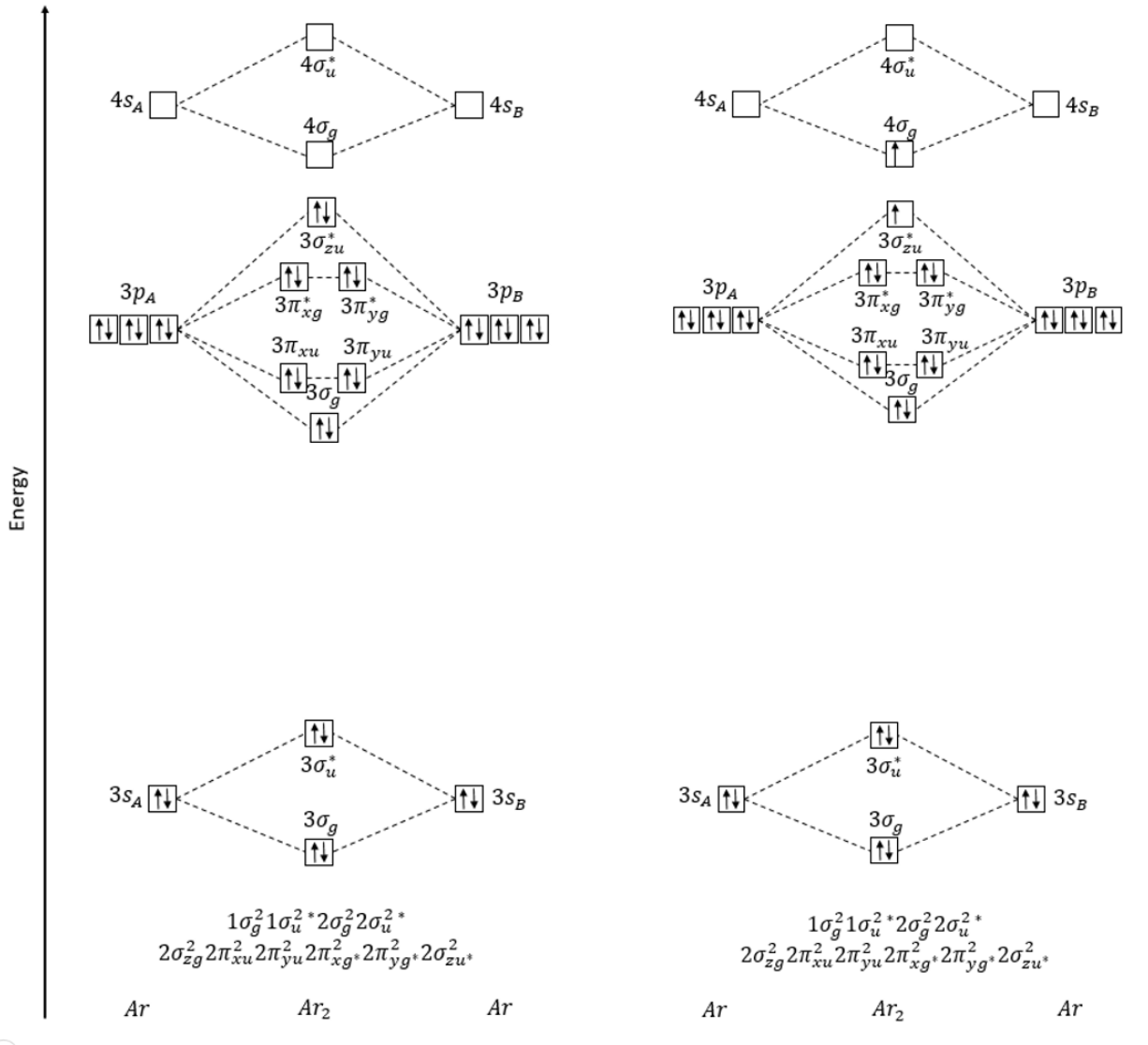

Figure 2.2: Left: Ar_2 Right: Ar_2^* molecular orbitals formation. The figure on the right shows the excitation from $3\sigma_u^*$ into $4\sigma_g$ molecular orbital.

2.2.2 *Ab initio* Calculations

In literature, Argon excimer using *ab initio* calculations was studied for $4s$ and $4p$ excited configurations by Spiegelmann *et al.* [31] using CIPSI [72]. These are one of the best *ab initio* calculations and has been benchmark to most of the work aiming to study excited Argon systems. For these CI calculations, the ground state is $3p^6\ ^1\Sigma_{g0}^+$ and the excited states are located in $np^5(n+1)s$ and $np^5(n+1)p$ configurations. They used relativistic pseudopotential curves to generate valence and Rydberg orbitals [30]. The basis set used for the calculation is ANO-pVTZ type orbitals [87] which is completed by adding $(4s4p3d)$ contracted to $[2s2p1d]$ to represent the diffuse Rydberg orbitals [31, 30]. Unfortunately the authors reported only few points in the repulsive region which is limited for interpolation. Also, these were done in 1984 with limited computational power and the number of configurations in CIPSI were limited. Therefore, with the increased computational capability we intend to obtain short-range potentials, maybe recover dispersion energy with the method to get better results than CIPSI calculations [31] and validate them.

With that in mind, in the following part, we will discuss the *ab initio* calculations like RASSCF, CASPT2 and MRCI using MOLCAS to obtain excimer PECs. We will compare them to previous CI results. The

following are the inputs and parameters taken into consideration to perform MOLCAS calculations. All the inputs used are given in detail in appendix A.

- **Basis set**: The basis set available in the literature are extensive but not diffuse enough and the selection of optimal basis set is equally relevant to the method selected as it defines the space in which calculations are done.

  In the current calculation using MOLCAS to study excited Argon, we select non-relativistic basis set *aug-cc-pVQZ* [87] and extend it by adding ($3s2p1d$) orbitals to introduce the diffuse Rydberg characteristics. The exponents for the expansion are given in the table 2.1. We do not try to reduce or optimise the basis and leave it uncontracted. This basis is used through this thesis while performing *ab initio* MOLCAS calculations to study excited Argon system, unless mentioned otherwise.

Table 2.1: Exponents α_i of the Gaussian added to have further diffuse orbitals on the existing basis set *Ar.aug-cc-pVQZ*. [87]

s	p	d
0.0229	0.01526	0.0598
0.00862	0.00535	
0.003241		

- **Symmetry Selection**: The calculation cannot be done in the $D_{\infty h}$ symmetry group with MOLCAS and it is performed in the D_{2h} symmetry group in this quantum chemistry code. For singlets, $^1\Sigma_g^+$ state is the second state in A_g symmetry, $^1\Sigma_u^+$ state is the lowest state in A_u symmetry and, as the $^1\Pi$ states are degenerate, they can be obtained in either B_{1u} or B_{2u} symmetry. For the triplets, the only difference is $^3\Sigma_g^+$ which is the lowest state in A_g symmetry.

- **SCF Reference Orbitals**: The SCF reference orbitals are essential component while doing MOLCAS. With that in mind, as we are trying to simulate an excited dimer, it is reasonable to consider the core orbitals to be ionised. This is done by systematically removing a total of an electron from the valence $3p$-orbital for each Argon atom. This helps to generate tighter core orbitals on which further calculations are based. Therefore, rather then having doubly occupied valence orbitals, we have them partially occupied.

- **CASSCF/RASSCF**: The implementation of multi-reference SCF methods using MOLCAS is done in the framework of CASSCF (Complete Active Space Self Consistent Field) and RASSCF (Restricted Active Space Self Consistent Field) calculations.

The full inputs of each calculation is available in appendix A. The reference state are obtained by considering single excitation from the $3p$ orbitals. As shown in the Figure 2.3, the $3p$-orbitals are located in RAS1 which is associated to the hole and the $4s$ and $4p$ orbitals in RAS2 (or in RAS3) where all possible configurations are taken into account for an electron. By selecting multiple orbitals (roots) in the CASSCF calculations and giving sufficient weight, the lowest orbitals are optimised. Note that the schematic Figure 2.3 is valid for long separation distance between 2 atoms. At short range the molecular orbitals generated by $4s$ and $4p$ orbitals may be strongly mixed with higher energy orbitals.

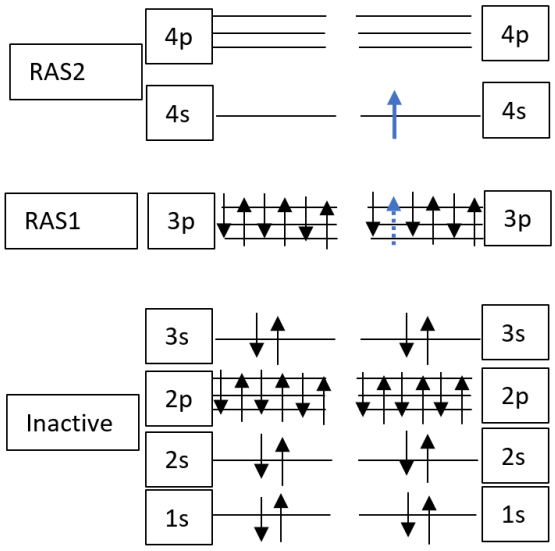

Figure 2.3: RASSCF configuration space used for Ar_2^*. The configurations are made from excitation of an electron from RAS1 to RAS2 active space. In this, there are 12 active electrons coming from the argon $3p$ orbitals.

- **CASPT2**: The success of CASPT2 calculations is highly dependent on the reference orbitals and wave functions obtained using RASSCF calculations. This method is essentially used to recover the dispersion forces using perturbation theory. For the given system, it is essential to do multi-state CASPT2 where the minimum number of roots are obtained in RASSCF calculations. However, the correlation restored by perturbations in these calculations does not have the same effect on all states. For nearly degenerate states ordering can easily be changed from previous RASSCF calculations. Moreover, the intruder states in RASSCF can often introduce discrepancies in the calculated PECs, as we will see later.

- **MRCI**: Besides CASPT2, CI-based calculations also helps to recover the dispersion forces. However, using such large basis to perform MRCI calculations is very difficult. This can be understood by looking at Figure 2.3, where the reference configurations associated to excitation is formed by hole being in 3p-orbital and particle being in $4s$ or $4p$ orbitals. The MRCI calculations is based on the configurations obtained by all single and double excitations from these reference configurations. This in turn leads to huge configuration space, even for minimum active orbitals.

  We still need to generate the multi-reference orbitals and it is done in the similar spirit using RASSCF calculation. However, it is important to have multiple excited orbital in RASSCF for better MRCI results as we observed unwanted accidents while considering the first excited state only. For MRCI calculation, we freeze the core associated to $1s$ $2s$ $2p$ orbitals and we put the $3s$ orbital as inactive (at most 2 holes) and the $3p-4s$ as active orbitals. This is done to reduce the configuration space to take only valence orbitals and first excited state configurations into account and then using MRCI routine to look for the minimum states necessary. It is not possible to include $4p$ states in MRCI using MOLCAS due to the reference space size, which is too large for this quantum chemistry code.

2.2.3 Calculation Results

In section 1.2, we introduce the *ab initio* method previously used to get the PECs for argon excimer. To recall, the best CI-based method using CIPSI was done by Spiegelmann [31] which serves as reference PECs for the following discussions of the Ar_2^* PECs obtained using RASSCF, CASPT2 and MRCI methods in MOLCAS quantum chemistry code.

Figure 2.4 shows the PECs obtained for the Ar excimer using RASSCF, CASPT2 and MRCI methods respectively. The quality of RASSCF PECs which serves as reference to other multi-reference calculations is quite reasonable, i.e., the PECs do not have any unwanted jumps or accidents along the curve. However, the same is not true for CASPT2 PECs, which can been seen the Figure 2.4b. The PECs are not smooth and present some unwanted jumps and is difficult to control. It is likely to be the result of coupling or crossings with intruder states in RASSCF reference calculations, for which the correlation brought by the CASPT2 method changes the energy ordering or crossing position. It can be thought that by introducing more states in RASSCF, the lower states might be better. However, this is not the case because the coupling from the higher states will still there and besides that the near degeneracy of states at larger inter-atomic distance makes it even harder to resolve the unwanted jumps. It is possible to remove these orbitals by not optimising the RASSCF orbitals, but this leads to shallower well depth. Therefore, this method is not well suited for the argon system.

In the CASSCF results, it is observed that the $^{1,3}\Sigma_u^+$ states and all the $^{1,3}\Pi_{u,g}$ states are not deep enough which we attribute to the lack of dynamic correlation in CASSCF calculations. The dispersion forces are well recovered in both CASPT2 and MRCI calculations when compared to previous CI-based results [31]. The calculations performed using MOLCAS with extensive basis and making use of cation makes the potential well deeper giving higher dissociation energy with respect to calculations done by Spiegelmann [31] who used slightly small basis sets (see table 2.2).

It is also important to point that the "hump" in $^{1,3}\Sigma_g^+$ is well reproduced in our calculations as it is in the previous calculations [29, 30, 32, 31]. This is important as the another CI-based calculations by Mizukami *et al.* [33] did not observe this.

The results of the *ab initio* calculations are presented in table 2.2 in comparison to previous CI-based results [31]. Further discussion on excimer PECs will be done later in section 4.1.

Table 2.2: *Ab initio* results using MOLCAS compared with previous CI-based calculation [31]. R_e corresponds to the minimum with dissociation energy D_e.

	$^3\Sigma_u^+$	R_e (au)	D_e (cm^{-1})	$^1\Sigma_u^+$	R_e (au)	D_e (cm^{-1})
This work (CASSCF)		4.60	4652		4.60	5700
This work (MRCI)		4.51	6109		4.50	6909
This work (CASPT2)		4.50	6700		-	-
Spiegelmann *et al.* [31] (CIPSI)		4.61	5694		4.59	6234

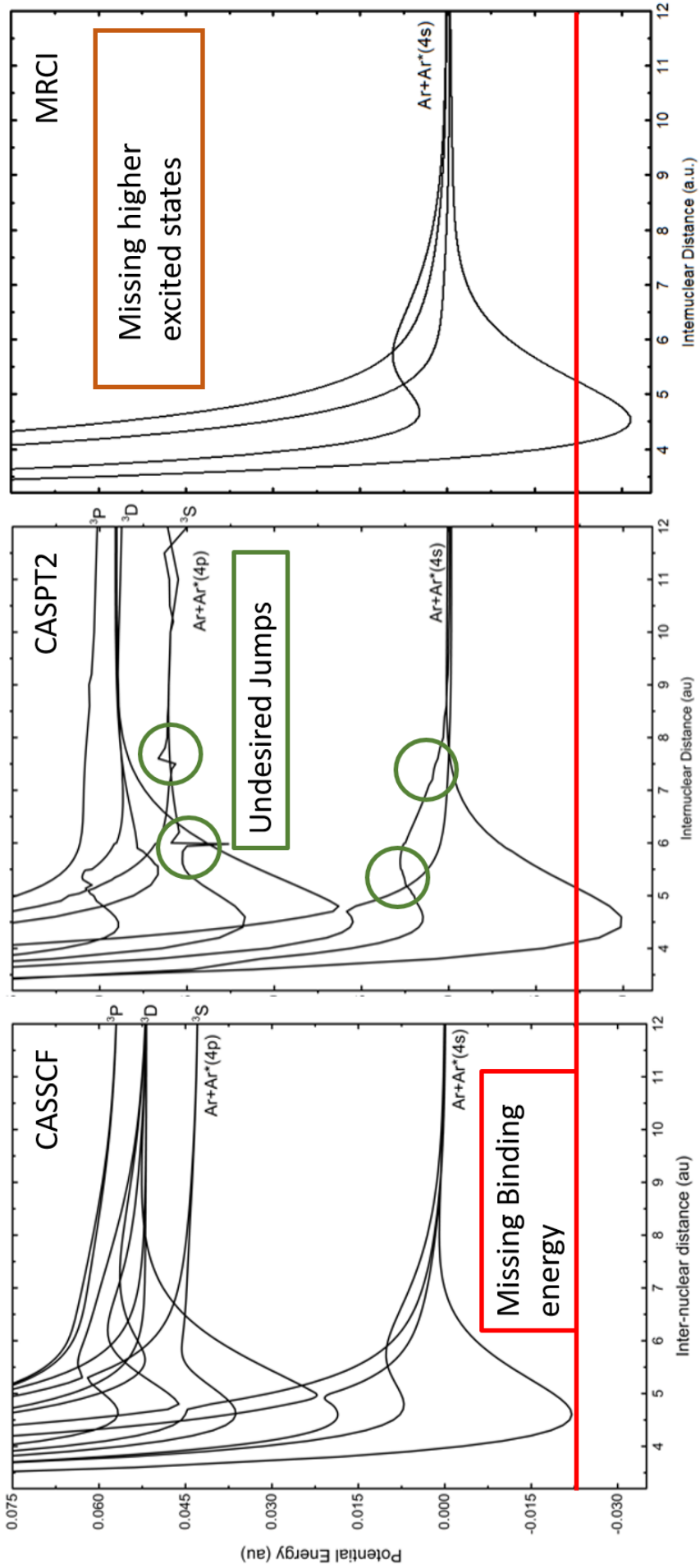

Figure 2.4: Ar_2^* PEC from MOLCAS calculations a) CASSCF plot b) CASPT2 plot and c) MRCI potential energy curves. These dimer plots obtained using MOLCAS are shifted to 0 Hatrees where the reference for each is the Σ_u^+ state. The red line shows the difference in dissociation energy due to missing dispersion energy in CASSCF calculations, the green circle shows the undesired jumps in CASPT2 and brown box shows the missing higher exited states in MRCI calculation in MOLCAS.

2.3 Ar_2^+ PECs using CCSD(T)

This section on CCSD(T) calculations of ionic dimer is used to parametrise the ionic-DIM model. These results are used for the development of the semi-empirical method introduced in section 3.1.

Following the molecular orbitals presented in section 2.2.1, the molecular states associated to single electron ionisation are $^2\Sigma_u^+$, $^2\Sigma_g^+$, $^2\Pi_u$ and $^2\Pi_g$. The CCSD(T) method is suitable for ground state calculations. However, as the spatial-symmetries for the ionized atom are different from each other, by performing the calculation in each symmetry group and looking for the lowest energy state it is possible to obtain these 4 PECs associated to Ar_2^+. These calculations are performed in D_{2h} symmetry, the lowest energy state is computed in A_u, A_g, B_{1u} and B_{2g} symmetry groups for $^2\Sigma_u^+$, $^2\Sigma_g^+$, $^2\Pi_u$ and $^2\Pi_g$ respectively.

For each CCSD(T) calculation we start to build the reference SCF orbitals by taking cation core in the same spirit as done previously for Ar_2^*. In the case of Ar_2^+ this is done by removing an electron systematically from the valence $3p$ shell. In CASSCF calculation we take only one occupied orbital with an electron. This is done to perform restricted open shell Hartree-Fock calculation, which is necessary for CCSD(T). Finally, by having only inner most $1s$ core orbital frozen, in this calculation we take into account inner-shell orbital and core-valence orbital correlations.

Table 2.3: Characteristics of the Ar_2^+ ground state. R_e minimum energy position, D_e potential well depth with respect to the asymptotic value. *The value reported in reference [41] is $D_0 = 10604$ cm^{-1} rather than D_e and we corrected it from the ground state vibrational energy and the spin-orbit coupling.

State	method	R_e (au)	D_e (cm^{-1})	Reference
$^2\Sigma_u^+$	CCSD(T) aug-cc-pV5Z	4.52	11117	This work
	CCSD(T) ANO-RCC	4.53	11280	This work
	CCSD(T) ANO-RCC + BSSE	4.54	10960	This work
	MRCI ANO-RCC	4.53	11168	This work
	DFT	4.59	11225	Michels *et al.*[88]
	CI	4.64	10243	Spiegelmann *et al.* [31]
	Exp. Ginter	4.52	11239*	Ginter *et al.* [41]
	Exp. + SOC	4.56	11212	Mastalerz *et al.* [89]
	Exp.	4.54	10594.9	L.Poission *et al.* [90]

The calculations are performed using two different basis sets, the first one is non-relativistic Ar.aug-cc-pV5Z [87] and the other relativistic Ar.ano-rcc [91]. The scalar relativistic corrections are not very large (differs by $\approx 1\%$ in well depth) and the basis set superposition error (BSSE), which overestimates the energy due to basis overlap, is not very important. With the inclusion of relativistic correction, the core binding is improved very slightly, but this is not important. Also, as seen in the table 2.3, the dissociation energy aug-cc-pV5Z basis is closer to experimental values, we use the non-relativistic basis for further DIM calculation.

The combined experimental and computational work done by Mastalerz *et al.* [89] estimates the spin-orbit coupling (SOC) and shows that it depends on the inter-atomic distance. These results are comparable to the CCSD(T) results using aug-cc-pV5Z, as shown in Figure 2.5, compared to previous CI calculation [31] that overestimated the inter-atomic distance and underestimates the binding energy. In contrast, the DFT method [88] overestimates the inter-atomic distance but correctly estimates the binding energy. However, though using CCSD(T) with pV5Z basis we underestimates the inter-atomic distance, but it is in better agreement with MRCI with large basis and other experimental calculation. CCSD(T) results are corrected for vibrational energy by removing the ground state vibration energy for an atom and for constant spin-orbit coupling. With these corrections taken into account, the CCSD(T) results using aug-cc-pV5Z are a

bit better than previous CI calculations and comparable with the experimental observations. Therefore, the PECs obtained using aug-cc-pV5Z-basis without BSSE are used in the following work, as illustrated in the Figure 2.5.

We discovered the work of Mastalerz *et al.* [89] after doing the computations, and the results presented in this these are thus obtained with PV5Z. Using the results from Ref. [89] would give us slightly shallower PEC and slightly longer equilibrium distance (R_e) as shown in the Figure 2.5.

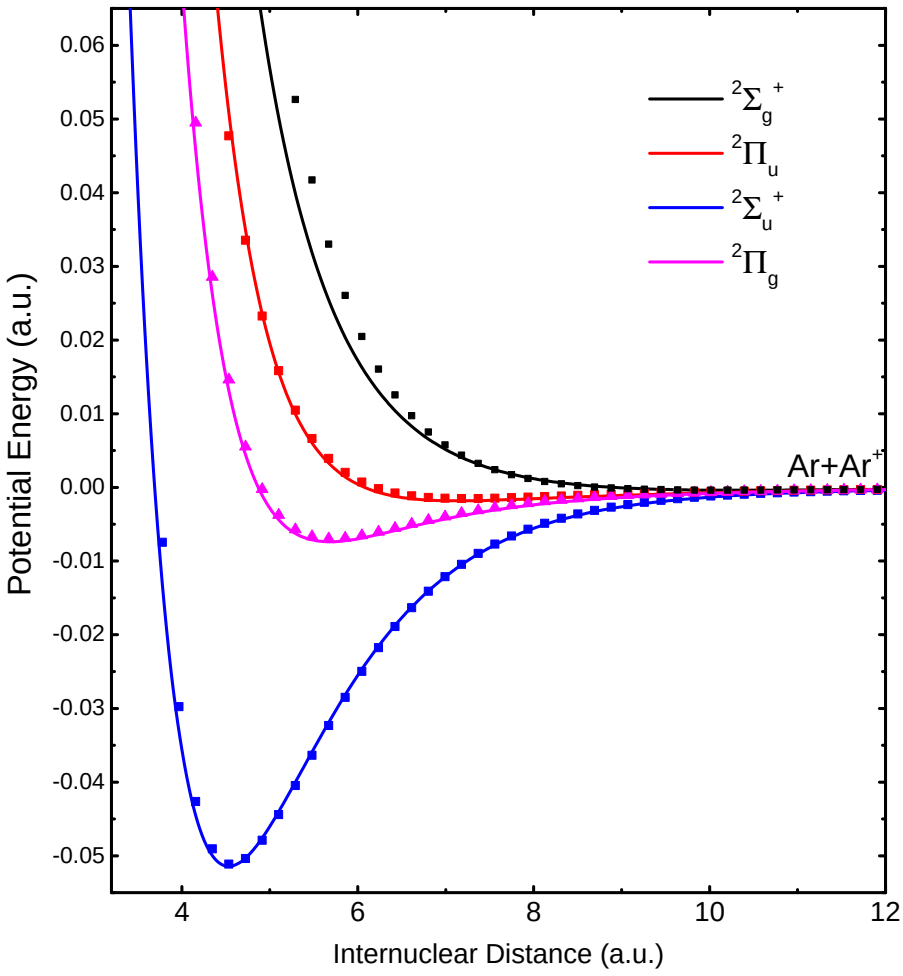

Figure 2.5: CCSD(T) PECs of Ar_2^+ plot from MOLCAS using aug-cc-pV5Z basis (Lines) and Mastalez *et al.* [89] (Points). The 0 is associated to the ionic dimer dissociation.

2.4 Ar_3^* Calculations

Following the observations for excimer, it is not difficult to predict that doing *ab initio* calculations on excited argon trimer will be challenging. The molecular dynamics is obviously out of scope using an *ab initio* method, however it is possible to explore different geometries of the isomers associated to excited trimer. In literature, there are three isomers for Ar_3^* as: Linear Symmetric isomer in $D_{\infty h}$ symmetry [74, 92], isosceles triangular isomer in C_{2v} symmetry [74, 92] and linear asymmetric isomer in $C_{\infty h}$ symmetry [77] as shown in Figure 2.6.

In this section we will discuss the essential parameters to set to have good reference wavefunctions using

RASSCF and then doing CASPT2 calculations. The spirit of buildup of reference wavefunctions is same as it was for the dimer, i.e., starting from initial SCF calculations on the cation and then doing RASSCF calculations for the neutral. We use the same excimer non-relativistic basis *Ar.aug-cc-pVQZ* [87] with extension for diffuse given in table 2.1.

To build reference wavefunctions using RASSCF approach, it is essential to set up proper inputs, taking into consideration the symmetry group and orbital occupation for each isomer. This is important because all isomers are not in the same symmetry and thus the orbitals involved in bonding change from linear to triangular geometries. Also, these calculations are computationally expensive, each point taking around 15 min, and it is important to minimise the number of points to be explored on the PES for each isomer. Therefore, the explored geometries are close to expected structure previously reported.

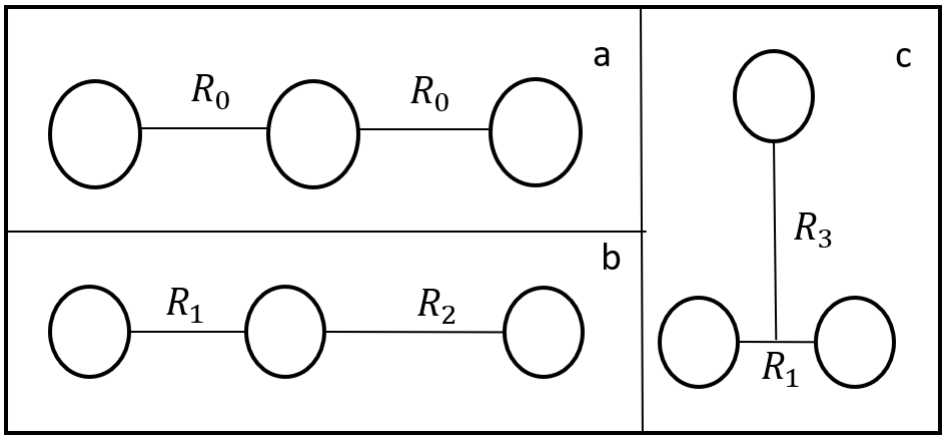

Figure 2.6: Isomers of Ar_3^*. (a) Linear symmetric isomer in $D_{\infty h}$ symmetry (b) Linear asymmetric isomers in $C_{\infty h}$ symmetry group and (c) Triangular isomer in C_{2v} symmetry group

It is important to point that $D_{\infty h}$ symmetry can be computed from other two $C_{\infty h}$ and C_{2v} symmetry groups, which are subgroup of $D_{\infty h}$. The energy associated to the $D_{\infty h}$ isomer is however not the same for these 2 symmetries. This comes from different orbital occupancies for cases b and c, as shown in Figure 2.6, in which the calculations performed do not correspond to the same occupation of the orbitals. The detailed inputs for MOLCAS associated to $C_{\infty h}$ and C_{2v} are given in appendix A.

A general observation while doing these calculations shows that, the dissociation energy associated to each isomer from RASSCF calculation is very small (≈ 10 cm^{-1}). This is obviously due to the lack in dispersion forces which are essential for RG clusters. Being not very informative about dissociation, it nevertheless gives a hint that the $D_{\infty h}$ isomer might not be the lowest energy isomer for Ar_3^*. We further explored this point using CASPT2 calculations and we will not focus on 2.6c geometry.

We performed CASPT2 calculations in the C_{2v} symmetry group for linear geometries to explore linear-symmetric and asymmetric isomers. While exploring the PES, we do not need to change any input parameter and the calculations are thus consistent. The $D_{\infty h}$ geometry is first explored by varying the interatomic distance R_0, as shown in Figure 2.7. We see that for $R_0 = 4.80$ a.u., there is a minimum with $D_e^b = 6342$ cm^{-1}, where D_e^b is the dissociation energy, i.e. the energy taken with respect to the infinite separation of the three atoms given as:

$$Ar_3^* \rightarrow Ar^* + Ar + Ar \tag{2.26}$$

However, this dissociation limit is not what we are interested in. Another dissociation channel D_e arises

when an eximer is formed with a ground state atom given by:

$$Ar_3^* \rightarrow Ar_2^* + Ar \tag{2.27}$$

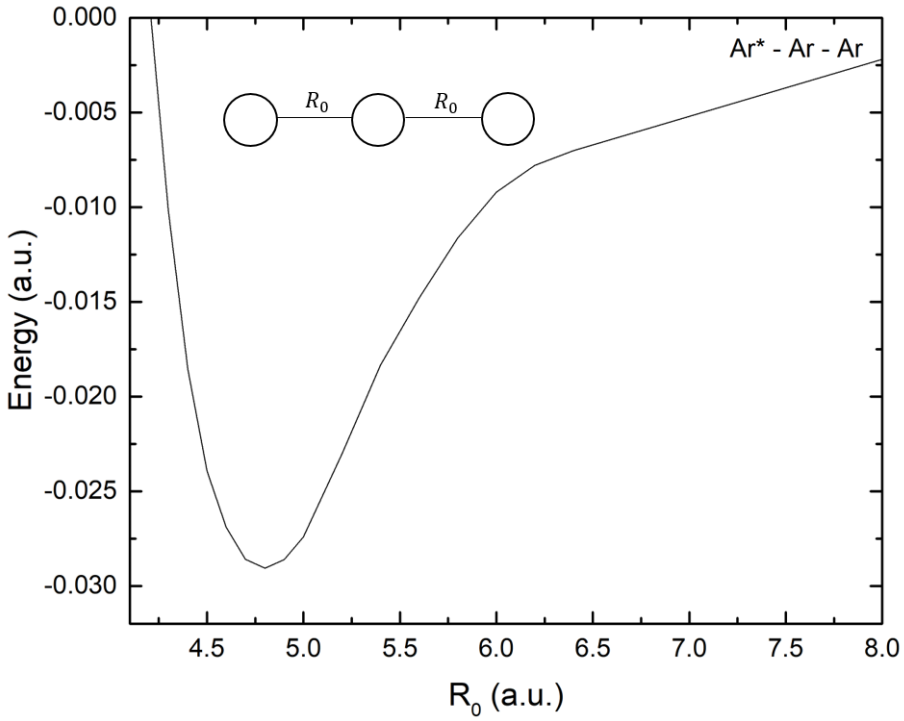

Figure 2.7: Exploring the PES for Ar_3^* in colinear geometry ($D_{\infty h}$ symmetry) using CASPT2 calculations. The plot shows the change in energy with increasing the inter-atomic distance R_0. The dissociation limit is three Argon atoms separated with one of them carrying excitation given in 2.26. The lowest energy point associates to $R_0 = 4.8$ a.u.

The red plot is Figure 2.8 corresponds to the situation where the distance between the two Ar atoms (R_1) is kept fixed to 4.8 au (corresponding to the equilibrium distance of Ar_2^*) and the distance R_2 to the third Ar atom is varied. In this figure we clearly observe that linear symmetric isomer in $D_{\infty h}$ does not have the lowest energy. When fixing $R_1 = 4.80$ au, the minimum is obtained for $R_2 \simeq 5.5$ au. The non-smooth curves reveal the instability of the method. They are associated to the convergence of the RASSCF method, which depends strongly on the input geometry. Despite our efforts to obtain a better, and in-particular smoother RASSCF reference calculations, we were not able to eliminate them. Though not fully conclusive, it is a clear hint that the linear-symmetric is probably not the lowest isomer of Ar_3^*.

We tried to explore the PES by varying the excimer distance (R_1) to search the lowest energy isomer. The black curve in Figure 2.8 shows the potential energy curve associated to the excimer distance $R_1 = 4.50$ au. The lowest energy point is obtained for a distance of an atom, which can be considered to be in ground state, to the closest excimer atom of $R_2 = 5.9$ au. The PEC is however not smooth, this demonstrates the limitations of the CASPT2 calculations.

It is interesting to note that the black star in Figure 2.8 is associated to the lowest energy point in $D_{\infty h}$ symmetry which is significantly higher than the dissociation D_e with excimer, given by 2.27. This is surprising, considering that it is the lowest energy isomer reported in literature [74]. Therefore, using CASPT2 calculations we observe that the linear-asymmetric in $C_{\infty h}$ isomer is lower than dissociation limit by about 340 cm^{-1} and linear-symmetric $D_{\infty h}$ isomer is higher in energy than the dissociation limit by about 380 cm^{-1}.

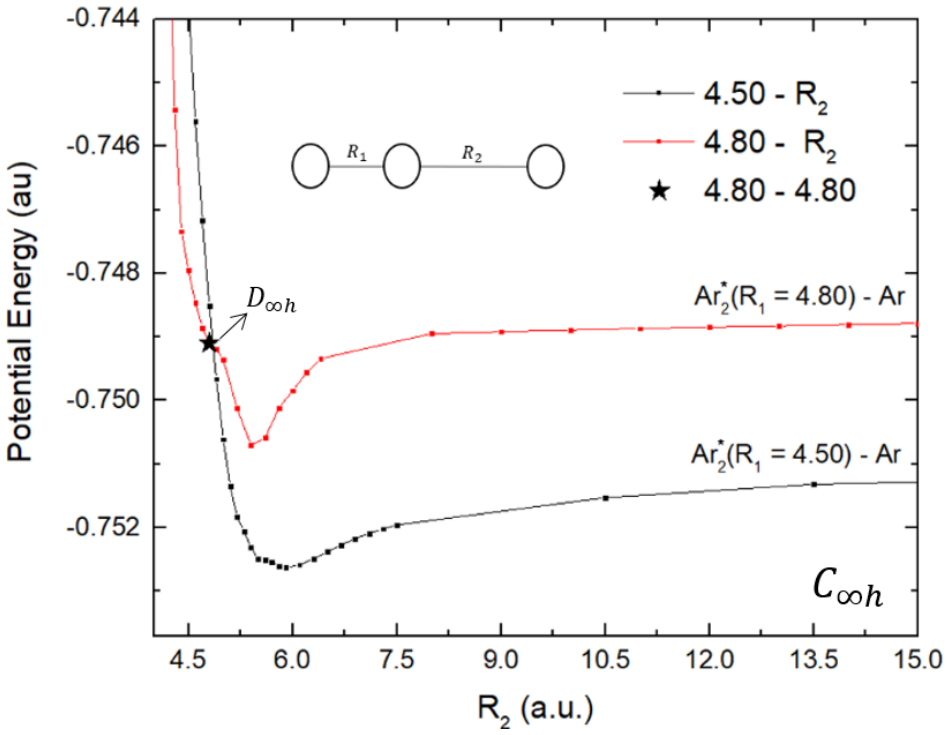

Figure 2.8: Red curve is obtained by keeping the distance between two atoms constant at $R_1 = 4.80$ a.u. (forming Ar_2^*) and varying distance R_2 which can be thought of as a ground state argon atom. Black curve is obtained with fixed $R_1 = 4.50$ a.u. and varying the inter-atomic distance R. The star corresponds to lowest energy point in Figure 2.7.

The results of CASPT2 calculation using MOLCAS are compared to previously reported isomers for the excited Argon trimer, given in the table 2.4. The isomers reported by Naumkin [74] shows the $D_{\infty h}$ to be the lowest isomer and they did not observe the $C_{\infty h}$ linear-asymmetric isomer. This point needs further exploration.

The C_{2v} geometry is not explored using CASPT2 calculation as it is different symmetry from $D_{\infty h}$. See appendix A for further explanation. However, using CASSCF approach we did observe this geometry as Naumkin [74] and Goubert [92] did. It is probably another minimum, which will be further explored in chapter 4. The comparison with these results is given in table 2.4.

Table 2.4: Geometry and dissociation energy of the lowest-energy isomer of Ar_3^* in each symmetry and performed by different types of calculations. The negative D_e corresponds to an energy above the dissociation limit.

Isomer	R_0 (a.u.)	R_1	R_2	R_3	D_e cm^{-1}	reference
$D_{\infty h}$	5.17					CASSCF
	4.80				-380	CASPT2
	5.12				903	Naumkin [74]
	4.79				806	Goubert [92]
C_{∞}		4.60	14.85			CASSCF
		4.50	5.85		340	CASPT2
C_{2v}		4.60		20		CASSCF
		4.60		16	307	Naumkin [74]
		4.63		9.5	200	Goubert [92]

2.5 Conclusion

In this chapter we introduced different *ab initio* methods to solve the electronic Schrödinger equation in rare-gas systems. For the electronic structure calculations we have seen that it is essential to use some post-HF multi-reference method with correlations to get accurate potential energy curves of Ar dimer and trimer.

The success to get reliable excimer PECs was limited. The PECs of Ar_2^* using RASSCF calculations were not deep enough and the dissociation energy is significantly small due to lack of correlations. The correlations are taken into account by using MRCI and CASPT2 calculations. Though the results are comparable with previous CI based work [31], the dependence of CASPT2 calculations on reference wavefunctions make the PECs not reliable. With the MRCI method, we obtain smooth PECs, however the higher states are not accessible due to large configuration space which can not be taken into account in MOLCAS. Hence, the CI based *ab initio* calculations done by Spiegelmann [31] gives the best and most reliable excimer PECs for the moment with higher excited states. Although MRCI and CASPT2 calculations were not a success, they gave a hint that the CI PECs could further be improved. The shortcomings of the previous CI calculations [31] could be due to the selection of small atomic basis set in which the number of primitive Gaussian for each orbitals were not sufficient or the orbital exponents which participate in formation of Rydberg orbitals could be taken to be more diffuse.

We used CCSD(T) method to obtain PECs for the ionic Ar_2^+ system. PECs obtained using aug-cc-pV5Z basis without BSSE are in agreement with the extrapolated experimental results. And the relativistic corrections are small regarding the shape of the PECs.

In CASPT2 calculation, we observed that the lowest energy isomer for an excited trimer is probably not linear-symmetric in $D_{\infty h}$ as previously reported by Naumkin [74] with the DIM approach. This is also consistent with some observations by Durand [77] using a semi-empirical pseudo-potential based method. Therefore, we do not conclude yet about the lowest energy isomer for the excited argon trimer.

The *ab initio* studies without further simplifications can go this far. To study bigger systems, we need non-*ab initio* methods which may provide us the opportunity to study excited states, which is discussed in the following chapter.

Chapter 3

Non *Ab Initio* Model

In the literature, there are two alternative models inspired from quantum chemistry previously used to study RG excited states. The simplest one being the *diatomics-in-molecules* (DIM) model proposed by Ellison [93] which has been rigorously studied and implemented for small ionic clusters up to (N≈4). The DIM method was further expanded to study ionic argon clusters up to the size of 50 [94, 95]. Though this method is fast and does not need to perform explicit electronic structure calculations, the accuracy of its results depend on the selection of atomic configurations and on the dimer potential energy curves which are usually obtained from some experiment or *ab initio* calculation. Following the experience in previous chapter 2, it is to be noted that getting reliable excited dimer PECs is by no means easy. Due to strong coupling between several degenerate excited states, it is difficult to obtain true diabatic Ar_2^* PECs. Besides that in DIM model, the accuracy for diffuse orbitals associated to these states is difficult to establish as, *a priori* the strong overlap between the higher excited states in not accounted for. To represent this correctly in the DIM approach, a large number of diabatic excited states need to be supplied, which is another challenge.

Taking the 4 lowest excited PECs ($\Sigma^+_{u,g}$ and $\Pi_{u,g}$) of Ar_2^* obtained using CI-based calculations [31] while ignoring their adiabatic nature, Naumkin and Wales [74] calculated the lowest energy isomers using the DIM method. However, we were unable to validate their results using an *ab initio* method for Ar_3^* as discussed in chapter 2. Our results for the trimer are consistent with the one reported by Durand and Spiegelmann [77], but these results are not conclusive.

An alternative model given by Duplàa and Spiegelmann [34] is inspired by the proposition to study excited states of RG atoms by Mulliken [25]. This is based on the large HOMO-LUMO energy gap and highly diffuse nature of Rydberg orbitals. Mulliken proposed to add a Rydberg orbital to mimic the excited state on an ionic RG core. Duplàa and Spiegelmann [34] treat the interactions of such Rydberg electron in a hole-particle pseudopotential (HPP) scheme. They defined a configuration basis-set in which the Rydberg electron interacts with an ionized rare gas atom and with the rest of the atoms in their ground state. The corresponding wave function is formed by combination of such configurations, where the hole is localised on an atomic site and the particle is not constrained to be localised. They applied the HPP model to study Ar_2^* [48] and Xe_2^* [96] with spin-orbit coupling and reproduced spectroscopic data in agreement with experimental observations.

Following the success of HPP model to predict Ar_2^* properties and its possibility to be extended to larger clusters, we intend to investigate the lowest energy excited structure for Argon clusters using this model. This provides us with an alternative model to the DIM one.

In this chapter, we first present the formalism of the HPP model and then the DIM model. Our motivation

to use DIM model comes from the fact that, eventually, we intend to perform Molecular Dynamics, which is difficult with the HPP approach due to the number of states but is possible using DIM.

3.1 Hole-Particle-Pseudopotential (HPP) Formalism

The HPP method was proposed to investigate excited electronic structures of molecules and small clusters. As discussed previously, the idea is to represent the interaction of the Rydberg electron with an ionized Ar atom and ground state neutral atoms of the cluster using one-electron pseudopotential.

This method is essentially a simplified CI defined by singly excited configurations associated to creation of a hole in $np\sigma$ spin-orbital of a rare gas atom and creation of a particle in χ_ζ spin-orbital of the cluster. The hole orbital is ideally localised on an atomic site and its overlap with other atoms is neglected whereas the particle orbital extend throughout the cluster and its overlap needs to be evaluated carefully with all atomic sites. The figure 3.1 shows two possible configurations associated to hole being localised on atom A or atom B. The full configuration space is built by having hole on each atom, i.e., treating all atoms in the same way.

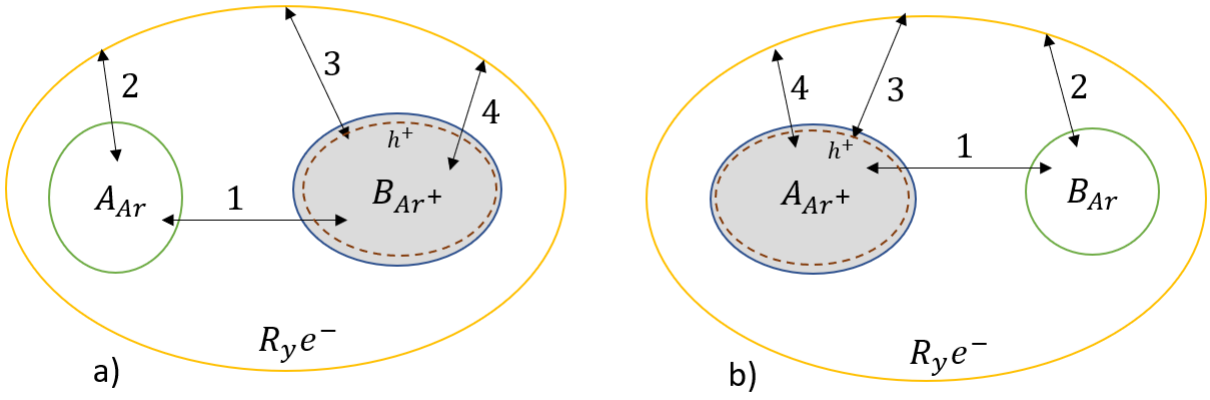

Figure 3.1: Simplified representation of two configuration in HPP model where the system is built by having ionic core with diffuse Rydberg electron. (1) Neutral-ionic core interactions, (2) ground state atom with Rydberg electron interactions (3) hole with Rydberg electron interactions and (4) ionic core with Rydberg electron interactions, which are also different cases in the Hamiltonian.

Here again, we intend to find the solution of the electronic Hamiltonian that comes out of BOA. Now the Hamiltonian is divided into two main parts: the core contribution is calculated with the DIM approximation and the excited electron contribution is treated using a one-electron pseudopotential approximation. We are not going to calculate spin-orbit couplings using HPP model in this work. However, the original authors successfully implemented spin-orbit couplings using the scheme proposed by Cohen and Schneider [27].

The hole-particle configuration basis is defined by the creation of a hole using annihilation operator $a_{A\mu\zeta}$ that removes a valence np spin-orbitals $\chi_{A\mu\zeta}$ on atomic site A $\in [1,N]$, where μ is the spatial orientation ($\mu = x,y,z$) and $\zeta = (\alpha,\beta)$ the characteristic spin numbers. The Rydberg orbital is formed in spin-orbitals $\phi_{i\alpha}$ using particle creation operator, $a^\dagger_{i\alpha}$: with spin α in i^{th} spatial orbital.

The Rydberg orbitals form an orthonormal basis set, and we assume that they are orthogonal to the hole orbitals. The hole-particle configuration basis is thus defined as:

$$|\Phi^{i\alpha}_{A\mu\zeta}\rangle = a^{\dagger}_{i\alpha}a_{A\mu\zeta}|\Phi_0\rangle \tag{3.1}$$

and it forms an orthonormal set of configurations. This gives the single excitation from the neutral ground state $|\Phi_0\rangle$ by creating a hole in spin-orbital $\chi_{A\mu\zeta}$ while promoting it to Rydberg spin-orbital $\phi_{i\alpha}$. A cluster wave function for a singly excited state is given by:

$$\Psi = \sum_{A,\mu,\zeta,i,\alpha} c^{i\alpha}_{A\mu\zeta}\Phi^{i\alpha}_{A\mu\zeta} \tag{3.2}$$

where Ψ is thus a linear combination of these configuration functions.

Now we express the many-body effective Hamiltonian in the basis set:

$$H^{i\alpha,j\beta}_{A\mu\zeta,B\nu\sigma} = \langle\Phi^{i\alpha}_{A\mu\zeta}|H_{el}|\Phi^{j\beta}_{B\nu\sigma}\rangle \tag{3.3}$$

In this model, the Hamiltonian is constructed in blocks where first we calculate the core contributions and then excited electron contributions. We distinguish four different kinds of matrix elements, $H^{i\alpha,j\beta}_{A\mu\zeta,B\nu\sigma}$, depending on whether the hole and the Rydberg orbitals are the same or not in the two configurations.

Case 1: *The diagonal part of the Hamiltonian*

For the first configuration in figure 3.1, the core is made of atom A being ionised while other atoms are in their ground state. In the diagonal part of the Hamiltonian we take all such interactions forming the ionic core. Besides that, all the interactions between the particle and ionic core of same spin orbitals are taken into account.

$$H^{i\alpha,i\alpha}_{A\mu\zeta,A\mu\zeta} = \langle\Phi^{i\alpha}_{A\mu\zeta}|H_{el}|\Phi^{i\alpha}_{A\mu\zeta}\rangle \tag{3.4}$$

$$= E^{+}_{A} + \sum_{B\neq A} E_B + \sum_{B\neq A} V^{+}_{\mu\zeta}(AB) + \sum_{B\neq A}\sum_{C\neq A,C>B} V(BC) + h^{i\alpha,i\alpha}_{A\mu\zeta} \tag{3.5}$$

$$= H^{core}_{A\mu\zeta} + h^{i\alpha,i\alpha}_{A\mu\zeta} \tag{3.6}$$

Collecting the core terms which represent the energy of Rg^{+}_{n} ion with a hole in spin orbital $\chi_{A\mu\zeta}$ while neglecting the three and four body terms as in DIM scheme, we have:

$$H^{core}_{A\mu\zeta} = E^{+}_{A} + \sum_{B\neq A} E_B + \sum_{B\neq A} V^{+}_{\mu\zeta}(AB) + \sum_{C\neq A,C>B} V(BC) \tag{3.7}$$

where E^{+}_{A} is the energy of the ionized atom in the corresponding configuration, E_B is the sum of the energies of ground state atoms, $V^{+}_{\mu\zeta}(AB)$ is the interaction term between an ionized and ground state atoms and $V(BC)$ accounts for the interactions between the ground state atoms. The second term in equation 3.6 is the interaction energy of excited electron with the core which will be later

approximated in pseudopotential formalism.

$$\begin{aligned} h^{i\alpha,i\alpha}_{A\mu\zeta,A\mu\zeta} &= \langle\phi_{i\alpha}| - \frac{\Delta}{2}|\phi_{i\alpha}\rangle \\ &+ \langle\phi_{i\alpha}| - \frac{Z_A}{r_A}|\phi_{i\alpha}\rangle + \sum_{\lambda\varepsilon\neq\mu\zeta}\left(\langle\phi_{i\alpha}\chi_{A\lambda\varepsilon}|\phi_{i\alpha}\chi_{A\lambda\varepsilon}\rangle - \langle\phi_{i\alpha}\chi_{A\lambda\varepsilon}|\chi_{A\lambda\varepsilon}\phi_{i\alpha}\rangle\right) \\ &+ \sum_B\left\{\langle\phi_{i\alpha}| - \frac{Z_B}{r_B}|\phi_{i\alpha}\rangle + \sum_{\lambda\varepsilon}\left(\langle\phi_{i\alpha}\chi_{B\lambda\varepsilon}|\phi_{i\alpha}\chi_{B\lambda\varepsilon}\rangle - \langle\phi_{i\alpha}\chi_{B\lambda\varepsilon}|\chi_{B\lambda\varepsilon}\phi_{i\alpha}\rangle\right)\right\} \end{aligned} \tag{3.8}$$

Case 2: *One-Hole difference*

The off-diagonal matrix elements for the coupling between the holes of two different atomic sites. These are hole-delocalisation (hopping integrals) terms. They are given by;

$$H^{i\alpha,i\alpha}_{A\mu\zeta,B\nu\sigma} = F^+_{\mu\nu}(AB) + \sum_{C\neq A,B} F^+_{\mu\nu}(AB,C) + \langle\chi_{A\mu\zeta}\phi_{i\alpha}|\chi_{B\nu\zeta}\phi_{i\alpha}\rangle + \langle\chi_{A\mu\zeta}\phi_{i\alpha}|\phi_{i\alpha}\chi_{B\nu\zeta}\rangle \tag{3.9}$$

where $F^+_{\mu\nu}(AB)$ and $F^+_{\mu\nu}(AB,C)$ are two and three-body contribution terms respectively. Also, for same center when $A = B$ and $\mu \neq \nu$, we get the coupling between different orientation of the hole orbitals.

Case 3: *One-Particle Difference*

The states formed for same hole but different particle spin-orbitals accounts for non localised Rydberg orbital coupling:

$$\begin{aligned} H^{i\alpha,j\alpha}_{A\mu\zeta,A\mu\zeta} &= \langle\phi_{i\alpha}| - \frac{\Delta}{2}|\phi_{j\alpha}\rangle \\ &+ \langle\phi_{i\alpha}| - \frac{Z_A}{r_A}|\phi_{j\alpha}\rangle + \sum_{\varepsilon\neq\mu\zeta}\left(\langle\phi_{i\alpha}\chi_{A\lambda\varepsilon}|\phi_{j\alpha}\chi_{A\lambda\varepsilon}\rangle - \langle\phi_{i\alpha}\chi_{A\lambda\varepsilon}|\chi_{A\lambda\varepsilon}\phi_{j\alpha}\rangle\right) \\ &+ \sum_B\left\{\langle\phi_{i\alpha}| - \frac{Z_B}{r_B}|\phi_{j\alpha}\rangle + \sum_{\lambda\varepsilon}\left(\langle\phi_{i\alpha}\chi_{B\lambda\varepsilon}|\phi_{j\alpha}\chi_{B\lambda\varepsilon}\rangle - \langle\phi_{i\alpha}\chi_{B\lambda\varepsilon}|\chi_{B\lambda\varepsilon}\phi_{j\alpha}\rangle\right)\right\} \end{aligned} \tag{3.10}$$

which is essentially same as equation 3.8 except for $i \neq j$.

Case 4: *Non-Vanishing off-diagonal term involving two-electron difference*

The two-electron integral provides proper multiplet splitting and hole particle orbital momentum coupling to generate the proper eigenstates of the angular momentum for the atom:

$$H^{i\alpha,j\beta}_{A\mu\zeta,B\nu\lambda} = \langle\phi_{i\alpha}\chi_{A\mu\zeta}|\phi_{j\beta}\chi_{B\nu\lambda}\rangle - \langle\phi_{i\alpha}\chi_{A\mu\zeta}|\chi_{B\nu\lambda}\phi_{j\beta}\rangle \tag{3.11}$$

Until now the parts of the Hamiltonian are exact based on Configuration Interaction scheme.

In HPP scheme, there are several approximations given by Duplaa and Spiegelmann, which makes this model faster than CI based methods and making it a semi-empirical method. This method bears some resemblance to the configuration interaction singles (CIS) method based on absolutely localised molecular orbitals (ALMO-CIS), which includes charge transfer between closest neighbours in its most recent development [97]. However, the Hamiltonian coupling the configurations in the HPP method is further approximated to obtain a simplified evaluation of its matrix elements and also to restore, to some extent, some correlation missing in the CIS method, which leads for example to dispersion force. One of them is to treat core interactions and hole-transfer withinin DIM approximation. This is reasonable because for ionic system DIM

is shown to reproduce closely the *ab initio* results [76]. Next, the interaction of the Rydberg electron with the ionic core is treated in the core-polarization pseudopotential approximation. Finally, the two-electron integrals are calculated with an approximation involving no hole overlap for different centers.

3.1.1 DIM Approximation for Core and Hole-Transfer

The detailed DIM method is discussed later in section 3.2. This approximation is valid for RG systems as there is a large gap between ionic excited states and the states associated to the core configurations made of one hole in $np-$valence atomic orbitals (where $n = 3$ for Argon). In DIM, we neglect the three-body term, while determining the two-body terms for the isolated dimer equivalent systems. The two-body terms are considered for each pair as formalised by Amarouche *et al.* [98]. For each atomic pair AB the potential $V_{\mu}^{+}(AB)$ and hopping integral $F_{\mu\nu}^{+}(AB)$ can be obtained through proper rotations, using unitary rotation matrix R as discussed in section 3.2, mapping from the fixed cartesian orthogonal frame to the frame associated to dimer (AB) direction. The $V_{\mu}^{+}(AB)$ and $F_{\mu\nu}^{+}(AB)$ can be obtained from experimental results or some *ab initio* calculations.

If $\mathbf{R}$ is the vector given for the dimer AB in the cartesian plane, then the PEC without spin-orbit coupling leading to $\lambda = \mu = \nu$ where $\lambda = \Sigma, \Pi_x, \Pi_y$ associated to ${}^2P_X(\lambda)$ for X = A,B. The potential $V_{\lambda}^{+}(\mathbf{R})$ and hopping integrals $F_{\lambda}^{+}(\mathbf{R})$ can be obtained as given by Amarouche *et al.* [98]:

$$V^{+}_{\Sigma_{u+g}}(\mathbf{R}) = \frac{1}{2}[E_{^2\Sigma_u^+}(\mathbf{R}) + E_{^2\Sigma_g^+}(\mathbf{R})] \quad , \quad V^{+}_{\Pi_{u+g}}(\mathbf{R}) = \frac{1}{2}[E_{^2\Pi_g}(\mathbf{R}) + E_{^2\Pi_u}(\mathbf{R})] \tag{3.12}$$

and

$$F^{+}_{\Sigma_{g-u}}(\mathbf{R}) = \frac{1}{2}[E_{^2\Sigma_g^+}(\mathbf{R}) - E_{^2\Sigma_u^+}(\mathbf{R})] \quad , \quad F^{+}_{\Pi_{g-u}}(\mathbf{R}) = \frac{1}{2}[E_{^2\Pi_g}(\mathbf{R}) - E_{^2\Pi_u}(\mathbf{R})] \tag{3.13}$$

Which in matrix form is given by:

$$\begin{pmatrix} V^{+}_{\Sigma_{u+g}}(AA) & -F^{+}_{\Sigma_{g-u}} \\ -F^{+}_{\Sigma_{g-u}} & V^{+}_{\Sigma_{u+g}}(BB) \end{pmatrix} \quad \text{and} \quad \begin{pmatrix} V^{+}_{\Pi_{u+g}}(AA) & -F^{+}_{\Pi_{g-u}} \\ -F^{+}_{\Pi_{g-u}} & V^{+}_{\Pi_{u+g}}(BB) \end{pmatrix} \tag{3.14}$$

For ionic DIM, PECs ($E_{^2\Sigma_u^+}$, $E_{^2\Sigma_g^+}$, $E_{^2\Pi_u}$ and $E_{^2\Pi_g}$) were obtained using DFT method proposed by Matrin *et al.* [99] in the original work. As it has been mentioned previously, the accuracy of DIM methods depends on the parametrization, i.e., we need to get proper ionic dimer potential energy curves. This is obtained here by including single, double and triple (from perturbation theory) excitations in coupled-cluster calculations (CCSD(T)). The details of the calculations were discussed in section 2.3.

The ground state interactions potential $V(AB)$ is obtained using highly accurate inter-atomic potential given by Aziz [100] for Argon.

3.1.2 Pseudopotential Treatment of Rydberg Electron

The pseudopotential treatment of electron using Core Polarisation Pseudopotential (CPP) is of interest because it helps to restore the correlations effects which are missing in CIS calculations, as proposed in AMLO-CIS method as well. The polarization helps the model to restore the dispersion force making the potential fall as $1/R^6$. Both correlation effects and dispersion forces are important in RG systems.

The diagonal and off-diagonal particle contributions can be expressed as Fock operator,

$$F^*_{A\mu\zeta} = \frac{\Delta}{2} - \frac{Z_A}{r_A} + \sum_{\lambda\varepsilon\neq\mu\zeta}(J_{A\lambda\varepsilon} - K_{A\lambda\varepsilon}) + \sum_{B\neq A}\left\{-\frac{Z_B}{r_B} + \sum_{\lambda\varepsilon}(J_{B\lambda\varepsilon} - K_{B\lambda\varepsilon})\right\} \tag{3.15}$$

where J and K are Coulomb and exchange operators. It characterises the interactions of Rydberg electron with a space and spin-polarized hole in spin-orbital $\chi_{A\mu\zeta}$. Now we introduce an isotropic space and spin-averaged pseudopotential where Coulomb and exchange operators are averaged on different space and spin orientation for hole
$\mu\zeta = \{p_{x\alpha}, p_{x\beta}, p_{y\alpha}, p_{y\beta}, p_{z\alpha}, p_{z\beta}\}$. The averaged operator F^*_A is defined as:

$$F^*_A = \frac{1}{6}\left[F^*_{Ax\alpha} + F^*_{Ax\beta} + F^*_{Ay\alpha} + F^*_{Ay\beta} + F^*_{Az\alpha} + F^*_{Az\beta}\right] = \frac{1}{6}\sum_{A\mu\zeta} F^*_{A\mu\zeta} \tag{3.16}$$

We split the Hamiltonian into an average isotropic part, where the interactions with the core are considered in a mean-field approach and anisotropic part to restore hole anisotropy:

$$H^{i\alpha,j\alpha}_{A\mu\zeta,A\mu\zeta} = \langle\phi_{i\alpha}|F^*_A|\phi_{j\alpha}\rangle + \langle\phi_{i\alpha}|F^*_{A\mu\zeta} - F^*_A|\phi_{j\alpha}\rangle \tag{3.17}$$

Hence we get an average Fock operator, which gives the electron-core interactions as:

$$f^*_A = -\frac{\Delta}{2} - \frac{1}{r_A} + W^+_A + \sum_{B\neq A} W_B \tag{3.18}$$

where $-1/r_A + W^+_A$ gives the interaction of the Rydberg electron with the frozen isotropic ion A^+ and W_B gives its interaction with the frozen neutral atoms in their ground state.

To take core-polarization into account an operator [101] is introduced given $f_{A,pol}$ depending on localisation which is added to f^*_A,

$$f_{A,pol} = -\frac{1}{2}\alpha^+_{1A}\mathbf{E}^2_A - \sum_{B\neq A}\left(\frac{1}{2}\alpha_{1B}\mathbf{E}^2_B + \frac{1}{2}\alpha_{2B}(\nabla\mathbf{E}_B)^2\right) \tag{3.19}$$

where $\mathbf{E}_A$ and $\mathbf{E}_B$ are electric field operators created by ionic cores of A and B, α^+_{1A} and α_{1B} are the dipole polarizabilities and α_{2B} is the quadrupole polarizibility corrected for dynamical dipole effect of ionized and neutral ground state rare gas atoms respectively.

We do not use the Θ step functions in the electric field operators for core polarization as given by Duplaa. For both Ar^+ and Ar, we use instead exponential as given by Müller [101] as:

$$C(r,\rho_c) = 1 - \exp^{-\gamma\mathbf{r}^2} \tag{3.20}$$

The parameters γ are given in table 3.1 for Ar^+ and in table 3.2 for Ar.

$e^- - Rg^+$ (electron-ionic atom) pseudopotential

The ionic pseudopotential W^+_A in Eq 3.18 is extracted from all-electron averaged relativistic HF calculations for the lowest states with an excited atomic orbital characterised by $l = 1, 2$ and 3 symmetries for the configurations $3p^5 4s$, $3p^5 4p$ and $3p^5 3d$. The $l-$dependent pseudo-orbitals are obtained using the parametrization by Duplaa and Spiegelmann [34]. However, we used a different polarization form as explained above.

$$W_A^+(\mathbf{r}) = \hat{V}_{\text{loc}}(\mathbf{r}) + \sum_l \hat{P}_l \sum_i c_{li} e^{-\lambda_{li} r^2} \tag{3.21}$$

where $\hat{P}_l = \sum_m |Y_{lm}\rangle \langle Y_{lm}|$ is the projector onto l-subspace, $\hat{V}_{\text{loc}}(\mathbf{r})$ is the common mean field potential generated by the core. The pseudopotential parameters for these orbitals are given in the Table 3.1. For each value of l, the pseudopotential is made of a sum of Gaussian functions indexed by i.

Table 3.1: CPP parameters for the ionic argon atom with dipole polarization. In second partition, first lines given $\hat{V}_{local}$ parameters and the next two lines is non-local with $l = 0$ and $l = 1$ respectively.

Polarisation	Cut-off	c_{0i}	λ_{0i}	c_{1i}	λ_{1i}	c_{2i}	λ_{2i}
$\alpha_{1A}^+ = 7.895$	$\gamma = 0.30$	-2	0.7	1.0492	0.6215	-0.2290	0.3744
		-10	1.5	3.4083	0.6215	1.5529	0.3744
		-26	12.5				

$e^- - Rg$ (electron-neutral atom) pseudopotential

Based on the similar argument about the non-existence of negative ion in the original paper, the electron-argon pseudopotential and the associated core-polarization pseudopotential are produced from elastic $e^- - Ar$ scattering phase shift, which are $l-$dependent. We use here the electron-Argon interaction parameters provided by E. Jacquet *et al.* [102] as shown in Table 3.2 with quadrupole polarization. The latter is smaller than the dipole contribution, however it is not completely negligible at short distance.
The electron-core interaction is given like for Ar^+ core is given by:

$$W_B(\mathbf{r}) = \sum_l \hat{P}_l \sum_i c_{li} e^{-\lambda_{li} r^2} \tag{3.22}$$

Similar to electron-cation pseudopotential, for each value of l, the pseudopotential is made of a sum of Gaussian functions indexed by i.

Table 3.2: CPP parameters for the argon atom with polarization up to the quadrupole [102]

		c_{0i}	λ_{0i}	c_{1i}	λ_{1i}	c_{2i}	λ_{2i}
$\alpha_{1A} = 11.08$	$\gamma = 0.58$	90.0	1.25	8.20	0.55	-2.90	1.5
$\alpha_{1B} = 48.24$		0.12	0.25	0.22	0.14	-6.00	1.0
$\alpha_{2A} = 8.33$						-0.30	0.2

3.1.3 Two-electron integrals

We evaluate two-electron integrals so as to get the exchange contribution to achieve spin multiplet and term splitting which are important in rare-gas clusters. Indeed, the pseudopotential for Ar^+ alone is not sufficient to restore the electron-hole coupling, as it misses the e^-−hole anisotropy because the average Fock operator 3.18 generates a spherically symmetric atomic orbital which needs to be recoupled. The angular momentum coupling between the singly occupied $\chi_{A\mu\zeta} = 3p$ orbital and the Rydberg $\phi_{i\alpha}$ orbital is necessary to restore the spherical symmetry. We do not consider here the spin-orbit coupling, which can be introduced in the DIM treatment of the ionic core. Furthermore, it is advantageous to work with spin-adapted configurations as it reduces the size of the Hamiltonain for $M_S = 0$. Considering symmetry-adapted configuration for

singlet ($S=0$) and triplet ($S=1$). The associated configurations are:

$$|\phi_i^\dagger \chi_{A\mu}; S=0\rangle = \frac{1}{\sqrt{2}}\{|\phi_{i\alpha}^\dagger \chi_{A\mu\alpha}\rangle + |\phi_{i\beta}^\dagger \chi_{A\mu\beta}\rangle\} \tag{3.23}$$

$$|\phi_i^\dagger \chi_{A\mu}; S=1\rangle = \frac{1}{\sqrt{2}}\{|\phi_{i\alpha}^\dagger \chi_{A\mu\alpha}\rangle - |\phi_{i\beta}^\dagger \chi_{A\mu\beta}\rangle\} \tag{3.24}$$

Now for the evaluation of the matrix elements of the type $\langle \phi_i^\dagger \chi_{A\mu}; S|\frac{1}{r_{12}}|\phi_j^\dagger \chi_{A\nu}; S\rangle$, we need an explicit $\chi_{A\mu} = 3p$ orbital to evaluate the splitting term. This is done by taking the difference between $3p$-orbital average and the orientation dependent element. For this, we use the *cc-pVTZ* basis set for $3p$ shell of Argon, which is made of 6 Gaussian type orbitals.

Following Duplaa, we consider only the coupling of hole orbitals localised on the same core A: $\chi_{A\mu}, \chi_{A\nu} \in A$. A simplification introduced by Duplaa and Spiegelmann is to project the Rydberg orbitals ϕ_i, ϕ_j on the basis set orbitals bound to atom A. This should not be a strong approximation as the $3p$-orbitals for Argon atom are well localised. This assumption makes the diagonalization process numerically more stable and at the same time it simplifies the evaluation of the integrals, as only the projections are to be calculated iteratively.

However, the lack of *a priori* orthogonality between the $3p$ Ar orbitals and the Rydberg basis localised on the same atom is a problem. It is because the Rydberg orbitals are the eigenfunctions of a model Hamiltonian, while the $3p$ orbitals are not the eigenfunctions of the same Hamiltonian. Nevertheless all the symmetry rules regarding the matrix elements are respected, and we recover a good approximation of the multiplet by using a simple global scaling η for the matrix element. In the current thesis, we select $\eta = 0.5$.

For simplification, in the following part, we set $x = \phi_i, y = \phi_j, a = \chi_{A\mu}$ and $b = \chi_{A\nu}$. First we evaluate primitive matrix elements for the selected Gaussian basis sets using the LibInt library [103]. After performing contraction step, we get the matrix elements as:

$$(xy|ab) = \int d\mathbf{r}_1 d\mathbf{r}_2 x(1)y(1)a(2)b(2)\frac{1}{r_{12}} \tag{3.25}$$

$$(xb|ya) = \int d\mathbf{r}_1 d\mathbf{r}_2 x(1)b(1)y(2)a(2)\frac{1}{r_{12}} \tag{3.26}$$

Using these two generic integrals, we obtain the matrix elements between spin-adapted configurations. They are first evaluated on the Rydberg basis set bound to an atom $A(x_A, y_A)$ and then they are transformed by computing the overlap $\langle x|x_A\rangle$ and $\langle y|y_A\rangle$ for the Rydberg orbitals, x and y.

Therefore, the matrix element in symmetry adapted basis is given by:

$$\langle x^\dagger a; S|\frac{1}{r_{12}}|y^\dagger b; S\rangle = (xy|ab) + (-1)^S (ay|xb) \tag{3.27}$$

Here we see the effect of exchange term in different spin states.

Now the evaluation of the effective coupling for the model is done by getting the difference between the average potential, the coulombic and exchange term. For each pair a, b we define an effective potential V_{ab}

coupling x and y given by:

$$\langle x|V_{aa}|y\rangle = \bar{V}_A^* - (xy|aa) \qquad : S = 1 \tag{3.28}$$

$$= \bar{V}_A^* - (xy|aa) + 2(xa|ay) \qquad : S = 0 \tag{3.29}$$

$$\langle x|V_{ab}|y\rangle = -(xy|aa) \qquad : S = 1 \tag{3.30}$$

$$= -(xy|aa) + 2(xa|ay) \qquad : S = 0 \tag{3.31}$$

where $\bar{V}$ is the average pseudopotential. This anisotropic, spin dependent potential defines the coupling for all kind of elements (same hole-orbitals or not and same particle orbitals or not).

3.1.4 Hole-Particle Configuration Basis for Argon

The hole-particle basis as defined by equation 3.1 gives the configurations, $|\Phi^{i\alpha}_{A\mu\zeta}\rangle = a^\dagger_{i\alpha} a_{A\mu\zeta}|\Phi_0\rangle$, for hole distribution among $3p$ orbitals of all the ground state Argon atoms and the promotion of an electron to orbital. Rydberg orbitals, $|\phi_i\rangle$, are built from contracted GTO-type basis set, i.e., $(11s/10p/10d) \rightarrow [5s/4p/3d]$ which makes a total of 32 basis functions per atom. We need to construct an orthogonal basis of Rydberg orbitals to generate a proper set of orthogonal configurations.

To do so, we define the hole to be localised on atom-A given by Ar^+ and all other atoms are taken to be in their ground state. For the given configuration we construct a one-body Hamiltonian. We diagonalise this one-body Hamiltonian to get first set of orbitals S_A. Note that, as the number of configurations on each atom is 32, the total size of the basis set is $\{N_{atoms} \times 32\}$. We repeat this for each atom, A,B,C,... taken to be the ionic center while all the other are neutral.

Taking the lowest 4 energy orbitals, which we expect to match as closely to $4s$ and $4p$ atomic orbitals, we form a smaller basis. We orthogonalize this basis using Löwdin orthogonalization technique [104] as it keeps the original character of the orbitals while yielding minimum rotations. This process is helpful for further diagonalization. We thus obtain the first Rydberg series basis S_1 of size $\{N_{atoms} \times 4\}$.

To complete the basis, we project $\{N_{atoms} \times 32\}$ onto perpendicular space of S_1 so as to keep the orthonormality. Doing this, we obtain over-complete S_2 basis. Then we perform Singular Value Decomposition (SVD), which is equivalent to diagonalization of overlap matrix to obtain canonical orbitals by setting a lower threshold to the eigenvalues as $E_n/E_1 < 10^{-6}$ (threshold between the largest eigenvalue E_n and the lowest kept eigenvalue E_1). We keep only the orbital associated to eigenvalues higher than this threshold. This process ensures that the Rydberg basis set is made of linearly independent basis functions. Such a process is necessary to guarantee the stability of the diagonalization. If we lower the threshold too much, we obtain a numerically bound set because of the overlap between diffuse orbitals and the diagonalization in the configuration space becomes ill-conditioned.

Finally we get the basis which is used to evaluate the Hamiltonian in equation 3.3 and the size of basis $N_{true} \leq \{N_{atoms} \times 32\}$ due to large overlap and highly diffuse Rydberg orbitals. On doing so, our Rydberg orbitals are not orthogonal to the $3p$ core orbitals which limits the exact computation of transition amplitudes and this can be further improved.

Table 3.3: Basis exponents(ζ) and contractions (cont.).. The 4s, 3p and 2d remaining functions are pure GTO with the most diffuse exponents.

4s		4p		3d	
ζ	cont. (10^{-3})	ζ	cont. (10^{-3})	ζ	cont. (10^{-3})
9.000	1.368603	3.600	0.4899265	6.0000	7.599220
3.600	-2.88237	1.440	-0.7723731	2.4000	49.59946
1.440	11.77905	0.576	14.58812	0.9600	99.21801
0.576	37.91322	0.230	-78.96873	0.3840	84.30229
0.230	-339.0916	0.092	42.16848	0.1536	123.9965
0.092	70.08756	0.037	513.6374	0.0614	222.4205
0.037	740.1672	0.015	519.2499	0.0246	460.7102
0.015	399.2642	0.006	29.05260	0.0098	359.0689
0.006	-43.33854	0.0025	4.393040	0.0039	14.89564
0.0025	20.88537	0.0010	-1.773896	0.0016	2.615211
0.0010	-5.637969				

3.1.5 Electronic Distribution and Electric Dipole

The electronic distribution can be estimated from the knowledge of hole-distribution. This is rather straightforward for DIM and HPP models as the configuration basis set assumes a well localised hole on a given atom.

Taking the expansion coefficient c_{xa} for a given excited state wave function in the configuration associated with a hole in orbital a and a particle in orbital x, the amount of hole on atom A for this wave function is given by:

$$q_A = \sum_x \sum_{a \in A} |c_{xa}|^2 \tag{3.32}$$

However, electronic distribution is a bit more complicated. As DIM method is based on atomic configurations, the corresponding wave function can not be used to obtain the electronic densities faithfully. On the contrary, for the HPP model with explicit description of the Rydberg electron, it is possible to get the information on this density.

The description of electronic density using popular Mulliken charges is not desirable due to the diffuse nature of the Rydberg electron. Therefore we instead calculate the static electric dipole associated with the given state. The electric dipole **d** is given by,

$$\mathbf{d} = \sum_{A=1}^{N} q_A \mathbf{R}_A - \sum_{xy} \gamma_{xy} \mathbf{r}_{xy} \tag{3.33}$$

where the one-body density matrix is defined as $\gamma_{xy} = \sum_a c_{xa} c_{ya}$ and the matrix element is $\mathbf{r}_{xy} = \langle x|\mathbf{r}|y\rangle$.

3.1.6 Transition Amplitudes

To get the absorption spectrum for a given geometry we need to calculate the transition amplitude between the states.

In the HPP model, the corresponding $3p$ orbitals are not provided for Argon and this problem is bypassed by using the $3p$ orbitals from pVTZ basis set [87] which was used to evaluate the two-body matrix elements. Though these orbitals are not strictly orthogonal to the Rydberg orbitals, the dipole transition matrix has the correct symmetry and this is sufficient to obtain the trends of transition amplitude for comparing with experiment.

Following the previously introduced notations, the transition amplitude for a given excited eigenstate defined by its expansion coefficients c_{xa} is given by:

$$f = \frac{2}{3}\omega \left| \sum_{xa} c_{xa} \mathbf{r}_{ax} \right|^2 \tag{3.34}$$

where ω is the transition energy from the reference state and $\mathbf{r}_{xa} = \langle a|\mathbf{r}|x\rangle$ is the transition dipole vector between the hole orbital a and the Rydberg orbital x.

3.2 Diatomic-In-Molecule (DIM) Method

The Diatomic-in-Molecules (DIM) model was invented by Ellison[93] and this is a technique for computing approximate electronics energies of polyatomic molecules using the information about their atomic and diatomic fragments. As explained by Tully[105], in the original paper, the polyatomic wavefunction can be expanded in terms of a canonical set of valence bond wavefunction, composed of anti-symmetrized product of atomic and diatomic functions.

The DIM model is easy to implement when compared to other quantum mechanical methods as there is no need to calculate integrals to evaluate the electronic Hamiltonian matrix elements of the polyatomic molecule. Therefore, since its inception, it has been rigorously studied and further developed by Tully, Kuntz and others [105, 106, 107, 108, 109]. It has been successfully used to model up to (n=40 atoms) ionic rare-gas clusters [94, 95], In the following section we will give a brief introduction to this method and describe how it can be implemented to study excited rare-gas systems.

The power of the DIM method lies in its ability to solve the time independent Schrodinger's equation for a polyatomic molecule with the limited and easy-to-obtain information about atomic and diatomic species that are constituent of the polyatomic system. Therefore, the definition of the Hamiltonian and polyatomic wave function describing such system forms the backbone of the DIM model.

For any diatomic molecule (AB), we can write the Hamiltonian $\hat{H}_{AB}$ as:

$$\hat{H}_{AB} = \hat{H}_A + \hat{H}_B + \hat{V}_{AB} \tag{3.35}$$

where $\hat{H}_A$ and $\hat{H}_B$ are the atomic Hamiltonians of A and B respectively and $\hat{V}_{AB}$ contains all the inter-atomic interaction potential-energy terms depending on the electron and nuclear coordinates common to atom A and B. Then based on the *atoms-in-molecules* expression $\hat{H} = \sum_A \hat{H}_A + \sum_A \sum_{B>A} \hat{V}_{AB}$,

$$\hat{H}_{\mathrm{DIM}} = \sum_{A}^{M} \sum_{B>A}^{M} \hat{H}_{AB} - (M-2) \sum_{A}^{M} \hat{H}_A \tag{3.36}$$

where M is the total number of atoms in the polyatomic molecule.

Now, we define $|\Phi^{\mathrm{pbf}}\rangle$ as a *polyatomic-basis functions* (pbf), which is an anti-symmetrized product of atomic basis function in valence-bond method,

$$\Phi^{\mathrm{pbf}}(1,2,\ldots,n) = \mathscr{A}_n \phi(1,2,\ldots,n) = \mathscr{A}_n A_{\alpha i} B_{\beta j} C_{\gamma k} \ldots \tag{3.37}$$

where $\mathscr{A}_n$ is a n-electron anti-symmetrizer and $A_{\alpha i}, B_{\beta j}, C_{\gamma k}, \ldots$ are atomic basis functions $i, j, k, \ldots$ of species $\alpha, \beta, \gamma, \ldots$ respectively. We assign n_A electrons to atom A, n_B electrons to atom B and so on, such that the total number of electrons is $n = n_A + n_B + \cdots + n_M$.

Therefore, the wave function for the l^{th} electronic state solving the electronic Hamiltonian is given as a linear combination of n-electron *polyatomic basis functions* given as,

$$\Psi^l(1,2,\ldots,n) = \sum_a c_a^l \Phi_a^{\mathrm{pbf}}(1,2,\ldots,n) \tag{3.38}$$

where c_m^l are the expansion coefficients for state l associated to pbf m. The typical Hamiltonian matrix elements are given by,

$$H_{nm} = \langle \Phi_n^{\mathrm{pbf}} | \hat{H}_{\mathrm{DIM}} | \Phi_m^{\mathrm{pbf}} \rangle \tag{3.39}$$

and the overlap matrix of the polyatomic basis function is,

$$S_{nm} = \langle \Phi_n^{\text{pbf}} | \Phi_m^{\text{pbf}} \rangle \tag{3.40}$$

By simple diagonalization of the Hamiltonian matrix, it is possible to obtain the coefficients as proposed by Kuntz [108] and Tully [106].

In practice, with the information of atomic and diatomic potential energies for a given set of coordinates, it is possible to obtain the energy of the polyatomic system. The determination of the Hamiltonian is done by performing rotation of the free atomic and diatomic matrix elements to bring them from their local (atomic) frame to the global (molecular) frame. While doing so, it is possible to avoid explicit calculation of the overlap matrix and we can consider it to be unity.

3.2.1 DIM Approximations

A The first assumption of the DIM model is the formation of *polyatomic basis functions* in valence-bond model. This is a good approximation when the orbitals taking part in bonding and anti-bonding are mainly the valence orbitals. However, this is not obvious for Rydberg orbitals due to their diffuse nature.

B The anti-symmetrizer $\mathscr{A}$ is set to unity and the overlap between the atomic basis is set to be unity as well. This is a reasonable assumption if we consider the overlap between atomic centers to be negligible. However, this approximation is questionable when the inter-atomic distance is much smaller than the electronic cloud.

C This method is better than atoms-in-molecules as two-body interactions are taken into account. However, three-body terms are neglected. Doing this, we lose some of the polarization effect that can come into play play when 3 atoms are considered. However, in most cases, these effects are very small and can be neglected.

3.2.2 Configuration Basis

To define the basis configurations, for the current system which is an excited Argon cluster, all the species are the same with only one of them in an excited state. Hence, $\alpha = \beta = \gamma = \cdots =$ Ar and we can write the anti-symmetrized pbf for our system as:

$$\Phi_a = A_i B_j C_k \ldots \tag{3.41}$$

where Ar at position A is in state i, Ar at position B in state j and so on. Only configurations like $A_i B_0 C_0 \ldots$, $A_0 B_j C_0 \ldots$, etc are considered.

The electron of the excited atom is not ionized and is considered to be localised on the same atomic centre as the hole generated to promote the electron from the ground state. For our DIM model, the excited state for an atom is obtained from singly excited configuration $3p^5 4s$, $3p^5 4p$, $3p^5 3d, \ldots$. However, in the current study we will consider only the first excited configurations associated to $3p^5 4s$.

To get the excited state, we start with the following Slater determinant, which is a fair approximation of the $^1S_{1/2}$ ground state of Ar atom, when correlation effects are neglected:

$$|A_0\rangle = |3\overline{p}_{-1} 3p_{-1} 3\overline{p}_0 3p_0 3\overline{p}_1 3p_1\rangle$$

where $\overline{p}$ is for β spin or spin down state. From this reference atomic ground state, an excited state can be written as;

$$\widehat{a}_x^\dagger \widehat{a}_a |A_0\rangle \equiv x^\dagger a |A_0\rangle \equiv |x^\dagger a\rangle$$

where, $\widehat{a}_x^\dagger$ is a creation operator of an electron in spin orbital x and $\widehat{a}_a$ is an annihilation operator of electron in spin orbital a corresponding to a hole creation in orbital a. For a given atom and given spatial orbital x, we have 6 hole possibilities. While taking into account the two spin orientations of the excited orbital x for each configuration we can generate 12 determinants associated to the $3p^5 4s$ configurations.

Following the steps defined in previous section of DIM introduction, it is essential at this point to adapt our configuration basis on which we will perform rotations. They are not ideally suited at this moment as they are not eigenfunctions of L^2. A basis set made of such eigenfunctions can however easily be constructed from the above determinant for each shell associated to an orbital x. Using such an L-adapted basis set will make the rotation algorithm simpler, because we can achieve in one single matrix multiplication what would be otherwise done by rotating each orbital, i.e. 6 successive rotations. In the particular case of the determinants $|x^\dagger a$ are proper eigenfunctions of L^2. This is generally not the case and $3p^5 4p$ or $3p^5 3d$ configurations are combinations of such elementary Slater determinants. We shall thus note the atomic functions accordingly as $A_m = |^{2S+1}P; M_L; M_S\rangle$, which is sufficient for the $3p^5 4s$ configurations. The associated configurations are given in appendix B.

3.2.3 Atomic and Diatomic Fragments

- **Atomic Fragments**

  The matrix element of the atomic fragment are the energies associated to the excited or ground state atoms. For instance, the matrix elements for atom A are,

  $$H_{A,nm} = \langle A_m | \hat{H}_A | A_n \rangle = E_{A,nm} \delta_{nm} \tag{3.42}$$

  This can be shown in matrix form as,

  $$\begin{pmatrix} E_{A,11} & \dots & 0 \\ \vdots & \ddots & \vdots \\ 0 & \dots & E_{A,mm} \end{pmatrix} \tag{3.43}$$

- **Diatomic Fragments**

  According to our choice of single excited configuration, we have only two types of diatomic fragments given as $A_i B_0$ for excited Ar*-Ar dimer and $B_0 C_0$ for ground state Ar-Ar dimer.

  The matrix elements for two identical ground state atoms is given as:

  $$\begin{aligned} H_{BC,nm} =& \langle A_n B_0 C_0 \dots | \hat{H}_{DIM} | A_m B_0 C_0 \dots \rangle \\ =& \langle C_0 | \langle B_0 | \hat{H}_{BC} | B_0 \rangle | C_0 \rangle \langle A_n | A_m \rangle \prod_{D \neq A,B,C} \langle D | D \rangle \end{aligned}$$

  while considering the overlap $\langle D|D\rangle = 1$ we have the pairwise matrix element associated to same specie dimer as,

  $$H_{BC,nm} = E_{BC} \delta_{nm} \tag{3.44}$$

Now to get the matrix elements associated to the non-identical species (excited and ground state argon atom), i.e., evaluation of the Hamiltonian of element A in state m with atom B^{th} atom in the ground state,

$$H_{AB,nm} = \langle B_0 A_n | \hat{H}_{AB} | A_m B_0 \rangle \prod_{D \neq A,B} \langle D|D\rangle \tag{3.45}$$

while considering the overlap $\langle D|D\rangle = 1$ as done previously, we get,

$$H_{AB,nm} = \langle B_0 A_n | \hat{H}_{AB} | A_m B_0 \rangle \tag{3.46}$$

Using the matrix representation of the potential energy terms, we can build the full Hamiltonian for a system of three atoms with excitation on atom A represented by an asterisk as:

$$H_{A^*BC} = \begin{pmatrix} h_{A^*} & h_{A^*B} & h_{A^*C} \\ h_{BA^*} & h_B & h_{BC} \\ h_{CA^*} & h_{CB} & h_C \end{pmatrix} \tag{3.47}$$

where h_{A^*}, h_B and h_C are monatomic hamiltonians for atoms A^*, B and C respectively and, where as an example,

$$h_{A^*} = \begin{pmatrix} E_{X_1} & & \\ & E_{X_2} & \\ & & \ldots \end{pmatrix} \tag{3.48}$$

where E_X are the eigenenergies of the excited atom A. h_{A^*B} and h_{A^*C} represent the coupling of atoms (B and C) with the excited atom A^*, and h_{BC} is the coupling between two ground state atoms obtained in the frame oriented along each dimer (A^*B, A^*C and BC).

However, the evaluation of this matrix element is not straightforward. As discussed previously, the elements in this matrix are known in a frame bound to each molecule. Hence rotations are to be performed to evaluate these matrix elements in a common frame. This is discussed below in detail.

3.2.4 Rotations

First we need to align the atomic basis functions with the common fixed coordinate system of our lab. It is necessary to know how these basis functions behave upon rotation through angles (θ, ϕ). For atom A, the rotated wave function is given by [108],

$$\mathbf{A}'_m = \sum_s A_s \mathbf{R}_{sm}(\theta, \phi) \tag{3.49}$$

We use the standard rotation matrix, $\mathbf{R}(\theta, \phi)$, as the atomic basis functions chosen are eigenfunctions of the angular momentum operators for the atom. Atomic basis function in the ground state ($^1S_{\frac{1}{2}}$) are spherically symmetric, the species in ground state, are rotationally invariant. This is not the case for $|^{2S+1}P; M_S M_L\rangle$ states, which are the pbf of excited Ar system.

The basis functions are constructed from the *direct products* of the basis A_m and B_0 for the dimer AB. I.e., the rotation of pbf is a direct product of rotation of each atomic fragment as, $\mathbf{R}_{A_m} \otimes \mathbf{R}_{B_0} \otimes \mathbf{R}_{C_0} = \mathbf{R}_{A_m}[\otimes 1]$. Hence, we rotate only the excited fragment which is convenient and particular to this system as all the other are in their ground state and spherically symmetric.

Hence the new matrix elements for the diatomic species is given as,

$$\overline{H}_{AB,mn} = \sum_{kl} \mathbf{R}_{nk} H_{AB,kl} \mathbf{R}^{-1}_{km} \tag{3.50}$$

from equation 3.46. We use Wigner rotation matrix adapted for $L = 1$.

3.2.5 Hole-Delocalization

The matrix for diatomic fragments represented in a localised pbf basis of atomic functions is given by:

$$H_{AB} = \begin{pmatrix} h_A & h_{AB} \\ h_{BA} & h_B \end{pmatrix} = \frac{1}{2} \begin{pmatrix} E_{\Pi_{g+u}} & & & E_{\Pi_{g-u}} & & \\ & E_{\Sigma^+_{u+g}} & & & E_{\Sigma^+_{u-g}} & \\ & & E_{\Pi_{g+u}} & & & E_{\Pi_{g-u}} \\ E_{\Pi_{g-u}} & & & E_{\Pi_{g+u}} & & \\ & E_{\Sigma^+_{u-g}} & & & E_{\Sigma^+_{u+g}} & \\ & & E_{\Pi_{g-u}} & & & E_{\Pi_{g+u}} \end{pmatrix} \tag{3.51}$$

where $\Lambda_{u+g} = \frac{1}{2}(\Lambda_u + \Lambda_g)$ and $\Lambda_{g-u} = \frac{1}{2}(\Lambda_g - \Lambda_u)$ for $\Lambda = \Sigma, \Pi$. Therefore, as an example, $E_{\Sigma^+_{u+g}} = \frac{1}{2}(\Sigma^+_u + \Sigma^+_g)$ and so on.

Where we have the four lowest adiabatic PECs for the excited dimer in each $M_S = 0, 1$ ($^{1,3}\Sigma^+_u$, $^{1,3}\Sigma^+_g$, $^{1,3}\Pi_g$ and $^{1,3}\Pi_u$). This corresponds to the hole delocalization in orbitals of the related symmetry. This transformation between u and g are well defined for single Σ states on identical atom which makes this a model system. However, for multiple Σ states this is not as straightforward.

Using Canonical unitary transformation matrix U, we have the effective Hamiltonian in the delocalised basis as,

$$H^{\text{ad}}_{AB} = U^{\dagger} H_{AB} U \tag{3.52}$$

The canonical unitary transformation allows the transformation between delocalized and localised states. And this transformation is independent of the inter-atomic distance.

3.2.6 Spin-Orbit Coupling

To include Spin-Orbit Couplings in DIM is not very difficult. As shown by Tully [110], it can be added to the $\hat{H}_{\text{DIM}}$ before solving the secular equation to get the eigenvectors as,

$$\hat{H}_{\text{tot}} = \hat{H}_{\text{DIM}} + \hat{H}_{\text{SOC}} \tag{3.53}$$

where $\hat{H}_{SOC}$ is the spin orbit coupling Hamiltonian given by;

$$\hat{H}_{SOC} = \sum_i \xi(r_i) \mathbf{l}_i . \mathbf{s}_i \tag{3.54}$$

$\xi(r_i)$ is obtained in a central-field potential $U(r_i)$ as observed by electrons i. Assuming the matrix elements, $\xi(r_i) = \zeta_{nl}$, to be constant for all electrons with the same nl quantum numbers, which is matched to experimental results to match the fine-structure splitting. Therefore, the coupling can be approximated as;

$$V_{SO} = \sum_i \zeta_{n_i l_i} \mathbf{l}_i . \mathbf{s}_i \tag{3.55}$$

In this semi-empirical approach, as discussed by Cohen and Schneider [27], the two-electron effects are taken implicitly but cannot be validated and the orbitals are considered to be not too distorted by inter-atomic forces. In such a case, we have the molecular spin-orbit coupling as the sum over individual atomic contributions given by;

$$V_{\mathrm{SO}}^{\mathrm{mol}} = \sum_{a,i} \zeta_{n_i^a l_i^a}^a \mathbf{l}_i^a . \mathbf{s}_i^a \tag{3.56}$$

for a atoms.

We represent the spin-orbit matrix elements in the separated-atom limit DIM basis as;

$$V_{\mathrm{SO}} = \langle L_i M_{L_i} S_i M_{S_i} | \hat{H}_{SOC} | L_j M_{L_j} S_j M_{S_j} \rangle \tag{3.57}$$

where L_i is the total angular momentum of atom i, M_{L_i} is its projection S_i is the total spin of atom i and M_{S_i} its projection on the quantification axis. We consider that the excitation is only in $4s$-orbital which is coupled to hole in $3p$-orbital. We consider only SOCs within the atom, the SOCs with other atoms is neglected. In the work of Mastalerz *et al.* [89], they showed that with the SOCs with other atomic sites is not negligible, however it is smaller than the spin-orbit within the atom and neglecting it is a reasonable approximation. Spin-Orbit interaction matrix for Ar$[3p^5 4s]$, $L = 1$, is given by;

$$V_{\mathrm{SO}} = \left(\begin{array}{ccc|c} A & B & & C \\ B^T & & B & D \\ & B^T & -A & E \\ \hline C^T & D^T & E^T & \end{array}\right) \tag{3.58}$$

where, the upper-left 3x3 block corresponds to triplets and the lower right empty block corresponds to singlet states. The states are rated by block of increasing M_L and by increasing M_S inside each block. Each square matrix is given by, for triplet,

$$A = \begin{pmatrix} -\alpha & 0 & 0 \\ 0 & 0 & 0 \\ 0 & 0 & +\alpha \end{pmatrix} \quad B = \begin{pmatrix} 0 & 0 & 0 \\ +\alpha & 0 & 0 \\ 0 & -\alpha & 0 \end{pmatrix}$$

and the triplet-singlet couplings are given by;

$$C = \begin{pmatrix} 0 & 0 & 0 \\ -\alpha & 0 & 0 \\ 0 & +\alpha & 0 \end{pmatrix} D = \begin{pmatrix} -\alpha & 0 & 0 \\ 0 & 0 & 0 \\ 0 & 0 & -\alpha \end{pmatrix} E = \begin{pmatrix} 0 & +\alpha & 0 \\ 0 & 0 & +\alpha \\ 0 & 0 & 0 \end{pmatrix}$$

where α is the atomic spin-orbit constant taken from NIST database.

3.3 Diabatization

As discussed by several previous authors [25, 48, 27] and in chapter 1, the potential energy curves are influenced by the avoided crossings between diabatic-like potential curves at short and medium distance range. These are classified in two types by Duplaa and Spiegelmann, the first one being weakly and very locally avoided crossings, where two avoiding states are clearly built on configurations which differ through both core and particle (two particle difference). This occurs in lower and higher $^{3,1}\Pi_{u,g}$ states, for example. The second type concerns the strong avoided crossing for the lowest $^{3,1}\Sigma_g^+$ states where, at short distance, we find a barrier also referred to as a hump. This is depicted in figure 3.2 as an example obtained from CASSCF MOLCAS calculations.

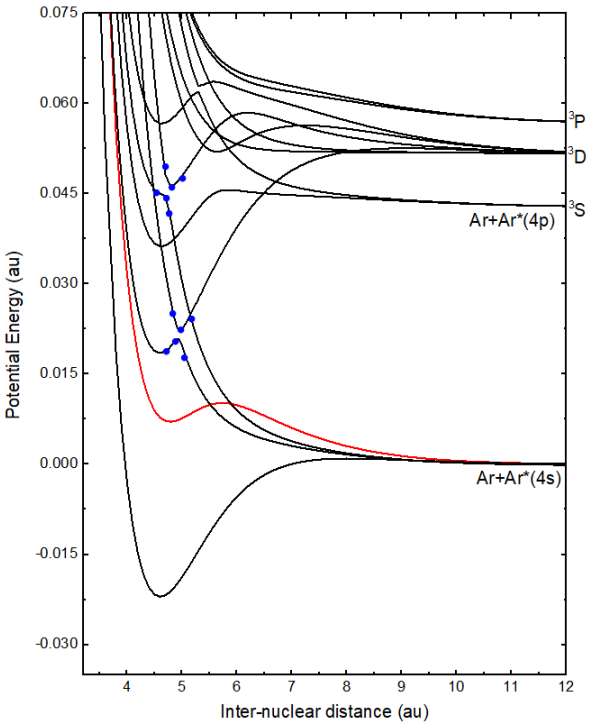

Figure 3.2: The Ar_2^* PECs obtained using CASSCF calculation in MOLCAS. This figure shows the hump in repulsive $^3\Sigma_g^+$ state dissociating to 4*s* limit in red. Blue dots show the points of non-avoided crossings in $\Pi_{u,g}$ states.

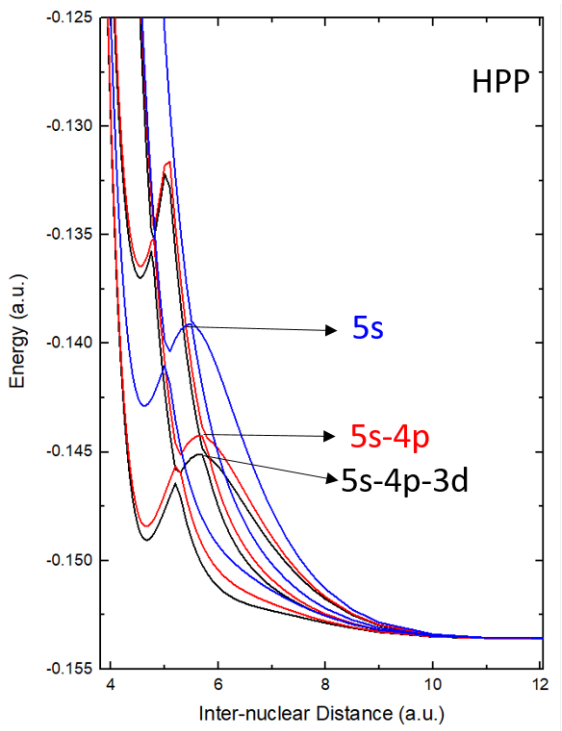

Figure 3.3: PECs showing the effect of coupling from higher states. Solid Lines: 5s4p3d states; Dashed Line: 5s4p states; Dashed-Dotted Lines: 5s states.

The resolution of the states with the non-avoided crossings is straight forward which can be done by interchanging the PECs. Which is related to theoretical procedure, like diagonalisation, that sorts states by order of increasing energy. However, for the avoided crossings it is not that simple due to strong couplings. The presence of this hump has been suggested since the initial study of Mulliken [25] for Xe_2^*. Cohen and Schneider [27], in their work on Ne_2^*, suggested that this hump results from the avoided crossing between two diabatic Σ_g^+ states correlating asymptotically to the Ne+Ne$^+$(3s) and the Ne+Ne*(4p) dissociation limits. Gadea and Spiegelmann [31] emphasised a bit more the role of the ionic core configurations and suggested that the observed hump resulted from the avoided crossing between the diabatic repulsive configurations $[^2\Sigma_g^+]\sigma_g^*4s$ and attractive $[^2\Sigma_u^+]\sigma_u^*4p$ states in the ionic core (Ar_2^+). However using HPP it was possible to suppress all the p-orbitals from the basis, and still observe the hump, though with a smaller barrier, as depicted in figure 3.3. This means that the $[^2\Sigma_g^+]\sigma_g^*4s$ and $[^2\Sigma_u^+]\sigma_u^*4s$ contribute significantly to the formation of the hump. A schematic illustration of the contributing configurations is given in Figure

3.4 for σ type orbitals. The $^2\Pi_{u,g}$ core configurations associated to $\sigma_u p$ and $\sigma_g p$ may also contribute to the hump. This makes the $1^S\Sigma_g^+$ state of the Ar_2^+ dimer a genuine multi-configuration state.

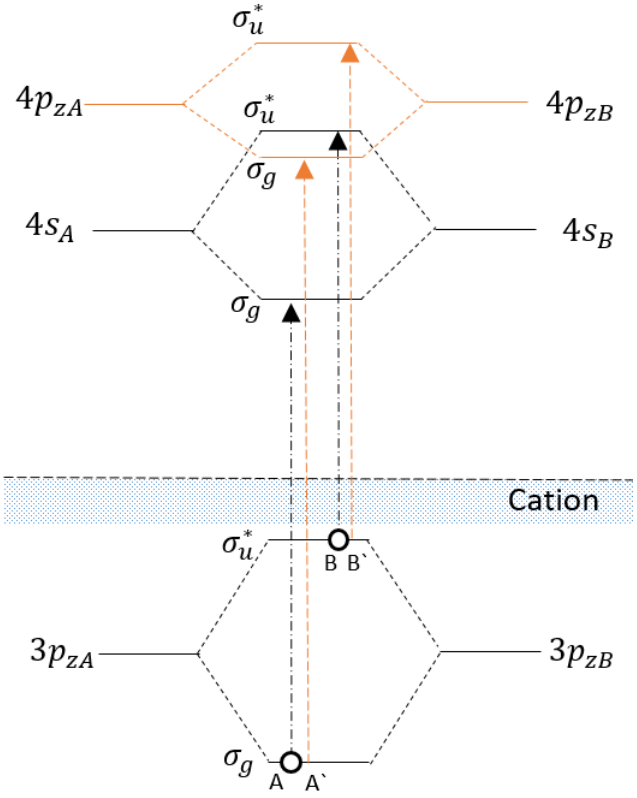

Figure 3.4: Illustration to form Σ_g^+ configurations. (Not to scale)

The Σ_g configurations are formed by promotion of a $3p\lambda_u$ or $3p\lambda_g$ orbital electron to a nx Rydberg orbital with the same symmetry λ_u or λ_g respectively, where $\lambda = \sigma, \pi$. The repulsive configurations are made when the core is in $^2\Sigma_g^+$ symmetry, with a hole in $\sigma_g 3p$ orbital, as shown in A and A`. The attractive configurations are generated by creation of hole in $\sigma_u 3p$ orbitals to form a $^2\Sigma_u^+$ core, as shown in B and B`. The PECs representative of these configurations are dominated by the cationic core energy, and therefore the higher PECs can be reproduced by shifting them according to their asymptotic limits, Spiegelmann *et al.* [48, 31] illustrated such effects. The coupling of such states leads to formation of the hump.

From a DIM perspective, atomic orbitals and configurations should be used instead of the above molecular orbital description. It is of course possible to substitute the molecular orbitals by their expansion into atomic orbitals, and expand the molecular-orbitals based configuration to obtain atomic configurations. In doing so, we obtain configurations with 5 occupied orbitals on an atom and 7 orbitals in the other. In other words, we obtain Ar^+Ar^- ionic configurations associated to charge transfer. It is unfortunately not particularly easy to generate dimer PECs associated to this kind of configurations. Moreover, the multiplicity of combinations makes the problem computationally expensive.

Following our previous discussion, the avoided crossing of the Σ_g^+ state is not easy to resolve as we do not have a correct estimate of the couplings which come from mixing of several higher configurations. Ideally, if we can identify all the coupled states and uncouple them using rotations, we would obtain the true diabatic PECs. However, this is not trivial for excited argon because, firstly there are several Rydberg states which are not easy to identify because of high degeneracy and then these states strongly coupled. Or using some *ab initio* method obtain the anionic $(Ar^+ - Ar^-)$ PECs using which we can be used to determine the couplings.

We shall instead provide an *ad hoc* state which is supposed to encapsulate the effect of all the higher-energy states so as to obtain diabatic Σ_g^+ state. Such a state is by no means physical and needs some approximations. In the following section we propose a method to estimate such an *ad hoc* state.

3.3.1 Method Used

The uncoupling between two adiabatic states is achieved by unitary transformation [111] which is defined as:

$$\begin{pmatrix} A & \\ & B \end{pmatrix} = U^{\dagger} \begin{pmatrix} \alpha & \delta \\ \delta & \beta \end{pmatrix} U \tag{3.59}$$

where A and B are adiabatic state energies, α and β are the diabatic state energies with δ being the coupling between them.

In the present case, A state is the adiabatic $^{1,3}\Sigma_g^{\mathrm{a}}$, B is an estimated *ad hoc* adiabatic state which restores the coupling with the higher-energy states. α is diabatic $^{1,3}\Sigma_g^{\mathrm{d}}$ and β is a dummy diabatic state.
Assuming that, A, B and α are know, we solve 3.59 to get the couplings as:

$$\delta^2 = (A-\alpha)(\alpha - B) \tag{3.60}$$

and finally we get the diabatic PEC β used to parameterize the DIM hamil-tonian, as:

$$\beta = \alpha + \delta\left(1 - \frac{1}{\tan\theta}\right) \tag{3.61}$$

where θ is the angle of rotation. See appendix B.2.

The DIM model using the PECs obtained by the diabatization process will be referred to as Di-DIM.

The full Di-DIM Hamiltonian is given by:

$$H_{\text{Di-DIM}} = \begin{pmatrix} h_A & h_{AB} \\ h_{BA} & h_B \end{pmatrix} \tag{3.62}$$

where $h_A = h_B$ and h_{AB} are arranged as $(A_x A_y A_z^{\alpha} A_z^{\beta})$ for each spin multiplet,

$$h_A = \frac{1}{2}\begin{pmatrix} E_{\Pi_{g+u}} & & & \\ & E_{\Pi_{g+u}} & & \\ & & (\alpha)E_{\Sigma^+_{u+g}} & \delta_{\Sigma_{u+g}} \\ & & \delta_{\Sigma_{u+g}} & (\beta)E_{\Sigma^+_{u+g}} \end{pmatrix} \tag{3.63}$$

and

$$h_{AB} = \frac{1}{2}\begin{pmatrix} E_{\Pi_{g-u}} & & & \\ & E_{\Pi_{g-u}} & & \\ & & (\alpha)E_{\Sigma^+_{u-g}} & \delta_{\Sigma_{u-g}} \\ & & \delta_{\Sigma_{u-g}} & (\beta)E_{\Sigma^+_{u-g}} \end{pmatrix} \tag{3.64}$$

where $\delta_{\Sigma_{u\pm g}}$ are the coupling terms obtained from diabatization. $E_{\Lambda_{g\pm u}}$ are the energies obtained form the PECs as defined in section 3.2.5.

3.3.2 Di-DIM Parametrisation

It is possible to use any method to get the PECs (eg, a DIM model). In our case we are going to use Ar_2^* PECs obtained using the HPP method as discussed in the following chapter 4. This provides us with state A of equation 3.59, ie ${}^{ad}\Sigma_g^+$, where 'ad' is for the adiabatic state as shown in figure 3.5.
Using the relation between u and g symmetries;

$$\Sigma_{u+g}^+ = \frac{1}{2}\left({}^{d}\Sigma_u^+ + {}^{d}\Sigma_g^+\right) \rightarrow {}^{d}\Sigma_g^+ = 2\times\Sigma_{u+g}^+ - {}^{d}\Sigma_u^+ \tag{3.65}$$

Using HPP, it is possible to obtain adiabatic PECs (eg: $\Sigma_{u\pm g}^+$) PECs. This is done by freezing one of the atom in the ground state and exploring all the possible states of the excited atom.

This was proposed by Cohen and Schneider to obtain diabatic states of Ne_2^* [27]. These potential curves are obtained in Σ symmetry. Now the selection of B-state is not easy. This is an *ad hoc* state, i.e., it is not really present in the Ar_2^* PECs obtained using HPP method or any other method. Since there is no way of knowing the true nature of coupling or the *ah hoc* state, it is approximated by comparing the lowest energy isomer obtained for the trimer while varying the depth of the *ah hoc* state. The B-state is selected to dissociate at $4p\ {}^3S$ limit as shown. Figure 3.5 shows the diabatized potential curves for triplet. The change in the dissociation limit does not alter the results, provided it is high enough.

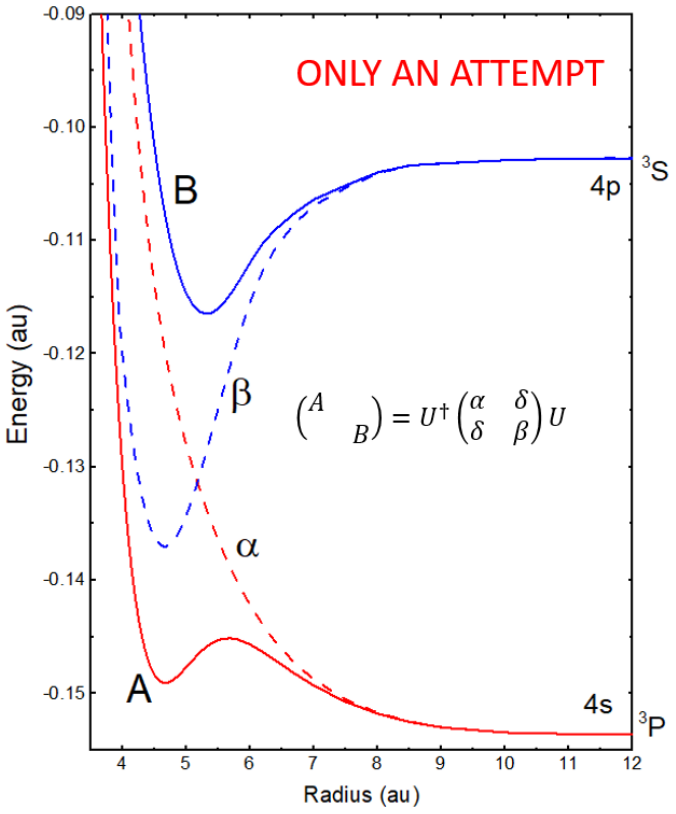

Figure 3.5: Diabatised potential-energy curves A (${}^{ad}\Sigma_g^+$) and B (*ad hoc* state) are the adiabatic states, while α (${}^{d}\Sigma_g^+$) and β (dummy state) are the diabatic potential curves for the triplet state.

Note that the initial work by Cohen and Schneider on Neon [27] assumed the *ah hoc* state to be np excited orbital only and they observed a barrier in the diabatic curve whereas we do not observe any barrier after the minima as seen in β curve of figure 3.5. However the reason for considering an *ah hoc* state is because by just considering $4p$ states in parametrisation of DIM, we were not able to reproduce the lowest-energy structure of the trimer. We also neglect the SOCs between the *ad hoc* state in this work for simplicity.

Chapter 4

Results and Discussions

In this chapter we will start by discussing the argon excimer PECs obtained using the HPP model and compare them to the original work [34, 48] and our *ab initio* (CASSCF, CASPT2 and MRCI) calculations using MOLCAS for Ar_2^*. Then we discuss the consequences of the changes brought in the method. Using *ab initio* methods we will validate the HPP model and compare the salient features of the excimer potential energy curves with previous results. Following that, we will explore the trimer PES which helps us to interpret larger clusters and discuss why and how they are different from previous works [74, 92]. We discuss larger isomers obtained using HPP, compare them with previous work [74] and show the role played by the excited trimer.

A qualitative comparison of lowest-energy isomers is presented using different diatomics-in- molecules methods parameterized using; a) CI-based [31] calculations as done by Naumkin and Wales [74] (N-DIM) b) or HPP dimer PECs (H-DIM) calculated in this thesis. These structures of isomers are also compared to lowest energy geometries obtained using Di-DIM.

4.1 Excimer Potential Energy Curves

The excimer potential energy curves obtained using the HPP model are shown in Figures 4.1 and 4.2 for triplet and singlet states respectively. They follow the trend predicted by Mulliken [25], he studied the asymptotic behaviours of the PECs of diatomic molecules that dissociate into resonant states (ground and excited).

The nature of Rydberg states in Ar_2^* has been given in detail by Duplaa and Spiegelmann [48] in their original article about the HPP method. They identified all the PECs for $3p^5ns$, $3p^5np$ and $3p^5nd$ configurations by considering diabatic-like Rydberg states through association of a given core with an unpromoted diabatic orbital compatible with global spin and space symmetry, as discussed in section 3.3. For the $3p^54s$ configurations, the separated atoms generate only unpromoted orbitals namely σ_g^*, and one expects attractive $^{3,1}\Sigma_u^+$ states ($^2\Sigma_u^+\sigma_u^*$ configurations), mostly repulsive $^{3,1}\Pi_{u,g}$ states ($^2\Pi_{u,g}\sigma_{u,g}^*$ configurations) and almost repulsive $^{3,1}\Sigma_g^+$ states ($^2\Sigma_g^+\sigma_g^*$ configurations). Based on the discussions by Duplaa and Spiegelmann [48], there are few takeaways for excited argon dimer potential energy curves. Firstly, the singlet and triplet states are roughly parallel and excimer states are highly dependent on the ionic core in which, $^2\Sigma_u^+$ is attractive, $^2\Pi_{g,u}$ are moderately repulsive and $^2\Sigma_g^+$ is very repulsive leading to strongly attractive $^{3,1}\Sigma_u^+$ excimer states.

The lowest-energy excimer states are $^{3,1}\Sigma_u^+$ states in each spin-symmetry. Table 4.1 presents the comparison of equilibrium distances R_e and dissociation energies D_e with previous and MOLCAS *ab initio* results

Table 4.1: Comparison for $^3\Sigma_u^+$ and $^1\Sigma_u^+$ states with different types of calculations. R_e is the equilibrium distance and D_e is the dissociation energy.

		R_e (au)	D_e (cm^{-1})
$^3\Sigma_u^+$	This work (HPP)	4.52	7019
	This work (CASPT2)	4.50	6700
	This work (MRCI)	4.51	6109
	This work (CASSCF)	4.60	4652
	Duplaa *et al.* [48]	4.60	6928
	Saxon [29]	4.67	5484
	Spiegelmann *et al.* [31]	4.61	5694
	Yates *et al.* [32]	4.68	4436
	Mizukami et al. [33]	4.66	4032
	Castex 81 et al. [30]	≈ 4.70	5807
$^1\Sigma_u^+$	This work (HPP)	4.52	7089
	This work (MRCI)	4.50	6909
	This work (CASSCF)	4.60	5700
	Duplaa *et al.* [48]	4.597	7017
	Spiegelmann *et al.* [31]	4.592	6234
	Yates *et al.* [32]	4.68	4807
	Mizukami et al. [33]	4.65	4516
	Castex 81 et al. [30]	≈ 4.60	6372

without spin-orbit couplings. The minimum distance R_e is lower than all the previous calculations which was in the range of $4.59 - 4.70$ a_0. and we have greater dissociation energies. This table illustrates the sensitivity to the details of the calculations.

For HPP, this can be associated firstly to the tightly bound ionic dimer used in our calculation. The depth (D_e) and length (R_e) of the Σ_u^+ states depend highly on the Ar_2^+ PECs used as input in the HPP model. We used more attractive ionic potentials which reproduced better experimental results in comparison to previous *ab initio* calculations. These results are discussed in section 2.3. In particular, for the cation $^2\Sigma_u^+$ state, we took $R_e^+ = 4.52$ a_0, $D_e^+ = 11117$ cm^{-1} in this work (using CCSD(T)-pV5Z) while in original HPP model they had $R_e^+ = 4.59$ au, $D_e^+ = 11225$ cm^{-1} using DFT. Duplaa and Spiegelmann argued that their *ab initio* calculations for Ar_2^+ underestimated the ion binding energy. The most recent results obtained by Mastalez *et al.* suggests that the actual ionic PECs is somewhat closer to the one used by Duplaa, namely $R_e = 4.57$ au and $D_e = 11212$ cm^{-1}.

The Ar_2^* lowest energy triplet state equilibrium distance by Duplaa and Spiegelmann is $R_e = 4.60$ au which is slightly larger than the parent ionic $R_e^+ = 4.59$ au. In contrast, the equilibrium distance for the triplet state in our calculations is $R_e = 4.51$ au, which is very so slightly smaller than the parent ionic state $^2\Sigma_u^+$ $R_e^+ = 4.52$ au. This is consistent with the observations done by using similar MRCI calculations for the excited and cation argon dimer where we find $R_e = 4.51$ au for the excited dimer and $R_e^+ = 4.54$ au for the ionic dimer. However, this point needs further exploration which is out of scope of this thesis at this point.

The other reason for shorter R_e for $^3\Sigma_u^+$ state in our work can be associated to the selection of parameters defining the Rydberg orbital. Although we use the same number of contractions as done in the original work of Duplaa and Spiegelmann [48], we do use slightly more diffuse orbitals. Due to more diffuse characteristics of the Rydberg orbital, they interfere less in the binding orbitals and henceforth reducing the excimer inter-atomic distance. Duplaa and Spiegelmann give the same argument but to justify the longer excimer distance.

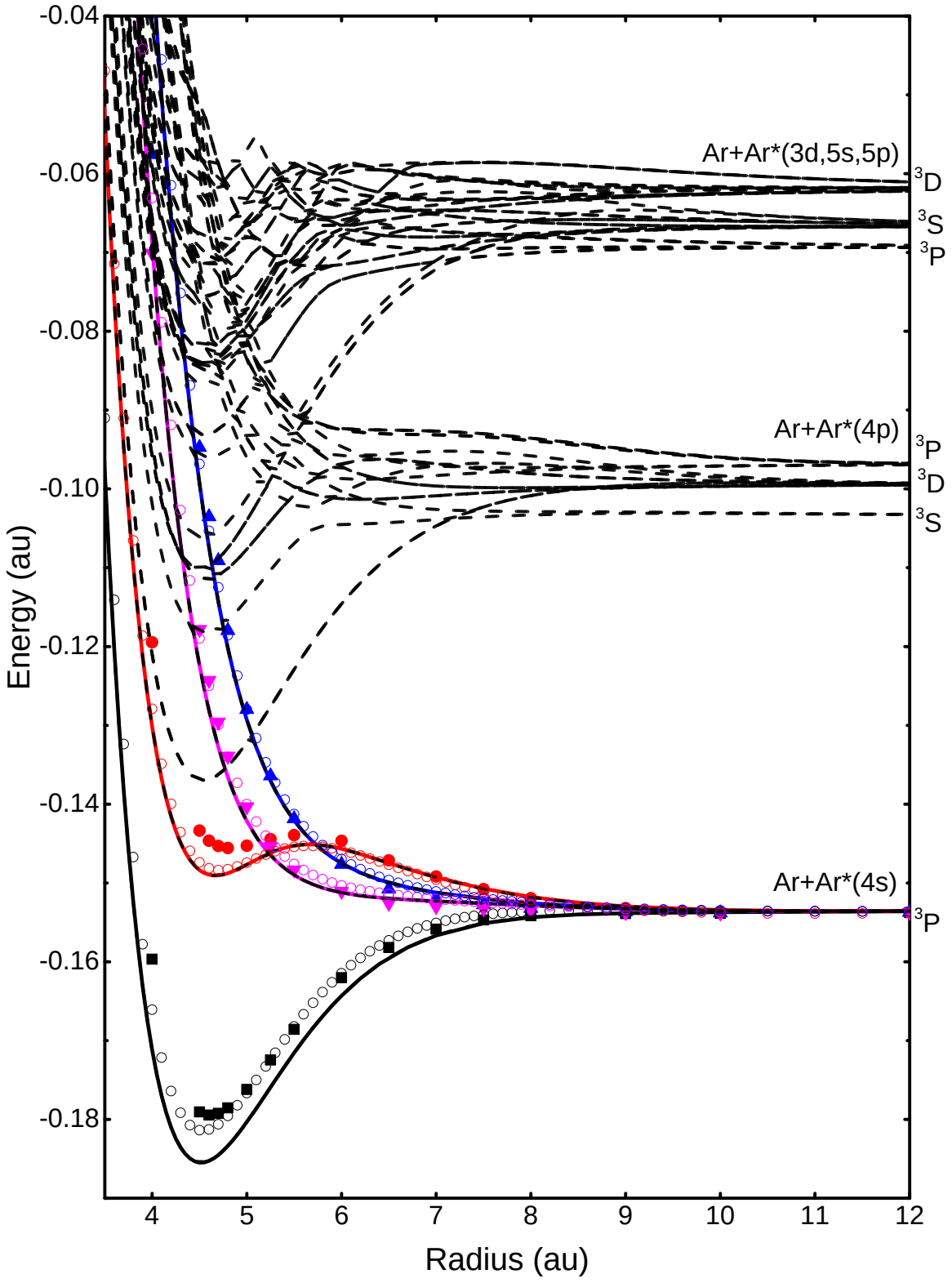

Figure 4.1: PECs for triplets obtained using HPP (Solid lines for the 4 lowest-states and dashed lines for higher-energy states) method compared to CI based calculation [31] (filled symbols) and our MRCI MOLCAS calculations (hollow symbols). Black symbols: $^3\Sigma_u^+$, Red: $^3\Sigma_g^+$, Magenta: $^3\Pi_g$ and Blue: $^3\Pi_u$.

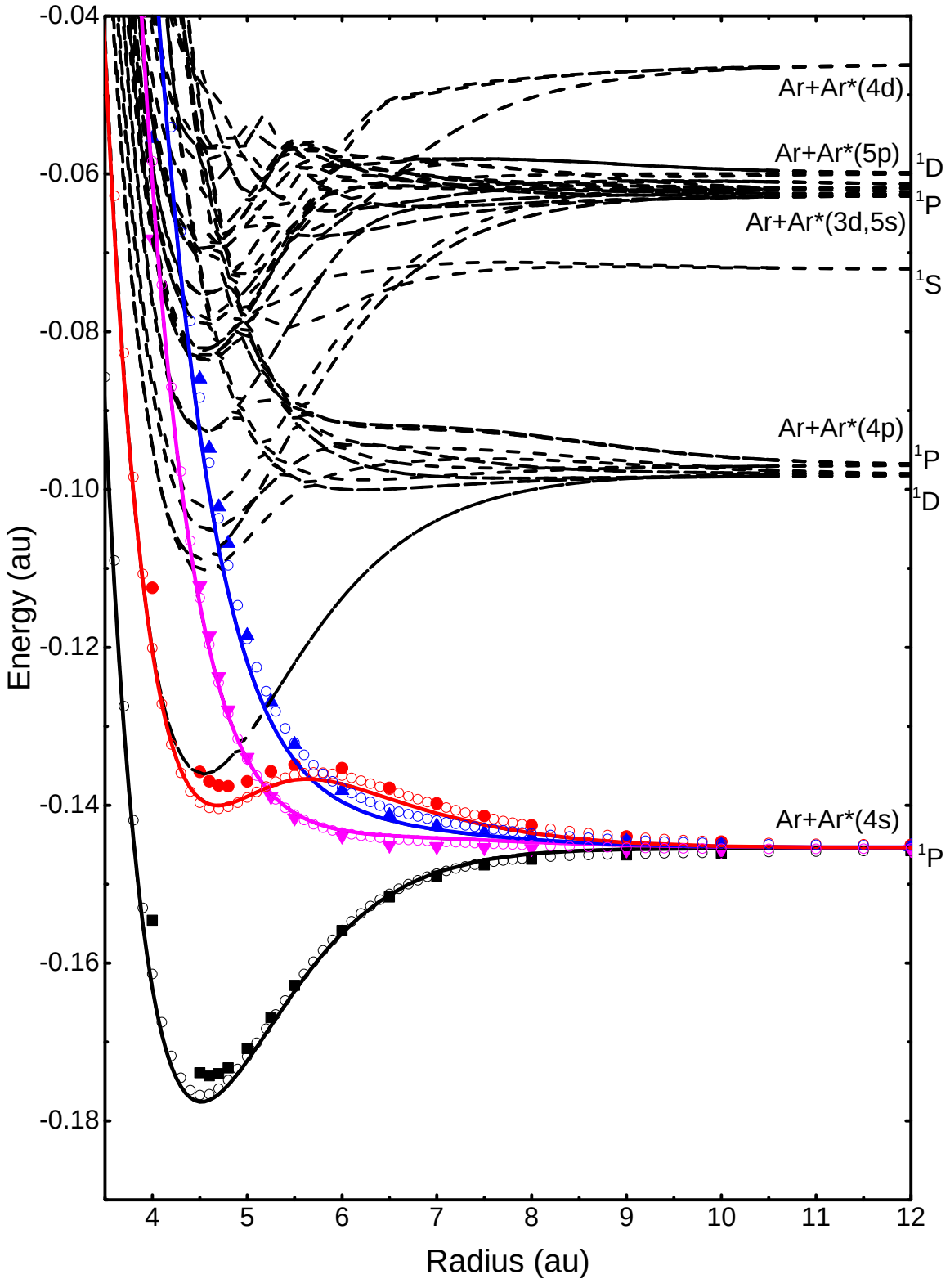

Figure 4.2: PECs for singlets obtained using HPP (Solid lines for the 4-lowest states and dashed lines for higher states) method compared to CI based calculation [31] (filled symbols) and our MRCI MOLCAS calculations (hollow symbols). Black Symbols: $^1\Sigma_u^+$, Red: $^1\Sigma_g^+$, Magenta: $^1\Pi_g$ and Blue: $^1\Pi_u$.

In *ab initio* calculations performed with MOLCAS, given in table 4.1, using MRCI we obtain $R_e = 4.51$ au and $R_e = 4.50$ au using CASPT2 calculations. Our MRCI and CASPT2 calculations are not corrected for BSSE, which would probably elongate the equilibrium distance R_e and reduce dissociation energy D_e. However, some correlation is missing in these calculations which are likely to produce the opposite effect. Also, the MRCI results are not corrected for Davidson's correction which elongates the minimum by 0.005 au and increases the binding energy by 50 cm^{-1}.

The different parametrisation of the cation used for HPP in this thesis compared to original work is carried forward to the dissociation energies, which are also reduced with respect to ion, as they are higher compared to previous results. It is to be noted that the binding energy of HPP (both ours and that of Ref.[48]) is almost 900 cm^{-1} deeper than the results from CI methods and around 300 cm^{-1} than the results from CASPT2 method for triplets. For triplet $D_e = 7019$ cm^{-1} (0.870 eV) and for singlet state we have $D_e = 7089$ cm^{-1} (0.879 eV).

We also note that singlet D_e in both HPP are close to the MRCI PECs (within 200 cm^{-1}) whereas for the triplet this difference is much larger (around 900 cm^{-1}). In other words, the difference between singlet and triplet binding energies in HPP are almost same whereas using an *ab initio* MRCI and CASSCF calculations the singlets have much higher binding energies, see Table 4.1. This indicated that the singlet PECs obtained using HPP are better than the triplets obtained using same calculations, and this is one of the shortcoming of HPP model. Therefore, unfortunately, HPP does not discriminate so much between singlet and triplet. This can be understood by looking at the way we treat the coupling term (fine structure) which is responsible for multiplet splitting. The multiplet splitting is calculated by projecting atomic orbitals to get the molecular Rydberg orbital. The singlet-triplet difference is similar to the one for single atom, i.e., it does not change with the interatomic distance, except by the 4*s* orbital.

Table 4.2: Comparison for $^3\Sigma_g^+$ and $^1\Sigma_g^+$ states with different types of calculations. R_e and R_m correspond to the equilibrium and saddle point distance, with energies V_e and V_m defined with respect to the appropriate dissociation limit. $\Delta = V_m - V_e$ is the barrier height.

		R_e (au)	R_m (au)	V_e (cm^{-1})	V_m (cm^{-1})	Δ (cm^{-1})
$^3\Sigma_g^+$	This work (HPP)	4.67	5.65	974	1840	867
	This work (CASSCF)	4.80	5.75	1554	2238	684
	This work (MRCI)	4.55	5.68	1240	2138	898
	This work (CASPT2)	4.61	5.65	972	1835	863
	Duplaa *et al.* [48]	4.71	5.60	1013	1747	734
	Saxon [29]	4.76	5.87	853	1913	1060
	Spiegelmann *et al.* [31]	4.84	5.57	1750	2108	359
	Yates *et al.* [32]	4.68	5.71	1613	2097	484
$^1\Sigma_g^+$	This work (HPP)	4.69	5.63	1145	1884	739
	This work (CASSCF)	4.74	5.78	2052	3495	1440
	This work (MRCI)	4.50	5.72	467	2380	767
	Duplaa *et al.* [48]	4.71	5.60	1027	1760	733
	Spiegelmann *et al.* [31]	4.78	5.67	1681	2281	600
	Yates *et al.* [32]	4.83	5.73	1710	2290	580

Picking up on the previous discussion about the avoided crossing states, the lowest gerade $^{3,1}\Sigma_g^+$ states have been particularly tricky and sensitive to calculate as these are repulsive states with a barrier to dissociation. This barrier height (the energy difference between minimum point and maximum point on hump before dissociation) associated to different calculations is summarised in table 4.2. The equilibrium distance has been shown to be usually larger than the one in ungerade symmetry in most of the previous calculations.

In our case, for triplet ${}^3\Sigma_g^+$ is $R_e = 4.67$ au and singlet ${}^1\Sigma_g^+$ is $R_e = 4.69$ au. These distances are larger than that of R_e of ${}^{3,1}\Sigma_u^+$ states. The barrier height for the triplet is 866.7 cm^{-1} (0.107 eV) and for the singlet is 738.8cm^{-1} (0.091 eV). These are intermediate values compared to previous work but higher than Duplaa and Spiegelmann's HPP results. Also, in our calculations the barrier height for the triplet is more than 100 cm^{-1} higher than the singlet, which is greater than previous HPP result. Regarding the height, the results from HPP are in agreement with MRCI and CASPT2 *ab initio* results from MOLCAS.

Regarding the hump in ${}^{1,3}\Sigma_g^+$ PECs, Cohen and Schneider [27] assigned it to an avoided crossing between the diabatic PECs formed from $3s$ and $3p$ excited electrons in the case of Neon. The same argument was presented by Duplaa and Spiegelmann [48, 31]. However, based on our observations, this avoided crossing is not just the consequence of diabatic coupling between the $4s-4p$ states but from couplings among much more states as well as discussed in section 3.3. We confirmed this by observing the hump even after systematic removal of np states using our HPP model. As discussed in section 3.3, the barrier is also the result of two excited configurations associated with two different core configurations, namely repulsive ${}^2\Sigma_g^+$ and attractive ${}^2\Sigma_u^+$, combined respectively with σ_g and σ_u orbitals which can come from σ_u of $4s$ or $4p$.

The rest of the states are observed to follow similar trend as reported by Duplaa and Spiegelmann [48]. In particular, the strongly bound ${}^{1,3}\Pi_g$ states are diabatically correlated with the $4p$ separated atom limits ${}^{1,3}D$. In the $4p$ dissociation limit, the S, P, and D limits are ordered as expected for the Ar atom. The splitting between the triplet states is evaluated correctly, as it comes from the coulomb interactions which leads to relative splitting values of 1 and $3/2$ for the ${}^3D-{}^3P$ and ${}^3S-{}^3D$ splittings, respectively. This ratio comes from the symmetry, which is necessarily fulfilled by the HPP model. The amplitude of the splitting is determined by the $4p-3p$ Coulomb direct integral and our scaling factor is consistent with the $4s$ singlet-triplet splitting due to exchange $4s-3p$ integrals. However, we observe that the ${}^1S-{}^1P$ splitting is too large and the ${}^1D-{}^1P$ splitting too small. These splittings depends on the $4p-3p$ integrals, which seems not very well evaluated in our approach. It is likely that the lack of orthogonality between the $3p$ hole orbitals and the $4p$ Rydberg orbitals is responsible for this result. In the original work [34], the amplitude of these integrals was adjusted separately for the $4s$ and $4p$ shells, producing a better result. In further work, an improved pseudo-potential for Ar^+ might be used so that the Rydberg orbitals will be orthogonal to the $3p$ orbitals, which would correct for such a deficiency of the present HPP parameterization.

However, it is not very important in the minimisation process we perform on triplet states. Therefore, it is safe to say that the excimer potentials obtained using the hole particle pseudopotential (HPP) method are reasonable and it is possible to obtain reliable higher excited states which are not easily accessible with *ab initio* methods or other reasonably cheap semi-empirical methods.

4.2 Trimer potential-energy surfaces

The work on the excited argon trimer to get the lowest energy isomer and possible PES was done using N-DIM limited to 4s configurations [74, 92, 112]. In section 2.4 we have seen the possible isomers previously predicted and the lowest energy isomer was reported to be symmetric, of $D_{\infty h}$ symmetry, with the excitation delocalized over all three argon atoms, but concentrated on the central atom. However, based on our CASPT2 calculations, we found that the isomer in $D_{\infty h}$ is not the lowest energy isomer as discussed in section 2.5.

With the aim to use an approximate HPP method, which can be scaled up for trimer calculations easily, we present further investigation. With our own parametrized HPP model given in section 3.1, we found that,

indeed, the symmetry of the trimer is lowered to $C_{\infty h}$. The PES for trimer in collinear geometry is shown in Figure 4.3. The surface plot associated to the rotation of one argon atom around the excimer is shown in Figure 4.4. Both plots show that the lowest energy isomer is indeed the linear asymmetric in $C_{\infty h}$ symmetry group. The dissociation energy of the trimer toward $Ar_2^* + Ar$ is of the order of 290 cm^{-1}, only 45% larger than the ground state dissociation energy of the electronic ground state trimer toward $Ar_2 + Ar$, which is approximately 200 cm^{-1}. The CASPT2 dissociation energy of the trimer is around 340 cm^{-1} which is quite comparable to the HPP result. However, both of these values are much less than the DIM value of about 1300 cm^{-1} obtained from our own DIM parametrization with the potential energy curve of Ar_2^* obtained with the HPP model and also less than the value of 900 cm^{-1} reported in reference [74, 112]. The difference with the two DIM parameterization is consistent with the fact the HPP model produces a deeper potential energy curve for the $1^3\Sigma_u^+$ than the CI results [31] used for DIM parameterization in reference [74, 112].

As illustrated in Figure 4.3, the saddle point in $D_{\infty h}$ symmetry is about 510 cm^{-1} above the minimum obtained for $R_1 = 4.52$ a_0 and $R_2 = 6.04$ a_0 atomic units and its symmetric geometry by exchange of R_1 and R_2. Similar results are obtained using CASPT2 with symmetric geometry with an energy of 720 cm^{-1} higher than the minimum obtained for $R_1 = 4.50$ and $R_2 = 5.90$ au. Both are higher than the dissociation limit (220 cm^{-1} in HPP and 380 cm^{-1} in CASPT2) and we do not expect any significant tunnelling communication between the two symmetric minima. The vibrational motion is thus unlikely to restore the $D_{\infty h}$ symmetry, even for highly excited vibrational states.

The following discussion is based on the calculations using HPP unless mentioned otherwise. The symmetry breaking from $D_{\infty h}$ to $C_{\infty h}$ is associated to the appearance of a significant electric dipole d of the order of 0.3 au, which reveals a charge transfer toward the outer atom most tightly bound to the middle atom. This effect reflects clearly the difference with the DIM model as parameterized here, which neglects any charge transfer configuration and, thus, does not allow the existence of such a dipole. In the HPP model, the hole charge distribution is located mostly on the excimer with a comparable sharing of the charge on both centers. However, the distribution of the hole at the $D_{\infty h}$ saddle point geometry is similar in the HPP and DIM models, with a marked localisation of the hole on the central atom, although there is no observed minima for this geometry.

There are no other energy minima for Ar_3 in its lowest excited state. There is however another smooth saddle structure with T-shape geometry in C_{2v} symmetry observed with the HPP model. The geometry is similar to the one obtained from N-DIM method [92, 112] however it is a local minimum in N-DIM. This geometry is associated with an excitation distributed over the excimer and a ground state atom captured in its long-range minimum. As the excited dimer is neutral and there is no charge transfer to be taken into account, the DIM method performs rather well in predicting T-shape geometry. I.e., the N-DIM can predict the geometries when no charge transfer takes place.

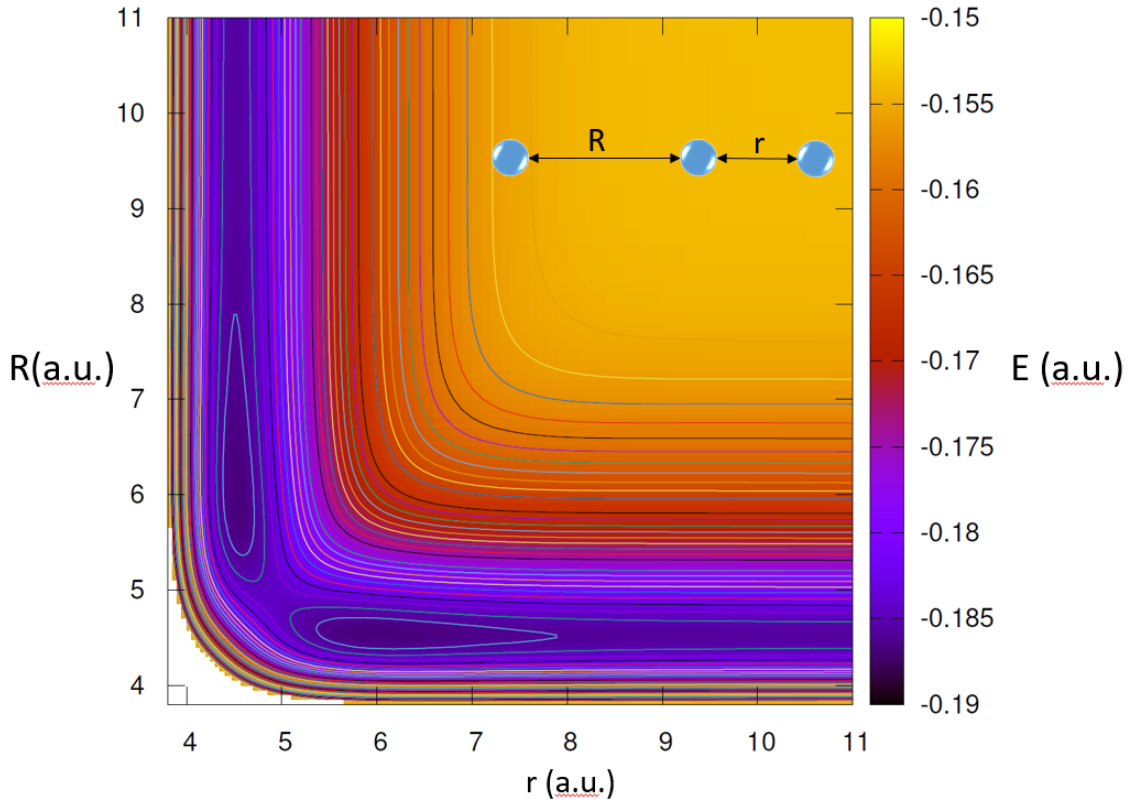

Figure 4.3: Potential Energy Surface of Ar_3^* in $C_{\infty v}$ symmetry group. r and R are interatomic distances illustrated in the figure.

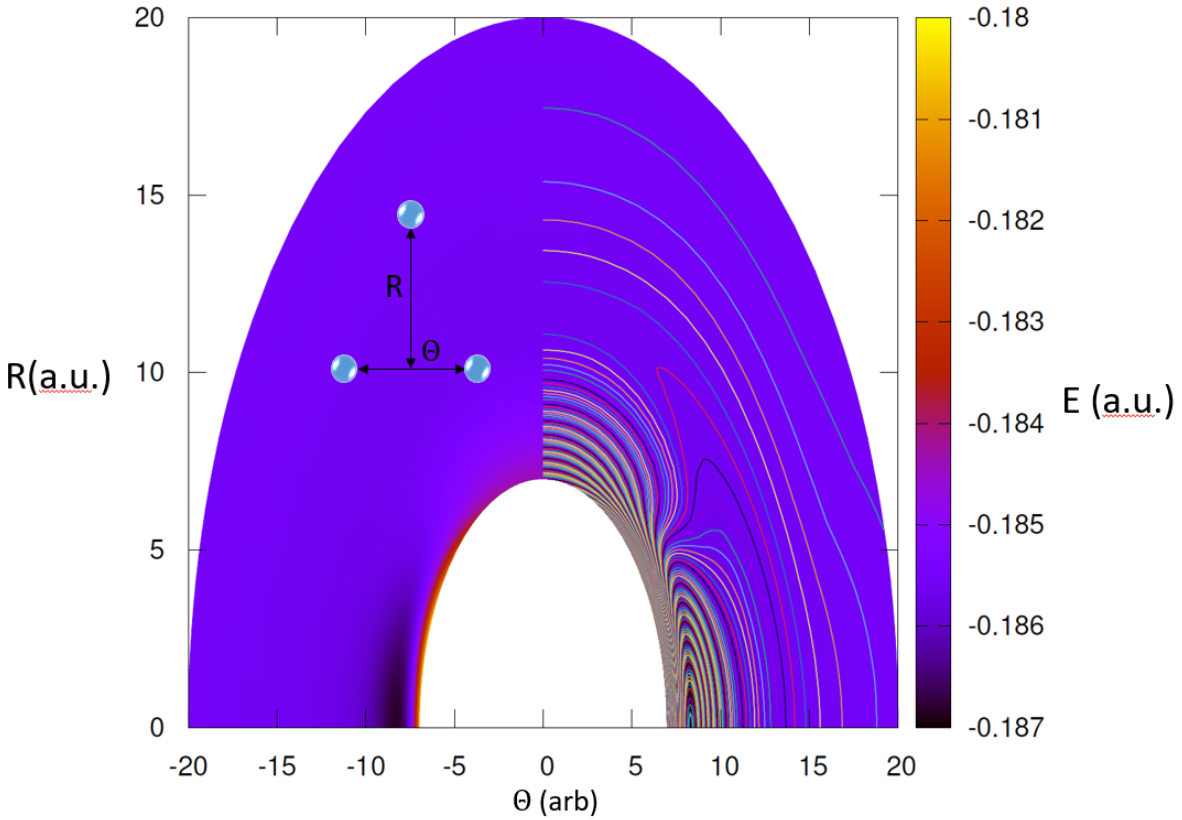

Figure 4.4: Potential Energy Surface for the fixed Ar_2^* $r = 4.67$ au, one Argon atom is rotated (from $0° - 90°$) at a distance R about this dimer to explore the surface connecting $C_{\infty h}$ and $D_{\infty h}$ symmetry groups.

4.3 Geometries of Ar_N^* Clusters with HPP

The effect on the geometry in solids is less significant than that observed in a cluster. This is because, the ground state geometries in bulk are expected to be in Face Centred Cubic (FCC) structure for rare-gas and the creation of an excited state or the removal of atoms produces a local change in geometry but does not bring global changes. In clusters, the ground state atoms are loosely bound with dominant Icosahedron structures. These geometries have been obtained using Lennard- Jones (LJ) [113, 114, 115] or Aziz [100] potentials. With introduction of excitation in such system, there is a possible rearrangement of the atoms bringing global change in geometry.

A few geometries of excited argon cluster in their lowest electronic excited state have been given by Naumkin [74] using 4s limited N-DIM parametrized using CI-based calculations [31]. As previously noted, in the study of Naumkin [74] study, the trimer plays a central role. We observe the same in the lowest-energy isomers of excited Argon clusters obtained using HPP model as well.

The geometries provided by Naumkin and Wales are characterised by an excited $D_{\infty h}$ trimer connected to a neutral cluster, with one of the three atoms of the excited trimer being one of the surface atom of the cluster. Therefore, a dimer is observed to be protruding from the (N-2) cluster. As an example, we show the minimum geometry isomer predicted with DIM by Naumkin and Wales in Figure 4.5 (a) for N=9. The central atom is equidistant from the cluster and the outer Argon atom, respecting the lowest energy trimer $D_{\infty h}$ geometry. Now using the HPP method, the observation that the trimer to be attached to the cluster, is true. However, since the lowest energy trimer is no longer symmetric, the outermost atom is close to the central atom, forming the Ar_2^* excimer and the distance to the remaining argon atom is larger, which reminds the geometry of the free Ar_3^*. In other words, we say that the excited dimer (Ar_2^*), is attached to the neutral (N-2) cluster. This can be seen in Figure 4.5 (b) for the same (N=9) isomer, where, for the protruding dimer, the central atom is now closer to the outermost atom than to the neutral cluster. This observation is consistent for all lowest-energy isomers predicted from the N-DIM and HPP models (N = 9, 10 and 11).

Before we discuss further, it is useful to give some general remarks about the minimisation process and related observations. The minimisation using conjugate gradient method, where numerical energy gradients are obtained by finite differences, given in appendix C.3 for the HPP model is slow. It is therefore desirable to start from a guess geometry close to minimum. This is done using an approximate method as discussed in appendix C, where we take the trimer potential and try to accommodate the ground state atoms in that potential. Obviously this is not an ideal minimisation process, however it provides us a guess geometry for HPP model to start from. We have used some of the small size geometries obtained by Naumkin and Wales [74], however, for larger clusters, as they obtained these with the trimer potential, associated to their $D_{\infty h}$ Ar_3^* potential, they are not very useful. With our $C_{\infty h}$ Ar_2^*-Ar trimer potential being dominated, by the excitation localised on the dimer, we expect different geometries. The computationally expensive HPP minimisation is thus replaced by a fast approximate method. This speeds up the minimisation process by providing a better starting geometry.

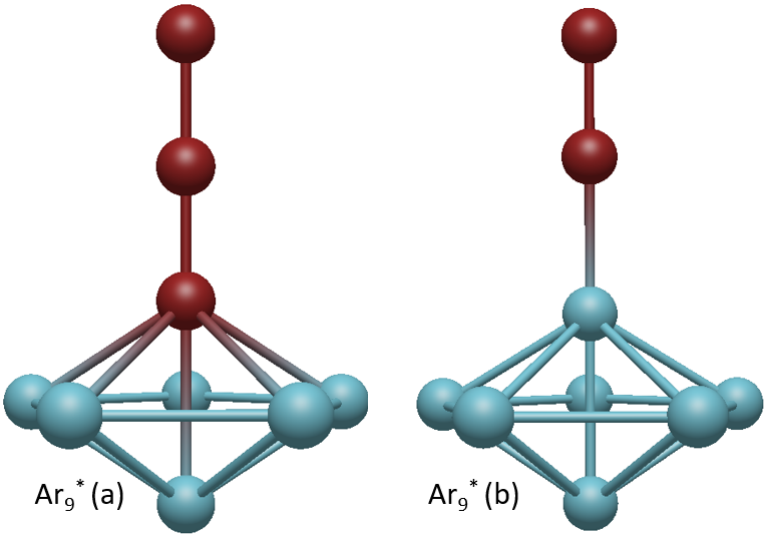

Figure 4.5: The difference between the trimer geometry for the excited argon cluster with N=9. Figure (a) shows the isomer the middle atom to be at equidistant from the cluster and the single atom on top obtained by Naumkin and Wales using N-DIM [74] and (b) shows that central atom is closer to the single atom outside than to the cluster using HPP model calculation (This work).

Using approximate methods we observed that the minimum energy structures obtained were not significantly different from those predicted with HPP, i.e. the structure obtained from the approximate method was almost lying in the lowest-energy potential well and with gradient descent method of minimum search lead us directly to the relevant isomer. However, it is also to be kept in mind that $^3\Sigma_u^+$ potential energy surface of excited argon clusters is very flat. With slight rotation of some big cluster, the difference in energy of the lowest-energy isomer and the next isomer is seen to be as small as 10 cm^{-1}. This makes it rather difficult to ascertain the true minimum for the bigger isomers, as it is obviously not possible to explore the full potential-energy surface.

Table 4.3: Characteristics of Ar_N clusters in their lowest excited triplet state. IP is the ionisation potential of the lowest triplet state at its equilibrium geometry. The comment indicates whether the geometry is similar to the geometry obtained by relaxation with the N-DIM model.

Isomer	Symmetry	IP(eV)	Dipole (au)	Energy (au)	D_e^* (cm^{-1})	D_e (cm^{-1})	comment
2	$D_{\infty h}$	3.67	0.00	-0.18549	0	50	
3	C_{∞}	3.59	0.33	-0.18683	147	99	
4a	$D_{\infty h}$	3.54	0.00	-0.18832	207	149	
4b	C_s	3.59	0.39	-0.18774	164	149	same as N-DIM
5	C_{3v}	3.53	0.74	-0.18904	195	180	
6	C_{3v}	3.53	0.75	-0.19052	221	202	
7a	C_{2v}	3.56	0.64	-0.19183	232	231	
7a′	C_s	3.55	0.40	-0.19182	232	231	same as N-DIM
8	C_{2v}	3.48	0.89	-0.19356	253	243	
9	C_{5v}	3.56	0.36	-0.19532	270	262	same as N-DIM
10	C_s	3.54	0.45	-0.19690	278	277	same as N-DIM
11	C_{2v}	3.54	0.51	-0.19903	297	290	same as N-DIM
12	C_{3v}	3.53	0.54	-0.20107	311	307	
13	C_{2v}	3.49	0.74	-0.20278	316	330	

The HPP results for the lowest-energy isomers for each system size up to (N = 13) are summarised in table 4.3. Besides the lowest energy isomers, in the table we also give the two extra isomers for N = 4, to compare with previous lowest energy isomers [74], and for N = 7, to show how close in energy two

isomers can be. Here we give the symmetry, the electric dipole (d) and the ionisation potential (IP) at the equilibrium geometry of the excited state for the lowest triplet state. We also give the dissociation energy per atom bound to the tightly bound excimer Ar pair and defined as $D_e^* = \frac{E_N^* - E_2^*}{N-1}$. For comparison, we give the binding energy per atom for ground state geometry and defined as $D_e = \frac{(E_N - E_1)}{N}$.

The general trend in all the geometries associated to lowest energy isomer is similar to what was observed by Naumkin [74] using N-DIM. Similarly we note a protruding excimer (excited dimer), which in our case is not necessarily a part of the excited trimer, attached to the ground state cluster, which can be seen in figures 4.7 and 4.8 with an exception for N = 4. The structures obtained using HPP exhibit relatively high symmetry, which is in contrast to the lowest energy geometries obtained using the DIM model. The difference exists mainly in tilting the excimer with respect to the symmetry axis of the cluster. Nevertheless, the symmetry of some of the geometries agrees using both models, like for Ar_9 (C_{5v}), Ar_{10} (C_s) and Ar_{11} (C_{2v}).

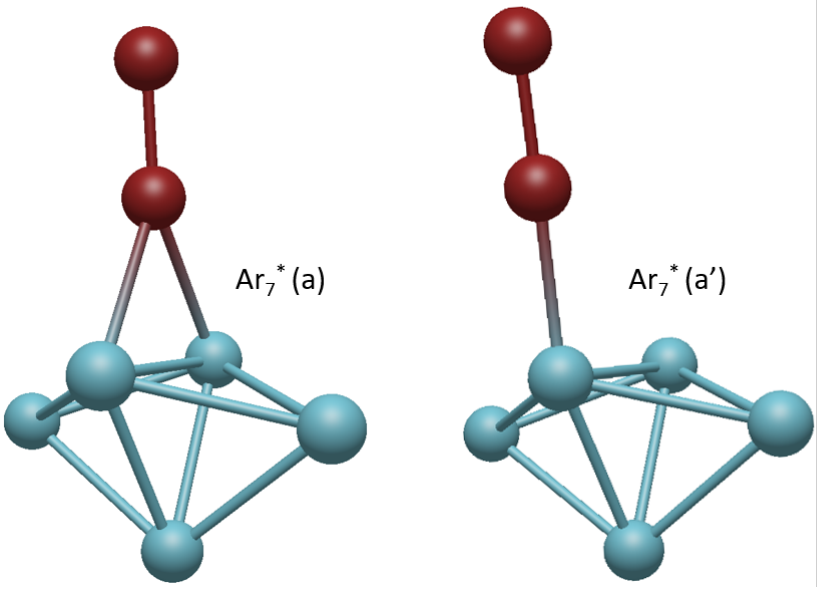

Figure 4.6: Two lowest energy isomers with energy difference of 2 cm^{-1}.

For the triplet state geometries, the clusters are characterised by a significant electric dipole directed toward the most protruding atom, which varies with cluster size. A general trend, the dipole is larger when the protruding dimer is closer to the rest of the cluster. The existence of such a a dipole suggests that electronic surface states are energetically more favourable than bulk states and the diffuse Rydberg orbital is thus pushed out of the cluster by the Pauli repulsion. Like for Ar_3^*, the N-DIM model in its present parameterization and approximation cannot reproduce such an effect. Regarding the hole, it is mainly located on the most tightly bound dimer, with a comparable sharing among the corresponding two atoms.

The sensitivity of the charge distribution to the geometry is well illustrated by considering the Ar_7 cluster. In this case, the HPP and DIM relaxation produces only slightly different isomers, as it can be observed in Figure 4.6. The DIM-relaxed isomer is associated to a small shift of the excimer with respect to the rest of the cluster, which lowers the symmetry from C_{2v} to C_s. This small modification of the geometry is sufficient to reduce the dipole by 50 %, though the difference in energy between these two geometries is as small as 2 cm^{-1}. This small energy difference illustrates also quite well the flatness of the PES.

For the small clusters studied here, the binding energy is strongly dominated by the most tightly bound

Ar pair, with a binding energy of the order of 7000 cm^{-1}. The binding energy per atom without considering the most tightly bound dimer, D_e^*, grows from 150 to 320 cm^{-1}. This variation is quite comparable to the binding energy per atom at the electronic ground state geometry, $D_e \approx 100$ cm^{-1}. This shows that the excited dimer is only slightly more bound to the cluster than a single Ar atom. This small difference is the main reason for the weak modifications brought to electronic ground state geometry of the $N-2$ remaining atoms by the presence of the dimer. The difference is marked for the Ar_3 and Ar_{4a} isomers and then decreases as the size of the cluster increases.

The exception to the observed trend of excimer being attached to neutral atoms is for Ar_4^*. With HPP, the lowest energy isomer for N = 4 is the one where excimer is sandwiched between two ground state atoms. This forms a linear $D_{\infty h}$ geometry where it is advantageous to break the ground state bond to benefits from excimer attraction from both sides. Therefore, this isomer gives a sneak peak to the possibility of having an excited state being captured in a neutral cluster for very large isomers. This isomer is not accessible with DIM possibly due to missing charge transfer configurations. Although this is an interesting isomer, this type of isomer, in which an excimer is being captured between two or more neutral atoms is not seen in any of the bigger lowest energy isomers we observed.

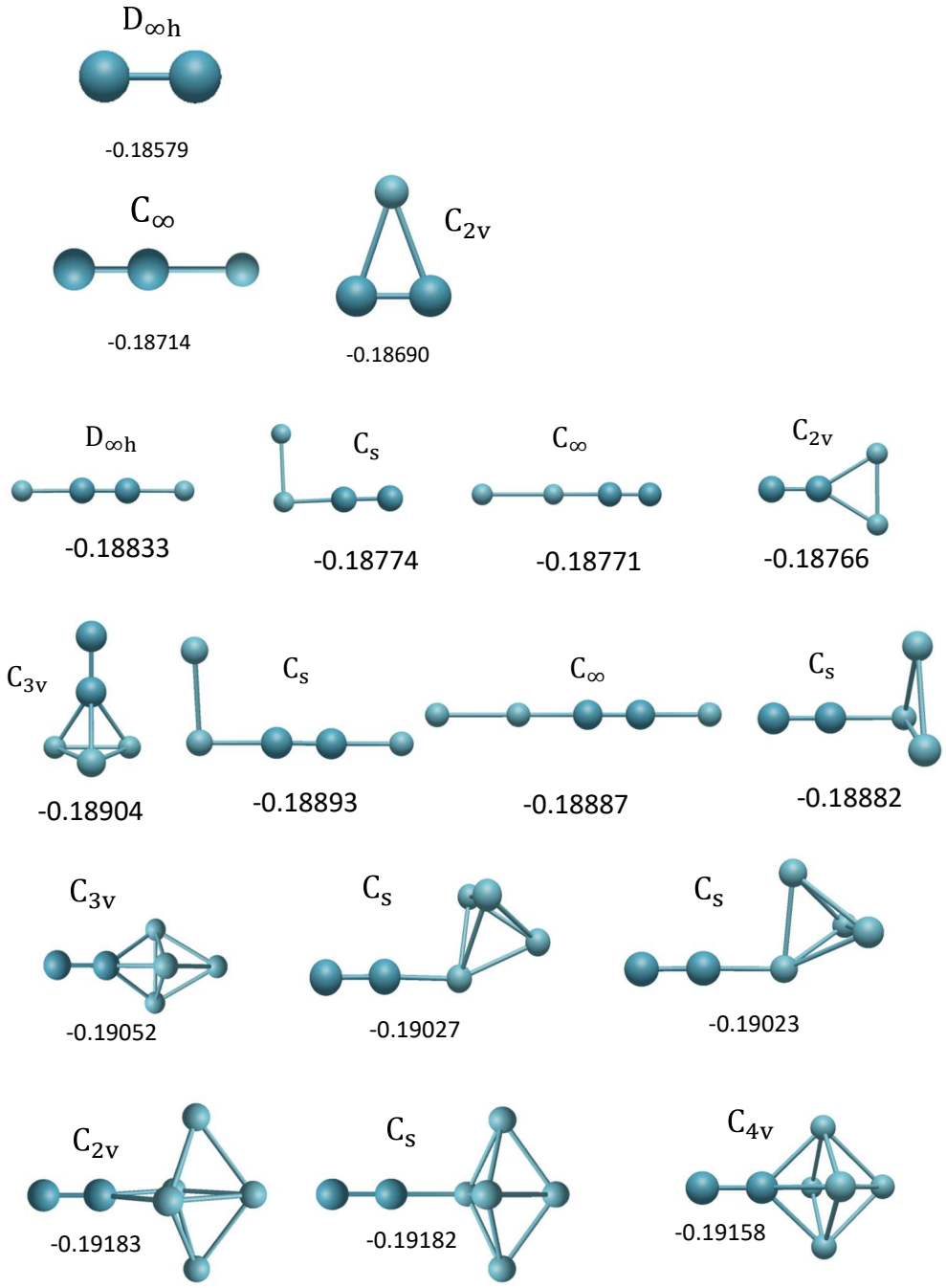

Figure 4.7: All isomers obtained from HPP for Ar_N^* for $2 \leq N \leq 7$.

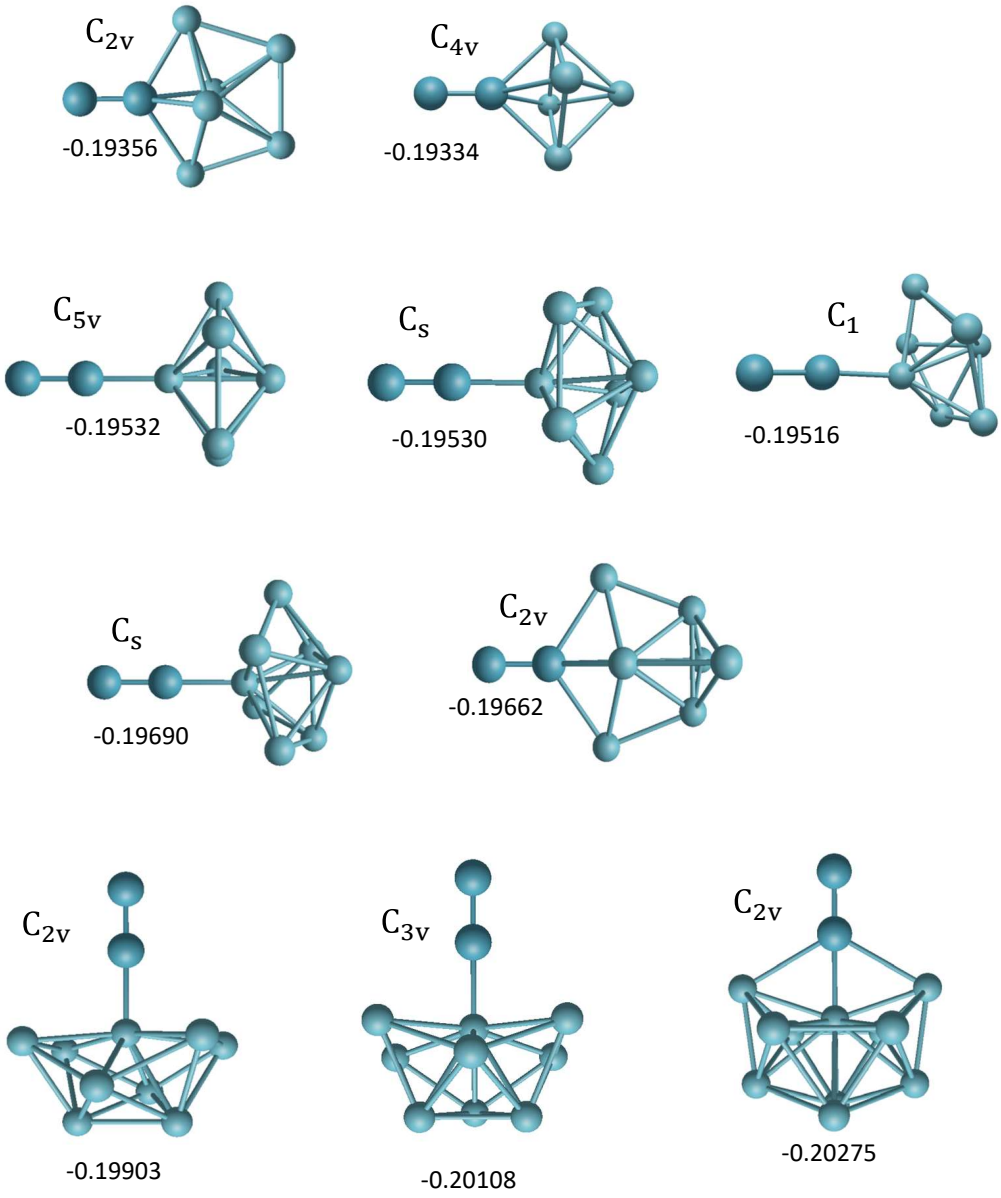

Figure 4.8: All isomers obtained from HPP for Ar_N^* for $8 \leq N \leq 13$.

4.4 Spectroscopy

4.4.1 Absorption Spectrum

The UV absorption spectrum computed with the help of the HPP model provides a link with experimental measurements. We should however content ourselves with general trends because mass selection of neutral clusters is a difficult task and we cannot perform a one-to-one comparison with experimental results for a given size. The UV excitation spectrum associated to luminescence below 11 eV has been recorded experimentally to investigate the size dependence [54, 50]. For small sizes, the spectrum is characterised by surface absorption peaks, which loose relative intensity when the clusters size extent beyond several thousand atoms.

We present in Figure 4.9 a series of absorption spectra obtained at the ground state geometries deduced from the work of Naumkin and Wales [74]. We see clearly the development of the $4s$ band, well separated from higher absorption energies. The $4p$ band does not give any significant absorption as expected because the $3p-4p$ transition does not contribute to dipole transition in the Ar atom. The absorption around 14 eV corresponds to the contribution of higher excited configuration like $3d$ and $5s$, which are included in the HPP model. The intensity of these bands below the ionisation threshold grows with the cluster size. We also notice the appearance of a band around 13 eV, which also gains in intensity with the increasing cluster size. This band corresponds rather well to the second surface exciton band observed experimentally [54, 50]. It is associated to very diffuse orbitals, which extended rather far from the cluster.

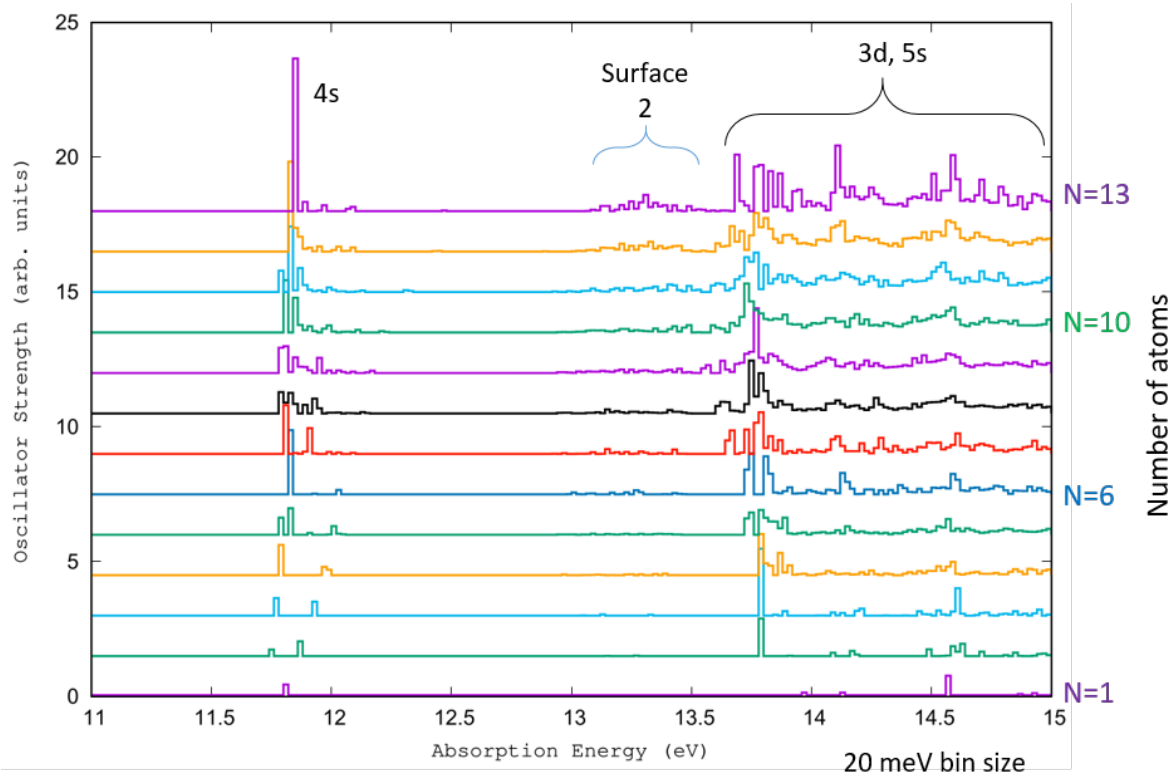

Figure 4.9: Absorption oscillator strength spectrum at the geometry of the ground-state lowest-energy isomer. The bin width is 20 meV. The cluster size increases upward from $N = 1$ to $N = 13$

4.4.2 Emission Spectrum

For the triplet excited state, the weak SO coupling allows dipole transition toward the singlet ground state with a rather long lifetime. At the relaxed geometry of the lowest triplet electronic state, the transition energy from the excited state to the ground state fluctuates around an average value of 9.42 eV, slightly lower than the corresponding value for the dimer of 9.47 eV. The variation with the cluster size or isomer geometry does not exceed ± 0.10 eV. We observe only one sizeable exception for $N = 6$. In this case, the more compact geometry is unfavourable for the electronic ground state, and the transition energy from the lowest triplet reduces to 9.25 eV. The energy difference between the lowest triplet state and the next triplet states is of the order of 1 eV and varies slightly with the cluster size. These trends are rather similar to the DIM results reported by Naumkin and Wales [74], though the geometries are more symmetric for the HPP model.

4.4.3 Ionisation Potential

Regarding the ionisation potential of the lowest triplet state at its equilibrium geometry summarised in table 4.3, we observe also some small fluctuations around the average value of 3.54 eV, slightly below the dimer value of 3.68 eV. It is interesting to put this ionisation potential in perspective with the two-colour experiment of Liétard *et al.* [10], though the clusters investigated in this experiment ($N \approx 500$) are significantly larger. An ionisation potential of 3 eV or more requires at least two IR photons at 1.56 eV to launch electron emission. The fast disappearance of the one-photon electron emission signal in after 1.5 picosecond indicates the rapid relaxation of the excited electronic wavepacket. However, the probe energy is not high enough in this experiment to probe the lowest triplet state with one single probe photon and the two-photon signal seems too weak to be conclusive.

4.5 Results using Di-DIM

Similar to previous DIM calculations by Naumkin and Wales [74], we are interested in the 4 lowest potential energy curves of singlets and triplets given as, $^{3,1}\Sigma^{+}_{u,g}$ and $^{3,1}\Pi_{u,g}$. There are extracted from HPP dimer results. However, as discussed in section 3.2, these PECs are not truly diabatic. It was essential to insert another higher state to mimic the Σ_g couplings to resolve avoided crossing. They are, "higher-energy state", "the 4p limit $4p$ limit shown by red and blue curves in the Figure 4.10 for triplets.

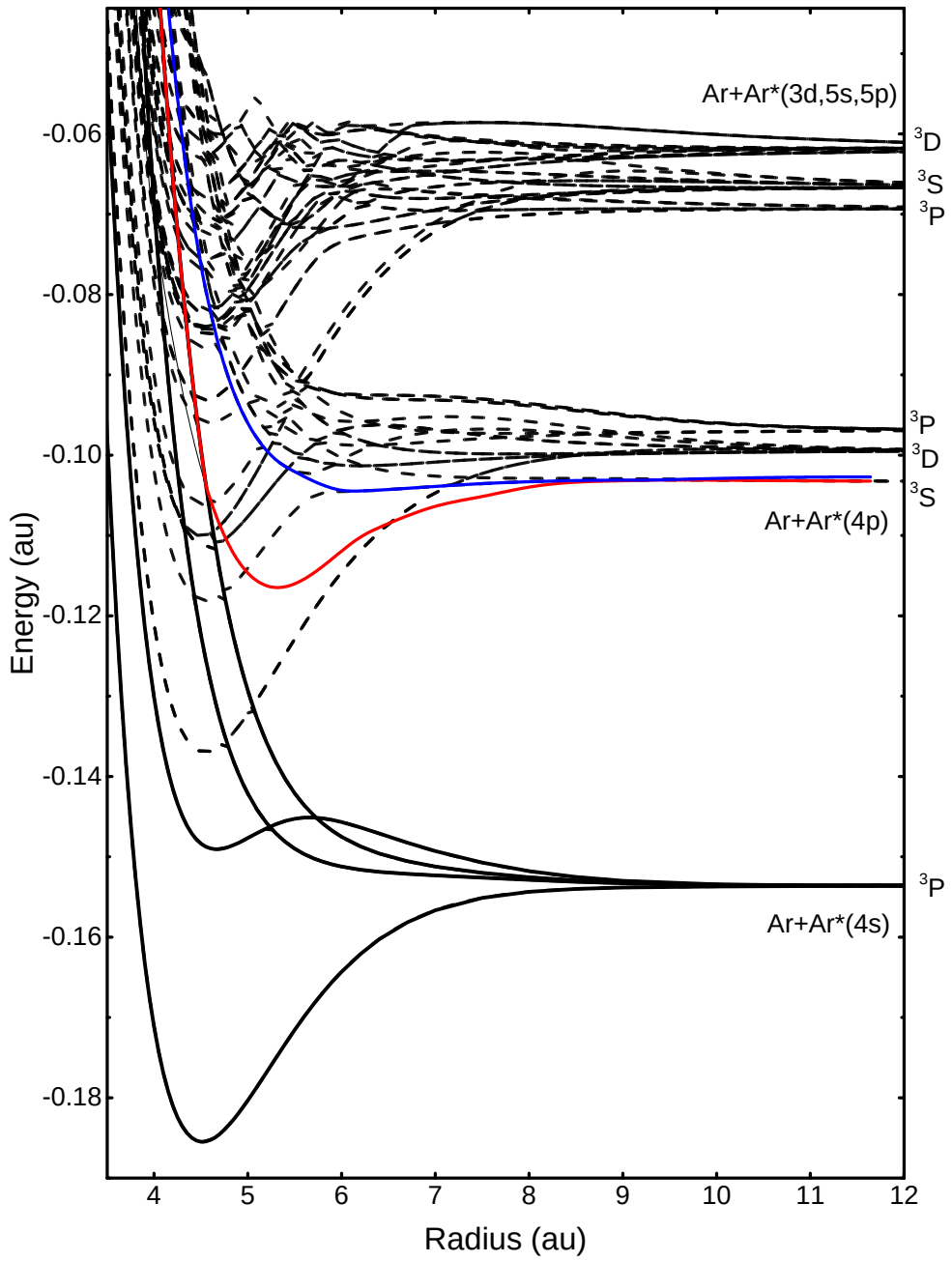

Figure 4.10: The excimer PECs calculated using HPP with blue $(2)^3\Sigma^{+}_{u}$ and red curves $(2)^3\Sigma^{+}_{g}$ showing the *ad hoc* states used to restore the diabatic characteristic of Σ^{+} state.

The lowest-energy PECs are very similar to those obtained within the HPP approach. However, for larger systems this is not the case, as we will discuss it in the following section.

4.5.1 Excited Argon Trimer

The trimer PES with (Di-DIM) and without (H-DIM) diabatization are shown in figures 4.11 and 4.12 respectively for linear geometries. Comparing these two plots shows clearly the effect of diabatization. The HPP dimer PECs are used in both the methods to parametrize using the DIM. It is clear that without diabatization we obtain the minimum in $D_{\infty h}$ symmetry as reported by Naumkin [74] and Goubert [92]. With diabatization we obtain a $C_{\infty v}$ similar to HPP used as reference as discussed in previous section. The Di-DIM proves better transferability by having diabatic PECs.

Though we observe the linear-asymmetric isomer being formed by lowering the symmetry as in HPP, the dissociation energy of the two models is not the same. The dissociation energy of the trimer for $Ar_2^* - Ar$ is 160 cm^{-1} with Di-DIM, and 290 cm^{-1} with HPP. This is also much less than the CASPT2 value of 340 cm^{-1}. However it is not as large as 1300 cm^{-1}, which is obtained using H-DIM without diabatization. Though the trimer results from Di-DIM are in better agreement with the isomers obtained using the HPP model, it is important to point that, the distance between the excimer and the ground state atom from Di-DIM is shorter (5.60 au) as compared to the one from HPP (6.10 au) and CASPT2 (5.90 au).

The *ad hoc* PEC is able to reproduce the effect of higher states in the Di-DIM method. As the nature of this PEC is difficult to establish, since no function is available to generate such a curve, it is the best I could build. This *ad hoc* state is the best which could be achieved is the current scope of work. However, the selection of *ad hoc* state does not significantly change the inter-atomic distance or the dissociation energy. For *ad hoc* states with different dissociation limits, the trimer dissociation energy changes by about 10-20 cm^{-1}, which is not significant, and the corresponding interatomic distance by about 0.002 au. As we explore the C_{2v} symmetry, we see a saddle being formed in HPP which is missing in Di-DIM. The T-shape geometry in C_{2v} symmetry which was a saddle in HPP, is now observed to be a local minima in Di-DIM similar to H-DIM and N-DIM, as shown in Figure 4.13. This is probably due to the effects from the P, D states rotations, which would indeed be different from S state, which are missing in Di-DIM model. These two things point in the direction to include more higher states with their respective coupling to have results in better agreement with HPP calculations.

The excitation is fully located on the excimer with a ground state atom attached at a distance of ≈ 10 au. As mentioned previously, this geometry is pretty well reproduced as compared to HPP as there is no need to take into account the charge transfer which is not properly done in Di-DIM.

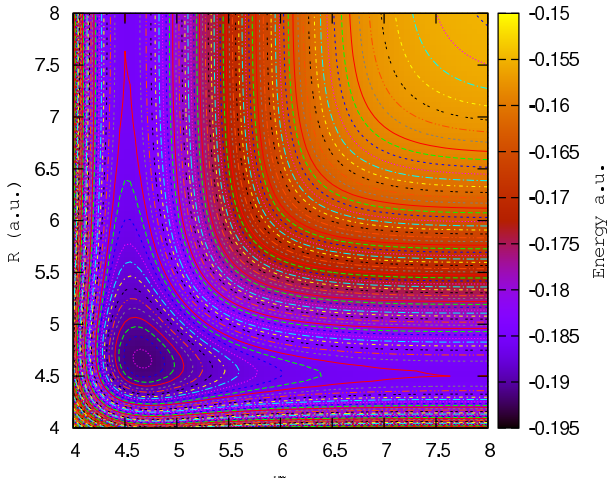

Figure 4.11: Ar_3^* surface plot without diabatization forming the minima for linear-symmetric in C_{2v} symmetry.

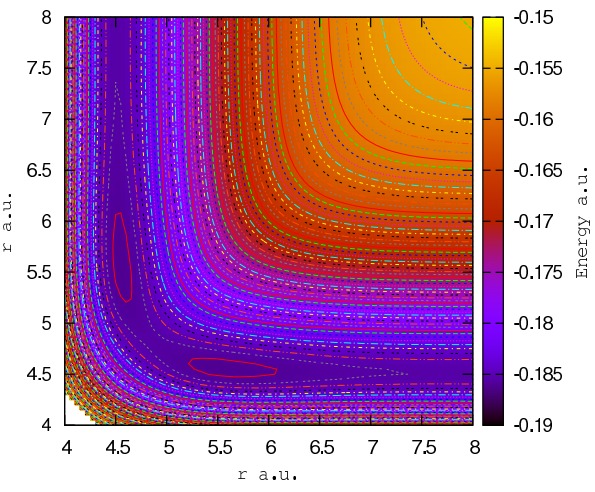

Figure 4.12: Ar_3^* surface plot with diabatization forming the minima for linear asymmetric in $D_{\infty h}$ symmetry.

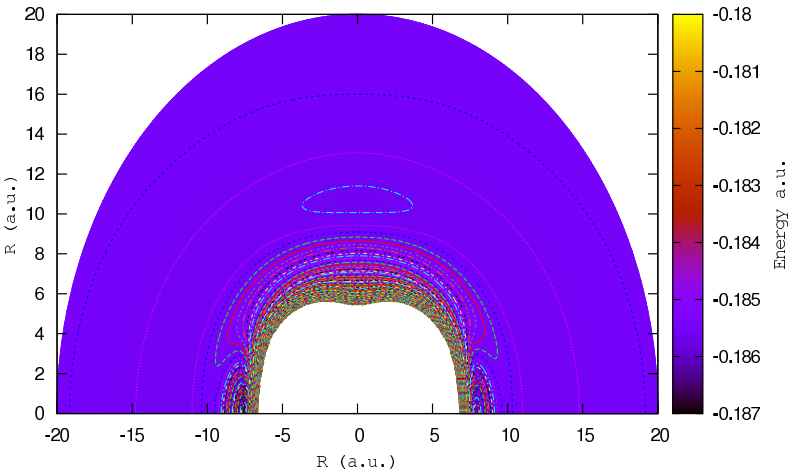

Figure 4.13: Ar_3^* surface plot in C_{2v} symmetry while rotating the ground state atom around excimer using Di-DIM.

4.5.2 More on Geometries of Ar_N^* Clusters

Although the trimer results are not sufficient, they are consistent with the HPP and CASPT2 observations. We now explore the bigger clusters, discuss the effect of diabatization and its importance in the lowest energy isomers.

The lowest energy structures in Di-DIM are obtained using damped molecular dynamics. The lowest energy isomers obtained using Di-DIM are summarised in Figure 4.15. The general trend of an excimer attached to (N-2) the ground state cluster similar to that observed in HPP. This is different from N-DIM or H-DIM, where an excited trimer is attached to ground state cluster. In N-DIM, 80% of excitation (hole) is located on the central atom of the excited trimer while the rest is shared by the remaining two atoms. In Di-DIM, the total excitation (hole) is shared equally among the two outermost atoms, as obtained in HPP calculations. The trimer lowest energy isomer geometry forms the basis on which most of the larger isomers are built, in close correspondence with HPP and N- DIM results. Though with Di-DIM model it is not possible to have dipole similar to HPP. However, with diabatization and using the approximate *ad hoc* PECs it was possible to obtain geometries of lowest energy isomers similar to the one obtained using HPP. The distance of the excimer in most of geometries observed using Di-DIM is shorter compared to that derived from HPP calculations.

As the PECs used to parametrize the Di-DIM are taken from the HPP model, the dimer has the same PECs with the addition of *ad hoc* PEC and the excimer inter-atomic distance $R_e = 4.52$ au is identical to the HPP result.

Similar to HPP for $N = 4$, the excimer is located between two ground state atoms. However, unlike HPP, the two neutral atoms are not equidistant from the excimer which. Interestingly, this isomer is not observed without diabatization in N-DIM or H-DIM. We consider now the same example of $N = 9$ whose lowest-energy isomer geometry is very similar using HPP and N-DIM (H-DIM) methods. In Di-DIM, the lowest energy isomer has an excimer attached at a longer distance than the excimer distance found in HPP calculations systematically with respect to Ar_3^*. This isomer also breaks the rotational symmetry along the excimer: the excimer is tilted in one direction as shown in Figure 4.14. This is similar to symmetry breaking observed in $N = 4$.

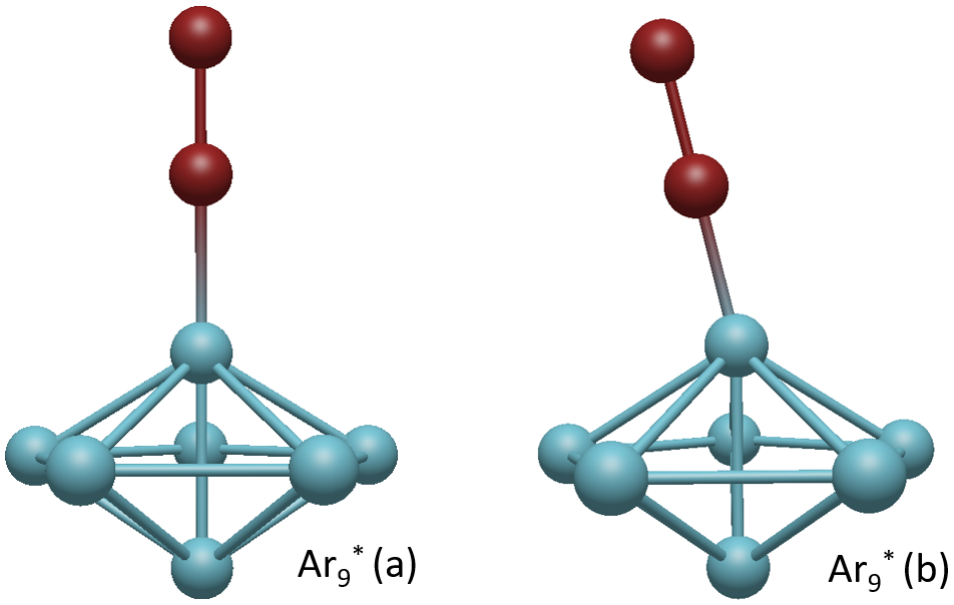

Figure 4.14: This figure shows the difference between the geometry for the excited argon cluster of N=9 for HPP and Di-DIM. Figure (a) shows the isomer obtained using HPP and (b) shows the isomer obtained using Di-DIM which is tilted showing symmetry breaking.

The Di-DIM results are summarised in table 4.4 for cluster sizes up to N = 15, supplemented by the cluster size N = 55 which corresponds to a rare-gas magic number. Besides that we also give an additional magic number cluster with N=55. Similar to discussion in geometries of HPP, we give an additional isomer for $N = 4$ which is similar to lowest energy isomer observed using H-DIM and $N = 7$ to show the smoothness of the PES. We also give the dissociation energies obtained using D-DIM (${}^{A}D_e^*$) compared to HPP dissociation energies (${}^{B}D_e^*$), where $D_e^* = \frac{(E_N^* - E_2^*)}{(N-1)}$. The ground state dissociation energy D_e.

It can be seen that the dissociation energy increases with the cluster size while reaching the continuum limit for larger clusters. The main difference between the dissociation values between the HPP and Di-DIM is the fact that, the excited cluster dissociation values obtained using HPP are systematically higher than the ground state dissociation values. Whereas, for Di-DIM the dissociation values are lower than the ground state dissociation limit (except for $N = 4$, which is closer to HPP). Though they are not lower than single ground state atom dissociation (100 cm^{-1}).

For cluster size around $N = 15$, half of the maximum number of bonds per atom (i.e. 6) which corresponds to the half of the cohesion energy ($\approx$ 300 cm^{-1}) of an argon cluster with 12 bonds per atom ($\approx$ 600 cm^{-1}). With increasing size at $N = 55$ the bulk limit is not reached due more surface states than the bound states. The dissociation energy reaches a limit when the bound states are more than the surface states which happens for large cluster $N \approx 10^4$ atoms.

The Di-DIM geometries of the lowest energy isomers are shown in 4.15 for $2 \leq N \leq 15$. The lowest geometry isomers are a mixture of lowest energy isomers obtained using HPP, DIM by Naumkin and others somewhere is middle of the two. Similar to HPP, all the excitation is localised on the dimer thereby having the geometry in which an excimer is attached to $N-2$ ground state cluster. The exception to this is only for $N = 4$ where the excimer is located in between the two ground state atoms, similar to HPP.

Table 4.4: Characteristics of Ar_N clusters in their lowest excited triplet state. The comment indicates whether the geometry is similar to the geometry obtained by relaxation with the Di-DIM model. ${}^{A}D_e^*$ and ${}^{B}D_e^*$ are the dissociation energies of Di-DIM and HPP respectively.

isomer	Symmetry	Energy (au)	${}^{\mathrm{A}}D_e^*$ (cm^{-1})	${}^{\mathrm{B}}D_e^*$ (cm^{-1})	D_e (cm^{-1})	comment
2	$D_{\infty h}$	-0.18549	0	0	50	-
3	C_∞	-0.18620	79	147	99	Similar to HPP
4	$D_{\infty h}$	-0.18766	159	164	149	Similar to HPP
5	C_∞	-0.18826	153	195	180	Similar to N-DIM
6	C_∞	-0.18997	197	221	202	Similar to N-DIM
7	C_∞	-0.19120	209	232	231	Similar to N-DIM
8	C_∞	-0.19278	229	253	243	
9	C_∞	-0.19430	242	270	262	Similar to both
10	C_∞	-0.19539	242	278	277	Similar to both
11	C_∞	-0.19743	263	297	290	Similar to both
12	C_∞	-0.19946	280	311	307	
13	C_∞	-0.20514	360	316	330	Similar to both
14	C_∞	-0.20428		-	331	Similar to N-DIM
15	C_∞	-0.20685	335	-	337	Similar to N-DIM
55	C_∞	-0.30584	487	-	477	-

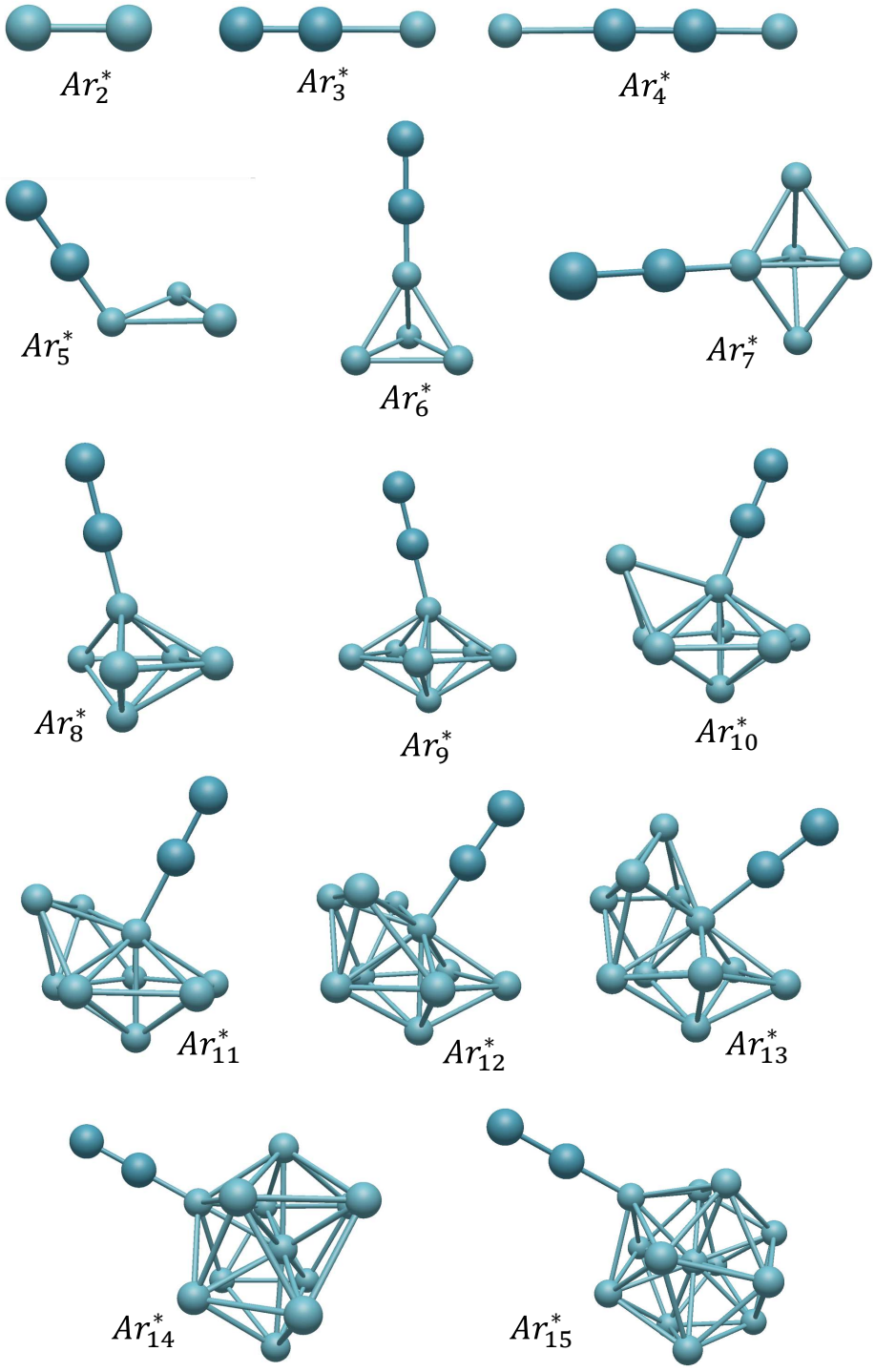

Figure 4.15: All isomers obtained using DIM with diabatization for Ar_N^* for $2 \leq N \leq 15$.

Part II

Dynamics

Chapter 5

Introduction to dynamics of STEs in RGCs: State of the art

As pointed out in the introduction and in part I, it is needed to study the time evolution of the electronic structure as the wave-packet evolves through the manifold of electronic states and of the excitation in rare-gas clusters. In ideal conditions, it is desirable to model nuclear and electronic motions quantum mechanically, while going beyond the adiabatic regime. In part I I of this thesis, we have been looking at the electronic structure and geometry of the lowest excited state of argon clusters using some *ab initio* methods (CASSCF, RASSCF, MRCI, CASPT2) and semi-empirical method like HPP and Di-DIM. On most of these methods it is not computationally possible to perform dynamics without further approximations. We have already solved the electronic motion in the field of fixed nuclei, following BOA. It is thus possible to follow the nuclei motion based on the forces calculated on the electronic states to observe the time evolution of the system. This strategy is usually referred to as *Non-adiabatic Mixed-Quantum Classical* dynamics [116, 117, 118]. This has been discussed in great detail in the review by R.C. Otero and M. Barbatti [119].

However, a real system does not evolve on a single state and it is imperative to have a method in which the system can evolve among electronic states. There are several methods developed over the last decades like; Trajectory Surface Hopping (TSH) [110], mean-field Ehrenfest (MFE) [116, 117, 120], multiple-spawning (MS) [121, 122], mixed-quantum-classical Liouville equation (QCLE) [116, 117], non-adiabatic Bohmian dynamics [123, 124] and coupled-trajectory mixed quantum classical method [125] to study such systems. TD-DFT based methods are obviously desirable, however, as we have discussed in introduction, the functional defining excitation evolution in rare-gas clusters are not readily available. In this work we want to get an *on-the-fly* PES evaluation methods, i.e., where electronic structure is calculated at each time step. Among the above methods, for the propagation of trajectory on the PES, the MFE distinguishes from TSH by the computation of the forces and the treatment of non-adiabatic couplings. In MFE, the non-adiabatic processes are included by following the electronic wave packet and the forces acting on the ions results from the mean field associated to this wave packet. On the contrary, stochastic hopping probability is calculated based on kinetic couplings which is used in TSH, and the forces are associated to a given adiabatic state on which the system evolves classically.

To study excited states of argon clusters, the HPP model gives best estimate of the electronic structure, however it becomes computationally inaccessible for system sizes greater than 15 atoms. Moreover, on-the-fly calculations require the evaluation of the electronic structure at each time step, which is hardly feasible with the HPP model. The DIM model is fast and has been used previously used for dynamics of small

systems.

In this chapter we will introduce the basics of non-adiabatic dynamics and select the method best suitable for our system. In the following chapters we will introduce our theoretical model, which is validated using a 2-state system evaluated analytically using mathematica. Following that, we present our results on the study of Ar_3^* and Ar_7^* using Di-DIM method for the PES and TSH for the non-adiabatic dynamics.

5.1 Introduction to Molecular Dynamics

The Time Dependent Schrodinger equation (TDSE) for evolution of electronic wave-packet is given by,

$$i\hbar\frac{\partial}{\partial t}\Psi(\mathbf{r},\mathbf{R},t) = \hat{H}\Psi(\mathbf{r},\mathbf{R},t) \tag{5.1}$$

where Ψ is the total exact wave function defined in the Born-Huang approach,

$$\Psi(\mathbf{r},\mathbf{R},t) = \sum_K \Phi_K(\mathbf{r};\mathbf{R})\chi_K(\mathbf{R},t) \tag{5.2}$$

$\Phi_K(\mathbf{r};\mathbf{R})$ is the electronic wave function depending parametrically on nuclear coordinates obtained by solving electronic structure problem and $\chi_K(\mathbf{R},t)$ gives the nuclear dynamics. $\hat{H}$ is the hamiltonian given in Eq. 1.1.

As we solve Eq. 5.1 using the total wave-function 5.2, we separate the nuclear and electronic parts. We get the solution to the electronic part in an orthonormal basis Φ_K, which are the eigenvectors of the electronic Hamiltonian $\hat{H}_e(\mathbf{r};\mathbf{R})$. The states Φ_K obtained by diagonalisation of $\hat{H}_e(\mathbf{r};\mathbf{R})$ are orthonormal to each other.

By projecting the TDSE on eigenvector $\langle\Phi_L|$ and integrating over all the electronic coordinates, we get the associated nuclear equation of motion as;

$$i\hbar\frac{\partial}{\partial t}\chi_K(\mathbf{R},t) = \left[\hat{T}_n(\mathbf{R}) + E_K^e(\mathbf{R})\right]\chi_K(\mathbf{R},t) + \sum_L C_{KL}(\mathbf{R})\chi_L(\mathbf{R},t) \tag{5.3}$$

where $E_K^e(\mathbf{R})$ is the potential energy surface of the nuclei in K^{th} electronic state. $C_{KL}(\mathbf{R})$ gives the non-adiabatic coupling between electronic states K and L.

In BOA, non-adiabatic coupling terms are neglected and it is often a good approximation to study the dynamics on ground states. However, to study the dynamics on excited states, there might be a region where multiple potential energy surfaces come close to each other in energy and they can be non-adiabatically coupled. In such a case it becomes necessary to have proper description of $C_{KL}(\mathbf{R})$ coupling terms.

The electronic problem can be treated with *ab initio* or semi-empirical methods, as discussed earlier in this thesis, and we now intend to solve the motion of nuclei. When nuclei are treated quantum mechanically, there are several ways to estimate the function $\chi_K(\mathbf{R},t)$ defining them. We can represent it on the grid, as point trajectories or with some trajectory basis functions (example: Gaussian). The quantum description of nuclei is exact, but makes the problem computationally expensive and eventually impractical for large numbers of atoms and their associated configurations. Therefore, for larger systems, like the one we are interested in, it is reasonable to drop the quantum mechanical description of nuclei and treat them as classical particle while keeping a quantum description for electrons.

5.1.1 Classical Approximation for Nuclei

The Born-Oppenheimer approximation in chapter 1 allows us to consider nuclear motion classically making this Mixed Quantum Classical Dynamics (MQCD) using Ehrenfest trajectories or surface hopping.

The classical motion of nuclei is treated under the Born-Oppenheimer approximation, the multisurface character of the problem being taken into account by using mean-field or surface- hopping approaches.

$$\Psi(\mathbf{r},\mathbf{R},t) \rightarrow \Phi(\mathbf{r};\mathbf{R})\chi(\mathbf{R},t)\exp\left[\frac{i}{\hbar}\int_{t_0}^{t} dt' E_e(t')\right] \tag{5.4}$$

Using Eq. (5.4) to solve equation (5.1), we get two coupled time dependent equations for Φ and χ. With application of classical approximation ($\hbar \rightarrow 0$), we get the equation associated to evolution of χ, which is shown to be equivalent to classical equation of motion for slow moving particle i, given by J.C. Tully [118] and in review article [119]. Therefore, the equation of motion for each classical nucleus, i, in the average potential of the fast moving particles, is given by:

$$\dot{\mathbf{R}}_i = \frac{\mathbf{P}_i}{\mathrm{M}_i} \tag{5.5}$$

$$\dot{\mathbf{P}}_i = \left\langle \Phi \middle| -\frac{\partial \hat{H}}{\partial \mathbf{R}_i} \middle| \Phi \right\rangle \tag{5.6}$$

where P_i and M_i are the linear momentum and the mass of nucleus i, and R_i is its position. And the electronic wave packet evolution is given by;

$$i\hbar\frac{\partial}{\partial t}\Phi(\mathbf{r};\mathbf{R}) = \hat{H}_e(\mathbf{r};\mathbf{R})\Phi(\mathbf{r};\mathbf{R}) \tag{5.7}$$

Within the Ehrenfest dynamics, an average potential is used to propagate the wave packet. The non-adiabatic couplings are taken into account in this potential by explain. For our system, it is desirable to evolve the wave packet on a desired adiabatic state, which is not in the scope of Ehrenfest dynamics.

5.1.2 Wave Packet Evolution on Non-adiabatically Coupled States

To follow the wave packet evolution on a desired adiabatic state, we start with the electronic wave function, which is a linear combination of the electronic states given by;

$$\Phi(\mathbf{r};\mathbf{R},t) = \sum_m c_m(t)\phi_m(\mathbf{r};\mathbf{R}) \tag{5.8}$$

with time dependency in the coefficients $c(t)$, $|c_m(t)|^2$ gives the population of the state m. Using this to solve the equation of motion, we get the differential equations governing the dynamics of $c_n(t)$ coefficients.

$$i\hbar\dot{c}_n = \sum_m c_m(t)\left(E_{nm}(\mathbf{R}) - \sigma_{nm}^{NAC}(\mathbf{R})\right) \tag{5.9}$$

where $E_{nm}(\mathbf{R}) = \langle\phi_n(\mathbf{R})|\hat{H}_e|\phi_m(\mathbf{R})\rangle$ and $\sigma_{nm}^{NAC}(\mathbf{R}) = \dot{\mathbf{R}}.\left\langle \phi_n(\mathbf{R}) \middle| \frac{\partial}{\partial \mathbf{R}}\phi_m(\mathbf{R}) \right\rangle$. If adiabatic states are chosen for ϕ_n then, $E_{mn}(\mathbf{R}) = E_m(\mathbf{R})\delta_{mn}$.

We get $\sigma_{nm}^{NAC}(\mathbf{R})$ which gives the non-adiabatic coupling between the two states m and n. Now there are several methods available which allows us to follow an adiabatic state with non-adiabatic coupling, which is discussed in the following section.

5.2 Non-Adiabatic Couplings

The electron cloud surrounding the atom is supposed to instantaneously(adiabatically) accommodate to the nuclear motion in BOA. However this is not always the case. To follow the electron motion and perform a nonadiabatic dynamics, nonadiabatic couplings must be computed

These couplings can be understood as follows. With the evolution of a system (nuclear motion), electron cloud (density) evolves as well. As the electron cloud deforms, the currently followed adiabatic state and other adiabatic states are coupled together. I.e., to understand the evolution of electron cloud, it is important to understand the characteristic of other possible state(s) and how are they are coupled. To simulate this theoretically, we take the derivative overlap of the two states (kl) and depending on the result, which is the coupling, the electron cloud (population) is distributed among them. The kinetic coupling can also be written as:

$$\sigma_{kl}^{NAC} = \left\langle \phi_k(t) \middle| \frac{\partial}{\partial t} \phi_l(t) \right\rangle \tag{5.10}$$

The strength of the coupling σ_{kl}^{NAC} gives how similar is the character of the two states. This is clear if we look at the electronic structure of the system as shown in figure 5.1. For an electronic cloud evolving on the blue state it will continue to evolve on the same state without decaying to the lower- energy state. When the NAC is stronger, the upper blue state can jump on the lower state and continue on the lower blue curve and visa versa for the electronic cloud on the orange state. In this process, depending on the strength of the coupling, as shown in the bottom two images of Figure 5.1, the distribution of the electronic cloud (density) varies. With stronger coupling, more electron density from upper state will be transferred to the lower state and in the case of weak coupling less electron density will be transferred.

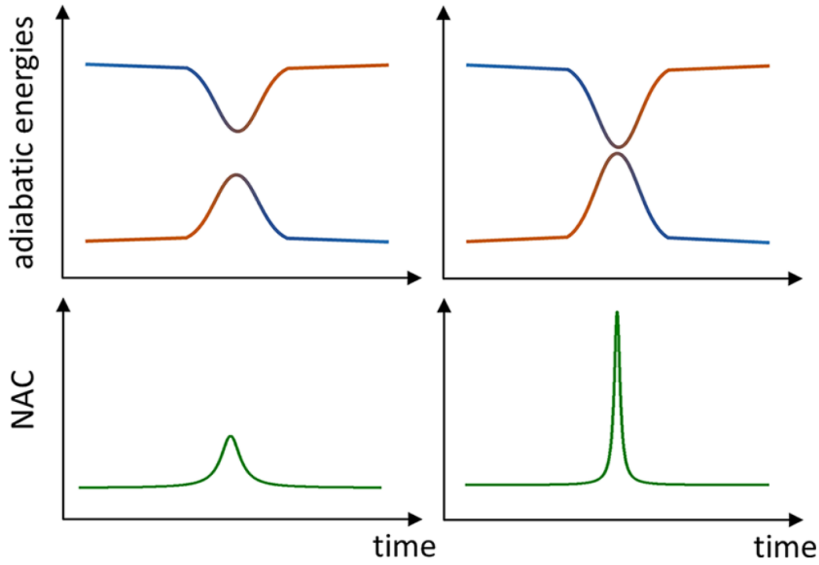

Figure 5.1: Illustration of Non-Adiabatic Coupling as a function of time is adapted from NA-MQC Dynamics review article by Otero and Barbatti [119]. In left figure, with weak coupling the peak is small whereas in the right figure.

The evaluation of non-adiabatic couplings by no means is trivial, and with increasing system size and number of states this becomes increasing challenging. In multiconfigurational approaches like MCSCF, MRCI and lately in MS-CASPT2, they can be obtained for small systems with a limited number of states [126, 127, 128, 129, 130, 131]. Other analytical formulations of non-adiabatic couplings based on TDDFT with Linear Response (LR) theory have been developed [132, 133, 134, 135, 136, 137, 138, 139], which have shown promising results but unfortunately can not be used for rare-gas matrix. These methods are expensive and are ideal for small systems. For bigger systems we need a faster method. One way to evaluate

equation-of-motion without explicitly calculating derivative coupling is by using finite-difference method as proposed by Hammes-Schiffer and Tully (HST) [140]. This has been further improved by Meek and Levine by having coupled averaged over a time interval after interpolating the wave function using unitary transformation. In their method of *norm-preserving interpolation* (NPI) scheme, they take the logarithm of the overlap matrix which allows considerable speed gain [141].

A rich literature is available to implement NAC for small systems where the evolution of wave function is known and therefore σ_{kl}^{NAC} can be calculated analytically is most cases. However, studies of the excitation dynamics of big clusters without the knowledge of the wave function evolution are scarce. In this thesis we have introduced a method to evaluate this.

5.3 Non-adiabatic dynamics of rare- gas clusters

The fragmentation of rare-gas ionic clusters by electron impact, photoionization, or photoexcitation have been thoroughly studied in the literature. The majority of works involving the study of ionic rare gas systems is based on the combination of a DIM model, where SO couplings were taken into account, to describe the cluster potential-energy surfaces with a mixed quantum-classical method to perform the dynamics on these surfaces. The results of ionic system studies is summarised in a review article by Bonhommeau *et al.* [142].

We did not find any work on the evolution of electronic wave packets for excited neutral clusters. With the aim to understand the excitation decay in the Ar rare-gas clusters, our theoretical approach is motivated by the work done to study ionic rare gas systems. Ar_N^+ dynamics has been studied by Ehrenfest and surface hopping dynamics. Ehrenfest dynamics was employed in HWD method (Hemiquantal Dynamics) with whole DIM basis by Amarouche *et al* [143] to study the fragmentation of small argon clusters. Their remark about this type of calculation being close to *ab initio* is unclear. Besides that, the trajectory is propagated on an average potential, i.e., not on true adiabatic surfaces, which makes the assignment of the fragmentation channels rather subjective. The work of Janecek *et al.* [144] used DIM+SO method to calculate the PES. However, the coefficients evolved on adiabatic surfaces. Further work by Janecek *et al.* [145] showed the difference between mean-field dynamics and surface hopping for different rare gas ionic trimers. They reported that mean-field approaches do not give reliable fragmentation results for Kr_3^+ and Xe_3^+ (except for Ar_3^+) when compared to experiments and surface hopping dynamics.

The surface hopping (quantum transitions) based method used for molecular dynamics has been implemented by several authors [146, 147, 148, 149, 150] due to its simplicity and ease of application. This method allows to evolve the wave-packet on an adiabatic surface at any given time. The non-adiabatic transitions are reproduced by hops between surfaces. Using this method, the distribution of fragmentation of Ar_n^+ was observed to be in better agreement with the experimental observations as compared to Ehrenfest dynamics [142]. Ar^+ and Ar_2^+ are the main fragments produced and larger ionic fragments arise when the parent ion size increases. Bigger ionic clusters in the fragmentation channels are observed with the increasing initial cluster size.

The proper treatment of non-avoided crossings and degenerate states [151] will be presented in the following chapter 6 and we will discuss its consequence in conclusion.

Chapter 6

Theoretical Model

We present a theoretical model to study the time evolution of the Rydberg states of excited neutral rare-gas clusters. Our model is based on previous works on ionic clusters as discussed in the previous chapter. In the following method, we use the Potential Energy surface (PES) obtained using the Di-DIM method introduced in section 3.2. The evolution of the wave packet is based on the method proposed by Janecek *et al* [144] using the whole Di-DIM basis. The propagation of nuclei is done by using the Beeman method [152, 153] on adiabatic PES. The non-adiabatic dynamics is achieved with the surface-hopping proposed by Tully [80].

In this chapter, we start by introducing the method used to propagate the electronic wave packet, treat degeneracies, avoided and non-avoided crossings, calculate non-adiabatic couplings, and correct linear momenta at a hopping event to maintain the total energy of the system. Following that, we present a validation of our code obtained by comparing our propagation algorithm with *Mathematica* [154] for Ar_2^*.

6.1 Description of the method

The method is based on the calculation of the time-dependent Hamiltonian obtained by spline interpolation. The calculation of this Hamiltonian is done using the Di-DIM which has been discussed previously in section 3.2. In the following section we assume that, at each time, we have a well defined Hamiltonian for any nuclear configuration. The full derivation of this approach is given in appendix D. With Hamiltonian being the central point, we start by defining the time-dependent Hamiltonian in perturbation theory as:

$$\hat{H}(t) = \langle \hat{H} \rangle + \delta\hat{H}(t) \tag{6.1}$$

where $\delta\hat{H}(t) = \hat{H}(t) - \langle \hat{H} \rangle$ is a perturbation to the time-averaged Hamiltonian $\langle \hat{H} \rangle$. This time independent Hamiltonian is formed by following the average Hamiltonian theory proposed by Brinkmann [155].

Now we introduce a stationary orthonormal basis set $\sum_\alpha |\alpha\rangle\langle\alpha| = \mathbb{1}$ which diagonalises $\langle \hat{H} \rangle$. The time evolving wave function in Schrodinger's picture in this basis set is given by:

$$|\psi_S(t)\rangle = \sum_\alpha C_\alpha(t)|\alpha\rangle \tag{6.2}$$

We can go from the Schrodinger picture to the Interaction picture by using the unitary time-evolution operator $\hat{U}_0(t,t_0) = e^{-i\langle \hat{H} \rangle (t-t_0)}$ and defined as:

$$|\psi_S(t)\rangle = \hat{U}_0(t,t_0)|\psi_I(t)\rangle \tag{6.3}$$

On applying Eq. (6.3), in the time-dependent Schrodinger equation, we get in the interaction picture:

$$\frac{\partial}{\partial t}|\psi_I(t)\rangle = -i\hat{W}(t)|\psi_I(t)\rangle \tag{6.4}$$

where $\hat{W}(t) = \hat{U}_0^{\dagger}(t,t_0)\delta\hat{H}(t)\hat{U}_0(t,t_0)$ is the interaction Hamiltonian.
On solving this differential equation formally we get the time-dependent evolution of wave function as:

$$|\psi_I(t)\rangle = \hat{U}_I(t,t_0)|\psi_I(t_0)\rangle \tag{6.5}$$

where

$$\hat{U}_I(t,t_0) = \exp\left[-i\int_{t_0}^{t}\hat{W}(t')dt'\right] \tag{6.6}$$

is the Time-Displacement Operator given by Pechukas *et al* [156] in Feynman's representation [157] of the unitary operator. The unitary time-displacement operator is evaluated using Magnus expansion [158], where we consider the perturbation to be very small for a small time-step $\tau = t - t_0$. This means that in the Magnus expansion of the exponential in $\hat{U}_I(t,t_0)$ we neglect all the commutators like, $\left[\hat{W}(t),\hat{W}(t')\right]$, i.e., in first order of approximation $\left[\hat{W}(t),\hat{W}(t')\right] \to 0$. See articles [155, 156] and appendix D of this thesis.
Using the definition of the wave function $|\psi_I(t_0)\rangle = \hat{U}_0(\tau)\sum_\alpha C_\alpha(t_0)|\alpha\rangle$ and projecting it onto $[|\alpha\rangle]$ the basis set which diagonalise $\langle H\rangle$, we get the coefficient evolution as:

$$C_\beta(t) = \sum_\alpha e^{-iE_\beta\tau}\langle\beta|\hat{U}_I(t,t_0)|\alpha\rangle C_\alpha(t_0) \tag{6.7}$$

where the fast moving phase $e^{-iE_\beta\tau}$ is integrated exactly irrespective of the electronic time-step (τ). On solving in this approximation we evaluate the non-adiabatic couplings and get the time evolution of the coefficients as:

$$C_\beta(t) = \sum_\alpha e^{-iE_\beta\tau}M_{\beta\alpha}(t)C_\alpha(t_0) \tag{6.8}$$

where $M_{\beta\alpha}(t)$ accounts for the non-adiabatic couplings given in appendix D.1. All the coefficients $C_\beta(t)$ are then expressed in the diabatic DIM basis because of their continuous nature making the algorithm stable.

The coefficients of the adiabatic state A we wish to follow, $C_A(t)$, are obtained by projecting the propagated wave packet onto this adiabatic state at time t. The projection reads:

$$C_A(t) = \sum_a A_a(t)\sum_\beta Q_{a\beta}C_\beta(t) \tag{6.9}$$

where $A_a(t)$ are the coefficients of the adiabatic state A in the primitive DIM basis and obtained by diagonalization of the hamiltonian at time t. The unitary transformation matrix $Q_{a\beta}$ is the matrix, which diagonalizes the time-average hamiltonian $\langle\hat{H}\rangle$, expressed in the primitive DIM basis indexed by a.

6.1.1 Time-averaged Hamiltonian

In this subsection we show how the time averaged Hamiltonian $\langle \hat{H} \rangle$ that enters equation 6.1 is evaluated. The time averaging has to be done for each matrix element $H_{ab} = \langle a|\hat{H}|b\rangle$, where $|a\rangle$ is the DIM configuration basis, which is expanded on polyatomic basis formed by antisymmetrised product of atomic basis as shown in section 3.2. For better readability, we drop in the following the indexes a, b.

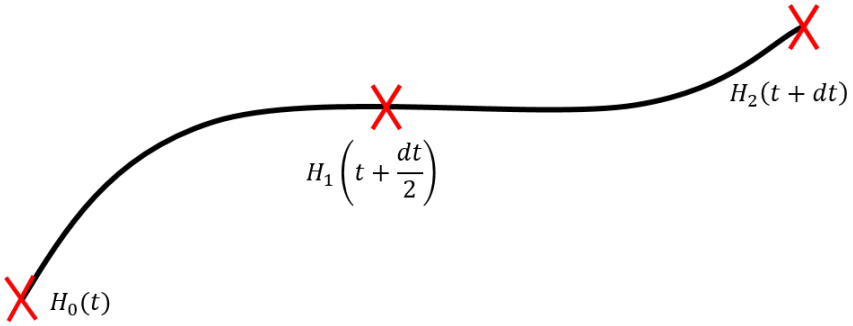

Figure 6.1: Evolution of the Hamiltonian

As shown in the figure 6.1, we evaluate the Hamiltonian $\hat{H}_0$ at time t using the DIM model, then evaluate $\hat{H}_1$ and $\hat{H}_2$ along the trajectory at time $t + dt/2$ and $t + dt$ respectively. Using these three points we solve the 2$^{\text{nd}}$ order polynomial equation $\hat{H}(t) = A + Bt + Ct^2$ to get the coefficients as:

$$\begin{pmatrix} A \\ B \\ C \end{pmatrix} = \begin{pmatrix} 1 & t & t^2 \\ 1 & \left(t+\frac{dt}{2}\right) & \left(t+\frac{dt}{2}\right)^2 \\ 1 & (t+dt) & (t+dt)^2 \end{pmatrix}^{-1} \begin{pmatrix} h_0 \\ h_1 \\ h_2 \end{pmatrix} \tag{6.10}$$

which gives the time evolving Hamiltonian equation between t and $t + dt$ where h_0, h_1 and h_2 are the matrix elements of $\hat{H}_0$, $\hat{H}_1$ and $\hat{H}_2$ respectively. The time-averaged Hamiltonian is given by;

$$\langle \hat{H} \rangle = \frac{1}{dt} \int_t^{t+dt} \hat{H}(t')dt' \tag{6.11}$$

Using the previously obtained Hamiltonian $\hat{H}_0$, $\hat{H}_1$ and $\hat{H}_2$, we get the time-averaged Hamiltonian analytically as:

$$\langle \hat{H} \rangle = \left(\frac{\hat{H}_0 + 4\hat{H}_1 + \hat{H}_2}{6} \right) \tag{6.12}$$

Eventually, the time evolution of each element of the perturbation matrix $\delta\hat{H}(t)$ is approximated by the form $A + Bt + Ct^2 - \langle \hat{H} \rangle$.

6.1.2 Treatment of Degenerate States

With the high density of states in RG clusters, the states are degenerate or nearly degenerate which makes the trajectory evolution difficult. Therefore, it is desirable to lift the degeneracy of the states. This is done by using a perturbative constraint to rotate the system without changing the energy using a method proposed in the dissertation [159] and work of Zanuttini *et al* [151]. In this method, for a given degenerate subspace D, a small perturbative constraint based on the eigenvalues is used to lift the degeneracy while ensuring the continuity of the trajectory. This is done for all the degenerate subspace at each nuclear step.

The perturbations are defined as:

$$T_{ij} = \sum_k C_{ik}^* V_k C_{kj} \tag{6.13}$$

where $V_k = a \times (k - n - 1)$; a is a scaling term and n is basis size. The coefficients C_{kj} are taken at t_0.

Now, to lift the degeneracy, a reduced-space D of degenerate states is created where they are rotated following the perturbation as:

$$V_{ij}^d = \sum_{ij} C_i^* C_j T_{ij} \tag{6.14}$$

and diagonalising to get new eigenvectors at time t.

6.1.3 Non-avoided Crossings

As the system evolves, an adiabatic state comes to a crossing, across which the symmetry changes, i.e., the adiabatic PECs obtained from evaluation of the electronic DIM Hamiltonian are not symmetry adapted. This is also referred to as cusp (conical intersection) where derivative coupling is ill-defined. This is shown in Figure 6.2. The left image shows the situation where for $t_1 \rightarrow t_2$, the adiabatic states $a(t_1) \rightarrow b(t_2)$ and $b(t_1) \rightarrow a(t_2)$, the symmetry of both states a and b has changed. We identify this situation by calculating the overlap of the state which is being followed with respect to all the other states. Away from the crossing, the self overlap between the state $S_{aa} \simeq 1$. Near the crossing this overlap is no longer unity ($S_{aa} \neq 1$). When the self overlap for a given state between two time-steps is below a threshold and the overlap with another state is above this threshold, we identify it to be a non-avoided crossing. Once resolved, the figure on the right shows the evolution of the states with same symmetry.

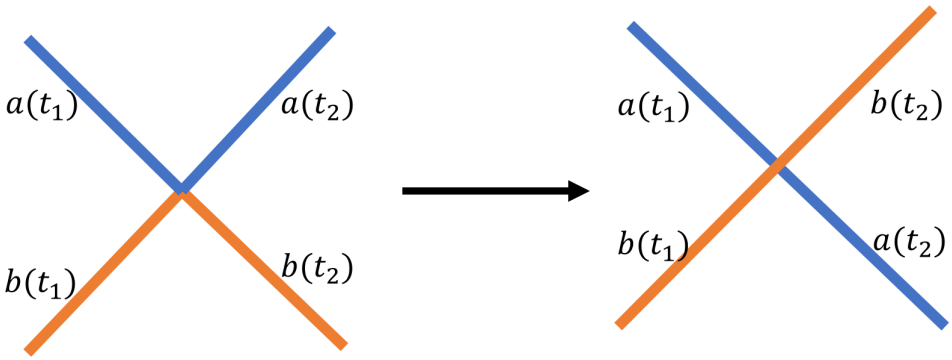

Figure 6.2: Treatment of non-avoided crossings.

The overlap of state a with state b between the times t_1 and t_2 is defined as:

$$S_{ab} = \langle a(t_1) | b(t_2) \rangle = \sum_i C_{ia}^*(t_1) C_{ib}(t_2) \tag{6.15}$$

where $a(t_1)$ and $b(t_1)$ are the eigenvectors obtained from diagonalizing the Hamiltonain $\hat{H}(t_1)$ in the atomic basis with the coefficients $C_{ia}(t_1)$. Similarly $a(t_2)$ and $b(t_2)$ are the eigenvectors for the Hamiltonain $\hat{H}(t_2)$ with the coefficients $C_{ia}(t_2)$, which are defined in previous section for $t_1 = t$ and $t_2 = t + dt$. The self overlap between two time-steps is given by, $S_{aa} = \langle a(t_1) | a(t_2) \rangle$.

The swap of state between a and b would happen if, $S_{aa} \leq 1 - \theta_1$ and $S_{ab} \geq 1 - \theta_2$. Where θ_1 is the threshold for maximum self overlap and θ_2 is the threshold for minimum overlap between states a and b. In

our model we choose; $\theta_1 = \theta_2 = 0.10$. The new state to follow is b if the overlap of state $a(t_1)$ is more than 90% with state $b(t_2)$ and less than 90% with state $a(t_2)$. While doing so, we need to change the phase of the new state as follows:

$$C_{ib}(t_2) = \left[\frac{S^*_{ab}}{|S_{ab}|}\right] C_{ib}(t_1) \quad \forall i \tag{6.16}$$

If the time-step is large and the phase-rotation is larger than expected (greater than 10%), then we would like to reset the coordinates and applied the same procedure with a smaller time step dt. However, in this work we do not use the adaptive time-step.

6.1.4 Non-Adiabatic Couplings

The evaluation of non-adiabatic couplings (NAC) for the surface hopping is done as follows. In equation 5.10 the NAC between the states m and n for a given trajectory in terms of adiabatic coefficient evolution is given by:

$$\sigma_{mn} = \left\langle C_m(t) \middle| \frac{\partial}{\partial t} C_n(t) \right\rangle \tag{6.17}$$

this can be evaluated for a small time-step dt as:

$$\sigma_{mn} = C^*_m(t) \left[\frac{C_n(t) - C_n(t-dt)}{dt}\right] \tag{6.18}$$

6.1.5 Avoided Crossing using Surface hopping

In this approach, once having calculated the evolution coefficient from equation 6.8, the nuclei needs to be propagated on a state adiabatically. This is shown in figure 6.3 where the states in "blue" and "orange" are coupled adiabatically. As shown in the left figure, without any adiabatic coupling, the system in state a will remain there for $t_1 \to t_2$. With the inclusion of non-adiabatic couplings, the two states get coupled and the wave-packet on states "blue" has a channel to go to state "orange" and vice versa. There are several computationally expensive method available to include this as discussed in chapter 5. In this thesis, we use a cheap probabilistic method known as Fewest Switching Surface Hopping (FSSH) as introduced by J.C. Tully [80]. Using this method of trajectory evolution has been shown to produce comparable results to much more computationally expensive methods.

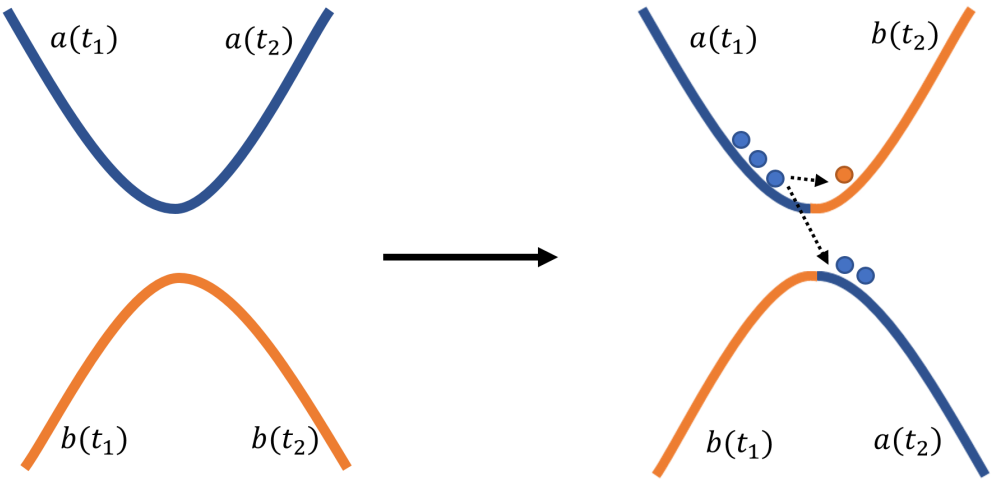

Figure 6.3: Treatment of avoided crossings.

While using FSSH, the wave function often decays to a lower-energy state when a hop happens. This implies that the states become incoherent. In our model we follow the wave packet and the trajectory population evolution is distributed over all the states.

The decision to hop or not is done using the stochastic fewest-switches algorithm, the the hopping probability from a state m to n in a time interval $[t, t+dt]$ is given by [119]:

$$g_{mn}(t,t+dt) \approx 2\int_t^{t+dt} d\tau \frac{\mathrm{Im}[C_n(\tau)C_m^*\sigma_{mn}(\tau)] - \mathrm{Re}[C_n(\tau)C_m^*\sigma_{mn}(\tau)]}{C_m\tau)C_m^*(\tau)} \tag{6.19}$$

For small dt, it is simplified to the hopping probability from $m \to n$ as:

$$g_{mn}(t,t+dt) = \mathrm{Max}\left[0, -2\frac{\mathrm{Re}[C_nC_m^*\sigma_{mn}]}{|C_m|^2}dt\right] \tag{6.20}$$

The hop will happen if the hopping probability from state m to n satisfies the following condition:

$$\sum_i^{n-1} g_{mi} \leq \varepsilon \leq \sum_i^{n} g_{mi} \tag{6.21}$$

where ε is a random number between 0 and 1.

Energy Conservation check for hop

For adiabatically coupled states a and b, as shown in figure 6.3, the force associated to the j^{th} atom for the transition from state $a \to b$ within the classical approximation is given by:

$$\mathbf{F}^j = \frac{d\mathbf{p}^j}{dt} \tag{6.22}$$

where $d\mathbf{p}^j = \mathbf{p}_b^j - \mathbf{p}_a^j = \mathbf{q}^j$ is the change in momentum of the j^{th} atom. The change in momentum for each atom can therefore is given by:

$$\mathbf{q}^j = \beta(\mathbf{F}_b^j - \mathbf{F}_a^j) = \alpha\hat{\mathbf{u}}_{ba}^j \tag{6.23}$$

where α is a constant of proportionality and the unit vector $\mathbf{u}_{ba}^j = \frac{\mathbf{F}_{ba}^j}{||\mathbf{F}_{ba}^j||}$. The forces are calculated analytically for the adiabatic state a and b individually given in appendix C.
Now the total energy between the two states should be conserved as,

$$E_a = \sum_j \frac{(\mathbf{p}_a^j)^2}{2m_j} + V_a(\mathbf{R}) \quad \& \quad E_b = \sum_j \frac{(\mathbf{p}_b^j)^2}{2m_j} + V_b(\mathbf{R}) \tag{6.24}$$

where $V_a(\mathbf{R})$ and $V_b(\mathbf{R})$ are the potential energies which are eigenvalues of the DIM Hamiltonain $\hat{H}_2(\mathbf{R})$ evaluated for each state a and b, respectively at time $t+dt$.
For continuity and conservation of energy, $E_a = E_b$ gives:

$$\sum_j \frac{(\mathbf{p}_a^j)^2}{2m_j} + V_a(\mathbf{R}) = \sum_j \frac{(\mathbf{p}_b^j)^2}{2m_j} + V_b(\mathbf{R}) \tag{6.25}$$

where $\mathbf{p}_b = \mathbf{p}_a + \mathbf{q}$. On solving this equation for $\mathbf{q}$ we get,

$$\sum_j \left[\frac{(\mathbf{q}^j)^2}{2m_j} + \frac{(\mathbf{p}_a^j . \mathbf{q}^j)}{m_j} \right] + V_{ba}(\mathbf{R}) = 0 \tag{6.26}$$

where $V_{ba}(\mathbf{R}) = V_b(\mathbf{R}) - V_a(\mathbf{R})$ and substituting $\mathbf{q} = \alpha \mathbf{u}_{ba}$ we get,

$$\alpha^2 \sum_j \frac{1}{2m_j} + \alpha \sum_j \frac{(\mathbf{p}_a^j . \mathbf{u}_{ba}^j)}{m_j} + V_{ba}(\mathbf{R}) = 0 \quad \Longrightarrow \quad \alpha^2 + \alpha \left(\frac{B}{A} \right) + \left(\frac{C}{A} \right) = 0 \tag{6.27}$$

where $A = \sum_j (1/2m_j)$, $B = \sum_j [(\mathbf{p}_a^j . \mathbf{u}_{ba}^j)/m_j]$ and $C = V_{ba}(\mathbf{R})$. Then on solving for α,

$$\alpha = -\frac{B}{2A} \pm \sqrt{\left(\frac{B}{2A} \right)^2 - \frac{C}{A}} \quad \Longrightarrow \quad \alpha = -M \pm \sqrt{N} \tag{6.28}$$

The hop is allowed only if $N > 0$. The sign is selected such that it yields a minimum value for α, i.e., $\alpha = -M - \sqrt{N}$ if $-M > 0$ else $\alpha = -M + \sqrt{N}$ if $-M < 0$.

The corrected linear momentum, p_b, after and accepted hop is therefore

$$\mathbf{p}_b = \mathbf{p}_a + \alpha \mathbf{u}_{ba} \tag{6.29}$$

6.2 Model Validation

The computation code needs to be validated before using it for physical analyses. For this, we took a minimum, well defined $4s$ excited state PECs of Ar_2^* obtained using *ab initio* using MRCI method as shown in section 2.2. As we want to evaluate the non-adiabatic molecular dynamics model presented in previous section 6.1, not the DIM model, the PECs used to parameterise DIM are obtained from MRCI calculation shown in previous part of this thesis. It is not important to use Di-DIM PECs as the inclusion of $4p$ state will make configuration space bigger and the reduction of bigger configuration basis to 2 state system is complicated.

There are 12 configurations associated to $4s$ excited argon excimer. A 12 configuration-space system is difficult to solve. However, taking advantage of symmetries and degeneracies it is possible to reduce this problem to a 2-state problem which can be solved with simpler algorithms. In this section, we first show the reduction to 2-state system and, then, we solve the two differential equations governing the evolution of coefficients with Mathematica, and compare the subsequent results with those predicted by our model.

First we select $M_J = 0$ only. This reduces the system to a 8-space, from which the Hamiltonian splits into blocks as:

$$H = \begin{pmatrix} A & B_0 \\ B_0 & A \end{pmatrix}$$

$A = A_0 + \kappa V_{so}$ where κ is the Spin Orbit coefficient for the argon atom. A_0 and B_0 are the diagonal matrix blocks,

$$A_0 = \begin{pmatrix} a_0 & & & \\ & a_1 & & \\ & & a_2 & \\ & & & a_0 \end{pmatrix} \quad \& \quad B_0 = \begin{pmatrix} b_0 & & & \\ & b_1 & & \\ & & b_2 & \\ & & & b_0 \end{pmatrix}$$

where a_0 is the energy of ${}^3\Pi_{u+g}$ state, a_1 is the energy of ${}^3\Sigma^+_{u+g}$ state and a_2 is the energy of ${}^1\Sigma^+_{u+g}$ state. The b_0 is the energy of ${}^3\Pi_{g-u}$ state, b_1 is the energy of ${}^3\Sigma^+_{g-u}$ state and b_2 is energy of ${}^1\Sigma^+_{g-u}$ state.
The full Hamiltonian with SOC is:

$$\begin{aligned} H &= \begin{pmatrix} A & B_0 \\ B_0 & A \end{pmatrix} \\ &= \begin{pmatrix} A_0 & 0 \\ 0 & A_0 \end{pmatrix} + \begin{pmatrix} 0 & B_0 \\ B_0 & 0 \end{pmatrix} + \begin{pmatrix} \kappa V_{so} & 0 \\ 0 & \kappa V_{so} \end{pmatrix} \end{aligned}$$

and

$$V_{so} = \begin{pmatrix} 1 & -1 & 1 & 0 \\ -1 & 0 & 0 & 1 \\ 1 & 0 & 0 & 1 \\ 0 & 1 & 1 & 1 \end{pmatrix},$$

Now applying by the unitary transformation which separates u and g states as:

$$\begin{aligned} Q^+HQ &= \frac{1}{\sqrt{2}} \begin{pmatrix} \mathbb{1} & \mathbb{1} \\ \mathbb{1} & -\mathbb{1} \end{pmatrix} \begin{pmatrix} A & B_0 \\ B_0 & A \end{pmatrix} \frac{1}{\sqrt{2}} \begin{pmatrix} \mathbb{1} & \mathbb{1} \\ \mathbb{1} & -\mathbb{1} \end{pmatrix} \\ &= \begin{pmatrix} A+B_0 & \\ & A-B_0 \end{pmatrix} \end{aligned}$$

The spin orbit V_{so} is not affected by the transformation by Q which separates $H_{gg} = A + B_0$ and $H_{uu} = A - B_0$. Hence we can write:

$$H_{uu} = \begin{pmatrix} a & -\kappa & \kappa & 0 \\ -\kappa & b & 0 & \kappa \\ \kappa & 0 & c & \kappa \\ 0 & \kappa & \kappa & a \end{pmatrix}$$

where $a = {}^3\Pi_u + \kappa V_{so}$, $b = {}^3\Sigma^-_u$ and $c = {}^3\Sigma^+_u$.
Further, we can couple the two ${}^3\Pi_u$ states, which are degenerate for any given distance to get states with positive and negative symmetries, i.e. ${}^3\Pi^+_u$ and ${}^3\Pi^-_u$. The transformation is time independent and leaves the Σ_u states unchanged while mixing ${}^3\Pi_u$ states. The transformation matrix R reads:

$$R = \begin{pmatrix} \frac{\sqrt{2}}{2} & 0 & 0 & \frac{\sqrt{2}}{2} \\ 0 & 1 & 0 & 0 \\ 0 & 0 & 1 & 0 \\ \frac{\sqrt{2}}{2} & 0 & 0 & -\frac{\sqrt{2}}{2} \end{pmatrix} = R^+$$

Now applying this transformation we get:

$$R.H_{uu}.R^{+} = \begin{pmatrix} \frac{\sqrt{2}}{2} & 0 & 0 & \frac{\sqrt{2}}{2} \\ 0 & 1 & 0 & 0 \\ 0 & 0 & 1 & 0 \\ \frac{\sqrt{2}}{2} & 0 & 0 & -\frac{\sqrt{2}}{2} \end{pmatrix} \begin{pmatrix} a & -\kappa & \kappa & 0 \\ -\kappa & b & 0 & \kappa \\ \kappa & 0 & c & \kappa \\ 0 & \kappa & \kappa & a \end{pmatrix} \begin{pmatrix} \frac{\sqrt{2}}{2} & 0 & 0 & \frac{\sqrt{2}}{2} \\ 0 & 1 & 0 & 0 \\ 0 & 0 & 1 & 0 \\ \frac{\sqrt{2}}{2} & 0 & 0 & -\frac{\sqrt{2}}{2} \end{pmatrix}$$

$$= \begin{pmatrix} a & & \kappa\sqrt{2} & \\ & b & & -\kappa\sqrt{2} \\ \kappa\sqrt{2} & & c & \\ & -\kappa\sqrt{2} & & a \end{pmatrix}$$

We obtain a 2x2 block of positive and negative symmetries and the block of ($a = {}^3\Pi_u^+ + \kappa$) and ($c = {}^1\Sigma_u^+$) is,

$$H_{uu}^{+} = \begin{pmatrix} a & \kappa\sqrt{2} \\ \kappa\sqrt{2} & c \end{pmatrix}$$

The potential energy curves a(R) and c(R) cross and the coupling $\kappa\sqrt{2}$ is independent of time i.e., on the distance R. Now the diagonalization gives the adiabatic states and we can solve the TDSE to get the evolution of the coefficients of this two-state system as:

$$i\frac{d}{dt}\begin{pmatrix} c_1(t) \\ c_2(t) \end{pmatrix} = \begin{pmatrix} a(t) & k \\ k & c(t) \end{pmatrix}\begin{pmatrix} c_1(t) \\ c_2(t) \end{pmatrix} \tag{6.30}$$

where $a(t) = a(R)$ and $c(t) = c(R)$ are the functions obtained by spline interpolation of the PECs and $k = \kappa\sqrt{2}$.

Simulation

In this demonstration, an Ar atom is placed at the origin while the second one moves along the z-axis towards the stationary atom. As the atoms come close to each other, their states are perturbed leading to a change in populations via spin-orbit coupling between singlet and triplet states. The Hamiltonian elements $a(t)$, $c(t)$ and k in equation 6.30 are obtained from the DIM Hamiltonian. The PEC are $a(t) = {}^3\Pi_u^+(t) + \kappa$, where $\kappa = 477.193$ cm^{-1} is the spin-orbit constant, $c(t) = {}^1\Sigma_u^+(t)$ and $k = \sqrt{2}\kappa$.

The PECs obtained for these colliding dimer are obtained in dynamics for 10^5 a.u. (200 fs) with a time-step of 0.5 a.u. (12.05 as) in our model. As this method is sensitive to the time-step especially in the region of crossings, we deter- mined the maximum time step which can be reliably used during the dynamics: it is worth 2 au in our model.

This test system is a collision between two neutral argon atoms in an excited state. The distribution of initial excitation on the adiabatic states is; $|c_1(t_0)|^2 = 0.98$ and $|c_2(t_0)|^2 = 0.02$ with real amplitudes. With no hopping, the exchange of population only comes via non-avoided crossings. With the intention to validate the model, we looked at the adiabatic and diabatic evolutions of populations, non-diabatic couplings and hopping probabilities.

Figure 6.4 shows the comparison of the results obtained using *Mathematica* [154] by solving equation 6.30 and our model. The figure a) and b) in 6.4 shows respectively the adiabatic and diabatic population evolutions using *Mathematica* and model. The propagation with Mathematica for the diabatic states with fast phase oscillations matches perfectly with our numerical integration. As a result, the adiabatic population evolution as shown in figure (a) matches perfectly for the two methods. However, due to state crossing we see the population evolution across a non-avoided crossing in a2 by the change of colour. With a larger time-step, these fast oscillations are not integrated exactly leading to vulnerabilities in the calculation and eventually to the result. It is also worth mentioning that this system is very sensitive to initial conditions.

Furthermore, the non-adiabatic couplings and the hopping probability from the current state to the adiabatically coupled state is also shown. The non-adiabatic couplings and probability of jump are in perfect agreement in both the models.

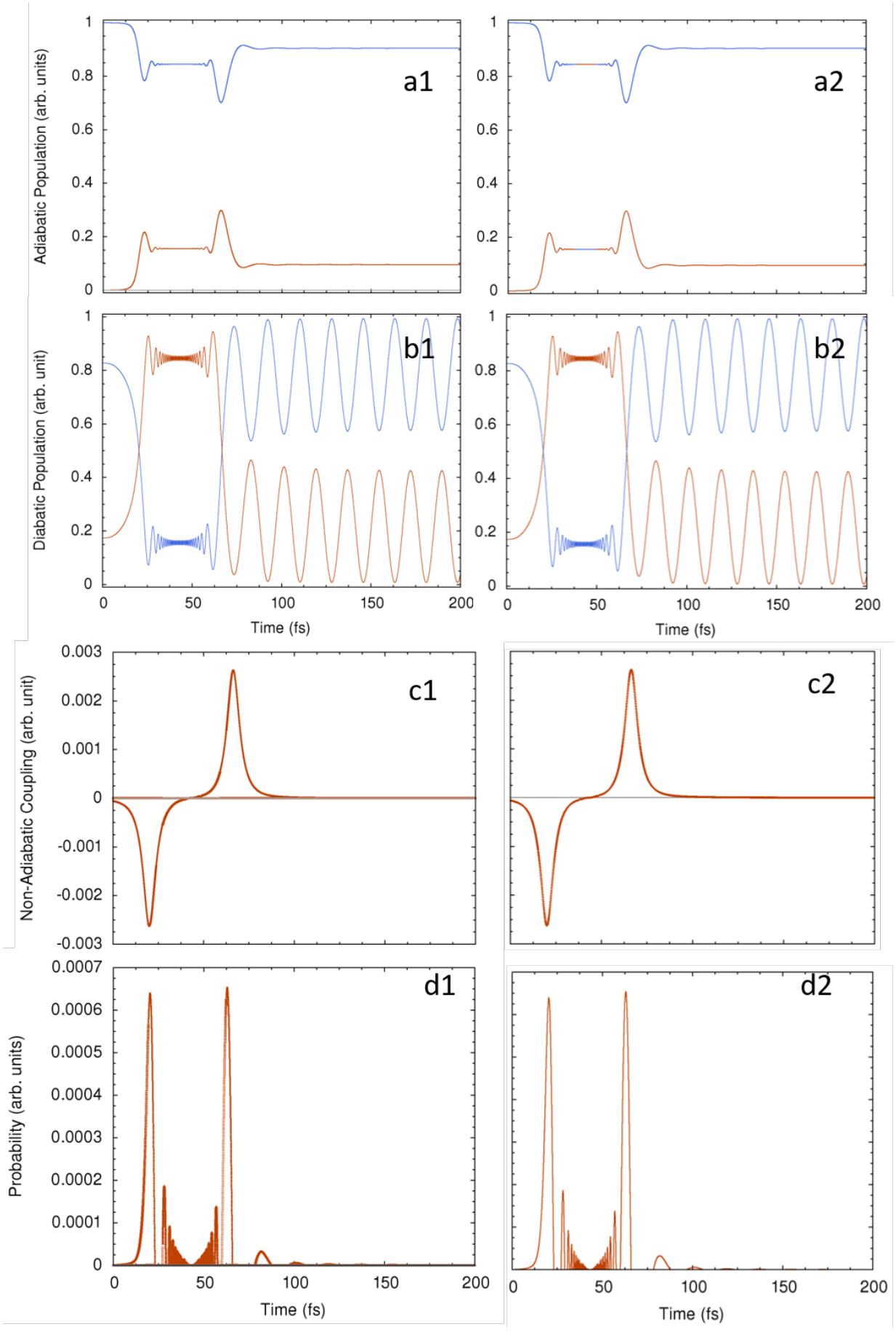

Figure 6.4: Comparison of our Model calculation (1) with *Mathematica* calculations (2)
(a) Adiabatic population evolution (b) diabatic population evolution (c) Non-adiabatic Couplings and (d) The Hopping probability between the two adiabatically coupled states.

Chapter 7

Results and Discussion

In this chapter we explore the PES for different system sizes. We start by presenting the possible fragmentation channels of Ar_n^*. Following that, we give some specificity associated to the dynamics like time-scale and time-step. Then, we simulate the collision of an Ar atom on an Ar^* excimer and that of an excited Ar atom (ie, Ar^*) on Ar_2, to discuss decay processes and the conditions for excitation transfers. Finally, we discuss the fragmentation of Ar_3^* and Ar_7^* clusters starting from their ground state geometry and lowest singlet excited state.

7.1 Fragmentation Channels

There are several fragmentation channels identified for Ar_n^*:

$$Ar_n^* \rightarrow Ar_{(n-m)}^* + Ar_{(m-l)} + lAr \tag{7.1}$$

where, $n > m$ and $m \geq l$. The first term in equation 7.1 corresponds to the formation of an excited atom, dimer or bigger cluster and the second term corresponds to the formation of dissociating ground state atoms. Note that l=m=0 corresponds to no dissociation.

To identify each term in equation 7.1 in our model, we can rewrite this equation equation as;

$$Ar_n^* \rightarrow (Ar_{n-m}^*)^p + (Ar_{m-l})^q + l(Ar)^r \tag{7.2}$$

where p, q and r are the distribution of excitation on each sub-channel and ideally $p+q+r=1$. As in this algorithm we do not collapse the wave function with the trajectory evolution across an avoided or non-avoided crossing, the sum can fall below 1. This is because the coefficients weight is distributed across the crossings. Thus, by the end of dynamics the excitation distribution becomes non conclusive if the weight is too low. This is a drawback of not collapsing after state switching. However, this is observed only 2 of all the trajectories and this has be discarded from statistics. For simplicity and discussion of the excitation, we normalise this sum to 1. Hence, in this work we consider the excitation to be localised on Ar_{n-m}^* if $p \geq 0.80$, i.e., more than 80% of excitation located on excited atom or cluster and consequently, $q+r \leq 0.20$, i.e., less than 20% of excitation is on other atoms.

The possibility to find the excitation delocalized over a large number of atoms arises when the final adiabatic state is degenerate. This leads to an excitation shared by several states which may yield a delocalization of the excitation over several atoms. This leads to the fragments in all the channels with shared excitation among several species. The existence of fractional excitation is a feature of TSH. Therefore, the

superscripts p, q and r can be thought of as a probability of excitation being localised in three different sub-channels. Consequently, when a measurement is taken the wave function is collapsed on the atom with the highest probability.

Another outcome of this dynamics is the sharing of the excitation by the excimer atoms at infinite distance. This is because of the degeneracy of the states. However, in our simulations, some perturbations are introduced by the presence of another atom which lifts the degeneracy leading to the excitation localisation.

Two atoms are considered to be dissociated if the inter-atomic distance between them is greater than 20 a.u.. This is selected so because the excited excimer has a shallow secondary minimum at long range (≈ 15 a.u.) which can capture a neutral atom.

7.2 Excitation Transfer on Collision in Trimer

We have explored two collision processes for the trimer in collinear geometry. In the first case, an excimer collides with a ground state atom and, in the second case, an excited atom collides with a ground state dimer. This is a test simulation, which is difficult to be done experimentally, however slow collision processes can be thought of as a part of excitation decay and transfer in a cluster where the excitation decay is initiated by the collision. The time scale for the simulations is between 10^5 to 5×10^5 (600-800 fs) with a time-step of 0.5 au (12.5 as). It is important to take a small time-step for proper evaluation of overlap.

Case 1 is presented in Figure 7.1. We start with the excimer distance to be 5.50 au and a ground state placed at 30.00 au approaching the excimer with velocity of 2.74×10^{-3} au. Ar^* is initially in its lowest-energy singlet excited state. 10 trajectories are run from this geometry and we observe the excitation transfer from the excimer to the single atom. The excitation transfer is dependent on the kinetic energy of the collision. In this system, we have high kinetic energy. As we see, after the collision, we observe atomisation. The following figure shows few example PEC and motion of ions associated to this collision process. We see in first example, with high kinetic energy, it is possible to go to a higher excited state. In the other example, we see the excitation being decayed to a lower triplet state.

The second case is presented in Figure 7.2, where a ground state dimer collides with an exited argon atom. The ground state dimer is set at 7.01 au with the excited atom approaching from a distance of 12.00 au with initial velocity of 1.23×10^{-3} au. The initial kinetic energy in this system is lower than the previous case and we can refer to this as slow collision process, with transfer of excitation from the atom to the dimer. This trajectory has a single jump during collision and has a possibility to decay to a lower-energy state, as observed in our discussion of the two-state model in chapter 6. In Figure 7.2, we observe the decay and transfer of excitation from the colliding atom to the atom on the other side leading to formation of two ground state atoms. These 2 atoms have some kinetic energy and might not bind together as a ground state dimer.

In contrast to the previous example at a higher collision energy, we observe most of the trajectories to hop between the degenerate states without going to a lower triplet state.

It is important to note that, both simulations showed us the possible excitation transfer between atoms. This can be associated to the transfer of the excitation from the a-STE to formation of m-STE's and eventual evaporation of atoms observed in experiments.

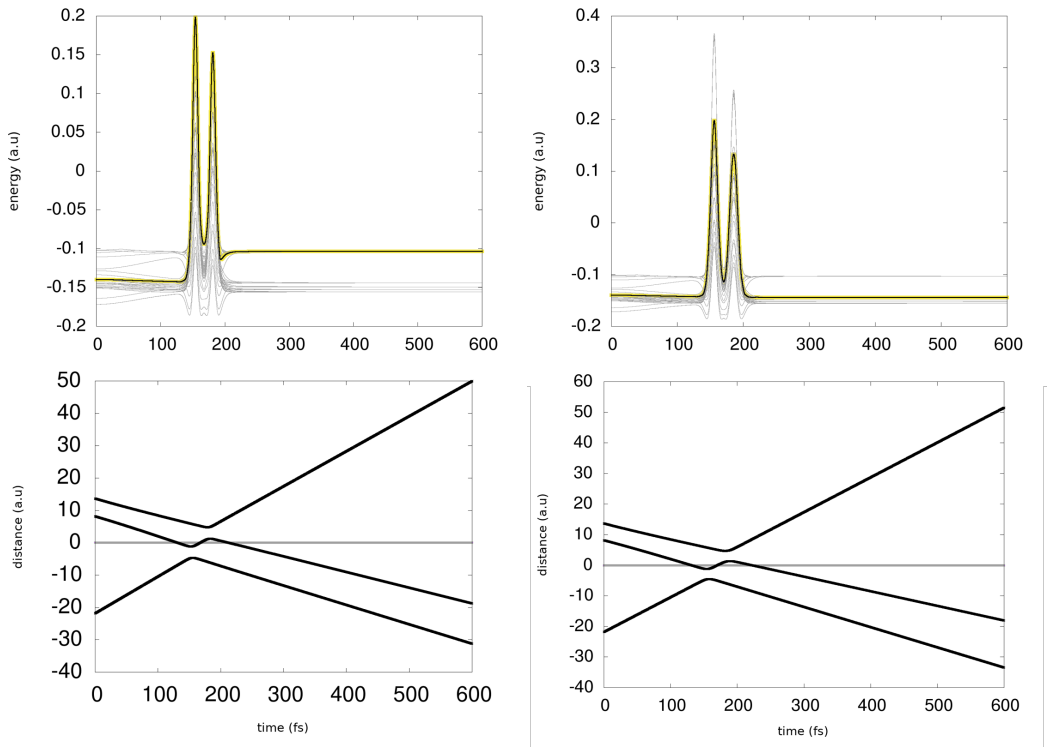

Figure 7.1: PECs and atomic motion for collision of a ground state atom with an excimer at high kinetic energy. Left: excitation to a higher PES Right: decay of the excitation to a lower PES.

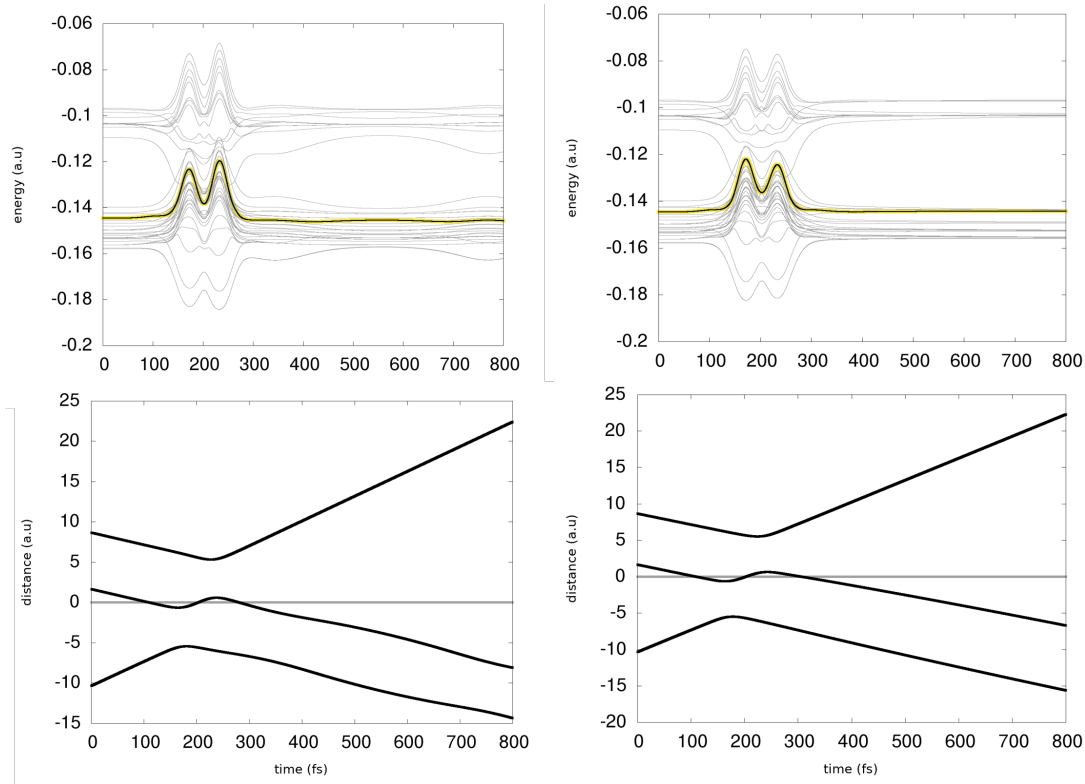

Figure 7.2: PECs and atomic motion for collision of an excited atom with ground state dimer. Left: excitation transfer leading to formation of an excimer. Right: excitation decay during the collision.

7.3 Ar_3^* Fragmentation from ground state geometry

The fragmentation dynamics of the trimer is done starting at a ground state geometry. The cluster is then promoted suddenly to one of the lowest-energy singlet exited state of Ar. There are 16 excited states including the *ad hoc* 4p-states for each atom, making a total of 48 states for Ar_3^*. The choice of the lowest singlet state is not perfectly well defined due to spin-orbit coupling. We consider the starting state #29, which has a 75% of singlet character. The dynamics is followed during 5 ps. We evolve 30 trajectories on the ground state geometry which is thermalised at T=20K for 5 ps initially. This gives possible random initial kinetic energy and position to each atom for these trajectories. We observe the relaxation to the lower triplet states by non-adiabatic couplings associated with spin-orbit couplings.

The possible dissociation channels for a trimer are limited. We have three-body dissociation (atomisation), two-body dissociation and no dissociation. For two-body dissociation, we can distinguish two cases which depend on the nature of the dimer (excited or not). These dissociation channels are:

$$Ar_3^* \rightarrow (Ar^*)^p + (Ar_2)^q \qquad m = 2 \quad l = 0 \tag{7.3}$$

$$Ar_3^* \rightarrow (Ar^*)^p + (Ar)^q + (Ar)^r \qquad m = 2 \quad l = 1 \tag{7.4}$$

$$Ar_3^* \rightarrow (Ar_2^*)^p + (Ar)^q \qquad m = 1 \quad l = 0 \tag{7.5}$$

Figure 7.3 shows the energy of a long lived trajectory with the motion of ions. It can be seen that an atom leaves the cluster in the beginning of dynamics leaving an excimer in a mixed singlet-triplet state up to 2.2 ps. This excimer dissociates by gaining kinetic energy as it goes to the lowest triplet state. This is one of the few trajectories in which we observe formation of an excimer before atomisation. Another example is shown in Figure 7.4b.

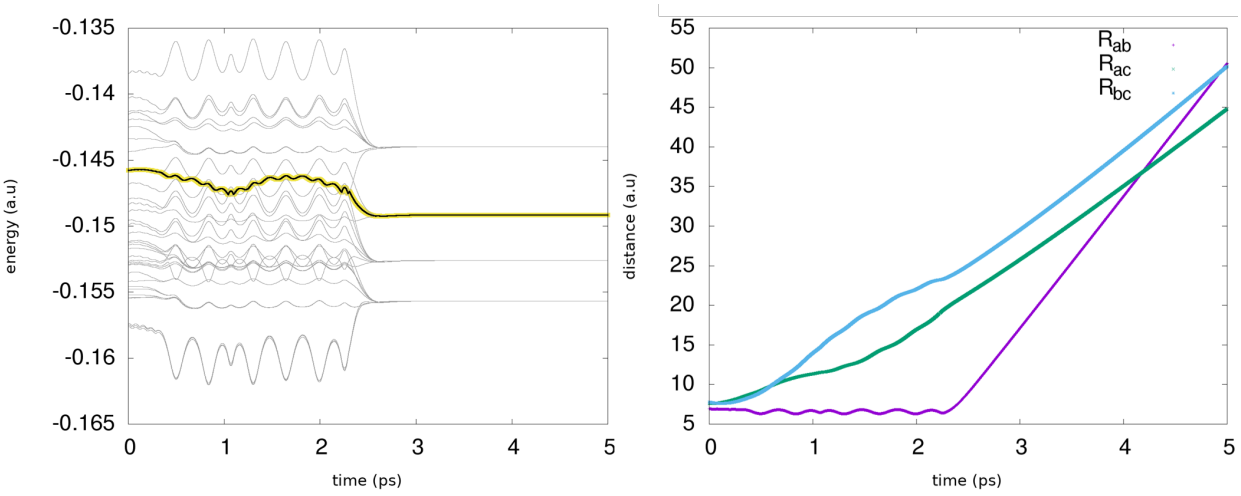

Figure 7.3: An example of a long- lived trajectory in Ar_3^* where R_{ab}, R_{bc} and R_{ac} in right side figure are the interatomic distances.

In Figures 7.4, we give examples of evolution of the system on adiabatic PECs which are presented as black bold and highlighted yellow. We observe 100% of the trajectories leading to atomisation, channel 7.4, with $p > 0.95$ in all the cases. The timescale of dissociation is different due to initial kinetic energies imparted to the atoms. We also observe the decay of excitation to lowest triplet excited state, as shown in Figure 7.4d. This is accompanied by formation of an excimer. However the energy in the system is much higher than excimer binding energy, and it atomises.

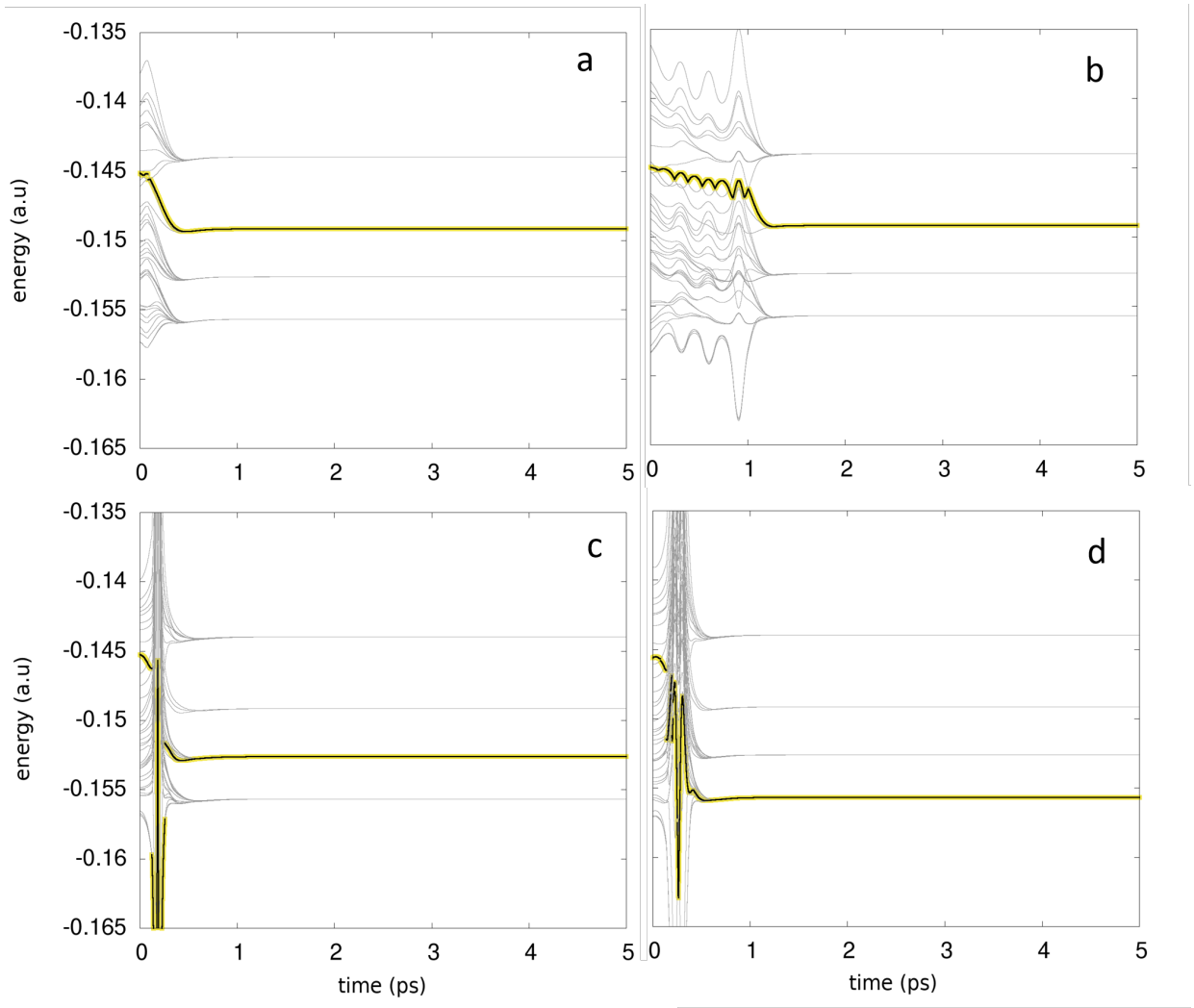

Figure 7.4: Figures (a-d) shows the PEC and trajectory evolution on some of the ground state geometry from the lowest singlet excited state. c and d shows the relaxation of excitation to form excimer which eventually dissociate.

Hence, following our observation, we can say that all the trajectories starting on a lowest-energy singlet excited state at ground state geometry of Ar_3 for small cluster, will eventually lead to the atomisation of the cluster. This is different from the results obtained for Ar^+ where both Ar^+ and Ar^+ fragments can form after atomisation and two-body dissociations, respectively. The excitation relaxation time exceeds 0.5 ps in very few cases.

To supplement the dynamical study on state 29, in few of the trajectories we started from a higher singlet state 35. In this case also observed the atomisation of Ar as well but the trajectories do not relax to a lower triplet state. Unlike ionised clusters, excited neutral clusters are highly unstable. It would be interesting to have some experimental observations to ascertain this conclusion.

7.4 Ar_7^* Fragmentation from ground state geometry

To study the excitation dynamics of Ar_7^* clusters, we proceed as for Ar_3^* clusters. The dynamics start at the cluster ground-state geometry and argon atoms are given an initial kinetic energy of 30 K. There are 16 excited states including the *ad hoc* 4p-states in the atomic basis set, making a total of 112 states for Ar_7^*. We assume instantaneous excitation at this geometry into one of the lowest singlet excited state, which is associated with state 73. This is the lowest-energy singlet state with a singlet character of at least 80%. Initially the excitation is broadly delocalized over the whole cluster. The excitation localisation is also observed to be dependent on the initial geometry. For instance, if couple of atoms are close to each other after the initial thermalisation, they will carry more excitation and if a cluster is formed with a separated atom, the separated atom is observed to have the excitation localisation on that single atom. The dynamics lasts for 5-10 ps with a time step of 0.5 au or 1 au. In the following dynamics, we have 40 trajectories distributed over different types of dissociation channels.

The dissociation channels can be categorised as:

$$Ar_7^* \rightarrow (Ar^*)^p + (Ar_{6-l})^q + l(Ar)^r \qquad m = 6 \tag{7.6}$$

$$Ar_7^* \rightarrow (Ar_2^*)^p + (Ar_{5-l})^q + l(Ar)^r \qquad m = 5 \tag{7.7}$$

$$Ar_7^* \rightarrow (Ar_3^*)^p + (Ar_{4-l})^q + l(Ar)^r \qquad m = 4 \tag{7.8}$$

The weight of the followed state sometimes goes to very small values, i.e., $p+q+r \ll 1$. In such a case, the trajectory is no longer really representative and we discard it (2 such cases of 40). In other cases, as discussed previously, we normalise $p+q+r$ to unity for the analysis.

We obviously do not have a direct comparison with experiment for such a small cluster size. This dynamics is achieved to explore dissociation channels which do not exist when the parent cluster is Ar. Due to limited time, unfortunately, we will not be able to give the statistical analysis of different dissociation channels, but we will discuss the possible dissociation channels and look for the effect of diabatisation.

7.4.1 Dissociation Channel: Atomisation

We start with the channel in which all the atoms blow apart, which is a sub-channel of Eq. 7.6, where $l = 6$ and is given by:

$$Ar_7^* \rightarrow (Ar^*)^p + 6(Ar)^r \tag{7.9}$$

This implies that the excitation is carried by a single atom without formation of any cluster. We observe 21% of the trajectories (8 out of 38) in this channel. We do not expect this percentage to increase significantly with increasing cluster size due to increasing cohesion energy of the ground state atoms. The values of p and r give the excitation distribution over different atoms. This is a channel where the excitation is mostly located on a single atom, ie the non-normalized value of p is more than 0.85. In this case, the excitation relaxes rapidly and the cluster fragments blows apart quickly. The normalised value is always $p > 0.98$.

Some of the trajectories decay rapidly (< 3ps) to a lower triplet state associated to $J = 0$ or 1. An example is shown shown on top of Figure 7.5. Access to low-energy triplet states with $J = 2$ is observed in only one of the trajectory, which is shown at the bottom of Figure 7.5. In this trajectory, as excitation relaxation happens on a cluster of 5 atoms at 4 ps, the atoms gain kinetic energy which is greater than the binding energy of the system, leading to atomisation. This trajectory has few more hops on its way to dissociation. All this happens within a short time of 1 ps. This shows that, as the system gains kinetic

energy, the relaxation dynamics becomes faster.

Besides the rapidly decaying trajectories, few other trajectories are observed to be in highly excited states, which have not relaxed to a lower state. These long-lived trajectories are not registered as atomised in our dynamics interpretation as the inter-atomic distances have not exceeded 20 au. However, following the motion of the trajectories and the observations in PECs associated to these systems, it is evident that they are going to dissociate. They are thus counted in the 22% of atomising trajectories.

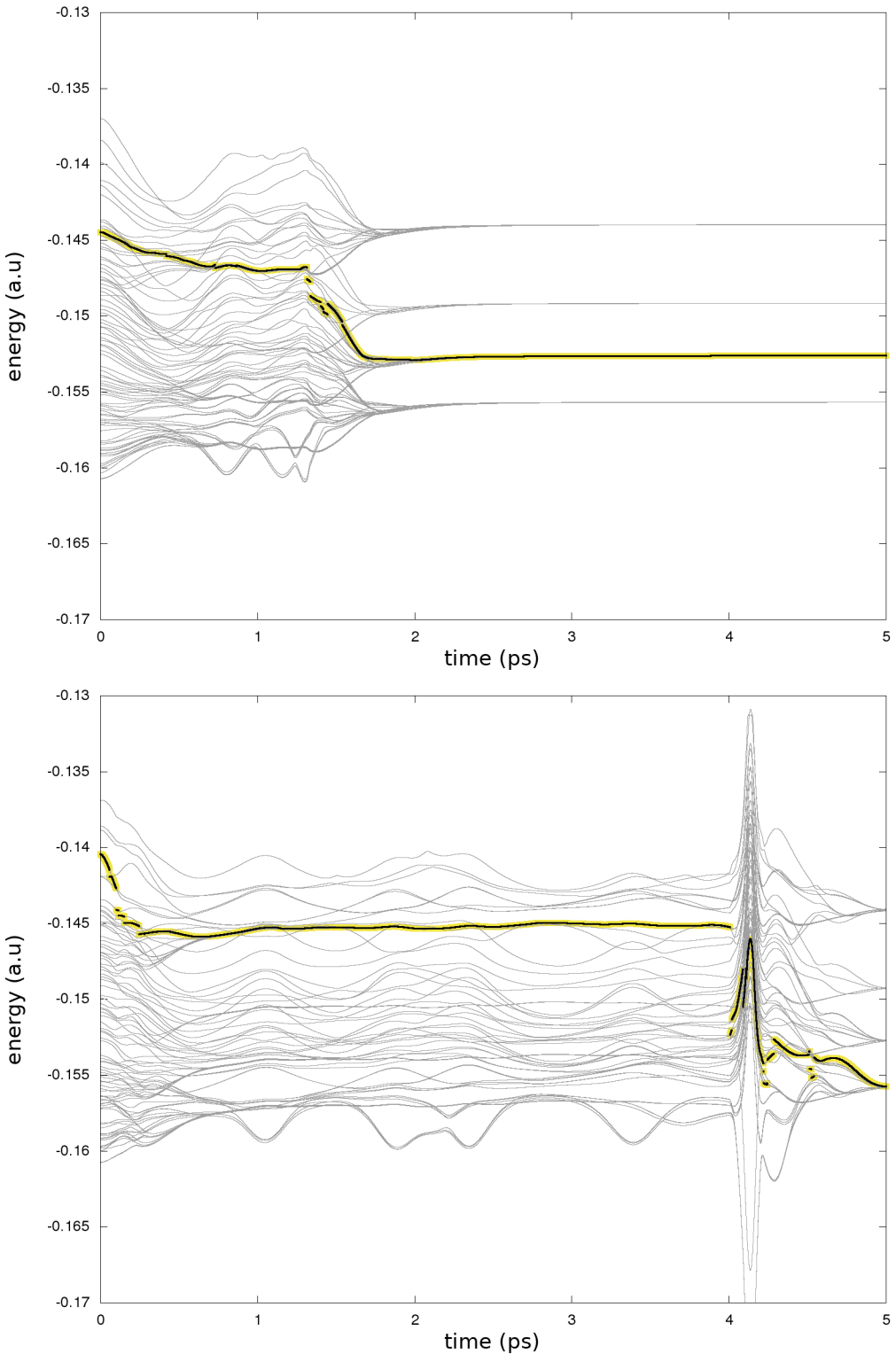

Figure 7.5: TOP: Trajectory (#59) decaying rapidly to the Ar_* dissociation limit with J = 1. BOTTOM: Long lived trajectory (#28) on cluster of atoms before leading to Ar^*, J = 2 dissociation limit.

Atomisation is not expected to be a common dissociation process for larger clusters. The other channels associated to evaporation of ground or excited atoms or clusters are more favourable. This is consistent with the sputtering experiment on large clusters, where they interpret their observation of luminescence as due to emission of excited atoms and excimer [10].

7.4.2 Dissociation Channel: Excited Atom Emission with Neutral Cluster Formation

In this dissociation channel, we look for the emission of an excited atom with formation of a ground state cluster.

The following dissociation channels are sub-channel of 7.6 as well. However, here we have formation of Ar_2, Ar_3, Ar_4 and Ar_5, which are given as;

$$Ar_7^* \rightarrow (Ar^*)^p + (Ar_2)^q + 4(Ar)^r \qquad l = 4 \tag{7.10}$$

$$Ar_7^* \rightarrow (Ar^*)^p + (Ar_3)^q + 3(Ar)^r \qquad l = 3 \tag{7.11}$$

$$Ar_7^* \rightarrow (Ar^*)^p + (Ar_4)^q + 2(Ar)^r \qquad l = 2 \tag{7.12}$$

$$Ar_7^* \rightarrow (Ar^*)^p + 2(Ar_2)^q + 2(Ar)^r \qquad l = 2 \tag{7.13}$$

$$Ar_7^* \rightarrow (Ar^*)^p + (Ar_5)^q + (Ar)^r \qquad l = 1 \tag{7.14}$$

In all the cases we observe normalised p to be greater than 0.70. We observed this dissociation channel in 66% of trajectories (25 out of 38). These trajectories are distributed as follows: 7 with formation of ground state dimer (32%) in channel 7.10, followed by 7 with formation of trimer (32%) in channel 7.11 and 8 (36%) gathering dissociation channels where larger clusters are produced

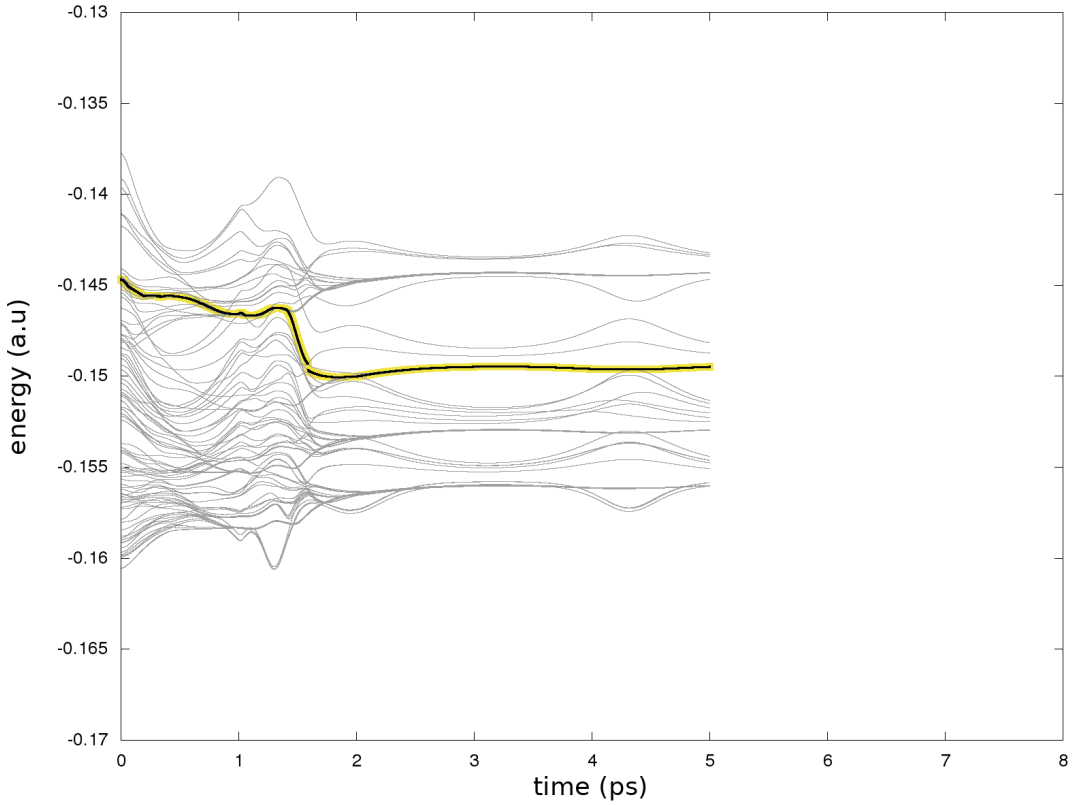

Figure 7.6: The trajectory (#74) leading to formation of $Ar^* + Ar_2 + 4Ar$, with slowly vibrating ground state dimer. This dynamics is performed for 5 ps. *Ad hoc* states are not shown here which are higher in energy. Final state is $J = 0$

As an example, in Figures 7.6 and 7.7, we show the dynamics leading to the formation of a ground state dimer with an evaporating excited atom. Starting from one of the lowest singlet state, the trajectory evolves on a mixture of singlet-triplet states, which then decays into a triplet state. In Figure 7.6, we see the relaxation of the adiabatic state to a $J = 0$ triplet state followed by a hop at 1.7 ps. In Figure 7.7 we observe several hops between 1.7-1.8 ps leading to $J = 2$ triplet state. Following relaxation, kinetic energy is gained by the excited atom, which then evaporates along ground state atoms. In Figure 7.6 we have slow and small amplitude oscillations, while these oscillations are faster and of larger amplitude in Figure 7.7. The difference between the two figures is due to the difference in their internal energy. In Figure 7.6 the system is on excited state 61 and the kinetic energy release in the system is small whereas, in Figure 7.7 the system is on excited state 18 and the kinetic energy release in this system is higher leading to a faster vibrating dimer. In Figure 7.7, following the adiabatic state after the hop, we see negligible oscillations of the current adiabatic state, highlighted in yellow. The small oscillations in the yellow PEC are due to the electronic states of the well separated oscillating ground state dimer while the excitation is carried by one of the leaving argon. For some of the non-followed states (not highlighted in yellow), the excitation is localised on the vibrating dimer, producing slightly larger amplitude in the potential energy periodic variation. We also identify the other excited PECs of Ar^*, highlighted in red at dissociation limit, which are almost parallel to the currently followed adiabatic state after 2.5 ps, during which the excited atom has separated enough and do not interact anymore with the ground state dimer. The PECs of Ar^* beyond 3 ps show the fine structure splitting of triplets for different $J = 0, 1$ and 2 and the singlet states. These PECs also show the excellent treatment of degeneracies in our algorithm.

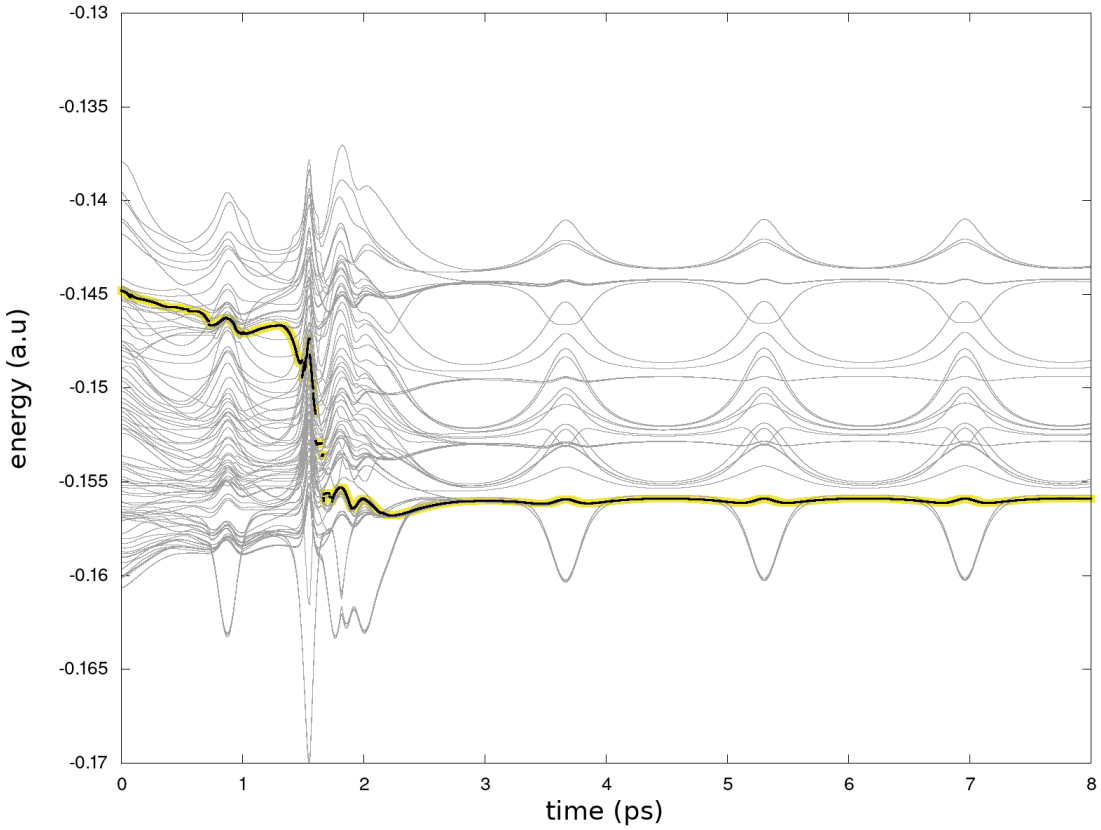

Figure 7.7: The trajectory (#6) on the PEC leading to the formation of a slowly oscillating ground state dimer. This dynamics is performed for 10 ps and we show the first 8 picoseconds. *Ad hoc* states are not shown here which are higher in energy. The highlighted curve represents the 4*s* dissociation limit of the excited atom and the corresponding, almost flat, PEC. the final state corresponds to $J = 2$.

In other situations associated with the formation of larger isolated clusters, we also observe, following relaxation, the excitation to be predominantly localised on an atom. The rearrangements of the cluster are a consequence of its internal energy. This internal energy may lead to the evaporation of several ground state atoms and to the formation of a smaller ground state cluster. The excess energy can also lead to the formation of several neutral clusters, like two argon dimers. This effect becomes significant when the cluster size increases. Furthermore, we observe that the linear momentum of the emitted excited atoms increases when the remaining ground state cluster size increases. This is expected as the kinetic energy is shared between less atoms.

7.4.3 Dissociation Channel: Excimer Emission

Channel 7.7 is associated to the evaporation or separation of an excimer (Ar_2^*) from other atoms in ground state. These ground state atoms can either be dissociating individually or in a form of ground state clusters. We found 16% trajectories (6 out of 38) forming an excimer together with ground-state atoms, produced by atomization, or a ground state cluster. The emission of the excimer with other ground state atoms is similar to atomisation but with an excitation located on the dimer. In our simulations, we observed;

$$Ar_7^* \rightarrow (Ar_2^*)^p + (Ar)^q + 4(Ar)^r \qquad m = 5 \quad l = 4 \tag{7.15}$$

$$Ar_7^* \rightarrow (Ar_2^*)^p + (Ar_{5-l})^q + l(Ar)^r \qquad 1 \leq l < 2 \tag{7.16}$$

Unfortunately, we do not observe excimer associated to the formation of the lowest triplet excited dimer. All the observed excimers are in a high excited state. For most of the trajectories, the dynamics is probably not long enough for them to have relaxed into lower triplet state. Moreover, such a relaxation is likely to break the excimer, thus leading to one of the excited atom channel.

The emission of excimer with formation of a ground state cluster is barely observed, but we observe few trajectories where a ground state cluster is formed alongside an excimer. However, these trajectories are in highly excited states. Nevertheless, this shows the possibility for the formation of ground-state clusters of variable sizes when increasing the system size.

It is important to note that, in the interpretation of the experimental observations, they do not report the excitation to be on three atoms. The identification of such a trimer is possibly quite difficult experimentally.

7.4.4 Using H-DIM

To understand the effect of diabatisation, we explored the same Ar_7^* system while using the dimer PECs which are not diabatised according to section 3.3. Instead, the four lowest-energy PECs built by the H-DIM method for each spin symmetry have been considered. This is associated to H-DIM method used to evaluate *on-the-fly* PES for trajectory evolution. To perform this dynamics, we used 10 trajectories with same initial conditions for the sake of consistency. However, the starting state is not the same since the atomic configuration space is reduced from 16 to 12 as there are no higher ($4p$) state included for each atom. The time limit of the calculation is 5 ps with a time step of 0.5 au. Though the dissociation channels are similar to Di-DIM simulations, we observed different dynamics. The major difference comes from the possibility for a sharing of the excitation among 3 atoms, which is consistent with the conclusions reported by Naumkin and Wales, who explored the lowest-energy triplet PES for the isomer of minimum energy. We did not perform enough statistics to report a reliable distribution of fragmentation channels at the moment.

This calculation was done to get the flavour of the effect of diabatisation on the dynamics. This obviously needs to be investigated in more detail.

Based on our limited observation, we found that the excitation localisation using this method leads to the formation of an excited atom or dimer, but the excitation is more delocalised. The excitation does not localize rapidly on an excimer or an atom as the system evolves. This leads to an excitation being distributed over a greater number of atoms than for Di-DIM simulations. In the dissociation channel, though the excitation is located on a single atom, almost 80% of excitation is spread over other adiabatic states. For example, in one of the trajectories, we observe the excitation to be on state 40, which is a triplet state, localised on a single atom. Though all the excitation in this state is being carried by this single atom, the value of un-normalised p is only 21% of the starting population is in this state. This means that the population does not tend to concentrate on a single adiabatic, as for Di-DIM.

7.4.5 Summary

With the Ar_7^* relaxation dynamics we explored several dissociation channels, which were previously unavailable in trimer simulation, then extending our study of the argon trimer. In this dynamics simulations, the main dissociation channels are the emission of either an excited atom , the formation of an excimer or both of them. They can either be accompanied by atomising ground state atoms or formation of smaller ground state clusters or both. We were able to explore all these cases. The results are presented in table 7.1. 84% of trajectories leads to the emission of excited argon atom and this is a mixture of sub-channels and different types of atoms. Among these 84%, the complete atomisation of the cluster represent 21% of the trajectories. The emission of excited atoms accompanied by ground-state clusters composed of 2 to 5 Ar atoms is also found. This represents the majority of trajectories.

The remaining 15% of the trajectories correspond to the formation of an excimer. In most of the trajectories, the excimer is emitted with other ground state atoms. However, the system does not decay to lower-energy triplet states after 5 ps.

Table 7.1: Distribution of Ar^* dissociation channels. 38 trajectories using Di-DIM parametrisation have been run.

Dissociation Channel		Number or trajectories	Total
Atomisation	$Ar^* + 6Ar$	8	
Excited Atom: 1	$Ar^* + Ar_2 + 4Ar$	7	
Excited Atom: 2	$Ar^* + Ar_3 + 3Ar$	7	
Excited Atom: 3	$Ar^* + Ar_4 + 2Ar$	5	
Excited Atom: 4	$Ar^* + Ar_5 + Ar$	4	
Excited Atom: 5	$Ar^* + 2Ar_2 + Ar$	1	32
Excimer: 1	$Ar_2^* + 5Ar$	2	
Excimer: 2	$Ar_2^* + Ar_4 + Ar$	2	
Excimer: 3	$Ar_2^* + Ar_3 + 2Ar$	2	6

It is also instructive to explore the relaxation by having just singlet states in the system. Thus, we removed the possibility for singlet and triplet mixing. The PES are slightly different and the hopping probability among the adiabatic states is reduced. By keeping only singlet states, we observed that the system atomizes with excitation localising on one of the dissociating atom. Since we only have non-adiabatic non-

adiabatic couplings and not the spin-orbit couplings, fewer hops occur. When a non-adiabatic hop occurs, it imparts kinetic energy which leads to atomisation, as the trajectories are not binding in high singlet state. By starting lower-energy excited state, the system relaxes to a lower-energy state but not to the lowest-energy excited state within the 10 ps in the dynamics. This implies that the relaxation dynamics is slower without spin-orbit coupling. Starting on a lower singlet state, we observe the formation of some ground state clusters but no bound excimers. Using pure triplet states instead of singlet states in the simulations yields similar conclusions. These results are similar to the case of full configuration basis including both singlet and triplet states.

The system starts close to its ground state geometry with some initial random kinetic energy. The corresponding atomic momenta are not sufficient to enable efficient non-adiabatic dynamics. Therefore, the population spreads among many nearly degenerate states, but we do not observe the energy relaxation towards adiabatic states significantly lower in energy. If we increase the temperature of the system, it might be possible to observe more hops and thus faster relaxation.

These simulations are qualitative and give us the flavour of excitation dynamics using our algorithm. Nevertheless, even in this minimum simulation, we modeled dissociation processes observed in sputtering experiments. We observe the localisation of excitation on the excimer which was previously not done. We also proved the possibility for evaporation of excited atoms and formation of excimers.

Part III

Conclusion

Chapter 8

Conclusion and Prospects

8.1 Conclusion

In this thesis, we began by studying the electronic structure of the excited argon dimer (excimer) and trimer using *ab initio* calculations with the MOLCAS quantum chemistry code. We find that the *ab initio* PECs of Ar_2^* are not trivial to evaluate. The RASSCF calculation lacks dissociation energy, as these calculations miss dynamical correlations and therefore, the obtained binding energy of the rare-gas systems is insufficient. The PECs obtained using the CASPT2 method are limited by the perturbative treatment of the crossings and root flipping in the reference space due to the high degeneracy of the states. Finally, the PECs obtained by MRCI calculations are limited because of the computational limitations of the MOLCAS quantum chemistry code. However, despite these limitations, it was possible to obtain the best Ar_2^* PECs for the four lowest $4s$ excited states in each symmetry group using the MRCI method until now. Despite our best efforts, we were unable to determine higher excited states using MRCI with MOLCAS. They are better than previous CI-based calculations [31], thanks to the use of a large basis set. In our attempt to use *ab initio* methods to determine the lowest energy isomer corresponding to Ar_3^*, we conclude that; 1) The reliability of MRCI calculations performed with MOLCAS was restricted by computational limitations posed by the large configuration space. 2) Using RASSCF, we could perform trimer calculations, but they are not very informative due to missing dynamical correlations. 3) Using CASPT2, we were able to perform trimer calculations as well, but due to crossings in the reference states, undesired jumps due to intruder states and the inability of MOLCAS to perform C_∞ symmetry calculations properly, we were unable to ascertain the lowest excited trimer isomer for Ar. However, using CASPT2, we found that the minimum isomer is perhaps not linear symmetric as previously calculated using DIM in the literature [74]. *Ab initio* calculations for larger systems were not performed due to limitations of quantum chemistry codes. Therefore, we need to use an approximate method to further explore the lowest energy isomers.

Due to the limitations of DIM and the success of the HPP semi-empirical method, we were motivated to use the latter to study excited Argon clusters further. Using HPP we evaluated Ar_2^* PECs, which we show to be in close agreement with our MRCI calculations. As in the original work by Duplaa and Spiegelmann [48], we obtained high excited states, which are difficult to obtain with *ab initio* methods. However, we noted some discrepancies, like a deviation from MRCI dissociation energies of triplets and incorrect multiple splitting of the singlets in the excimer PECs. However, this is not important for determination of the lowest energy isomer. Using this method, we were also able to ascertain that the lowest energy isomer of the trimer was linear asymmetric $C_{\infty h}$, as obtained in CASPT2 calculations. We found that the triangular-shaped trimer

C_{2v} corresponds to a saddle point and the linear $D_{\infty h}$ geometry is unstable. Using DIM, in previous studies (noted as N-DIM), the linear $D_{\infty h}$ was the minimum and the asymmetric $C_{\infty h}$ isomer was not observed. We obtain the same results by using better PECs to parametrise the DIM, noted as H-DIM. Therefore, the quality of PECs did not influence the results. The geometry of the lowest-energy isomer is important, as the trimer sets the basis for most of the bigger lowest-energy isomers. We proposed an improvement to the DIM model, noted as the Di-DIM, where we introduced an *ad hoc* state to restore the Σ_g^+ states couplings, which was not done in previous DIM studies of excited Ar clusters. Using this Di-DIM model we show the relevance of diabatisation. We show that the coupling for Σ_g^+ PECs comes not only from previously anticipated dominant single $4p$ states but from several higher states making it harder to recover. With the introduction of this *ad hoc* state, we observed the symmetry breaking (lowering) from $D_{\infty h}$ to $C_{\infty h}$, as observed in HPP and CASPT2 for the lowest-energy isomer of Ar_3^*. The linear $D_{\infty h}$ geometry is unstable. However, as obtained in previous N-DIM calculations, we observed C_{2v} triangular-shaped isomer to be a local minimum while it is a saddle in HPP. This suggests improving the Di-DIM model by expanding the configuration basis set to include all the $4p$ states with their relevant couplings. This, however, proved to be a difficult task as it is not easy to identify well-defined diabatic states.

Furthermore, we investigated the excited states of neutral Ar_N clusters for $N = 2-13$ using the HPP and Di-DIM methods. The HPP method represents clear progress to any DIM model as it uses an explicit representation of the Rydberg orbitals and allows us to take into account efficiently and consistently highly-excited states near the ionisation threshold. Our study of the lowest excited triplet state geometries shows that the Ar_N clusters relax to form an excimer in between two inactive atoms in their ground state. This is in agreement with the N-DIM model. Wherein most of the geometries obtained with the HPP model for the lowest-excited triplet state can be described as an Ar_{N-2} cluster in its electronic ground state geometry bound to a protruding excimer. The excitation is localised on the protruding excimer and is, in most cases, associated with a significant electric dipole. This signs the transfer of electronic density out of the cluster and in the direction of the protruding dimer. We observed a single exception to this general behaviour, for $N = 4$ lowest energy isomer, for which the excimer is found between two inactive atoms.

While exploring the lowest energy isomers with Di-DIM for $N = 2-15$ we observed that the excitation was being localised on the protruding dimer, as observed in the lowest-energy isomers obtained using the HPP model. However, the geometry associated with the lowest energy isomers is not the same as obtained using the HPP model. We further observed a symmetry breaking of HPP lowest energy isomers, where the excimer attached to the ground state cluster is observed to be tilted. The isomers from Di-DIM are observed to be mixtures of both N-DIM and HPP ones. We also observed the exception for $N = 4$ in Di-DIM, like for HPP isomer. However, the Di-DIM isomer is linear asymmetric rather than $D_{\infty h}$ symmetric like HPP. This isomer does not exist in N-DIM. However, Di-DIM is limited due to the lack of possibility to include dipole-moment and higher excited states.

The analysis of the electronic ground state equilibrium geometry shows that the lowest excited states are degenerate and the holes are distributed among the cluster atoms. The ground state absorption spectrum shows a well-defined transition associated with the $4s$ configurations, whose energy around 11.8 eV does not depend significantly on the cluster size. The higher excited configurations mix together to form a much broader absorption band below the ionisation threshold. When the cluster size increases, the oscillator strength intensity increases progressively above 13 eV. This is consistent with the assignment of the 1 and 2 surface exciton bands observed experimentally [54, 160]. A direct comparison is however difficult as we would need the size and isomer distribution as well as their vibrational excitation distribution. For a direct

comparison with experimental results for solid argon, the HPP model might however be used in combination with the embedded cluster method to study bulk excitons.

The luminescence of the lowest-energy triplet state depends weakly on the cluster size, and the transition energy is quite comparable to the transition energy of the dimer. The existence of a stable geometry structured around an excited dimer strongly supports the various models and interpretations based on the assumption that the exciton relaxes toward the formation of an embedded excited dimer. For better understanding, it is imperative to perform a dynamical study of excitation relaxation on such clusters. The HPP model is certainly a reasonable method, though cumbersome, to develop such a numerical molecular dynamics simulation.

Embedded stable isomers observed using HPP and Di-DIM are either in a local minimum or on a saddle, which eventually will relax to form an excimer at the surface. As we are limited by the cluster size that can be explored using the HPP method, typically 13 atoms, we can not say it is inconceivable to have an embedded excited isomer in its lowest triplet state. However, using the Di-DIM method, we explored Ar^*_{55}, where we observed the lowest triplet excited state isomer to have an excimer attached to the rest of the neutral ground state cluster, similar to smaller clusters. The MD simulation is inaccessible using the HPP model presently due to the large configuration space and computational cost. Though currently not fully transferable from the HPP model, the Di-DIM method offers the possibility for dynamics as it retains the important characteristics of excitation localisation on the dimer as the HPP method does.

Using Di-DIM with spin-orbit couplings, we performed the mixed quantum-classical dynamics of clusters initially prepared in their ground state geometry and excited in the lowest-energy singlet excited state. The wave-packet propagation is achieved within the interaction picture. We introduced improvements to the propagation algorithm by reducing the perturbation using the average Hamiltonian approach. In doing so, we eliminated the fast electronic oscillations in the wave-packet propagation as we integrated analytically over a small time step. Small time-step and small perturbations lead to smooth evolution of the adiabatic population over the nuclear motion, without losing the phase. The coefficients are propagated in an arbitrary basis-set for each nuclear time-step before being projected to get the adiabatic population of the present state. The nuclei propagation uses the Beeman algorithm. The forces are calculated analytically. A simple state flipping algorithm is used, which evaluates self-overlap to follow the desired trajectory across non-avoided crossings. Fewest Switches Surface Hopping (FSSH) algorithm is used for avoiding crossings. Using this algorithm, we performed long dynamics, usually 10ps, despite a small time-step. Typically, the time-step used is 10as. This time step can be further increased or reduced with the possibility of making the dynamics faster or slower depending on the system.

This propagation algorithm is validated by a set of separate calculations performed on *Mathematica* [154] for Ar_2*. For such a cluster, it was possible to reduce the 12-state problem to a 2-state problem, a singlet and a triplet with spin-orbit couplings. The agreement between our model and Mathematica calculations for small time steps is remarkable. Based on this validation, we did preliminary dynamics on small-size clusters to check for the stability of our algorithm. We found that it is essential to keep the time-step small to avoid artefacts when integrating differential equations. We successfully showed the transfer of excitation and its dependence on the kinetic energy in the trimer system. We also showed the relaxation and transfer of excitation from a single excited atom to the ground state dimer leading to an excimer.

We also observed that, for a trimer at its ground state geometry prepared in its lowest singlet excited state, there is complete dissociation due to an excess of kinetic energy. This shows that a high excited state can not exist for a long time in a trimer and as it relaxes to a lower triplet state, the kinetic energy gained

by the atoms is much higher than the binding energy of the excimer. Over a time scale of 5 ps, we observed short (<1 ps) and medium (<3 ps) lived trajectories depending on their initial linear momentum, however, they all atomise before 3 ps.

To explore different dissociation channels we simulated the excitation relaxation in the Ar_7^* cluster. We started from their ground state geometry and prepared the cluster in its lowest singlet excited state, mimicking a cluster obtained by photo-excitation. Similar to Ar_3^*, this is not a pure singlet state. The relaxation of this system gives a deeper insight into the dynamical process involved and opens the way for exploring other dissociation channels. We observe three major channels among 38 trajectories; 1) complete atomisation of the ground state cluster noted in 21% of the trajectories, 2) separation or emission of an excimer from the ground state cluster is observed in 15% trajectories and 3) production of an excited atom together with a ground state cluster is the main dissociation channel and occurs in 66% of the trajectories. The main relaxation channel is thus the formation of Ar^* (85%), which dominates the observation of Ar_2^* (15%). We observed the formation of larger excited clusters in only a couple of trajectories in our 5-10 ps dynamics. They are unstable as they are in highly excited states, which would eventually lead to the formation of an excimer with emission of ground-state atoms or to the formation of small ground-state clusters with emission of excited or ground-state atoms. Therefore, the energy brought into the cluster by excitation is too large to maintain the cohesion of more than 2 atoms for the small clusters (N=7) investigated here. Hence, we do not observe any stable clusters bigger than a dimer carrying the excitation after relaxation. For a trajectory living in a highly excited state on a small cluster, the atomisation of the cluster is imperative.

In this work, we showed that excitation relaxation leading to dissociation can happen at the beginning of the dynamics or can last for more than 10ps depending on the initial motion of the nuclei. We find that the 5-10 ps time scale is insufficient for the relaxation of the current followed adiabatic states towards the lower energy states due to weak non-adiabatic couplings in the system coming from the kinetic coupling.

Even for small clusters like Ar_7^*, the density of states is high, and there are many degenerate or nearly degenerate adiabatic states. Due to this high degeneracy, we observe the distribution of population among many adiabatic states in the course of relaxation.

In our minimum dynamics on a small cluster ($N=7$), we noted the localisation of the excitation on an excimer or an atom in the beginning of the dynamics, i.e. within first few picoseconds. This observation is consistent with a previous experimental interpretation given by Moller *et al.* [51, 54, 160] and also by Lietard *et al.* [10] for Argon clusters. This is also consistent with the experimental work on solid argon by Riemann *et. al* [65, 66], who reported the formation of these excited species. They do not give any information about Ar_3^* or any other bigger excited cluster, which is probably very difficult to observe as excitation localises rapidly on an atom or an excimer.

We also illustrated the role played by diabatisation in dynamics by comparing the H-DIM and Di-DIM model dynamics results for Ar_7^* with the same initial conditions. Investigating $Ar_{7}*$ clusters, we found that the dissociation channels for dynamics using both models were similar. However, we observed the excitation localisation on three atoms when using the H-DIM model, which is not observed in the Di-DIM model. In H-DIM, the formation of an excimer is scarce and we might expect, for larger parent clusters, that proportion of excimer or bigger excited clusters would be much lower in H-DIM than in Di-DIM. Thus, the nature and the number of states used to parametrise the DIM model influences the outcome of the relaxation dynamics.

8.2 Future Work

Though we used MOLCAS to perform *ab initio* PEC calculations, the limitations posed to performing MRCI calculations confined our ability to obtain the excimer potential energy curves. It would be highly desirable to perform better CI calculations to determine the excited rare-gas PECs for a larger number of configurations as necessary for trimer calculations. However, these calculations will always be limited by the number of atoms and the correlated electrons.

HPP is a lucrative alternative to *ab initio* methods for the calculation of potential energy curves of rare-gas systems up to a few tens of atoms. It also has the potential to be used in dynamical simulations with *on-the-fly* evaluation of the PES. However, this method still has some challenges to be resolved before it can be used in dynamical simulations. As we observed during our presentation of Ar_2^* results, the 4p ^{1}S state asymptote is misplaced. We speculated this to be due to the approximate representation of exchange, whose accuracy is limited as we neglect the orthogonality between 3p and 4p orbitals. Moreover, as we use the same set of atomic Rydberg orbitals to define the singlets and triplets, the dissociation energy of the singlet and triplet lowest excited state ($^{1,3}\Sigma_u^+$) is very similar, and it is not the case in MRCI calculations. Although these do not play a significant role in this work, it would be imperative to resolve these issues to make the HPP method more robust.

The work in this thesis has provided a gateway to further possibilities for using the HPP method. It would be interesting to use the HPP model to study species other than rare-gas clusters to obtain PES of complex systems, like Alkali Halides salts, which resemble the rare-gas solids.

To use HPP as *on-the-fly* electronic structure calculation method, we need to make further simplifications to the model. For example, reducing the configuration space associated with each atom after formation and identification of the excimer in the system. I.e., after identifying the atoms on which the excitation localises, the large Rydberg basis-set is not particularly essential for all the other atoms. The remaining atoms can now be assigned to be in ground state. Furthermore, a better pseudopotential, which would describe more accurately the interaction of the Rydberg electron with the ionic and ground-state atoms would help speed the calculations and provide better results.

We also show the importance of couplings between the lowest Σ_g^+ states and the higher states when we implemented them in DIM and how important it is to have diabatic states. However, selecting an *ad hoc* state is not the best approximation. Therefore, it is imperative to formulate a method to determine the true nature of such a state, which would constitute the characteristics of all the higher missing states. To better understand the excitation migration through the cluster, it is important to have a correct representation of higher states and their associated couplings.

The dynamics algorithm proposed in this thesis is elementary, i.e., it is perfectly unitary and is not very well polished and is relatively inefficient. In future, there are various opportunities for technical improvement which would make this algorithm fast and efficient. Rather than diagonalisation of exponent, which is computationally expensive, it would be favourable to use an alternative or approximate unitary operator. By doing so, we expect to speed up the evaluation of the electronic motion propagator without compromising the accuracy of the analytical integration used in this work. Some of the techniques would involve, for example, separation of the nuclear and electronic time-step and more efficient diagonalisation strategies. For bigger clusters, having an adaptive time-step is desirable. It would be interesting to explore the possibility of evolving the wave-packet on multiple adiabatic states with a multiple spawning method.

The initial motivation of this work was to simulate the dynamics of the excitation in *picosecond* regime in $4p-4s$ excited states. However, due to challenges posed on the way, we were only able to implement it

for the $4s$ excited state which gave us the flavour of the end of dynamics. It would be possible to perform the dynamics of $4p$ and higher-energy states with HPP if we could speed it up or by including $4p$ states and their couplings in DIM. Both methods are not easy but are possible to implement and can be done to extend this work further.

Our dynamic model can be extended to study sputtering experiments and the dissociation of larger clusters. For Ar_7^* dynamics, we observed that the formation of excimers and ground state clusters concerned almost 85% of the dissociated fragments. Expecting, with increasing cluster size, bigger excited and ground state clusters. The observation of excitation migration in clusters bigger than 50 atoms is still going to be a challenge. This can probably be simulated by using an embedded cluster method, where the surrounding atoms are fixed in their ground state. Doing such dynamics, we could observe the migration of embedded excitation to the surface which might evaporate or lead to the formation of a self-trapped exciton.

Acronyms

a-STEs Atomic type Self-Trapped-Excitons

BOA Born-Oppenheimer Approximation

CASPT2 Complete Active Space Perturbation Theory 2

Di-DIM Diabatized-DIM

DIM Diatomics-In-Molecules

FCC Face-Centered-Cube

FE Free Exciton

FSSH Fewest Switching Surface Hopping

HOMO Highest Occupied Molecular Orbitals

HPP Hole-Particle Pseudopotential

LUMO Lowest Unoccupied Molecular Orbitals

m-STEs Molecular type Self-Trapped-Excitons

MQCD Mixed Quantum Classical Dynamics

MRCI Multi Reference Configuration Interaction

PECs Potential Energy Curves

RGC Rare Gas Clusters

SOC Spin-Orbit-Coupling

STEs Self-Trapped-Excitons

Bibliography

[1] Mukul Dhiman, Julie Douady, and Benoit Gervais. Geometry, absorption and luminescence of small Ar clusters. *Molecular Physics*, page e2049905, 2022.

[2] J Frenkel. On the transformation of light into heat in solids. I. *Physical Review*, 37(1):17, 1931.

[3] Guglielmo Lanzani. *The photophysics behind photovoltaics and photonics*. John Wiley & Sons, 2012.

[4] T Förster. Zwischenmolekulare energiewanderung und fluoreszenz. *Annalen der physik*, 437(1-2):55–75, 1948.

[5] David L Dexter. A theory of sensitized luminescence in solids. *The journal of chemical physics*, 21(5):836–850, 1953.

[6] Bernard Valeur and Mário Nuno Berberan-Santos. *Molecular fluorescence: principles and applications*. John Wiley & Sons, 2012.

[7] Rajesh Kancherla, Krishnamoorthy Muralirajan, Arunachalam Sagadevan, and Magnus Rueping. Visible light-induced excited-state transition-metal catalysis. *Trends in Chemistry*, 1(5):510–523, 2019.

[8] Hohjai Lee, Yuan-Chung Cheng, and Graham R Fleming. Coherence dynamics in photosynthesis: protein protection of excitonic coherence. *Science*, 316(5830):1462–1465, 2007.

[9] Volkhard Helms. *Principles of computational cell biology: from protein complexes to cellular networks*. John Wiley & Sons, 2018.

[10] Aude Lietard, Giovanni Piani, Marc Briant, Marc-André Gaveau, Sylvain Faisan, Vincent Mazet, Benoît Soep, Jean-Michel Mestdagh, and Lionel Poisson. Self-trapping relaxation decay investigated by time-resolved photoelectron spectroscopy. *Physical Chemistry Chemical Physics*, 20(16):11206–11214, 2018.

[11] RE Johnson and Mitio Inokuti. Electronic relaxation in rare-gas solids: Ejection of atoms by fast charged particles. *Nuclear Instruments and Methods in Physics Research*, 206(1-2):289–297, 1983.

[12] Shengting Cui, R. E. Johnson, and P. T. Cummings. Ejection of atoms upon self-trapping of an atomic exciton in solid argon. *Physical Review B*, 39(13):9580–9583, May 1989.

[13] S. T. Cui, R. E. Johnson, C. T. Reimann, and J. W. Boring. Ejection of excimers from the surface of solid argon upon exciton self-trapping. *Physical Review B*, 39(16):12345–12348, June 1989.

[14] E Roick, R Gaethke, P Gurtler, T O Woodruff, and G Zimmerer. Observation of surface-sensitive luminescence in solid argon; relation to self-trapping and relaxation of excitons. *Journal of Physics C: Solid State Physics*, 17(5):945–954, February 1984.

[15] K. S. Song and Richard T. Williams. *Self-Trapped Excitons*, volume 105 of *Springer Series in Solid-State Sciences*. Springer Berlin Heidelberg, Berlin, Heidelberg, 1996.

[16] Irene Ya Fugol'. Excitons in rare-gas crystals. *Advances in Physics*, 27(1):1–87, 1978.

[17] R.S. Knox. *Theory of Excitons*. Solid state physics: Supplement. Acad. Press, 1972.

[18] Gregory H Wannier. The structure of electronic excitation levels in insulating crystals. *Physical Review*, 52(3):191, 1937.

[19] John Dalton Wright. *Molecular crystals*. Cambridge University Press, 1995.

[20] Martin Pope and Charles E. Swenberg. Electronic Processes in Organic Crystals and Polymers. 1999.

[21] Dieter Seebach, Bernhard Seuring, Hans-Otto Kalinowski, Winfried Lubosch, and Bernd Renger. Synthesis and determination of the absolute configuration of pyrenophorin and vermiculin. *Angewandte Chemie International Edition in English*, 16(4):264–265, 1977.

[22] I.Ya. Fugol'. Free and self-trapped excitons in cryocrystals: kinetics and relaxation processes. *Advances in Physics*, 37(1):1–35, February 1988.

[23] Emmanuel I Rashba and MD Sterdzha. Excitons. *Moscow Izdatel Nauka*, 1985.

[24] Lord Rayleigh. Observations on the band spectra of mercury. *Proceedings of the Royal Society of London. Series A, Containing Papers of a Mathematical and Physical Character*, 119(782):349–357, 1928.

[25] Robert S Mulliken. Potential curves of diatomic rare-gas molecules and their ions, with particular reference to Xe_2. *The Journal of Chemical Physics*, 52(10):5170–5180, 1970.

[26] Gerhard Herzberg. Molecular spectra and molecular structure. Vol. 1: Spectra of diatomic molecules. *New York: Van Nostrand Reinhold*, 1950.

[27] James S Cohen and Barry Schneider. Ground and excited states of Ne_2 and Ne_2^+. I. Potential curves with and without spin-orbit coupling. *The Journal of Chemical Physics*, 61(8):3230–3239, 1974.

[28] Barry Schneider and James S Cohen. Ground and excited states of Ne_2 and Ne_2^+. II. Spectroscopic properties and radiative lifetimes. *The Journal of Chemical Physics*, 61(8):3240–3243, 1974.

[29] Roberta P Saxon and Bowen Liu. *Ab initio* calculations of the $^3\Sigma_g^+$ and $^3\Sigma_u^+$ states of singly excited Ar_2. *The Journal of Chemical Physics*, 64(8):3291–3295, 1976.

[30] MC Castex, M Morlais, F Spiegelmann, and JP Malrieu. Comparison between experimentally and theoretically determined potential curves of the Ar_2^* lowest states. *The Journal of Chemical Physics*, 75(10):5006–5018, 1981.

[31] F Spiegelmann and FX Gadea. Calcul théorique en couplage Λ-Σ du spectre électronique des excimères Ar_2 et Kr_2 corrélé aux configurations atomiques $np^5(n+1)s$ et $np^5(n+1)p$. *Journal de Physique*, 45(6):1003–1023, 1984.

[32] JH Yates, WC Ermler, NW Winter, PA Christiansen, YS Lee, and Kenneth S Pitzer. Ab initio potential energy curves for the low-lying electronic states of the argon excimer. *The Journal of chemical physics*, 79(12):6145–6149, 1983.

[33] Yoshihiro Mizukami and Hiroshi Nakatsuji. Potential energy curves of the ground, excited, and ionized states of Ar_2 studied by the symmetry adapted cluster-configuration interaction theory. *The Journal of chemical physics*, 92(10):6084–6092, 1990.

[34] P Duplàa and F Spiegelmann. A pseudopotential hole-particle treatment of neutral rare gas excimer systems. I. Formalism. *The Journal of chemical physics*, 105(4):1492–1499, 1996.

[35] W Beall Fowler. The Use and Misuse of Models in the Calculation of Energy Levels in Insulators. *Vacancies and Interstitials*, page 115, 1966.

[36] S. D. Druger and R. S. Knox. Theory of Trapped-Hole Centers in Rare-Gas Solids. *The Journal of Chemical Physics*, 50(8):3143–3153, April 1969.

[37] K. S. Song. Calculation on the Self-Trapped Hole in Solid Argon. *Canadian Journal of Physics*, 49(1):26–33, January 1971.

[38] Masakatsu Umehara. Theory for self-trapped holes in rare-gas solids. I. Formalism and result for solid argon. *Physical Review B*, 33(6):4237, 1986.

[39] Yoshio Tanaka. Continuous emission spectra of rare gases in the vacuum ultraviolet region. *JOSA*, 45(9):710–713, 1955.

[40] PG Wilkinson. The mechanism of the argon emission continuum in the vacuum ultraviolet. I. *Canadian Journal of Physics*, 45(5):1715–1727, 1967.

[41] Marshall L Ginter and J Gary Eden. Rydberg states of the rare gas dimers. *Canadian Journal of Chemistry*, 82(6):762–778, 2004.

[42] KP Killeen and JG Eden. Observation of ns $^3\Sigma_u^+$ $(1_u, 0_u^-) \rightarrow mp\ ^3\Pi_g$ Rydberg transitions of Ar_2 (n= 4; 5$\leq$ m$\leq$ 15) and Kr_2 (n= 5; 6$\leq$ m$\leq$ 16) in absorption. *The Journal of chemical physics*, 83(12):6209–6218, 1985.

[43] KP Killeen and JG Eden. Gerade Rydberg states and ns $3\Sigma_u^+$ $(1_u, 0_u^-)$ photoionization spectra of the rare gas dimers ($n = 2-6$). *The Journal of chemical physics*, 84(11):6048–6074, 1986.

[44] Gerhard Herzberg. Rydberg molecules. *Annual review of physical chemistry*, 38(1):27–56, 1987.

[45] DJ Kane, SB Kim, DC Shannon, CM Herring, JG Eden, and ML Ginter. Rydberg states of the Ar_2 molecule. *The Journal of chemical physics*, 96(9):6407–6422, 1992.

[46] CM Herring, SB Kim, JG Eden, and ML Ginter. Rotational analysis of the 7 p σ $^3\Sigma_g^+ \leftarrow$ a $^3\Sigma_u^+$ system of the Ar_2 molecule. *The Journal of chemical physics*, 101(6):4561–4571, 1994.

[47] PR Herman, PE LaRocque, and BP Stoicheff. Vacuum ultraviolet laser spectroscopy. V. Rovibronic spectra of Ar_2 and constants of the ground and excited states. *The Journal of chemical physics*, 89(8):4535–4549, 1988.

[48] P. Duplàa and F. Spiegelmann. A pseudopotential hole-particle treatment of neutral rare gas excimer systems. II. the Rydberg states of the Ar_2^* dimer. *Journal of Chemical Physics*, 105(4):1500–1515, 1996.

[49] V Yakhot, M Berkowitz, and RB Gerber. Theory of excimer vibrational relaxation and UV emission in solid neon. *Chemical Physics*, 10(1):61–66, 1975.

[50] J Wörmer, R Karnbach, M Joppien, and T Möller. Evolution of excitonic energy levels in Ar_N clusters: Confinement of bulk, surface, and deep valence shell excitons. *The Journal of chemical physics*, 104(21):8269–8278, 1996.

[51] J Wörmer, V Guzielski, J Stapelfeldt, G Zimmerer, and T Möller. Optical properties of argon clusters in the VUV. *Physica Scripta*, 41(4):490, 1990.

[52] G Zimmerer. Excited state spectroscopy in solids. *Proc. Int. School of Physics Enrico Fermi, Course*, 96, 1987.

[53] Volker Saile. One-and two-photon spectroscopy with rare gas solids. *Applied optics*, 19(23):4115–4122, 1980.

[54] J Wörmer and T Möller. On the nature of bulk and surface excitations in Argon clusters. *Zeitschrift für Physik D Atoms, Molecules and Clusters*, 20(1):39–42, 1991.

[55] T Laarmann, ARB De Castro, P Gürtler, W Laasch, J Schulz, H Wabnitz, and T Möller. Interaction of argon clusters with intense VUV-laser radiation: the role of electronic structure in the energy-deposition process. *Physical review letters*, 92(14):143401, 2004.

[56] T. Laarmann, K. von Haeften, A. Kanaev, H. Wabnitz, and T. Möller. Character of tightly bound excitons in small argon clusters: Insights from size-dependent energy shifts. *Physical Review B*, 66(20):205407, November 2002.

[57] O. Dössel, H. Nahme, R. Haensel, and N. Schwentner. Transient absorption and luminescence of rare gas crystals. *The Journal of Chemical Physics*, 79(2):665–670, July 1983.

[58] Norman H Tolk, Morton M Traum, John C Tully, and Theodore E Madey. *Desorption Induced by Electronic Transitions DIET I: Proceedings of the First International Workshop, Williamsburg, Virginia, USA, May 12–14, 1982*, volume 24. Springer Science & Business Media, 2013.

[59] Wilhelm Brenig and Dietrich Menzel. *Desorption Induced by Electronic Transitions DIET II: Proceedings of the Second International Workshop, Schloß Elmau, Bavaria, October 15–17, 1984*, volume 4. Springer Science & Business Media, 2012.

[60] P Børgesen, Jørgen Schou, H Sørensen, and C Claussen. Charged particle erosion of solid rare gases and dilute rare gas alloys. *Applied Physics A*, 29(2):57–61, 1982.

[61] L.F. Chen, G.Q. Huang, and K.S. Song. Desorption of atoms and excimers upon self-trapping of excitons in rare gas solids. *Nuclear Instruments and Methods in Physics Research Section B: Beam Interactions with Materials and Atoms*, 116(1):61–65, 1996. Radiation Effects in Insulators.

[62] I Arakawa. Exclton Induced Desorption at the Surface of Rare Gas Solids. *Molecular Crystals and Liquid Crystals Science and Technology. Section A. Molecular Crystals and Liquid Crystals*, 314(1):47–58, 1998.

[63] F Coletti, JM Debever, and G Zimmerer. Electron stimulated desorption of solid argon via exciton creation. *Journal de Physique Lettres*, 45(9):467–473, 1984.

[64] I Arakawa, M Takahashi, and K Takeuchi. Electron stimulated desorption of excited neutrals from the surface of solid rare gas. *Journal of Vacuum Science & Technology A: Vacuum, Surfaces, and Films*, 7(3):2090–2093, 1989.

[65] C. T. Reimann, W. L. Brown, D. E. Grosjean, and M. J. Nowakowski. Dimer desorption from solid argon films electronically excited by MeV He ions. *Phys. Rev. B*, 45:43–55, Jan 1992.

[66] C. T. Reimann, W. L. Brown, and R. E. Johnson. Electronically stimulated sputtering and luminescence from solid argon. *Phys. Rev. B*, 37:1455–1473, Feb 1988.

[67] D. E. Grosjean, R. A. Vidal, R. A. Baragiola, and W. L. Brown. Absolute luminescence efficiency of ion-bombarded solid argon. *Phys. Rev. B*, 56:6975–6981, Sep 1997.

[68] JW Keto, RE Gleason Jr, and GK Walters. Production mechanisms and radiative lifetimes of argon and xenon molecules emitting in the ultraviolet. *Physical Review Letters*, 33(23):1365, 1974.

[69] DC Lorents. The physics of electron beam excited rare gases at high densities. *Physica B+ C*, 82(1):19–26, 1976.

[70] D. J. O'Shaughnessy, J. W. Boring, S. Cui, and R. E. Johnson. Ejected-Atom Energy Spectra from Electronically Excited Rare-Gas Solids. *Physical Review Letters*, 61(14):1635–1638, October 1988.

[71] Max Born and Robert Oppenheimer. Zur quantentheorie der molekeln. *Annalen der physik*, 389(20):457–484, 1927.

[72] B Huron, JP Malrieu, and P Rancurel. Iterative perturbation calculations of ground and excited state energies from multiconfigurational zeroth-order wavefunctions. *The Journal of Chemical Physics*, 58(12):5745–5759, 1973.

[73] Isidore Last and Thomas F George. Theoretical study of small Ar_n^* clusters in low-lying electronic states. *The Journal of chemical physics*, 98(8):6406–6416, 1993.

[74] F. Y. Naumkin and D. J. Wales. Rydberg excitations in rare gas clusters: Structure and electronic spectra of Ar_n^* ($3 \leq n \leq 25$). *Molecular Physics*, 96(9):1295–1304, 1999.

[75] Francesco Aquilante, Luca D E Vico, Nicolas Ferré, Giovanni Ghigo, Per-åke Malmqvist, Pavel Neogrády, Thomas Bondo Pedersen, Michal Pito Nák, Markus Reiher, Björn O Roos, Luis Serrano-andrés, Miroslav Urban, Valera Veryazov, and Roland Lindh. Software News and Update MOLCAS 7 : The Next Generation. 2009.

[76] Fedor Yu Naumkin, Peter J. Knowles, and John N. Murrell. Towards reliable modelling of large clusters: on the overall accuracy of the diatomics-in-molecule method for rare gas cluster ions. *Chemical Physics*, 193(1-2):27–36, 1995.

[77] G Durand, P Duplàa, and F Spiegelmann. Pseudopotential approach of the electronic structure in clusters: application to Alkali Halides and Rare Gases. *Zeitschrift für Physik D Atoms, Molecules and Clusters*, 40(1):177–181, 1997.

[78] C Jonin, P Laporte, and F Spiegelmann. Pseudopotential hole–particle formalism for excitations in xenon molecules and clusters. I. Theory, atomic and molecular tests. *The Journal of chemical physics*, 117(7):3049–3058, 2002.

[79] C Jonin and F Spiegelmann. Pseudopotential hole–particle formalism for excitations in xenon molecules and clusters. II. The electronic structure of Xe_2^*. *The Journal of chemical physics*, 117(7):3059–3073, 2002.

[80] John C. Tully. Molecular dynamics with electronic transitions. *The Journal of Chemical Physics*, 93(2):1061–1071, 1990.

[81] Attila Szabo and Neil S Ostlund. *Modern quantum chemistry: introduction to advanced electronic structure theory*. Courier Corporation, 2012.

[82] Björn O Roos, Per Linse, Per EM Siegbahn, and Margareta RA Blomberg. A simple method for the evaluation of the second-order-perturbation energy from external double-excitations with a CASSCF reference wavefunction. *Chemical Physics*, 66(1-2):197–207, 1982.

[83] Kerstin Andersson, Per-Åke Malmqvist, and Björn O Roos. Second-order perturbation theory with a complete active space self-consistent field reference function. *The Journal of chemical physics*, 96(2):1218–1226, 1992.

[84] James Finley, Per-Åke Malmqvist, Björn O Roos, and Luis Serrano-Andrés. The multi-state CASPT2 method. *Chemical physics letters*, 288(2-4):299–306, 1998.

[85] Gunnar Karlström, Roland Lindh, Per-Åke Malmqvist, Björn O Roos, Ulf Ryde, Valera Veryazov, Per-Olof Widmark, Maurizio Cossi, Bernd Schimmelpfennig, Pavel Neogrady, et al. MOLCAS: a program package for computational chemistry. *Computational Materials Science*, 28(2):222–239, 2003.

[86] Niclas Forsberg and Per-Åke Malmqvist. Multiconfiguration perturbation theory with imaginary level shift. *Chemical Physics Letters*, 274(1-3):196–204, 1997.

[87] David E Woon and Thom H Dunning Jr. Gaussian basis sets for use in correlated molecular calculations. III. The atoms aluminum through argon. *The Journal of chemical physics*, 98(2):1358–1371, 1993.

[88] H.H. Michels, RH Hobbs, and LA Wright. Electronic structure of the noble gas dimer ions. I. Potential energy curves and spectroscopic constants. *The Journal of Chemical Physics*, 69(11):5151–5162, 1978.

[89] Remigius Mastalerz, Oliver Zehnder, Markus Reiher, and Frédéric Merkt. Spin–Orbit Coupling and Potential Energy Functions of Ar_2^+ and Kr_2^+ by High-Resolution Photoelectron Spectroscopy and ab Initio Quantum Chemistry. *Journal of chemical theory and computation*, 8(10):3671–3685, 2012.

[90] Marc Briant, Lionel Poisson, Majdi Hochlaf, Patrick de Pujo, Marc-André Gaveau, and Benoît Soep. ar_2 photoelectron spectroscopy mediated by autoionizing states. *Phys. Rev. Lett.*, 109:193401, Nov 2012.

[91] Björn O Roos, Roland Lindh, Per-Åke Malmqvist, Valera Veryazov, and Per-Olof Widmark. Main group atoms and dimers studied with a new relativistic ANO basis set. *The Journal of Physical Chemistry A*, 108(15):2851–2858, 2004.

[92] Luc Goubert, Eric Desoppere, Willem Wieme, Rudolf Polak, Ivana Paidarova, and Gert Due Billing. Semiclassical study of Ar_2^*(3. SIGMA. u+) excimers in a pure Ar afterglow by means of a diatomics-in-molecules potential energy surface for the Ar_3^* system. *The Journal of Physical Chemistry*, 99(42):15479–15487, 1995.

[93] Frank O. Ellison. A Method of Diatomics in Molecules. I. General Theory and Application to H_2O, journal = Journal of the American Chemical Society. 85(22):3540–3544, 1963.

[94] René Kalus, Ivana Paidarová, Daniel Hrivňák, Petr Paška, and Florent Xavier Gadéa. Modelling of Kr_n^+ clusters (n=2–20). I. Structures and energetics. *Chemical Physics*, 294(2):141–153, 2003.

[95] J. Galindez, F. Calvo, P. Paska, D. Hrivnak, R. Kalus, and F.X. Gadéa. DIM modelings for realistic simulations of ionic rare-gas clusters, test on structures and photoabsorption spectra of Ar_n^+ (n=3–8). *Computer Physics Communications*, 145(1):126–140, 2002. Structure and Dynamics of Weakly Bound Clusters and Aggregates.

[96] C. Jonin and F. Spiegelmann. Pseudopotential hole–particle formalism for excitations in xenon molecules and clusters. II. The electronic structure of Xe_2^*. *The Journal of Chemical Physics*, 117(7):3059–3073, 2002.

[97] Qinghui Ge, Yuezhi Mao, Alec F. White, Evgeny Epifanovsky, Kristina D. Closser, and Martin Head-Gordon. Simulating the absorption spectra of helium clusters (n = 70, 150, 231, 300) using a charge transfer correction to superposition of fragment single excitations. *The Journal of Chemical Physics*, 146(4):044111, 2017.

[98] M. Amarouche, G. Durand, and J. P. Malrieu. Structure and stability of Xe_n^+ clusters. *The Journal of Chemical Physics*, 88(2):1010–1018, 1988.

[99] Marlo Martin. Exciton Self-Trapping in Rare-Gas Crystals. *The Journal of Chemical Physics*, 54(8):3289–3299, 1971.

[100] Ronald A Aziz. A highly accurate interatomic potential for argon. *The Journal of chemical physics*, 99(6):4518–4525, 1993.

[101] Wolfgang Müller, Joachim Flesch, and Wilfried Meyer. Treatment of intershell correlation effects in ab initio calculations by use of core polarization potentials. Method and application to alkali and alkaline earth atoms. *The Journal of Chemical Physics*, 80(7):3297–3310, 1984.

[102] E Jacquet, D Zanuttini, J Douady, E Giglio, and B Gervais. Spectroscopic properties of alkali atoms embedded in Ar matrix. *The Journal of chemical physics*, 135(17):174503, 2011.

[103] E. F. Valeev. Libint: A library for the evaluation of molecular integrals of many-body operators over gaussian functions. http://libint.valeyev.net/, 2021. version 2.7.1.

[104] Per-Olov Löwdin. Quantum theory of cohesive properties of solids. *Advances in Physics*, 5(17):1–171, 1956.

[105] John C. Tully. *Diatomics-in-Molecules*, pages 173–200. Springer US, Boston, MA, 1977.

[106] John C. Tully. Diatomics-in-molecules potential energy surfaces. II. Nonadiabatic and spin-orbit interactions. *The Journal of Chemical Physics*, 59(9):5135–5144, 1973.

[107] P. J. Kuntz and J. J. Hogreve. Classical path surface-hopping dynamics. II. Application to Ar_3^+. *The Journal of chemical physics*, 95(1):156–165, 1991.

[108] P. J. Kuntz. *Interaction Potentials II: Semiempirical Atom-Molecule Potentials for Collision Theory*, pages 79–110. Springer US, Boston, MA, 1979.

[109] Michael B Faist and James T Muckerman. On the valence bond diatomics-in-molecules method. I. A projection operator reformulation. *The Journal of Chemical Physics*, 71(1):225–232, 1979.

[110] John C. Tully. Nonadiabatic molecular dynamics. *International Journal of Quantum Chemistry*, 40(S25):299–309, 1991.

[111] Sherin Alfalah, Daniel Kinzel, Jesús González-Vázquez, and Leticia González. Non-adiabatic photoisomerization versus photodissociation dynamics of the chiral fluoroethylene derivative (4-methylcyclohexylidene) fluoromethane. *Chemical Physics*, 369(2-3):138–144, 2010.

[112] FY Naumkin and DJ Wales. Diatomics-in-molecules potentials incorporating ab initio data: Application to ionic, Rydberg-excited, and molecule-doped rare gas clusters. *Computer physics communications*, 145(1):141–155, 2002.

[113] David J. Wales and Jonathan P. K. Doye. Global Optimization by Basin-Hopping and the Lowest Energy Structures of Lennard-Jones Clusters Containing up to 110 Atoms. *The Journal of Physical Chemistry A*, 101(28):5111–5116, July 1997.

[114] J. A. Northby. Structure and binding of Lennard-Jones clusters: $13 \leq N \leq 147$. *The Journal of Chemical Physics*, 87(10):6166–6177, November 1987.

[115] C. J. Tsai and K. D. Jordan. Use of an eigenmode method to locate the stationary points on the potential energy surfaces of selected argon and water clusters. *The Journal of Physical Chemistry*, 97(43):11227–11237, October 1993.

[116] Craig C Martens and Jian-Yun Fang. Semiclassical-limit molecular dynamics on multiple electronic surfaces. *The Journal of chemical physics*, 106(12):4918–4930, 1997.

[117] Raymond Kapral and Giovanni Ciccotti. Mixed quantum-classical dynamics. *The Journal of chemical physics*, 110(18):8919–8929, 1999.

[118] John C. Tully. Mixed quantum-classical dynamics. *Faraday Discussions*, 110:407–419, 1998.

[119] Rachel Crespo-Otero and Mario Barbatti. Recent advances and perspectives on nonadiabatic mixed quantum-classical dynamics. *Chemical reviews*, 118(15):7026–7068, 2018.

[120] Dónal Mac Kernan, Giovanni Ciccotti, and Raymond Kapral. Trotter-based simulation of quantum-classical dynamics. *The Journal of Physical Chemistry B*, 112(2):424–432, 2008.

[121] Michal Ben-Nun, Jason Quenneville, and Todd J Martínez. Ab initio multiple spawning: Photochemistry from first principles quantum molecular dynamics. *The Journal of Physical Chemistry A*, 104(22):5161–5175, 2000.

[122] Basile FE Curchod and Todd J Martínez. Ab initio nonadiabatic quantum molecular dynamics. *Chemical reviews*, 118(7):3305–3336, 2018.

[123] Ivano Tavernelli. Ab initio–driven trajectory-based nuclear quantum dynamics in phase space. *Physical Review A*, 87(4):042501, 2013.

[124] Basile FE Curchod, Ivano Tavernelli, and Ursula Rothlisberger. Trajectory-based solution of the nonadiabatic quantum dynamics equations: an on-the-fly approach for molecular dynamics simulations. *Physical Chemistry Chemical Physics*, 13(8):3231–3236, 2011.

[125] Federica Agostini, Seung Kyu Min, Ali Abedi, and EKU Gross. Quantum-classical nonadiabatic dynamics: Coupled-vs independent-trajectory methods. *Journal of chemical theory and computation*, 12(5):2127–2143, 2016.

[126] Jae Woo Park and Toru Shiozaki. Analytical derivative coupling for multistate CASPT2 theory. *Journal of chemical theory and computation*, 13(6):2561–2570, 2017.

[127] Jae Woo Park and Toru Shiozaki. On-the-fly CASPT2 surface-hopping dynamics. *Journal of chemical theory and computation*, 13(8):3676–3683, 2017.

[128] Michal Dallos, Hans Lischka, Ron Shepard, David R Yarkony, and Péter G Szalay. Analytic evaluation of nonadiabatic coupling terms at the MR-CI level. II. Minima on the crossing seam: Formaldehyde and the photodimerization of ethylene. *The Journal of chemical physics*, 120(16):7330–7339, 2004.

[129] Hans Lischka, Michal Dallos, Péter G Szalay, David R Yarkony, and Ron Shepard. Analytic evaluation of nonadiabatic coupling terms at the MR-CI level. I. Formalism. *The Journal of chemical physics*, 120(16):7322–7329, 2004.

[130] Thomas S Kuhlman, William J Glover, Toshifumi Mori, Klaus B Møller, and Todd J Martínez. Between ethylene and polyenes-the non-adiabatic dynamics of cis-dienes. *Faraday discussions*, 157:193–212, 2012.

[131] Toshifumi Mori, William J Glover, Michael S Schuurman, and Todd J Martinez. Role of rydberg states in the photochemical dynamics of ethylene. *The Journal of Physical Chemistry A*, 116(11):2808–2818, 2012.

[132] Vladimir Chernyak and Shaul Mukamel. Density-matrix representation of nonadiabatic couplings in time-dependent density functional (TDDFT) theories. *The Journal of Chemical Physics*, 112(8):3572–3579, 2000.

[133] Robert Send and Filipp Furche. First-order nonadiabatic couplings from time-dependent hybrid density functional response theory: Consistent formalism, implementation, and performance. *The Journal of chemical physics*, 132(4):044107, 2010.

[134] Ivano Tavernelli, Basile FE Curchod, and Ursula Rothlisberger. On nonadiabatic coupling vectors in time-dependent density functional theory. *The Journal of chemical physics*, 131(19):196101, 2009.

[135] Ivano Tavernelli, Basile FE Curchod, Andrey Laktionov, and Ursula Rothlisberger. Nonadiabatic coupling vectors for excited states within time-dependent density functional theory in the tamm–dancoff approximation and beyond. *The Journal of chemical physics*, 133(19):194104, 2010.

[136] Roi Baer. Non-adiabatic couplings by time-dependent density functional theory. *Chemical physics letters*, 364(1-2):75–79, 2002.

[137] Chunping Hu, Hirotoshi Hirai, and Osamu Sugino. Nonadiabatic couplings from time-dependent density functional theory: Formulation in the Casida formalism and practical scheme within modified linear response. *The Journal of chemical physics*, 127(6):064103, 2007.

[138] Chunping Hu, Osamu Sugino, and Yoshitaka Tateyama. All-electron calculation of nonadiabatic couplings from time-dependent density functional theory: Probing with the Hartree–Fock exact exchange. *The Journal of chemical physics*, 131(11):114101, 2009.

[139] Chunping Hu, Osamu Sugino, and Kazuyuki Watanabe. Performance of Tamm-Dancoff approximation on nonadiabatic couplings by time-dependent density functional theory. *The Journal of chemical physics*, 140(5):054106, 2014.

[140] Sharon Hammes-Schiffer and John C. Tully. Proton transfer in solution: Molecular dynamics with quantum transitions. *The Journal of chemical physics*, 101(6):4657–4667, 1994.

[141] Garrett A Meek and Benjamin G Levine. Evaluation of the time-derivative coupling for accurate electronic state transition probabilities from numerical simulations. *The journal of physical chemistry letters*, 5(13):2351–2356, 2014.

[142] David Bonhommeau, Nadine Halberstadt, and Udo Buck. Fragmentation of rare-gas clusters ionized by electron impact: new theoretical developments and comparison with experiments. *International Reviews in Physical Chemistry*, 26(2):353–390, April 2007.

[143] M Amarouche, FX Gadea, and J Durup. A proposal for the theoretical treatment of multi-electronic-state molecular dynamics: hemiquantal dynamics with the whole dim basis (HWD). A test on the evolution of excited Ar_3^+ cluster ions. *Chemical Physics*, 130(1-3):145–157, 1989.

[144] Ivan Janeček, Daniel Hrivňák, René Kalus, and Florent Xavier Gadéa. Theoretical modeling of postionization fragmentation of rare-gas trimer cations. *The Journal of chemical physics*, 125(10):104315, 2006.

[145] Ivan Janeček, Silvie Cintavá, Daniel Hrivňák, René Kalus, Michal Fárník, and Florent Xavier Gadéa. Postionization fragmentation of rare-gas trimers revisited with new theoretical approaches. *The Journal of Chemical Physics*, 131(11):114306, 2009.

[146] David Bonhommeau, Alexandra Viel, and Nadine Halberstadt. Dissociative ionization of neon clusters Ne_n, n=3 to 14: A realistic multisurface dynamical study. *The Journal of Chemical Physics*, 123(5):054316, August 2005.

[147] David Bonhommeau, Nadine Halberstadt, and Alexandra Viel. Fragmentation dynamics of argon clusters (Ar_n, n=2 to 11) following electron-impact ionization: Modeling and comparison with experiment. *The Journal of Chemical Physics*, 124(18):184314, May 2006.

[148] David Bonhommeau, Alexandra Viel, and Nadine Halberstadt. Fragmentation dynamics of ionized neon trimer inside helium nanodroplets: A theoretical study. *The Journal of chemical physics*, 120(24):11359–11362, 2004.

[149] P Lohbrandt, R Galonska, HJ Kim, M Schmidt, C Lauenstein, and U Buck. Electron Impact Fragmentation of Size Selected Ar_n (n= 4 to 9) Clusters. In *Atomic and Molecular Beams*, pages 623–636. Springer, 2001.

[150] Christof Steinbach, Michal Fárník, Udo Buck, Carrie A Brindle, and Kenneth C Janda. Electron impact fragmentation of size-selected krypton clusters. *The Journal of Physical Chemistry A*, 110(29):9108–9115, 2006.

[151] D Zanuttini, J Douady, E Jacquet, E Giglio, and B Gervais. Nonadiabatic molecular dynamics of photoexcited L_2^+ Ne_n clusters. *The Journal of Chemical Physics*, 134(4):044308, 2011.

[152] D. Beeman. Some multistep methods for use in molecular dynamics calculations. *Journal of Computational Physics*, 20(2):130–139, 1976.

[153] P. Schofield. Computer simulation studies of the liquid state. *Computer Physics Communications*, 5(1):17–23, 1973.

[154] Wolfram Research, Inc. Mathematica, Version 13.0.0. Champaign, IL, 2021.

[155] Andreas Brinkmann. Introduction to average Hamiltonian theory. I. Basics. *Concepts in Magnetic Resonance Part A*, 45A(6):e21414, 2016.

[156] Philip Pechukas and John C. Light. On the Exponential Form of Time-Displacement Operators in Quantum Mechanics. *The Journal of Chemical Physics*, 44(10):3897–3912, 1966.

[157] Richard P. Feynman. An operator calculus having applications in quantum electrodynamics. *Phys. Rev.*, 84:108–128, Oct 1951.

[158] Wilhelm Magnus. On the exponential solution of differential equations for a linear operator. *Communications on Pure and Applied Mathematics*, 7(4):649–673, 1954.

[159] David Zanuttini. *Simulation des molécules de métaux alcalins M2+ immergées dans des agrégats de néon: Structures, propriétés spectroscopiques, dynamiques non-adiabatiques*. PhD thesis, Caen, 2009.

[160] J. Wörmer, R. Karnbach, M. Joppien, and T. Möller. Evolution of excitonic energy levels in Ar_N clusters: Confinement of bulk, surface, and deep valence shell excitons. *The Journal of Chemical Physics*, 104(21):8269–8278, June 1996.

**

Appendix A

MOLCAS Input

In the following appendix we give the details related to MOLCAS quantum chemistry code files used for the energy calculations of the argon dimer and trimer.

A.1 Dimer MOLCAS Input

In the following section we give the inputs associated to excited argon dimer Ar_2^*. The following material is in conjunction with the discussions developed in section 2.2.2 of the thesis.

A.1.1 Symmetry Group

The following table gives the symmetry group in MOLCAS associated to the state of interest and their individual symmetry groups. This table also shows the minimum number of roots that should be selected to get the associated PECs. As the ground state is the lowest energy PEC in A_g symmetry group, it is important to have a minimum of 2 roots, whereas in all the other symmetry groups the lowest root gives the PECs we seek for.

Table A.1: Selection of Symmetry Group in: X Y Z ($D_{\infty h}$) Symmetry

Symmetry Group	MOLCAS number	Associated State	Minimum roots	Atomic Orbitals	No of Orbitals
A_g	1	Σ_g^+	2	$1s^A 2s^A, 2p_z^A 3s^A, 3p_z^A$	5
B_{1u}	5	Σ_u^+	1	$2p_x^A 3p_x^A$	2
B_{2g}	6	Π_g	1	$2p_y^A 3p_y^A$	2
B_{2u}	3	Π_u	1	-	0

A.1.2 SCF Input

For the Argon dimer in $D_{\infty h}$ symmetry for each atom we have the orbital population given in the table A.1. The SCF calculation done here is to build up orbitals associated to the cation Ar_2^+. This is done by removing an electron from the outermost dimer orbitals. As for each Ar atom the $3p$ orbitals contain 6 electrons, then for the dimer they contain 12 electrons. For the cation there should be 11 electrons. This is done by removing 0.166 electron from each outermost p orbital making the population 1.83. The input of SCF calculation for such system is:

```
******************************************
*       OM generation for Ar2            *
******************************************
&SCF &END
Occupied
5 2 2 0 5 2 2 0
OccNumbers
2.00 2.00 2.00 2.00 1.83
2.00 1.83
2.00 1.83
2.00 2.00 2.00 2.00 1.83
2.00 1.83
2.00 1.83
Threshold
0.5d-10 0.5d-10 0.5d-10 0.5d-10
End of Input
```

A.1.3 RASSCF Input

The following are the RASSCF inputs. The Symmetry and Spin need to be adapted based on the state we are looking for. The relevant symmetry and the minimum roots are given in table A.1. Based on the consequent calculation to RASSCF which generates the reference wavefunction, the number of roots and threshold change. The following is an example of RASSCF calculation in A_g symmetry, in triplet spin state and looking for 4 roots which are equally weighted. The threshold is tight as the excited states associated to argon are very close in energy and the following threshold is enough to have smooth PECs.

```
RASSCF
Symmetry
1
Spin
3
Inactive
4 1 1 0 4 1 1 0
Ras1
1 1 1 0 1 1 1 0
Ras2
2 1 1 0 2 1 1 0
Nactel
12 1 0
CiRoot
4 4 1
OutOrbitals
Canonical
THRS
1.0e-11 2.0e-08 2.0e-08
End of input
```

A.1.4 CASPT2

```
&CASPT2 &END
     MultiState       = 1 1
     MaxIter          = 100
     NoOrbitals
     MOLOrb
     Convergence      = 1.0e-08
End of input
```

A.1.5 MRCI

```
****************************************
*       Orbital transform - 8 frozen
****************************************
&MOTRA &END
LUMORB
Frozen
3 1 1 0 3 1 1 0
End of input

****************************************
*       calcul MRCI for Ar2* (1Sigma+)
****************************************
&GUGA &END
Title
GUGA for Ar2* (3Sigma_u+)
Nactel
12
SPIN
1
INACTIve
1 0 0 0 1 0 0 0
ACTIve
2 1 1 0 2 1 1 0
CIALL
5
End of input

&MRCI &END
Title
 MRCI for Ar2* (1Sigma+)
SDCI
NRROOTS
      1
ROOTS
      1
MAXITeration
49
End of input
```

A.2 Linear Trimer

In the C_∞ symmetry group we can obtain the energy of the linear symmetric and asymmetric isomers as Z-axis is no longer an axis of symmetry.

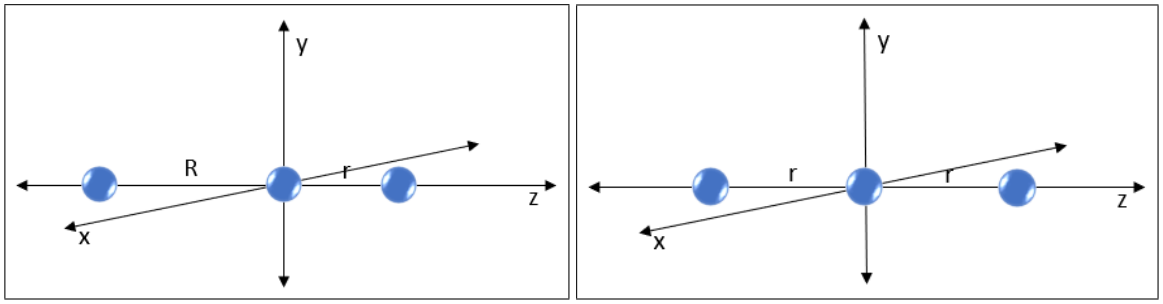

Figure A.1: Left: Linear asymmetric trimer. Right: Linear symmetric trimer.

A.2.1 Symmetry Table

Symmetry Group: XY, i.e. system is symmetric along XY plane. As we can see from the atomic arrangement, this is no more symmetric in XY-plane if we consider the atom to be on Z-axis with atom A at $(0,0,0)$.

Table A.2: Selection of Symmetry Group in: X Y (C_∞) Symmetry

Symmetry Group	MOLCAS number	Associated State	Minimum roots	Atomic Orbitals	Total No of Orbitals	3-atoms
A_g (A1)	1	Σ_g^+	2	$1s^A$	1	**15**
				$2s^A, 2p_z^A$	+2	
				$3s^A, 3p_z^A$	+2 = **5**	
B_{1u} (B1)	5	Σ_u^+	1	$2p_x^A$	1	**6**
				$3p_x^A$	+1 = **2**	
B_{2g} (B2)	6	Π_g	1	$2p_y^A$	1	**6**
				$3p_y^A$	+1 = **2**	
B_{2u} (A2)	3	Π_u	1	-	**0**	**0**

A.2.2 SCF Input

The SCF input changes with the symmetry group taken into consideration. Else, this input is constructed in the same spirit as for linear symmetric trimer with focus to create a hole in a 3p orbital.

```
&SCF
Occupied
15 6 6 0
OccNumbers
2.00 2.00 2.00 2.00 2.00  2.00 2.00 2.00 2.00 2.00  2.00 2.00 1.87 1.87 1.87
2.00 2.00 2.00 1.87 1.87  1.87
2.00 2.00 2.00 1.87 1.87  1.87
Threshold
0.5d-10 0.5d-8 0.5d-8 0.5d-8
End of Input
```

A.2.3 RASSCF Input

The lowest energy state of Ar_3^* is calculated in the A_1 symmetry. For the RASSCF calculation, the core orbitals are considered inactive and we put the hole orbitals in RAS1. As we want the hole to be in a $3p$ orbital and we know that the participating orbital from p-shell would be the one localised on Z-axis, we put only p_z- orbitals in RAS1. This is done to promote the convergence as p_x and p_y orbitals, which are not participating in the excitation and are rotating while performing optimisation which can lead to bad convergence. In RAS2, we select the orbitals where we want to promote the excited electron. We have selected only 4s orbitals in RAS2 because these are the primary orbital for excitation and we can also avoid non-convergence. Since the lowest energy root is close to other roots in this symmetry group, we are calculating two lowest energies.

```
&RASSCF
Symmetry
1
Spin
3
Inactive
12 6 6 0
Ras1
3 0 0 0
Ras2
3 0 0 0
Nactel
6 1 0
CiRoot
2 2 1
1 2
4 1
OutOrbitals
Canonical
THRS
1.0e-09 2.0e-05 2.0e-06
End of input
```

A.3 Trimer in C_{2v} Symmetry

In order to determine the correct occupied orbitals and their occupation for the triangular geometry of Ar_3^*, we need to think about the arrangement of orbitals for the given system.

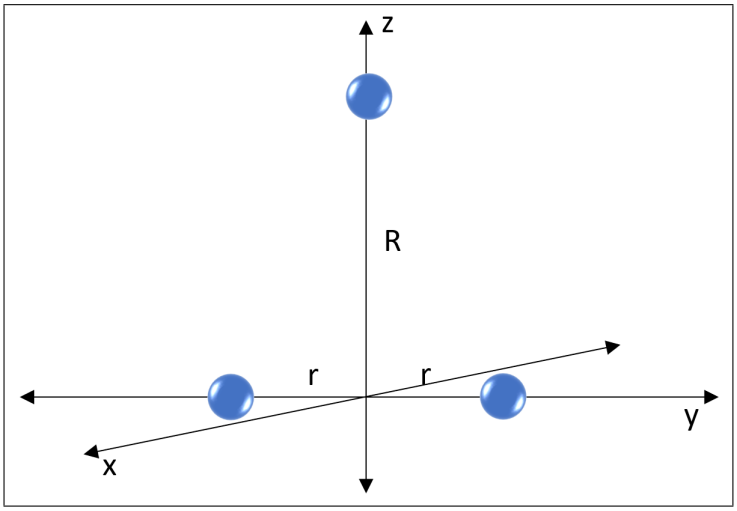

Figure A.2

A.3.1 Symmetry Table

Let's assume the atom B and C are placed symmetrically on the Y-axis for XZ plane and atom A is placed on the Z-axis (see figure A.2). Now we can write the orbitals which are associated to each symmetry group as follows:

Table A.3: Selection of Symmetry Group

Symmetry Group	Single Atoms	Bonding/Anti-bonding atoms	Number of Orbitals
A1	$1s^A$	$1s^B + 1s^C$	2
	$2s^A, 2p_z^A$	$2s^B + 2s^C, 2p_z^B + 2p_z^C, 2p_y^B - 2p_y^C$	+5
	$3s^A, 3p_z^A$	$3s^B + 3s^C, 3p_z^B + 3p_z^C, 3p_y^B - 3p_y^C$	+5=12
B1	$2p_x^A$	$2p_x^B + 2p_x^C$	2
	$3p_x^A$	$3p_x^B + 3p_x^C$	+2=4
B2		$1s^B - 1s^C$	1
	$2p_y^A$	$2s^B - 2s^C, 2p_z^B - 2p_z^C, 2p_y^B + 2p_y^C$	+4
	$3p_y^A$	$3s^B - 3s^C, 3p_z^B - 3p_z^C, 3p_y^B + 3p_y^C$	+4=9
A2		$2p_x^B - 2p_x^C,$	1
		$3p_x^B - 3p_x^C$	+1=2

A.3.2 SCF Inputs

The SCF input hardly differs from previous inputs because of the symmetry of the trimer isomer. Although we intended to remove an electron from whole p-orbital, but that causes problem with RASSCF optimisation. As we expect $p_x^{(A,B)}$ should not participate in the excitation so having them completely filled helps in orbital optimisation and eventually aids in convergence of RASSCF calculations.

```
&SCF
Occupied
12 4 9 2
OccNumbers
2.0 2.0 2.0 2.0 2.0 2.0 2.0 2.0 2.0 1.83 1.83 1.83
2.0 2.0 2.0 2.0
2.0 2.0 2.0 2.0 2.0 2.0 1.83 1.83 1.83
2.0 2.0
Threshold
0.5d-10 0.5d-8 0.5d-8 0.5d-8
End of Input
```

Another way to check if the orbitals that are taken into account for the given symmetry are good or not, we can run SCF calculations without specifying orbitals or their respective occupancies. This will not generate the cation as we intend to do, but will show us the favourable orbital occupation for the given symmetry group.

A.3.3 RASSCF Inputs

Despite efforts to improve, RASSCF calculations by optimising the SCF input, they were not sufficient to converge the results as some of the p orbitals were rotating freely. To improve the results further, we split the RAS input into two parts. The lowest energy root is located in B2 symmetry. For each Ar atom, we moved the 2p orbitals in the inactive space and included the 2s orbitals in the active RAS1 space. The excited orbitals include $4s$ and $4p$. We needed more roots as higher roots were intruding in the lowest roots and probably causing root flipping and we observed some unwanted jumps is the energy. In the first RAS, the number of iterations are limited because it is only intended to provide optimised orbitals for the next RAS were we will calculate the final energies. Now in the second RAS, similar to previous RAS all the inputs are same except, here we put $3s$ back into inactive orbitals as we want only $3p-4s$ transition energies. The weight on the first CI root is increased to optimise it further to have no jumps and better convergence.

```
******     RAS1      ******
RASSCF
Symmetry
3
Spin
3
Inactive
7 2 5 1
Ras1
5 2 4 1
Ras2
5 2 4 1
Nactel
24 1 0
CiRoot
3 3 1
OutOrbitals
Canonical
ITERations
50 50
THRS
1.0e-08 2.0e-04 2.0e-06
End of input
```

```
******     RAS2      ******
RASSCF
Symmetry
3
Spin
3
Inactive
9 2 6 1
Ras1
3 2 3 1
Ras2
2 0 1 0
Nactel
18 1 0
CiRoot
3 3
1 2 3
6 1 1
OutOrbitals
Canonical
THRS
1.0e-08 2.0e-05 2.0e-06
End of input
```

Appendix B

DIM calculations

B.1 Excited Configuration

B.1.1 Application to $3p^5 4s$ excited configuration

To get $3p^5 4s$ excited state, we put $x^\dagger = 4s$, so we can write this triplet ^3P excited state as:

$$|C, 4s^\dagger, {}^3P; 1, 1\rangle \tag{B.1}$$

where $C = 3p^5 4s$, $M_L = 1$ and $M_S = 1$.

$$|C, 4s^\dagger, {}^3P; 1, 1\rangle = |\overline{3p}_{-1} 4s^\dagger\rangle = |4s 3p_{-1} \overline{3p}_0 3p_0 \overline{3p}_1 3p_1\rangle$$

$\overline{3p}_{-1}$ is spin down. Now to reduce the angular momentum, we apply L^- as follows,

$$L^-|C, {}^3P; 1, 1\rangle = \sqrt{L(L+1) - M_L(M_L-1)}|C, {}^3P; 0, 1\rangle \tag{B.2}$$

it can be shown that the application of $L_- = \sum_i l_i^-$ as a determinant is equivalent to the application of $\sum_k l_k^-$, where k runs over the orbitals in the determinant.

$$\sum_k l_k |4s 3p_{-1} \overline{3p}_0 3p_0 \overline{3p}_1 3p_1\rangle = \sqrt{1(1+1) - 0(0-1)}|4s 3p_{-1} \overline{3p}_{-1} 3p_0 \overline{3p}_1 3p_1\rangle$$

on rearranging the orbital ordering we get,

$$|C, {}^3P; 0, 1\rangle = -|\overline{3p}_{-1} 3p_{-1} 4s 3p_0 \overline{3p}_1 3p_1\rangle = -\,|\,\overline{3p}_0 4s^\dagger\rangle$$

apply $L_-|C, {}^3P; 0, 1\rangle$ we get,

$$|C, {}^3P; -1, 1\rangle = |\overline{3p}_{-1} 3p_{-1} \overline{3p}_0 3p_0 4s 3p_1\rangle = |\,\overline{3p}_{-1} 4s^\dagger\rangle$$

Hence we get the transformation matrix elements as,

$$T_{4s} = \frac{1}{\sqrt{2}} \begin{pmatrix} 0 & 0 & 1 \\ 0 & -1 & 0 \\ 1 & 0 & 0 \end{pmatrix} \begin{pmatrix} \overline{3p}_1 4s^\dagger \\ \overline{3p}_0 4s^\dagger \\ \overline{3p}_{-1} 4s^\dagger \end{pmatrix} \tag{B.3}$$

B.1.2 Application to $3p^5 4p$ excited configuration

To get $3p^5 4s$ excited states, we put $x^\dagger = 4p_1$, so we can write this ^3D excited state as $|C, 4p_1^\dagger, ^3D; 2, 1\rangle$ where $C = 3p^5 4p$, $M_L = 2$ and $M_S = 1$.

$$| C, 4p_1^\dagger, ^3D; 2, 1\rangle = |\overline{3p}_{-1} 4p_1^\dagger\rangle = |4p_1 3p_{-1} \overline{3p}_0 3p_0 \overline{3p}_1 3p_1\rangle$$

Now to reduce the angular momentum, we apply L^- as in equation B.2,

$$L^- |C, ^3D; 2, 1\rangle = \sqrt{2(2+1) - 2(2-1)} |C, ^3D; 1, 1\rangle = \sqrt{4} |C, ^3D; 1, 1\rangle$$

$$\sum_k l_k |4p_1 3p_{-1} \overline{3p}_0 3p_0 \overline{3p}_1 3p_1\rangle = \sqrt{1(1+1) - 1(1-1)}$$
$$\{|4p_0 3p_{-1} \overline{3p}_{-1} 3p_0 \overline{3p}_1 3p_1\rangle + | 4p_1 3p_{-1} \overline{3p}_{-1} 3p_0 \overline{3p}_1 3p_1\rangle\}$$

after ordering the orbitals and using simplified notations we get,

$$|C, ^3D; 1, 1\rangle = \frac{1}{\sqrt{2}} \{|\overline{3p}_{-1} 4p_0^\dagger\rangle - |\overline{3p}_0 4p_1^\dagger\rangle\}$$

In the same spirit, on using L_- operator we can get all the following configuration,

$$|C, ^3D; 0, 1\rangle = \frac{1}{\sqrt{6}} \{|\overline{3p}_{-1} 4p_{-1}^\dagger\rangle - 2|\overline{3p}_0 4p_0^\dagger\rangle + |\overline{3p}_1 4p_1^\dagger\}$$

$$|C, ^3D; -1, 1\rangle = \frac{1}{\sqrt{2}} \{|\overline{3p}_1 4p_0^\dagger\rangle - |\overline{3p}_0 4p_{-1}^\dagger\rangle\}$$

and

$$|C, ^3D; -2, 1\rangle = |\overline{3p}_1 4p_{-1}^\dagger\rangle$$

To write the ^3P, we orthogonalize to ^3D states of same M_L and M_S, for the uppermost M_L in the P-shell, i.e. $M_L = 1$ and the lowest $M_L = -1$,

$$|C, ^3P; 1, 1\rangle = \frac{1}{\sqrt{2}} \{|\overline{3p}_{-1} 4p_0^\dagger\rangle + |\overline{3p}_0 4p_1^\dagger\rangle\}$$

$$|C, ^3P; -1, 1\rangle = \frac{1}{\sqrt{2}} \{|\overline{3p}_1 4p_0^\dagger\rangle + |\overline{3p}_0 4p_{-1}^\dagger\rangle\}$$

By using L_- on $|C, ^3P; 1, 1\rangle$ we get,

$$|C, ^3P; 0, 1\rangle = \frac{1}{\sqrt{2}} \{|\overline{3p}_{-1} 4p_{-1}^\dagger\rangle - |\overline{3p}_1 4p_1^\dagger\rangle\}$$

and the ^3S state by orthogonalization to both $|C, ^3D; 0, 1\rangle$ and $|C, ^3P; 0, 1\rangle$,

$$|C, ^3S; 0, 1\rangle = \frac{1}{\sqrt{3}} \{|\overline{3p}_1 4p_1^\dagger\rangle + |\overline{3p}_0 4p_0^\dagger\rangle + |\overline{3p}_{-1} 4p_{-1}^{\dagger 3}\rangle\}$$

B.1.3 Application to $3p^5 4d$ excited configuration

To get $3p^5 3d$ excited states, we put $x^\dagger = 3d_2^\dagger$, so we can write this ${}^3F$ excited state as $|C, 3d_2^\dagger, {}^3F; 3, 1\rangle$ where $C = 3p^5 3d$, $M_L = 3$ and $M_S = 1$.

$$|C, {}^3F; 3, 1\rangle = |\overline{3p}_{-1} 3d_2^\dagger\rangle = |3d_2 3p_{-1} \overline{3p}_0 3p_0 \overline{3p}_1 3p_1\rangle$$

Now to reduce the angular momentum, we apply L^- as follows,

$$L^- |C, {}^3F; 3, 1\rangle = \sqrt{3(3+1) - 3(3-1)} |C, {}^3F; 2, 1\rangle = \sqrt{6} |C, {}^3F; 2, 1\rangle$$

$$\sum_k l_k^- |3d_2 3p_{-1} \overline{3p}_0 3p_0 \overline{3p}_1 3p_1\rangle =$$

$$\sqrt{2(2+1) - 2(2-1)} \mid 3d_1 3p_{-1} \overline{3p}_0 3p_0 \overline{3p}_1 3p_1\rangle +$$

$$\sqrt{1(1+1) - 1(1-1)} \mid 3d_2 3p_{-1} \overline{3p}_{-1} 3p_0 \overline{3p}_1 3p_1\rangle$$

$$= \sqrt{4} \mid 3d_1 3p_{-1} \overline{3p}_0 3p_0 \overline{3p}_1 3p_1\rangle - \sqrt{2} \mid \overline{3p}_{-1} 3p_{-1} 3d_2 3p_0 \overline{3p}_1 3p_1\rangle$$

Hence,

$$|C, {}^3F; 2, 1\rangle = \sqrt{\frac{2}{3}} \mid \overline{3p}_{-1} 3d_1^\dagger\rangle - \sqrt{\frac{1}{3}} \mid \overline{3p}_0 3d_2^\dagger\rangle$$

In the same spirit by using L_- we get,

$$|C, {}^3F; 1, 1\rangle = \sqrt{\frac{6}{15}} \mid \overline{3p}_{-1} 3d_0^\dagger\rangle - \sqrt{\frac{8}{15}} \mid \overline{3p}_0 3d_1^\dagger\rangle + \sqrt{\frac{1}{15}} \mid \overline{3p}_1 3d_2^\dagger\rangle$$

$$|C, {}^3F; 0, 1\rangle = \sqrt{\frac{1}{5}} \mid \overline{3p}_{-1} 3d_{-1}^\dagger\rangle - \sqrt{\frac{3}{5}} \mid \overline{3p}_0 3d_0^\dagger\rangle + \sqrt{\frac{1}{5}} \mid \overline{3p}_1 3d_1^\dagger\rangle$$

By symmetry,

$$|C, {}^3F; -1, 1\rangle = \sqrt{\frac{6}{15}} \mid \overline{3p}_1 3d_0^\dagger\rangle - \sqrt{\frac{8}{15}} \mid \overline{3p}_0 3d_{-1}^\dagger\rangle + \sqrt{\frac{1}{15}} \mid \overline{3p}_{-1} 3d_{-2}^\dagger\rangle$$

$$|C, {}^3F; -2, 1\rangle = \sqrt{\frac{2}{3}} \mid \overline{3p}_1 3d_{-1}^\dagger\rangle - \sqrt{\frac{1}{3}} \mid \overline{3p}_0 3d_{-2}^\dagger\rangle$$

$$\mid C, {}^3F; -3, 1\rangle = \mid \overline{3p}_1 3d_{-2}^\dagger\rangle$$

Now we look for ${}^3D$ terms by orthogonalization to the $|C, {}^3F; 2, 1\rangle$ configuration,

$$|C, {}^3D; 2, 1\rangle = \sqrt{\frac{1}{3}} \mid \overline{3p}_{-1} 3d_1^\dagger\rangle + \sqrt{\frac{2}{3}} \mid \overline{3p}_0 3d_2^\dagger\rangle$$

By applying L_- consecutively to each state we get,

$$|C, {}^3D; 1, 1\rangle = \sqrt{\frac{3}{6}} \mid \overline{3p}_{-1} 3d_0^\dagger\rangle + \sqrt{\frac{1}{6}} \mid \overline{3p}_0 3d_1^\dagger\rangle - \sqrt{\frac{2}{6}} \mid \overline{3p}_1 3d_2^\dagger\rangle$$

$$|C, {}^3D; 0, 1\rangle = \sqrt{\frac{1}{2}} \mid \overline{3p}_{-1} 3d_{-1}^\dagger\rangle - \sqrt{\frac{1}{2}} \mid \overline{3p}_1 3d_1^\dagger\rangle$$

$$|C,^3D;-1,1\rangle = \sqrt{\frac{3}{6}}\,|\,\overline{3p}_1 3d_0^\dagger\rangle + \sqrt{\frac{1}{6}}\,|\,\overline{3p}_0 3d_{-1}^\dagger\rangle - \sqrt{\frac{2}{6}}\,|\,\overline{3p}_{-1} 3d_{-2}^\dagger\rangle$$

and

$$|C,^3D;-2,1\rangle = \sqrt{\frac{1}{3}}\,|\,\overline{3p}_1 3d_{-1}^\dagger\rangle + \sqrt{\frac{2}{3}}\,|\,\overline{3p}_0 3d_{-2}^\dagger\rangle$$

Now we get ^3P terms by orthogonalization to $|C,^3F;1,1\rangle$ and $|C,^3D;1,1\rangle$,

$$|C,^3P;1,1\rangle = a\,|\,\overline{3p}_{-1} 3d_0^\dagger\rangle + b\,|\,\overline{3p}_0 3d_1^\dagger\rangle + c\,|\,\overline{3p}_1 3d_2^\dagger\rangle$$

we get the coefficients by doing the cross product,

$$\begin{vmatrix} a \\ b \\ c \end{vmatrix} = \begin{vmatrix} \sqrt{\frac{6}{15}} & \sqrt{\frac{3}{6}} \\ -\sqrt{\frac{8}{15}} & \sqrt{\frac{1}{6}} \\ \sqrt{\frac{1}{15}} & -\sqrt{\frac{2}{6}} \end{vmatrix}_\times = \frac{1}{\sqrt{90}} \begin{vmatrix} \sqrt{1.1} - \sqrt{8.2} \\ -(\sqrt{1.3} + \sqrt{6.2}) \\ -\sqrt{8.3} - \sqrt{6.1} \end{vmatrix} = \begin{vmatrix} -\sqrt{\frac{1}{10}} \\ -\sqrt{\frac{3}{10}} \\ -\sqrt{\frac{6}{10}} \end{vmatrix}$$

Hence,

$$|C,^3D;1,1\rangle = -\sqrt{\frac{1}{10}}\,|\,\overline{3p}_{-1} 3d_0^\dagger\rangle - \sqrt{\frac{3}{10}}\,|\,\overline{3p}_0 3d_1^\dagger\rangle - \sqrt{\frac{6}{10}}\,|\,\overline{3p}_1 3d_2^\dagger\rangle$$

By symmetry,

$$|C,^3D;-1,1\rangle = -\sqrt{\frac{1}{10}}\,|\,\overline{3p}_1 3d_0^\dagger\rangle - \sqrt{\frac{3}{10}}\,|\,\overline{3p}_0 3d_{-1}^\dagger\rangle - \sqrt{\frac{6}{10}}\,|\,\overline{3p}_{-1} 3d_{-2}^\dagger\rangle$$

By $L_-|C,^3D;1,1\rangle$ we get,

$$|C,^3D;0,1\rangle = -\sqrt{\frac{3}{10}}\,|\,\overline{3p}_{-1} 3d_{-1}^\dagger\rangle - \sqrt{\frac{4}{10}}\,|\,\overline{3p}_0 3d_0^\dagger\rangle - \sqrt{\frac{3}{10}}\,|\,\overline{3p}_1 3d_1^\dagger\rangle$$

B.1.4 Transformation Matrix Elements

We collect the matrix elements according to their angular momentum as $\Lambda = 0, \pm 1, \pm 2$.
Now, for $\Lambda = 0$

$$T_{4s} = \begin{pmatrix} 1 & 0 & 0 \\ 0 & -1 & 0 \\ 0 & 0 & 1 \end{pmatrix} \begin{matrix} | \\ | \\ | \end{matrix} \begin{matrix} \overline{3p}_1 4s^\dagger\rangle \\ \overline{3p}_0 4s^\dagger\rangle \\ \overline{3p}_{-1} 4s^\dagger\rangle \end{matrix} \tag{B.4}$$

$$T_{4p} = \sqrt{\frac{1}{6}} \begin{pmatrix} 1 & -2 & 1 \\ \sqrt{3} & 0 & -\sqrt{3} \\ \sqrt{2} & \sqrt{2} & \sqrt{2} \end{pmatrix} \begin{matrix} | \\ | \\ | \end{matrix} \begin{matrix} \overline{3p}_{-1} 4p_{-1}^\dagger\rangle \\ \overline{3p}_0 4p_0^\dagger\rangle \\ \overline{3p}_1 4p_1^\dagger\rangle \end{matrix} \tag{B.5}$$

$$T_{3d} = \sqrt{\frac{1}{10}} \begin{pmatrix} \sqrt{2} & -\sqrt{6} & \sqrt{2} \\ \sqrt{5} & 0 & -\sqrt{5} \\ -\sqrt{3} & -2 & -\sqrt{3} \end{pmatrix} \begin{matrix} | \\ | \\ | \end{matrix} \begin{matrix} \overline{3p}_{-1} 3d_{-1}^\dagger\rangle \\ \overline{3p}_0 3d_0^\dagger\rangle \\ \overline{3p}_1 3d_1^\dagger\rangle \end{matrix} \tag{B.6}$$

and total transformation matrix is,

$$T_0 = T_{4s} \otimes T_{4p} \otimes T_{4d} \tag{B.7}$$

For $\Lambda = \pm 1$

$$T_{4p} = \sqrt{\frac{1}{2}} \begin{pmatrix} 1 & -1 \\ 1 & 1 \end{pmatrix} \begin{vmatrix} \overline{3p}_{-1} 4p_0^\dagger \rangle \\ \overline{3p}_0 4p_1^\dagger \rangle \end{vmatrix} \tag{B.8}$$

$$T_{3d} = \sqrt{\frac{1}{150}} \begin{pmatrix} \sqrt{60} & -\sqrt{80} & \sqrt{10} \\ \sqrt{75} & 5 & -\sqrt{50} \\ -\sqrt{15} & -\sqrt{45} & -\sqrt{90} \end{pmatrix} \begin{vmatrix} \overline{3p}_{-1} 3d_0^\dagger \rangle \\ \overline{3p}_0 3d_1^\dagger \rangle \\ \overline{3p}_1 3d_2^\dagger \rangle \end{vmatrix} \tag{B.9}$$

For $\Lambda = \pm 2$,

$$T_{3d} = \sqrt{\frac{1}{3}} \begin{pmatrix} \sqrt{2} & -1 \\ 1 & \sqrt{2} \end{pmatrix} \begin{vmatrix} \overline{3p}_{-1} 4p_1^\dagger \rangle \\ \overline{3p}_0 4p_2^\dagger \rangle \end{vmatrix} \tag{B.10}$$

B.2 Diabatization

$$\begin{pmatrix} A & \\ & B \end{pmatrix} = U^\dagger \begin{pmatrix} \alpha & \delta \\ \delta & \beta \end{pmatrix} U \tag{B.11}$$

where U is the rotation matrix defined as:

$$U = \begin{pmatrix} \cos\theta & -\sin\theta \\ \sin\theta & \cos\theta \end{pmatrix} \tag{B.12}$$

Therefore we have:

$$\begin{pmatrix} A & \\ & B \end{pmatrix} = \begin{pmatrix} \cos\theta & \sin\theta \\ -\sin\theta & \cos\theta \end{pmatrix} \begin{pmatrix} \alpha & \delta \\ \delta & \beta \end{pmatrix} \begin{pmatrix} \cos\theta & -\sin\theta \\ \sin\theta & \cos\theta \end{pmatrix} \tag{B.13}$$

$$= \begin{pmatrix} \cos\theta & \sin\theta \\ -\sin\theta & \cos\theta \end{pmatrix} \begin{pmatrix} \alpha\cos\theta + \delta\sin\theta & -\alpha\sin\theta + \delta\cos\theta \\ \delta\cos\theta + \beta\sin\theta & -\delta\sin\theta + \beta\cos\theta \end{pmatrix} \tag{B.14}$$

$$= \begin{pmatrix} \alpha\cos^2\theta + 2\delta\cos\theta\sin\theta + \beta\sin^2\theta & \delta(\cos^2\theta - \sin^2\theta) + \sin\theta\cos\theta(-\alpha+\beta) \\ \delta(\cos^2\theta - \sin^2\theta) + \sin\theta\cos\theta(-\alpha+\beta) & \alpha\sin^2\theta - 2\delta\cos\theta\sin\theta + \beta\cos^2\theta \end{pmatrix} \tag{B.15}$$

For $\delta(\cos^2\theta - \sin^2\theta) + \sin\theta\cos\theta(-\alpha+\beta) = 0$ we have:

$$\delta(\sin^2\theta - \cos^2\theta) = (\beta - \alpha)\sin\theta\cos\theta \tag{B.16}$$

$$\beta - \alpha = \frac{\delta(\sin^2\theta - \cos^2\theta)}{\sin\theta\cos\theta} \tag{B.17}$$

$$\beta = \alpha + \delta\left(1 - \frac{1}{\tan\theta}\right) \tag{B.18}$$

Appendix C

Computational Techniques

For both models we are going to neglect spin-orbit couplings so that singlet and triplet states can be treated separately. This is particularly helpful while performing energy minimization with the HPP model because neglecting spin-orbit couplings reduces the configuration space by half. For the HPP model we used conjugate gradient methods based on numerical derivatives and for the DIM model, as it is not difficult to get energy derivatives, we performed damped molecular dynamics.

C.1 Conjugate Gradient Method for Energy Minimization

It is tempting to use the steepest decent method in which minima is reached by taking small steps in the direction of decreasing gradient. This is adequate but not efficient as shown in figure C.1(a) where the many steps are taken to reach the bottom of the valley. Also, it is important that we look for the minima at the right angle, which necessarily will not lead us to the minimum. Therefore, we need another method.

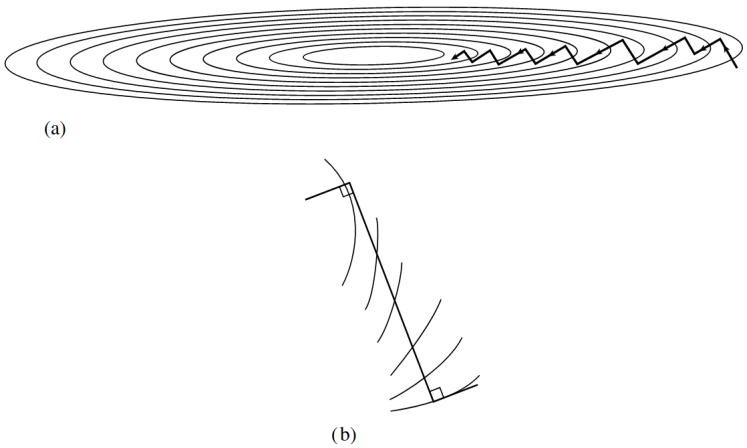

Figure C.1: (a) Steepest decent method in a long, narrow "valley" (b) Magnified one step in which at the starting point a perpendicular is drawn to the contour, and traverses in the straight line until minimum is reached.

Therefore, we really want a method not down the new gradient, but rather in the direction that is somewhat constructed to be *conjugate* to the old gradient, and as far as possible, to all previous directions traversed. This can be done using a *conjugate gradient* method.

A conjugate gradient method is usually employed for minimizing a function which can be approximated

by a quadratic form given by:

$$\begin{aligned} f(\mathbf{x}) &= f(\mathbf{P}) + \sum_i \frac{\partial f}{\partial x_i} x_i + \frac{1}{2} \sum_{i,j} \frac{\partial^2 f}{\partial x_i \partial x_j} x_i x_j + \dots \\ &\approx c - \mathbf{b}.\mathbf{x} + \frac{1}{2} \mathbf{x}.\mathbf{A}.\mathbf{x} \end{aligned} \tag{C.1}$$

following that the gradient is defined as,

$$\nabla f = \mathbf{A}.\mathbf{x} - \mathbf{b} \tag{C.2}$$

and for minimum $\delta(\nabla f) \to 0$.

For a given initial vector $\mathbf{g}_0$, the conjugate gradient method construct a sequence of two re-occurring vectors,

$$g_{i+1} = g_i - \lambda_i \mathbf{A}.\mathbf{h}_i \tag{C.3}$$

$$h_{i+1} = g_{i+1} + \gamma_i \mathbf{h}_i \tag{C.4}$$

for $h_0 = g_0$ and $i = 0, 1, 2, \dots$. With the vectors being orthogonal and conjugate, $\mathbf{g}_i.\mathbf{g}_j = 0$, $\mathbf{h}_i.\mathbf{A}.\mathbf{h}_j = 0$ and $\mathbf{g}_i.\mathbf{h}_j = 0$ for $j < i$. The scalar quantities can be defined as,

$$\lambda_i = \frac{\mathbf{g}_i.\mathbf{g}_i}{\mathbf{h}_i.\mathbf{A}.\mathbf{h}_i} = \frac{\mathbf{g}_i.\mathbf{h}_i}{\mathbf{h}_i.\mathbf{A}.\mathbf{h}_i} \tag{C.5}$$

$$\gamma_i = \frac{\mathbf{g}_{i+1}.\mathbf{g}_{i+1}}{\mathbf{g}_i.\mathbf{g}_i} \tag{C.6}$$

With the knowledge of Hessian matrix $\mathbf{A}$, using equation C.3 to find successively conjugate directions $\mathbf{h}_i$ along which to line-minimize. After N iterations the minimum would be reached.

However, the true power of this method lies in the fact that we can obtain the minimum without the knowledge of matrix $\mathbf{A}$. This can be done by having $g_i = -\nabla f(\mathbf{P}_i)$ for some point $\mathbf{P}_i$ from the quadratic function. Now, looking for a minimum in the direction h_i of f located at some point $\mathbf{P}_{i+1}$ and then setting $\mathbf{g}_{i+1} = -\nabla f(\mathbf{P}_{i+1})$. This is true when λ is chosen to take us to the line minimum.

With the knowledge of $\mathbf{g}_{i+1}$ and γ, using equation C.3 we can get h_{i+1} and then with iterative method we can reach the minimum. The algorithm defined so far is the original Fletcher-Reeves version. The expression of γ_i proposed by Polak and Ribiere is used in my work, namely:

$$\gamma_i = \frac{(\mathbf{g}_{i+1} - \mathbf{g}_i).\mathbf{g}_{i+1}}{\mathbf{g}_i.\mathbf{g}_i} \tag{C.7}$$

Another important point about the line search algorithm is that the accuracy of the conjugate gradient method depends on the efficiency of the minimum search algorithm for a line. In this work, the method implemented has compromised accuracy over speed, i.e., it is not a mid point search algorithm for the minimum. This is adapted from the book Numerical recipes in C.

C.2 Simplified PEC evaluation technique

As we shall see with the help of the HPP model for the smallest clusters, the geometric structure of pure Ar clusters in their lowest triplet state is dominated by an Ar_2^* carrying most of the electronic excitation and coupled to $N-2$ Ar atoms in their ground state. This suggests that we can represent the potential energy

surface (PES) in a simplified way by considering two- and three-body interactions only. Such an approximation resembles the DIM method, as we assign an approximate electronic configuration but we do not consider the possibility for couplings with other equivalent configuration. We thus consider a configuration such that atoms 1 and 2 form the excimer and are tightly bound at a distance close to the equilibrium distance of Ar_2^* in its lowest $^3\Sigma_u^+$ state while the other atoms $i \geq 3$ are in their ^1S ground state. We express the total energy of the whole system E_N as:

$$E_N = E_2^*(1,2) + \sum_i^N (E_3^*(1,2,i) - E_2^*(1,2)) + \sum_{i<j}^N E_2^0(i,j) \tag{C.8}$$

where $E_2^*(1,2)$ is the energy of the Ar_2^* excimer in its lowest $^3\Sigma_u^+$ state, $E_3^*(1,2,i)$ is the energy of trimer made of atoms $(1,2,i)$ in its lowest triplet state and $E_2^0(i,j)$ is the energy of the Ar_2 dimer in its ground $^1\Sigma_g^+$ state. The 3-body term for ground state atoms is neglected here, like for all calculations in this thesis.

To perform the calculation, we have simply evaluated the dimer energies $E_2^*(1,2)$ and $E_2^0(i,j)$ with respect to their interatomic distances distributed on a radial grid of points and the evaluation proceeds by cubic splines interpolation, which provides us with the energy and force in a consistent way. We have applied a similar method for the two-dimensional PES of the trimer assuming the dimer to be at its equilibrium distance. The quantity $E_3^*(1,2,i) - E_2^*(1,2)$ is thus evaluated on a grid defined by the distance of atom R_i to the centre of mass and the cosine of the angle θ_i between the vector $\mathbf{R}_i$ and the dimer axis vector $\mathbf{R}_{12}$. Note that the symmetry of the trimer surface allows us to restrict θ_i in the interval $[0, \pi/2]$. Since the PES varies more rapidly for small R_i and small θ_i, the grid is denser in this area. The PES is interpolated by means of a two-dimensional cubic spline on the grid.

The comparison of such an energy decomposition with the exact energy obtained from the HPP model tells us how good is such an approximation. For large clusters, this simplified model allows us to initialize quickly an initial guess for the cluster geometry, which is much faster than the HPP energy evaluation.

C.3 Damped Molecular Dynamics

Damped molecular dynamics might not be the most elegant method, however it gives the possibility to explore the potential energy surface to look for minima.

In this method rather than propagating the velocities obtained from the Beeman propagator, we set the kinetic energy to zero when the change in kinetic energy is very small. This implies that the system always tends to the lowest energy.

C.4 Beeman Algorithm

There are several integration algorithms based on Taylor's expansion of $\mathbf{R}_a(t+\delta t)$ and $\mathbf{V}_a(t)$. The integrator should be precise and fast, preserve the conservation of momentum and total energy, even for large time steps δt and should be computationally cheap. The Beeman predictor-correcter method is suitable to solve first-order differential equations. It is based verlet-velocity algorithms. In this method, the coordinates at the next time step is calculated based on the knowledge of the coordinates at the previous time step, velocities are corrected while maintaining the total energy of the system.

At each time step the Beeman algorithm evaluates the coordinates at the following time steps according

to:

$$\mathbf{R}_a(t+\delta t) = \mathbf{R}_a(t) + \mathbf{V}_a(t)\delta t + \frac{4\mathbf{F}_a(t) - \mathbf{F}_a(t-\delta t)}{6M_a}(\delta t)^2 \tag{C.9}$$

This extrapolation requires the knowledge of velocities which are obtained using;

$$\mathbf{V}_a(t) = \mathbf{V}_a(t-\delta t) + \frac{2\mathbf{F}_a(t) + 5\mathbf{F}_a(t-\delta t) - \mathbf{F}_a(t-2\delta t)}{6M_a}\delta t \tag{C.10}$$

The evaluation of positions and velocities for each step requires the forces acting on each atom. For initialisation, we know the atomic positions at time t_0 when forces are evaluated. To determine the position at $t_0+\delta t$, we use a lower-order interpolation method which involves the knowledge of forces at t_0 as:

$$\mathbf{R}_a(t_0+\delta t) = \mathbf{R}_a(t_0) + \mathbf{V}_a(t_0)\delta t + \frac{\mathbf{F}_a(t_0)}{2M_a}(\delta t)^2 \tag{C.11}$$

Similarly, to determine the velocity at $t_0+\delta t$, we use the simplified extrapolation to get the velocity using the forces evaluated at time t_0. The velocity evaluation is;

$$\mathbf{V}_a(t_0+\delta t) = \mathbf{V}_a(t_0) + \frac{\mathbf{F}_a(t_0)}{M_a}\delta t \tag{C.12}$$

This initialisation process is done only at the beginning of the dynamics.

C.5 Calculation of Forces

The forces are calculated analytically by computing the derivatives of the energy with respect to the atomic positions. In state i, the force $\mathbf{F}_a$ acting on atom a corresponds to the derivative of the potential energy with respect to its coordinates as;

$$\mathbf{F}_a = -\frac{\partial E_i}{\partial \mathbf{R}_a} \tag{C.13}$$

To evaluate this, we start from the eigenvalue equation $(H_e - E_i)|\phi_i\rangle = 0$ which is projected onto the atomic basis set $|m\rangle$ which is considered to be orthonormal. Therefore we have, H_{mn} as the matrix elements of the Hamiltonain and S_{mn} as the overlap matrix elements. The coefficients c_{im} which give the decomposition of the molecular orbital i on the atomic basis functions. Taking the derivative of this with respect to atomic positions (X) and projecting it onto state $\langle\phi_j|$;

$$\underbrace{\sum_{mn} c^*_{im} S_{mn} c_{in}}_{\langle\phi_j|\phi_i\rangle=1} E_i^X = \sum_{mn} c^*_{im}(H_{mn} - E_i S^X_{mn})c_{in} + \sum_n c^X_{in} \underbrace{\sum_m c^*_{jm}(H_{mn} - E_i S_{mn})}_{=0} \tag{C.14}$$

In the first term, by orthonormality, we have unity and the last term vanishes because we recognize the secular equation. We thus get the expression of the forces which act on the atoms of the system along the axis $\mathbf{u}_X$;

$$F_X = -E_i^X = -\sum_{mn} c^*_{in}(H^X_{mn} - E_i S^X_{mn})c_{im} \tag{C.15}$$

The elements H_{mn} are obtained by diagonalising the DIM Hamiltonian and the overlap S_{mn} between the two atoms is taken to be unity.

Appendix D

Dynamics

D.1 Coefficient evolution

Here we are going to solve the Time-Dependent Schrodinger equation (TDSE) within the Born-Oppenheimer approximation. Let's start with the definition of TDSE as (within the Schrodinger picture),

$$i\hbar\frac{\partial}{\partial t}|\Psi_S(t)\rangle = \hat{H}(t)|\Psi_S(t)\rangle \tag{D.1}$$

Now we define the Hamiltonian as, $\hat{H}(t) = \hat{H}_0 + \delta\hat{H}(t)$ in perturbation theory where $\hat{H}_0 = \langle\hat{H}\rangle$ is the time averaged Hamiltonian and $\delta\hat{H}(t) = \hat{H}(t) - \langle\hat{H}\rangle$. Then the wave function is given by $|\Psi_S(t)\rangle = \sum_\alpha C_\alpha(t)|\alpha\rangle$ with $|\alpha\rangle$ being the eigenstates obtained by diagonalising $\hat{H}_0$.
Converting the wave function to interaction picture,

$$|\Psi_S(t)\rangle = \hat{U}_0(t,t_0)|\Psi_I(t)\rangle \tag{D.2}$$

where $\hat{U}_0(t,t_0) = \exp\left\{i\hat{H}_0(t-t_0)\right\}$. Within the interaction picture, the wave function can be decomposed over adiabatic basis functions as,

$$|\Psi_I(t)\rangle = \sum_\alpha e^{-iE_\alpha(t-t_0)}C_\alpha(t)|\alpha\rangle \tag{D.3}$$

Now, using D.2 in equation D.1 we get,

$$i\hbar\frac{\partial}{\partial t}(\hat{U}_0(t,t_0)|\Psi_I(t)\rangle) = \hat{H}(t)\hat{U}_0(t,t_0)|\Psi_I(t)\rangle \tag{D.4}$$

$$\begin{aligned}
\frac{\partial}{\partial t}\hat{U}_0(t,t_0)|\Psi_I(t)\rangle + \hat{U}_0(t,t_0)\frac{\partial}{\partial t}|\Psi_I(t)\rangle &= -i(\hat{H}_0 + \delta\hat{H}(t))\hat{U}_0(t,t_0)|\Psi_I(t)\rangle \\
\hat{U}_0(t,t_0)\frac{\partial}{\partial t}|\Psi_I(t)\rangle &= -i\delta\hat{H}(t)\hat{U}_0(t,t_0)|\Psi_I(t)\rangle \\
\frac{\partial}{\partial t}|\Psi_I(t)\rangle &= -i\underbrace{\hat{U}_0^\dagger(t,t_0)\delta\hat{H}(t)\hat{U}_0(t,t_0)}_{\hat{W}(t)}|\Psi_I(t)\rangle
\end{aligned}$$

we get,

$$\frac{\partial}{\partial t}|\Psi_I(t)\rangle = -i\hat{W}(t)|\Psi_I(t)\rangle \tag{D.5}$$

On solving this differential equation we get:

$$|\Psi_I(t)\rangle = \hat{U}_I(t,t_0)|\Psi_I(t_0)\rangle \tag{D.6}$$

where, the time displacement unitary operator is defined as:

$$\hat{U}_I(t,t_0) = \exp\left\{-i\int_{t_0}^{t}\hat{W}(t')dt'\right\} \tag{D.7}$$

putting this in equation D.6 and projecting onto eigenstate $\langle\beta|$ we get,

$$e^{iE_\beta(t-t_0)}C_\beta(t) = \langle\beta|\hat{U}_I(t,t_0)\sum_\alpha C_\alpha(t_0)|\alpha\rangle \tag{D.8}$$

On doing some rearrangements we get,

$$C_\beta(t) = \langle\beta|\hat{U}_I(t,t_0)\sum_\alpha e^{-iE_\beta(t-t_0)}C_\alpha(t_0)|\alpha\rangle \tag{D.9}$$

$$= \sum_\alpha e^{-iE_\beta(t-t_0)}\langle\beta|\hat{U}_I(t,t_0)|\alpha\rangle C_\alpha(t_0) \tag{D.10}$$

To evaluate $\hat{U}_I(t,t_0)$, we are going to use Magnus Expansion as follows. Let's define,

$$\hat{U}_I(t,t_0) = e^{-i\bar{H}T} \tag{D.11}$$

where $T = t - t_0$,

$$\bar{H} = \bar{H}^{(1)} + \bar{H}^{(2)} + \bar{H}^{(3)} + \dots \tag{D.12}$$

and

$$\bar{H}^{(1)} = \frac{1}{T}\int_{t_0}^{t}\hat{W}(u)du$$

$$\bar{H}^{(2)} = \frac{1}{2iT}\int_{t_0}^{t_1}du\int_{t_0}^{t}du'\left[\hat{W}(u),\hat{W}(u')\right]$$

$$\dots$$

In this approximation we are going to consider $\left[\hat{W}(u),\hat{W}(u')\right] \approx 0$. With this approximation, the unitary operator is approximated as:

$$\hat{U}_I(t,t_0) \approx \exp\left\{-i\int_{t_0}^{t}\hat{U}_0^\dagger\delta\hat{H}(u)\hat{U}_0du\right\} = \exp\left\{-i\hat{K}(t)\right\} \tag{D.13}$$

where the matrix elements of $\hat{K}(t)$ in the basis $|\alpha\rangle$ are:

$$K_{\beta\alpha}(t) = \langle\beta|\hat{K}(t)|\alpha\rangle \tag{D.14}$$

If the basis set $|ji$ diagonalizes $\hat{K}(t)$ then we have,

$$\hat{K}(t) = \sum_j |j\rangle\lambda_j(t)\langle j| \tag{D.15}$$

Doing Taylor expansion of the exponential,

$$\begin{aligned}\exp\left\{-i\hat{K}(t)\right\} &= \mathbb{1} + (-i)\hat{K}(t) + (-i)^2\frac{\hat{K}^2(t)}{2} + \dots \\ &= \sum_j |j\rangle e^{-i\lambda_j(t)}\langle j|\end{aligned}$$

Now we have the coefficient evolution equation given by:

$$\begin{aligned}C_\beta(t) &= \sum_{\alpha,j} e^{-iE_\beta(t-t_0)}\langle\beta|j\rangle e^{-i\lambda_j(t)}\langle j|\alpha\rangle C_\alpha(t_0) \\ &= \sum_{\alpha,j} e^{-iE_\beta(t-t_0)}Q_{\beta j}e^{-i\lambda_j(t)}Q_{j\alpha}C_\alpha(t_0) \\ &= \sum_{\alpha} e^{-iE_\beta(t-t_0)}M_{\beta\alpha}(t)C_\alpha(t_0)\end{aligned}$$

Hence, we get the coefficients as,

$$C_\beta(t) = \sum_{\alpha} e^{-iE_\beta(t-t_0)}M_{\beta\alpha}(t)C_\alpha(t_0) \tag{D.16}$$

Modelling Excited Argon Clusters: Geometries, Spectroscopic Properties and Non-Adiabatic Relaxation Dynamics

We investigate Ar_2^* potential energy curves (PECs) using different *ab initio* techniques in MOLCAS, quantum chemistry code. We find that MRCI calculations give the best 4*s* PECs. We also studied the geometry of Ar_3^* in its lowest triplet state using CASPT2, which is different from the previous DIM model study by Naumkin and Wales. We further investigate this and the geometry of the lowest excitonic levels of small argon clusters, $Ar_{N=3-13}$, using the Hole-Particle Pseudopotential (HPP) formalism introduced by Dupláa and Spiegelmann. This formalism allows us to model the excited states associated with Rydberg orbitals with higher accuracy than previous DIM studies. Using HPP we predict the excitation to localise mostly on two atoms rather than three, for the relaxed geometry isomer of the lowest triplet state. We further show the effect of the diabatisation of PECs used to parameterise the DIM model using an additional *ad hoc* state, which uncouples the 4s $^{1,3}\Sigma_g^+$ state from the higher excited states. Using this Di-DIM, we observe symmetry breaking, similar to HPP. Following that, we propose Excitation Dynamics with Quantum Transition on the whole Di-DIM basis. Here, we give an algorithm for coefficient evolution based on time-averaged Hamiltonian to minimise the perturbations. *On-the-fly* adiabatic PECs is evaluated using Di-DIM method on which a trajectory is evolved non-adiabatically. The SOC is included within the Di-DIM method. The FSSH is employed for hops between adiabatic surfaces. We use this method to study excitation evolution and fragmentation in a small neutral argon cluster, ($N = 3,7$), which has not been done previously. We observe quick excitation localisation on an excimer followed by slow relaxation of the exciton. We observe that the nature and the number of states used as the input for DIM influences significantly the outcome of the relaxation dynamics.

Modélisation d'agregat d'Argon Excité : Géométries, Propriétés Spectroscopiques et Dynamique de Relaxation Non Adiabatique

Nous étudions les courbes d'énergie potentielle (PEC) Ar_2^* en utilisant différentes techniques *ab initio* intégrées au code de chimie quantique MOLCAS. Nous constatons que les calculs MRCI donnent les meilleurs PEC pou l'état 4*s*. Nous avons également étudié la géométrie de Ar_3^* dans son état de triplet le plus bas en utilisant CASPT2, qui diffère de l'étude précédente du modèle DIM par Naumkin et Wales. Nous étudions en plus la géométrie des niveaux excitoniques les plus bas pour des petits agrégats d'argon, $Ar_{N=3-13}$, au moyen du formalisme Hole-Particle Pseudopotential (HPP) introduit par Dupláa et Spiegelmann. Ce formalisme nous permet de modéliser les états excités associés aux orbitales de Rydberg avec une plus grande précision que les études DIM précédentes. En utilisant HPP, nous prédisons que l'excitation se situe principalement sur deux atomes plutôt que sur trois, pour l'isomère à géométrie relaxée de l'état triplet le plus bas. Nous montrons ensuite l'effet de la diabatisation des PEC utilisés pour paramétrer le modèle DIM au moyen d'un état *ad hoc* supplémentaire, qui découple l'état 4s $^{1,3}\Sigma_g^+$ de l'état états excités supérieurs. En utilisant ce Di-DIM, nous observons une brisure de symétrie, similaire à HPP. Ensuite, nous étudions la dynamique d'excitation avec transition quantique à travers toute la base Di-DIM. Ici, nous donnons un algorithme d'évolution des coefficients sur la base d'un hamiltonien moyenné dans le temps pour minimiser les perturbations. *On-the-fly* adiabatique PECs est évalué à l'aide de la méthode Di-DIM sur laquelle une trajectoire évolue de manière non adiabatique. Le SOC est inclus dans la méthode Di-DIM. Le FSSH est utilisé pour les sauts entre les surfaces adiabatiques. Nous utilisons cette méthode pour étudier l'évolution de l'excitation et la fragmentation dans un petit agregat d'argon neutre, ($N = 3,7$), ce qui n'a pas été fait auparavant. Nous observons une localisation rapide de l'excitation sur un excimère suivie d'une relaxation lente de l'exciton. Nous observons que la nature et le nombre d'états utilisés comme entrée pour DIM influencent de manière significative le résultat de la dynamique de relaxation.

KEYWORDS: Self-Trapped Excitons(STE's), Hole Patricle Pseudopotential (HPP), Rare-Gas Clusters (RGC), Argon Systems, Molecular Dynamics (MD), Diatomic-in-Molecule (DIM), Electronic Structure Calculation, Excitation dynamics, Mixed Classical Quantum Dynamics (MCQD), Excited Rare-Gas Clusters, Surface hopping, Time Averaged Hamiltonian, Non-adiabatic relaxation dynamics

Laboratory

Centre de recherche sur les Ions, les MAteriaux et la Photonique
CIMAP - GANIL
CEA/CNRS/ENSICAEN/UNICAEN
Boulevard Henri Becquerel, BP5133, 14070 CAEN cedex 5, France